UNIVERSITY OF LONDON THESIS

Degree PhD Year 2007 Name of Author WATARI, Moyu

In-plane Mechanochemistry at Model Biological Interfaces

BY

Moyu Watari

London Centre for Nanotechnology and Department of Medicine
University College London

Supervisors:
Dr. Rachel A. M^{c}Kendry
Prof. Dr. Michael A. Horton

Thesis submitted for the degree of Doctor of Philosophy at the University of London

July 2007

ProQuest LLC
789 East Eisenhower Parkway
P.O. Box 1346
Ann Arbor, MI 48106-1346

I, Moyu Watari, confirm that the work presented in this thesis is my own. Where information has been derived from other sources, I confirm that this has been indicated in the thesis.

Abstract

When a chemical or biological reaction occurs on one surface of a microfabricated cantilever, a surface stress is generated resulting in cantilever bending motion. This signal transduction mechanism has recently been employed to detect DNA hybridisation and protein recognition, and has attracted much attention as a novel label-free biosensor. However, the biosensing application of cantilevers can best be realised if we develop a fundamental understanding of *what causes the cantilever to bend?* In this thesis, I have performed systematic pH titration experiments using various self-assembled monolayers (SAMs) of alkanethiols $HS(CH_2)_n X$ on gold coated cantilevers, which represent a model organic system by virtue of the relatively well-defined surface chemistry. Differential surface stress measurements were taken to probe the biochemically specific interfacial forces, which were found to critically depend upon multiple factors including pH, ion species, and ionic strength of the aqueous environment, as well as chain length and terminal functional group of SAMs. These findings provide important insights into the fundamental origins of surface stress generation, which have broad implications in the study of biochemical interfaces from molecular thin films to cellular membranes.

父さんと、母さんへ。

命、短し 一 恋せよ、乙女！

From: "To Live" directed by Akira Kurosawa /
Lyrics by Fumio Hayasaka (1952)

Acknowledgements

This thesis would not have been possible without the support and encouragement of many people.

First and foremost, I must thank my supervisors Dr. Rachel McKendry and Prof. Mike Horton. It is only thanks to their academic guidance that I was able to complete my PhD research. I am grateful for their support in independent thinking and mechanical work as much as it was possible as a student. In particular, I would like to thank Dr. McKendry for her tireless guidance and encouragements, as well as for giving me the opportunity to work with cantilevers.

The collaboration with Jane Galbraith was a rare gift. I would like to thank Jane, who allowed me to share her knowledge of statistical science for the sake of statistical science. I would also like to thank her husband Dr. Rex Galbraith who brought me to her.

The highly optimised laboratory conditions at the IBM Rüschlikon enabled me to prepare high quality cantilever samples. I would like to thank Prof. Christoph Gerber, Dr. Hans Peter Lang, Prof. Martin Hegner, Dr. Emmanuel Delamarche, Dr. Michel Despont, and Ute Drechsler for their valuable support. In particular, I would like to thank Marilyne Sousa, who acquired excellent ellipsometry and XPS data although she had a high temperature and flu.

I would like to thank Prof. Alex Shluger and his group members including Dr. Maria Sushko, Dr. Andrej Gal, and Alexandros Kalampodikis, for the initial simulation projects. I would also like to thank Prof. John Harding, Dr. Dorothy Duffy, and Prof. Gabriel Aeppli for their lively interests in cantilevers and the ongoing collaborative work.

I would like to thank Prof. T. Randall Lee and all his group members and in particular, Justin Moore, La-ongnuan Srisimbot, Andrew Tangonan, and Katherine Cimatu, who looked after me cordially during my stay in Houston. I am only sorry that the cantilever experiments did not work.

I would like to thank Dr. Joseph Ndieyira for his generous character and his competent advices in electrochemical methods.

I would like to thank Dr. McKendry's husband Dr. Torsten Strunz who has been providing a background support for this project. Thank you very much also to baby Ingrid who tolerated my visits during the writing-up phase.

I would like to thank Prof. Trevor Rayment who provided great scientific insights during my upgrade viva, which I have only started to capture now.

I would like to thank all current and former members of the BMC and the LCN, in particular: Macarena Blanco and Jaco de Groot with whom I had started the PhD project and who have finished their projects a long time ago; Brian Nicholls who has always been very helpful; Dr. Steve Nesbitt for his English humour I could not *not laugh* at (whenever I understood it); Dr. Patrick Mesquida for occasional after-work beers; Benjamin Dück for taking me to piano concerts; Nafeesa Noordeen and Dr. Tania Maffucci for the regularly shared lone-working hours; Dr. Gudrun Stenbeck and Dr. Guillaume Charras for their help with the initial cell project; Dr. Christian Riener for his initial help with cantilevers; Dr. Adham Ramadan, Dr. Belinda Haupt, Dr. Laurent Bozec, Marco Wenger, Yaron Silberberg, Dr. Andrew Pelling, Alejandra Donoso, and Remi Piccone for their sociality.

I would like to acknowledge that this project was a joint project with Dr. Ashwin Seshia, Dr. James Ransley, and Wenmiao Shu, financially supported by the IRC in Nanotechnology. I am also grateful for the further financial support provided by the BMC, the LCN, the Graduate School, and the Overseas Research Students Award Scheme.

I would like to thank my friends for their patience toward my antisocial behaviour, in particular over the last six months.

I would like to thank my parents, my grandparents, Izuru, Ko, Fumi, Raimund, and all other family members for their constant support.

Finally, I would like to thank Michael Neumann for the shared experiences in London.

Table of Contents

List of Abbreviations

AFM	atomic force microscopy
ANOVA	analysis of variance
DIC	differential interference contrast microscopy
DNA	deoxyribonucleic acid
DRIE	dry reactive ion etch
HDT	1-hexadecanethiol, $HS(CH_2)_{15}CH_3$
MHA	16-mercaptohexadecanoic acid, $HS(CH_2)_{15}COOH$
PSD	position sensitive detector
RCS	region of constant sum
SAM	self-assembled monolayer
SLD	superluminescent diode
XPS	x-ray photoelectron spectroscopy

1. Introduction

Biosensors are important for medical diagnostics, drug analysis, and environmental protection. Biosensors comprise energy transducers and molecularly selective chemical components (Cunningham 1998). The key requirements for biosensors include a simple, rapid, reversible, and continuous detection in non-invasive, physiological environments, via the use of miniaturised-integrated devices in array format and produced at low costs. In addition to the classical glucose sensors for diabetes (Clark et al. 1958), massively parallel DNA chips (Fodor et al. 1991), and surface plasmon resonance with its integrated microfluidics and sensor chip technology (Sjölander and Urbanicky 1991), represent examples of successfully commercialised laboratory research (Ramsay 1998).

Microfabricated cantilevers, which rely on the transduction of biochemically specific surface stress changes, represent mechanical transducers without a need for radio- or fluorescent labelling. Cantilevers offer all the favourable capabilities of microfabricated devices, including parallelisation, miniaturisation, integration, and mass production (Vettiger et al. 2000), and have attracted much attention as a novel label-free biosensor in recent years. The range of biological systems that have been probed on cantilevers extends from DNA (Fritz et al. 2000a; McKendry et al. 2002; Fritz et al. 2002; Mukhopadhyay et al. 2005; Shu et al. 2005) to proteins (Fritz et al. 2000a; Backmann et al. 2005; Wu et al. 2001; Savran et al. 2004), and cells (Ilic et al. 2001; Park et al. 2005) and their commercialisation has been advanced by several companies (for example, Veeco Instruments Inc., Santa Barbara, CA, U.S.A.; Concentris GmbH, Basel, Switzerland; Protiveris Inc., Rockville, MD, U.S.A.; Cantion Inc., Lyngby, Denmark). However, the fundamental question remains: *what causes the cantilever to bend?* Despite the increasing number of publications that report cantilever biosensing applications based on phenomenological observations, to-date, the science that underpins this mechanotransduction mechanism has been scarcely addressed (Brunt 1997; Godin 2004b). Indeed, a range of different technical and economical issues has lead the multiple cantilever array sensor systems to

be withdrawn from the market, including the Veeco Scentris used herein in 2004 and numerous other commercial products alike.

The aim of this work is therefore to investigate the basic mechanisms underlying the generation of mechanochemical surface stress changes at model biological interfaces using alkanethiol self-assembled monolayers (SAMs) on cantilever arrays. In contrast to inherently complex biomolecules, which have multiple functional and zwitterionic groups, alkanethiols form well-defined SAMs on gold surfaces, where the surface properties are controlled by the chain length and terminal group (Nuzzo and Allara 1983; Bain et al. 1989). In particular, the acid-base properties of carboxylic acid terminating SAMs such as 16-mercaptohexadecanoic acid ($HS(CH_2)_{15}COOH$, herein termed MHA), which can be controlled via the pH of the aqueous environment, offer an ideal system for fundamental studies with broad applicability to colloidal science, catalysis, protein folding and membrane biophysics. While acid-base reactions of SAMs have previously been studied on cantilevers, results have varied widely (Raiteri, Butt, and Grattarola 2000; Fritz et al. 2000b) and have been typically limited due to either lack of mechanical sensitivity or the use of only single cantilever measurements. Single cantilever measurements are notoriously problematic since non-specific reactions, including changes in temperature, refractive index and reactions occurring on the non-functionalised sites of a cantilever can dominate the value of an absolute signal. Differential measurements using in-situ reference cantilevers tailored with control, non-reactive coatings have been shown to be essential to detect chemically specific surface forces and enable multiple reactions to be probed in parallel, under similar experimental conditions (Fritz et al. 2000a; Fritz et al. 2000b; McKendry et al. 2002; Shu et al. 2005).

The structure of this thesis is the following. Chapters 2, 3, and 4 are introductory. Basic properties of model alkanethiol SAMs will be reviewed in Chapter 2, focusing on the formation and equilibrium structure of long-chain SAMs of 1-hexadecanethiol ($HS(CH_2)_{15}CH_3$, herein termed HDT) and MHA. Since acid/base reactions of MHA on cantilevers and phosphoric acid in the aqueous phase are the most important chemical reactions involved in this work, Chapter 3 describes the basic concepts of acid/base chemistry, first in dilute aqueous solutions and then at the surface of a solid. In Chapter 4, surface stress is introduced as an interfacial excess quantity, first in relation to the theory of elasticity and then in relation to the theory of mechanochemistry. Chapter 5 details the materials and methods developed for measurements of surface stress. The results are outlined in Chapters 6 - 10. In Chapter 6, results obtained from investigations of measurement variabilities

are presented. Thereafter, Chapter 7 and Chapter 8 address the important roles of the aqueous environment, including the pH, ionic strength, and cations and anions in the generation of mechanochemical surface forces. Chapter 9 and Chapter 10 investigate the role of chemical structure of SAMs themselves, including acidic and basic terminal functionalities and different chain lengths of SAMs. Finally, the description of a global force balance model to describe surface stress measurements and future perspectives are presented in the final Chapter 11.

2. Model Self-Assembled Monolayers on Au(111)

The immense complexity of biochemical assemblies is fascinating. Nature has evolved biomolecules that have multiple and zwitterionic functional groups and self-assemble to form structures of higher order, from genes, proteins, to living cells (Watari 2003). In contrast, self-assembled monolayers (SAMs) of simple *n*-alkanethiols on Au(111), which form ordered and densely packed organic membranes with well-controlled surface chemistry and mechanical properties, provide model biological surfaces for fundamental studies. This chapter gives an overview of the basic properties of model alkanethiol SAMs, focusing on the formation and structure of long-chain hexadecanethiol ($HS(CH_2)_{15}CH_3$, herein termed HDT) and mercaptohexadecanoic acid ($HS(CH_2)_{15}COOH$, herein termed MHA).

2.1 Structural Components

Alkanethiol SAMs on Au(111) are two-dimensional molecular assemblies formed upon the spontaneous adsorption of sulphur atoms onto a gold surface, followed by the lateral packing of alkyl chains, with a net adsorption energy of −5 kcal/mol (Ulman 1996). The simplicity of these SAMs results from the low number of structural components: the gold surface, sulphur atoms, alkyl chains, and terminal functional groups (Fig. 2.1).

The Au(111) surface with its hexagonally close packed gold atoms has the lowest free energy. When alkanethiol molecules chemisorb onto the gold surface from solution, the resultant SAMs form a commensurate $(\sqrt{3}\times\sqrt{3})\,R\,30°$ structure. However the nature of the Au–S bond is yet not fully understood, and the electronegative sulphur atom is thought to cause the bond to be polar, with a bond strength of about 45 kcal/mol (Ulman 1996; Schreiber 2000). Hydrocarbon groups are non-polar, thus densely packed alkyl chains interact with one another via the attractive van-der-Waals interactions, with an interaction energy of about 1.5 kcal/mol (Dubois and Nuzzo 1992). The extent of the order and the rigidity, or more appropriately the softness, of SAMs is determined primarily by the length of the alkyl chains. Long-

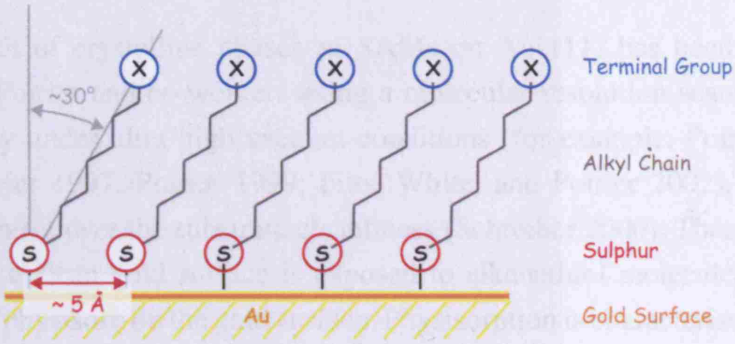

Fig. 2.1. Schematic of a SAM of simple alkanethiols on gold. A single thiol molecule consists of a sulphur atom, an alkyl chain, and a terminal functionality *X*.

chain SAMs with more than about ten carbon atoms in the chain are more ordered and solid-like, whereas shorter chain SAMs are more disordered, and fluid-like. Terminal groups form the surface layer of highly ordered SAMs, therefore determine the chemical functionality of these SAMs. Though at room temperature, they exhibit gauche defects thus do not contribute to the lateral packing of SAMs (Ulman 1996). In addition to the most simple, non-polar methyl terminal group CH_3, various other terminal groups are commonly used, including polar and ionisable terminal groups such as carboxylic acid COOH, hydroxyl OH, and amine NH_2, although in principle, virtually any organic compound may be covalently attached to the alkyl chain in order to tailor the chemical functionality of the SAM (Schreiber 2000).

The growth and structure of SAMs on Au(111) depend on the forces that act between molecules, atoms, and ions present at the fluid/SAM/Au/bulk cantilever interfaces. At equilibrium, these interfacial forces are balanced and the molecules, atoms, and ions assume their equilibrium distances. Surface stress is the in-plane component of these interfacial forces transduced onto the bulk cantilever material. Therefore, understanding the origins of surface stress requires an understanding of the interfacial forces that drive the self-assembly. The following sections give an overview of the most basic properties of these simple SAMs, however, details are referred to the literature (for example, Ulman 1991; Schreiber 2000; Dubois and Nuzzo 1992; Schwartz 2001; Poirier 1997; Vericat, Vela, and Salvarezza 2005).

2.2 Growth

The growth of crystalline phases of SAMs on Au(111) has been directly visualised by Poirier and co-workers using a molecular resolution scanning tunneling microscopy under ultra high vacuum conditions (for example, Poirier and Pylant 1996; Poirier 1997; Poirier 1999; Fitts, White, and Poirier 2002), which offer a precise control over the substrate cleanliness (Schreiber 2000). These studies show that when a clean gold surface is exposed to alkanethiol molecules, initially, the molecules physisorb on the gold surface. Physisorption is characterised by weak and non-specific van der Waals interactions, and occurs as a function of the mobility of the alkanethiols in the vapour phase. The strength of physisorption increases with contact area, that is the alkyl chain length. Subsequently, the sulphur head group chemisorbs on the gold surface. Chemisorption is characterised by the spontaneous formation of strong adsorbate-surface chemical bond, and occurs as a function of the residence time and the density of alkanethiol molecules on the gold surface.

At a very low surface coverage close to zero, the average distance between two alkanethiol molecules is large. In this so-called 'lattice gas' phase, there will be no interaction between the alkanethiol molecules. The interaction between an alkanethiol molecule and the gold surface is governed by the strong Au–S bond, and the weak van der Waals physisorption of the alkyl chain onto the gold surface. Under these conditions the molecular axis of the physisorbed molecules will be randomly distributed.

As the surface coverage increases, the average distance between two alkanethiol molecules decreases, and so the interaction between the alkanethiol molecules increases. At a normalised surface coverage of about 0.26 monolayers (ML) with respect to the saturation coverage, the commensurate 'lying-down' phase islands start to nucleate at the ridges of the so-called herringbone structure in equilibrium with the lattice gas phase, whereby the sulphur atoms are bound in the next nearest neighbour threefold-hollow sites and the molecular axis aligned with the surface plane. For decanethiol with a total number of ten carbon atoms per molecule, for example, a rectangular $c(\sqrt{3}\times 23)$ unit cell was observed, which corresponds to a molecular density of 82.8 $Å^2$ per molecule (Poirier 1999; Balzer et al. 1997).

Beyond the 'lying-down' phase, the 'stacked-lying-down' phases start and are characterised by the decreasing distance between the sulphur atoms and increased out-of-plane interdigitation of the alkyl chains. The interdigitation of the alkyl chains cause discreteness of the stacked-lying-down phases. For decanethiol, Poirier

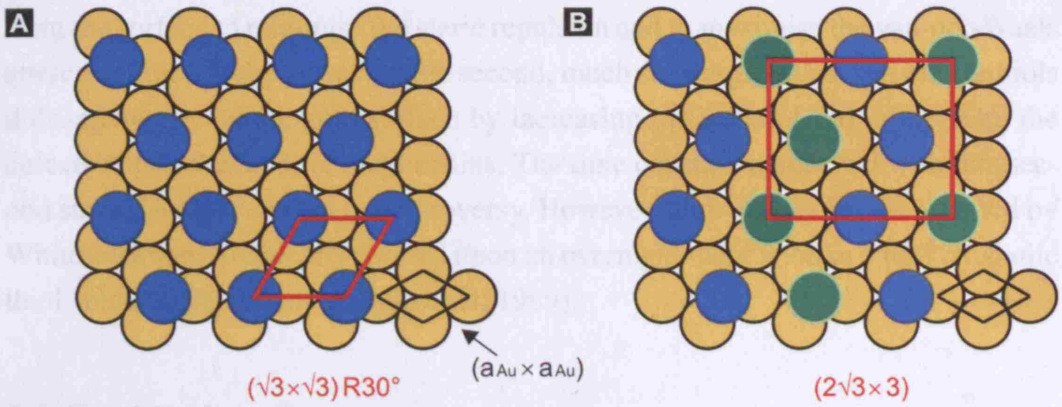

Fig. 2.2. Schematic to show (A) the $(\sqrt{3} \times \sqrt{3})\,\mathrm{R}\,30°$ lattice structure and (B) the $\mathrm{c}(2\sqrt{3} \times 3)$ superlattice structure of full-coverage alkanethiolate SAMs on Au(111). (B) is after Schreiber (2000) and different colours indicate symmetry equivalent molecules.

reported $\mathrm{c}(\sqrt{3} \times 19)$ unit cells with a density of 68.4 Å^2 per molecule at a normalised coverage of about 0.32 ML, and $\mathrm{h}(5\sqrt{3} \times \sqrt{3})\,\mathrm{R}\,30°$ unit cells with a density of 54.0 Å^2 per molecule at a normalised coverage of about 0.40 ML (Poirier 1999).

With increasing saturation of the stacked-lying-down phases, the 'standing-up' phase starts to nucleate that saturates finally at an *absolute* coverage of about 0.3 ML.[1] The saturation distance is larger than the distance of closest approach between two alkyl chains. Therefore, to minimise the free volume between the alkyl chains and to maximise the van-der-Waals attraction, the alkyl chains collectively tilt away from the surface normal and interlock to one another, with a tilt angle of $\sim 30°$. Both centred rectangular $\mathrm{c}(2\sqrt{3} \times 3)$ and hexagonal $(\sqrt{3} \times \sqrt{3})\,\mathrm{R}\,30°$ unit cells were found to co-exist, with the same nominal molecular density of 21.6 Å^2 per molecule and shown in Fig. 2.2 (Poirier 1999; Schreiber 2000; Vericat, Vela, and Salvarezza 2005).

The SAM growth is known to be associated with at least two time constants (Schreiber 2000; Schwartz 2001). When SAMs are formed from solution, as is the case for this thesis, the gold surface is initially covered by solvent molecules thus the physisorption of alkyl chains on the gold surface is negligible. The first, rapid growth stage in an 1 mM ethanolic thiol solution occurs reportedly in a few minutes and gives rise to 80 - 90% surface coverage. This stage is characterised by the chemisorption of sulphur atoms that displace the physisorbed alkyl chains from the gold surface at the same time. The alkyl chains, in turn, stretch progressively away

[1] Since the ratio between sulphur and gold atoms is 1:3 in the $(\sqrt{3} \times \sqrt{3})\,\mathrm{R}\,30°$ phase, the absolute saturation coverage of *n*-alkanethiol SAMs is about 0.3 ML. The absolute saturation coverage of bare sulphur on Au(111) is reportedly 0.6 ML (Biener, Biener, and Friend 2005).

from the surface to minimise the steric repulsion and to maximise the van-der-Waals attraction among themselves. In the second, much slower growth stage, alkanethiols diffuse laterally on the gold surface by increasing the packing and minimising the defects within the layer of alkyl chains. The time constant associated with this second stage has been subject to controversy. However, high quality SAMs reported by Whitesides were frequently formed upon an overnight incubation in 1 mM ethanolic thiol solution (for example, Bain et al. 1989).

2.3 Equilibrium Structure

Despite the simple molecular composition, the 'equilibrium' structure of alkanethiol SAMs on Au(111) remains subject to much debate in the literature. Major differences in the reported SAM structures may be attributed to

- sensitivity of measurement device toward crystalline or defective structure
- spatial resolution of measurement device, such as two-dimensional or three-dimensional, and microscopic or macroscopic
- in-situ or ex-situ measurement techniques
- gold morphology, that is, single crystal or evaporated
- factors related to sample preparation, including gold cleanliness and incubation time, as well as purity, concentration, and solvent of thiols

Differences in the equilibrium SAM structure have also been reported in theoretical studies. Therefore in addition to the differences arising due to the choice of force field, discrepancies in the literature may reflect the presence of real multiple metastable phases. In the following, equilibrium structure of alkanethiol SAMs on Au(111) is reviewed, focusing on SAMs of MHA and HDT that are standard SAMs in this work and in the literature (Schreiber 2000; Schwartz 2001; Vericat, Vela, and Salvarezza 2005; Dubois and Nuzzo 1992).

Early studies have reported the $(\sqrt{3}\times\sqrt{3})\,\mathrm{R}\,30°$ phases for unsubstitued, methyl terminating alkanethiol SAMs on Au(111) with an equilibrium S-S distance of 4.97 Å (Strong and Whitesides 1988). Long-chain SAMs formed on evaporated gold surfaces upon an overnight incubation in 1 mM ethanolic solution, which is a widely employed sample preparation protocol (Bain et al. 1989), were found to exhibit tilt angles between 20° and 40° (Porter et al. 1987; Nuzzo, Dubois, and Allara 1990), and an ellipsometric thickness of ~1.5 Å per methylene CH_2 group. Whereas Fenter et al. reported grazing incident angle X-ray diffraction studies on

single crystal gold surfaces and an average tilt angle of 30.5° ± 0.5° for SAMs of chain lengths 15 - 30 (Fenter, Eisenberger, and Liang 1993; Fenter et al. 1997).

The chain length dependence of the equilibrium SAM structure was investigated by Porter et al. and Bain et al. in a series of experiments using infrared spectroscopy, ellipsometry, contact angle goniometry, or thermal desorption studies, and found consistently that SAMs with $n < 10$ were more disordered and less densely packed than SAMs with longer chain lengths. Furthermore, electrochemical capacitance measurements reported by Porter et al. showed an increased permeability of short-chain SAMs toward ions present in the solution. Therefore, given the variability and disorder associated with the reported equilibrium structure of long-chain SAMs, short-chain SAMs can be expected to exhibit a substantively disordered equilibrium structure.

The effects of the terminal functionality of SAMs on the equilibrium structure, in particular with regard to the carboxylic acid COOH terminal functionality, have been subject to controversy. While the early studies by Porter et al. or Bain et al. did not report substantive effects of SAM terminal groups, Arnold et al. (2002) observed substantive disorder in carboxylic acid terminated, long-chain SAMs of MHA, which were attributed to the strong hydrogen bond interactions between acid terminal groups giving rise to the formation of dimers, as well as to attractive electrostatic interactions between the dipole of acids and the gold surface. However, diffraction studies by Li et al. (1995) reported the presence of the $(\sqrt{3} \times \sqrt{3})\,\mathrm{R}\,30°$ phase in SAMs of MHA, which remained even preserved upon exposing the SAMs to aqueous electrolyte solutions.

High resolution scanning tunneling microscopy studies have investigated the molecular structure of SAMs and reported that the majority of defects were generated at grain and domain boundaries (Poirier 1999; Vericat, Vela, and Salvarezza 2005). These studies suggested that SAMs at saturation coverage exhibited an equilibrium amount of domains and defects, rather than a single phase of close packed alkanethiols on Au(111). Therefore, reported discrepancies between diffraction studies that detected the crystalline structure and structure averaging infrared spectroscopy studies may be attributed to the presence of defects.

Recently, O'Dwyer et al. (2004) have investigated the effects of sputtered gold surface on the molecular structure of nonanethiol $HS(CH_2)_8CH_3$ SAMs. These SAMs were formed on Si(100) wafers sputtered with 4 nm of Cr and 30 nm of Au thin films, incubated in 1 mM ethanolic nonanethiol solution for 24 hours. They used the grazing incident angle X-ray diffraction studies technique to confirm the

predominantly (111) texture of the sputtered gold surface, as well as typical grain sizes of 25 - 40 nm. Fig. 2.3 shows a 60 nm × 60 nm scanning tunneling microscopy image taken on the resultant SAM (O'Dwyer et al. 2004). O'Dwyer et al. reported

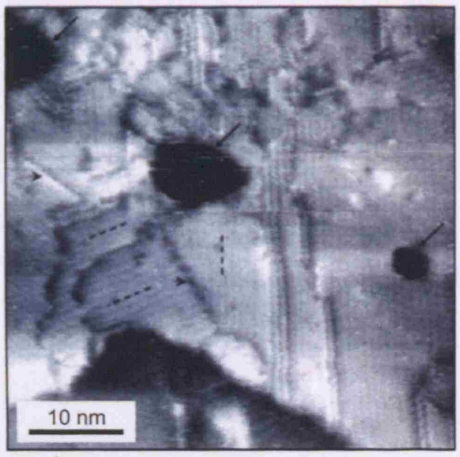

Fig. 2.3. Molecular resolution scanning tunneling microscopy image of nonanethiol $HS(CH_2)_8CH_3$ SAM on a sputtered, predominantly Au(111) surface. Adopted from O'Dwyer et al. (2004).

a hexagonal packing of the nonanethiol SAMs. However, the maximum defect-free feature size was estimated to be 20 nm, separated by translational and rotational boundaries. Multiple domains within a single grain were observed, in cases where the gold terrace size was larger than the grain size. Numerous gold step edges and a lower molecular coverage at the step edges were observed. Furthermore, pinholes with a depth of 0.25 nm were measured, which were attributed the presence of monoatmoic steps present on the Au surface. Although there are some differences in the experimental parameters, which will be discussed in more detail in Chapter 5, including the chain length, incubation time, and thiol concentration that may affect the overlayer structure and the defect density, a sputtered gold surface is similar in morphology and crystallinity to an evaporated gold surface. Therefore, the SAMs reported by O'Dwyer et al. may exhibit comparable properties to the SAMs probed in this work.

The use of simple alkanethiol SAMs on Au(111) represent the best practical approach to control the surface chemistry of model organic interfaces. Long-chain SAMs, including SAMs of HDT and MHA that are standard SAMs used in this work, may be considered ordered and densely packed structures compared with shorter chain length SAMs. However, SAMs prepared under optimal experimental conditions still exhibit defects. Therefore, when interpreting cantilever measure-

ments, it is important to consider both ordered and disordered structures in SAMs. Results obtained from characterisation measurements of SAM coated samples will be presented in Chapter 5.

3. Concepts of Acid/Base Chemistry

The aim of this thesis is to investigate changes in surface stress induced by ionisable SAMs, focusing on carboxylic acid terminated SAMs as a model biochemical system. When surface carboxylic acids deprotonate to yield negatively charged carboxylate ions, they will give rise to a range of different interfacial interactions, including the repulsion between the negatively charged carboxylate ions at the surface, the binding of cations in solution, or the alignment of water's dipoles. The formation and disruption of chemical bonds, as well as the ordering and disordering induced by the acid deprotonation will all contribute to changes in Gibbs free energy $\Delta G = \Delta H - T\Delta S$, where ΔG is Gibbs free energy change, ΔH is enthalpy change, T is temperature, and ΔS is entropy change, and therefore to the action of chemical forces that give rise to surface stress changes. This chapter provides an introduction to the acid/base chemistry.

3.1 Definition of Acids and Bases

According to the Brønsted-Lowry definition, an *acid* is a substance capable of donating a proton, and a *base* is a substance capable of accepting a proton. Hereupon, the terms 'acid' and 'base' will be used as defined by Brønsted and Lowry. Acid/base reactions are therefore proton-transfer processes that may be represented by the chemical equations as follows:

$$HA(aq) + H_2O(l) \rightleftharpoons H_3O^+(aq) + A^-(aq) \tag{3.1}$$

gives a dissociation reaction of an acid termed A.

$$B(aq) + H_2O(l) \rightleftharpoons BH^+(aq) + OH^-(aq) \tag{3.2}$$

gives a dissociation reaction of a base termed B (Bates 1973).

Although the definition of acids and bases is concise, an understanding of Eq. (3.1) and Eq. (3.2) requires a basic knowledge of acid/base chemistry. Firstly,

the symbol '⇌' indicates an equilibrium reaction. Secondly, the acidity of the resultant solution depends on the activities of dissolved substances. Thirdly, the subscript '(aq)' indicates a hydrated solute, whereas the subscript '(l)' indicates the solvent liquid water. Fourthly, surface acid/base reactions differ from acid/base reactions occurring in the homogeneous, dilute bulk solution. Chemical equilibria, acidity of solution, solvation, and interfacial acid/base reactions, will be in turn described in the following sections.

3.2 Chemical Equilibria

3.2.1 Equilibrium Condition

The Second Law of thermodynamics states that a chemical reaction occurs spontaneously in a given system, when it decreases the Gibbs free energy of that system, and equivalently, when it increases the entropy of the Universe (Atkins and de Paula 2006; Keeler and Wothers 2003).

Consider for example the acid dissociation reaction given by Eq. (3.1). The equation shows that one mole of protonated acid HA and one mole of water H_2O react to produce one mole of hydronium ion H_3O^+ and one mole of deprotonated acid A^- in the forward reaction, and vice versa in the reverse reaction. Therefore as this reaction proceeds, the change in the number of moles is the same for the reactants $dn_{HA} = dn_{H_2O} \equiv d\xi_{reactants}$, and so is for the products $dn_{H_3O^+} = dn_{A^-} \equiv d\xi_{products}$ for this particular reaction. As the total amount of matter is conserved, $d\xi_{reactants} = -d\xi_{products} \equiv -d\xi$, where $d\xi$ is called the *extent of reaction*. The partial molar Gibbs free energy is defined as the chemical potential $\mu \equiv \partial G/\partial n$, therefore the change in Gibbs free energy with respect to the extent of reaction reads $dG = (\mu_{HA} + \mu_{H_2O} - \mu_{H_3O^+} - \mu_{A^-})\, d\xi$. In other words, the change in Gibbs free energy associated with the extent of reaction equals the sum of the chemical potentials of the reactants minus the sum of the chemical potentials of the products. The partial molar quantity $(\partial G/\partial \xi)_{p,T}$, the change in Gibbs free energy with the extent of reaction, is also called the *reaction Gibbs energy* and abbreviated as $\equiv \Delta_r G$ (Atkins and de Paula 2006). According to the Second Law of thermodynamics, the sign of the reaction Gibbs energy at a given extent of reaction determines the spontaneity of the reaction. If $\Delta_r G < 0$, the sum of the chemical potentials of the reactants are larger than the sum of the chemical potential of the products, and the forward reaction is spontaneous. Whereas if $\Delta_r G > 0$, the sum of the chemical potentials of the

products are larger than the sum of the chemical potentials of the reactants, and the reverse reaction is spontaneous. Thus, the condition for the chemical equilibrium is $\Delta_r G = 0$, that is, the reaction proceeds in *neither* direction spontaneously. The equilibrium condition for chemical reactions in general may be expressed as

$$\Delta_r G \equiv \left(\frac{\partial G}{\partial \xi}\right)_{p,T} = \sum_j \nu_j \mu_j = 0 , \tag{3.3}$$

where ν_j is the stoichiometric number and μ_j the chemical potential for the jth substance participating in a reaction. The stoichiometric number is related to the number of moles and the extent of reaction as $dn_j = \nu_j d\xi$ for the jth substance, whereby the sign of ν_j is defined as positive for reactants and negative for products.

3.2.2 Activity of Ions

The state of matter is described by an equation of state. The *perfect gas* equation of state, $pV = nRT$, where R is the gas constant, describes how the thermodynamic properties pressure p, volume V, number of moles n, and temperature T, attributed to molecules comprising an ideal, that is, pure and dilute, gas are related to one another. By applying the thermodynamic relations to the perfect gas equation of state, molar Gibbs free energy, and equivalently chemical potential, at constant temperature as a function of pressure is obtained:

$$\mu = \mu^\circ + RT \ln \tilde{p} , \tag{3.4}$$

where the superscript '$\circ$' denotes the standard state and $\tilde{p} \equiv p/p^\circ$ is the relative pressure. The standard state of a substance is defined by convention, and any change in the state of the substance must be referred to the standard state. The standard state for a perfect gas at a given temperature is its pure form at 1 bar, therefore $\tilde{p}$ equals the pressure in the unit of bar.

Condensed phases are described by modified perfect gas equations, and so are liquid solutions. The chemical potential of a component of a liquid solution is related to its *activity* $\tilde{a}$ as

$$\mu = \mu^\circ + RT \ln \tilde{a} , \tag{3.5}$$

where the standard state, in which $\tilde{a} \equiv 1$, is defined as the pure state for a solvent and the state of infinite dilution for a solute. The activity of a solute can be expressed in terms of its molality by introducing the *activity coefficient* γ and

$$\tilde{a} = \gamma \tilde{m}\,, \tag{3.6}$$

where $\tilde{m} \equiv m/m^\circ$ is the relative molality. By convention, the standard solute molality is defined as 1 mol/kg, therefore $\tilde{m}$ corresponds to the solute molality in the unit of mol/kg. The activity coefficient of a solute can deviate significantly from unity, in particular if the solute is an electrolyte and its ions interact strongly electrostatically with each other (Atkins and de Paula 2006). It should be noted also that it is not possible to measure the activity coefficient of a single ion species present in an electrolytic solution. If it was possible, it would not be uniquely defined since it depends on all the other ion species present in the solution. Instead, the experimentally determined *mean* ionic activity coefficient $\gamma_\pm = \tilde{a}_\pm/\tilde{m}_\pm$ refers to the mean ionic activity $\tilde{a}_\pm = (\tilde{a}_+^{\nu_+}\,\tilde{a}_-^{\nu_-})^{1/(\nu_+ + \nu_-)}$ and the mean ionic relative molality $\tilde{m}_\pm = (\tilde{m}_+^{\nu_+}\,\tilde{m}_-^{\nu_-})^{1/(\nu_+ + \nu_-)}$ of ν_+ cations and ν_- anions produced from an electrolyte of activity $\tilde{a}$ and relative molality $\tilde{m}$ (Bates 1973).

The Debye-Hückel law was derived upon electrostatic and statistical considerations, which predicts the activity coefficient of individual ion species present in a dilute electrolytic solution $\lesssim 0.02\,\mathrm{M}$. The activity coefficient of individual ion species varies with the *ionic strength I* of the solution,

$$I = \frac{1}{2}\sum_j \tilde{m}_j z_j^2\,, \tag{3.7}$$

where $\tilde{m}_j$ is the relative molality and z_j is the valence of the jth ion species. The Debye-Hückel law then reads:

$$-\log\gamma_j = \frac{A\,z_j^2\,\sqrt{I}}{1 + B\,\text{å}\,\sqrt{I}}\,, \tag{3.8}$$

where γ_j is the activity coefficient of the jth ion species; the parameter å is the 'ion-size parameter' or 'mean distance of closest approach'; the parameters A and B are solvent specific and depend on the temperature and the dielectric constant of the solvent. At very low concentrations $\lesssim 1$ mM, Eq. (3.8) reduces to the Debye-Hückel limiting law, in which the term Bå equals zero. Though in general and as already mentioned earlier, activity coefficients of individual ion species are specific to the ionic composition of the entire solution, therefore activity coefficients obtained from Eq. (3.8) are to be taken as conventions only (Bates 1973).

3.2.3 Equilibrium Constant

The reaction Gibbs free energy Eq. (3.3) may be now formulated as a function of the activity of reactants and products, by inserting Eq. (3.5) to first obtain

$$\Delta_r G = \Delta_r G^\circ + RT \ln Q , \tag{3.9}$$

where $Q = \prod_j a_j^{\nu_j}$ is termed the *reaction quotient*. At equilibrium, $\Delta_r G = 0$, hence it follows

$$\Delta_r G^\circ = -RT \ln K , \tag{3.10}$$

where

$$K = \left(\prod_j a_j^{\nu_j} \right)_{\text{equilibrium}} \tag{3.11}$$

is the *equilibrium constant*.

For example, the acidic dissociation constant K_a associated with the acid dissociation reaction given by Eq. (3.1) is

$$K_a = \frac{a_{H_3O^+} a_{A^-}}{a_{HA}} = \frac{m_{H_3O^+} m_{A^-}}{m_{HA}} \frac{\gamma_{H_3O^+} \gamma_{A^-}}{\gamma_{HA}} . \tag{3.12}$$

Note that in this equation, the activity of water a_{H_2O} is assumed to be unity, which corresponds to the pure state of water thus valid for low concentrations of solutes. It is clear from this equation that K_a is a measure for the acidity of the substance A relative to the surrounding aqueous medium. If $K_a > 1$, then at equilibrium, A tends to donate proton to the aqueous medium, thus A is more acidic than water. Whereas if $K_a < 1$ and at equilibrium, A tends to withdraw proton from the aqueous medium, thus A is more basic than water.

3.3 Acidity of Aqueous Solutions

3.3.1 Dissociation of Pure Water

Pure water dissociates into hydrogen ions and hydroxyl ions,

$$2H_2O(l) \rightleftharpoons H_3O^+(aq) + OH^-(aq) , \tag{3.13}$$

whereby the dissociation constant of water $K_w = m_{H_3O^+} m_{OH^-} \gamma_{H_3O^+} \gamma_{OH^-}$ has a value of 1.008×10^{-14} at 25 °C (Bates 1973). The molality of hydrogen and hydroxyl ions under these conditions is $m_{H_3O^+} = m_{OH^-} = 1.004 \times 10^{-7}$. Considering that the concentration of pure water is ~55.5 moles per litre, the dissociation of pure water is extremely weak.

3.3.2 pH Scales

The pH scale after Sørensen is defined as

$$\mathrm{pH} \equiv -\log c_{\mathrm{H_3O^+}} , \tag{3.14}$$

where $c_{\mathrm{H_3O^+}}$ denotes the concentration of hydrogen ions. Since $K_w \sim 10^{-14}$, the concentrations of hydrogen and hydroxyl ions becomes equivalent at pH 7, which is termed the neutral point of the pH scale. Owing to the fact that the concentrations of hydrogen ions and hydroxyl ions rarely exceed 10 moles per litre, the practical range of the pH scale extends from −1 to 15 (Bates 1973).

However, since the acidity is determined by the activity of hydrogen ions, the concentration of hydrogen ions cannot be an exact measure of the acidity of a solvent medium. It appears therefore appropriate to replace the pH scale based on $\mathrm{p}\,a_{\mathrm{H_3O^+}} = -\log m_{\mathrm{H_3O^+}}\gamma_{\mathrm{H_3O^+}}$, the negative logarithm of the hydrogen ion activity, as was indeed proposed by Sørensen and Linderstrøm-Lang. However, whereas the concentration is a physically defined, measurable quantity, the activity of hydrogen ions depends on the activities of all other substances constituting the liquid solution thus is not uniquely defined. Apart from the $\mathrm{p}\,a_{\mathrm{H_3O^+}}$ scale proposed by Sørensen and Linderstrøm-Lang, there are several other pH scales, including the p*t*H scale based on the mean ionic activity $\mathrm{p}\,t\mathrm{H} \equiv -\log m_{\mathrm{H_3O^+}}\gamma_{\pm}$ proposed by MacInnes, Belcher, and Shedlovsky, which are discussed in Bates's textbook (Bates 1973).

It should be noted also that in general, the pH value determined by a commercial pH meter neither corresponds to the hydrogen ion concentration, nor to the (conventional) hydrogen activity. The pH value of an unknown solution X is obtained as

$$\mathrm{pH}(X) = \mathrm{pH}(S) + \frac{(E_X - E_S)\,F}{RT \ln 10} , \tag{3.15}$$

where $\mathrm{pH}(S)$ is the assigned pH of the standard solution S, E_X and E_S are the values of potential difference, or the electromotive force, of a pH cell with the electrodes immersed in the unknown solution X and the standard solution S, and F is the Faraday constant. This is due to the fact that the standard potential associated with E_X and the standard potential associated E_S are assumed to be identical, which neglects the specificity of hydrogen ion activity in the solutions X and S. Therefore, the measured pH represents a measure of the conventional hydrogen activity only if the test solution X is dilute and of similar composition as the standard solution S. Yet, the operational pH scale Eq. (3.15) serves to standardise the practical scale of the acidity and alkalinity (Bates 1973), thus of fundamental practical importance.

3.3.3 Buffers

Buffers were defined by van Slyke as 'substances which by their presence in solution increase the amount of acid or alkali that must be added to cause unit change in pH' (Bates 1973).

Consider again the example acid given by Eq. (3.1). The equation for equilibrium constant of the acid Eq. (3.12) can be rearranged to obtain the Henderson-Hasselbalch equation

$$\mathrm{p}\,a_{\mathrm{H_3O^+}} = \mathrm{p}\,K_\mathrm{a} - \log\frac{a_{\mathrm{A^-}}}{a_{\mathrm{HA}}}\,, \tag{3.16}$$

which states that if the $\mathrm{p}\,a_{\mathrm{H_3O^+}}$ of the solution deviates from the $\mathrm{p}\,K_\mathrm{a} \equiv -\log(K_\mathrm{a})$ of the acid, the acid will deprotonate or protonate to minimise the discrepancy, that is to *buffer* the $\mathrm{p}\,a_{\mathrm{H_3O^+}}$ and the pH of the solution. Because Eq. (3.12) or Eq. (3.16) represent exact thermodynamic relations, acids and bases regulate precisely the solution pH provided that the solution pH is close to their $\mathrm{p}\,K_\mathrm{a}$ values.

The most frequently used, 'standard' pH solutions in this work are aqueous mixtures of monobasic NaH_2PO_4 and dibasic Na_2HPO_4 sodium phosphate between pH values 3.5 and 8.4. The ionic strength of these pH solutions was maintained at a constant value of $I = 0.1$. Sodium phosphates are salts of phosphoric acid H_3PO_4. The three hydrogens of a phosphoric acid molecule dissociate with increasing solution $\mathrm{p}\,a_{\mathrm{H_3O^+}}$, that is in turn at the three $\mathrm{p}\,K_\mathrm{a}$ values 2.12, 7.21, and 12.67 (*The CRC Handbook of Chemistry and Physics*, 86$^{\mathrm{th}}$ ed., 2005) of phosphoric acid. It is important to note that even though the overall solution ionic strength was maintained at a constant value, the use of buffer involves inherently a pH-dependence of the ion species present in the solution (Fig. 3.1A). For example, the majority of phosphate anions will be in the monovalent form $H_2PO_4^-$ at pH 3.5, whereas at pH 8.4, the majority of phosphate anions will be in the divalent form HPO_4^{2-} (Fig. 3.1B). Moreover, ionic activities are highly specific to the composition of solution, therefore a constant ionic strength does not guarantee constant ionic activities. When interpreting pH or ion-specific effects involving buffer molecules, it is important to recall both the pH-dependence of ion concentrations and the associated changes in the mean ionic activities.

3.4 Solvation

Water is a polar solvent, which is due to the difference in the electronegativities of the oxygen and hydrogen atoms, in combination with the shape of water molecules

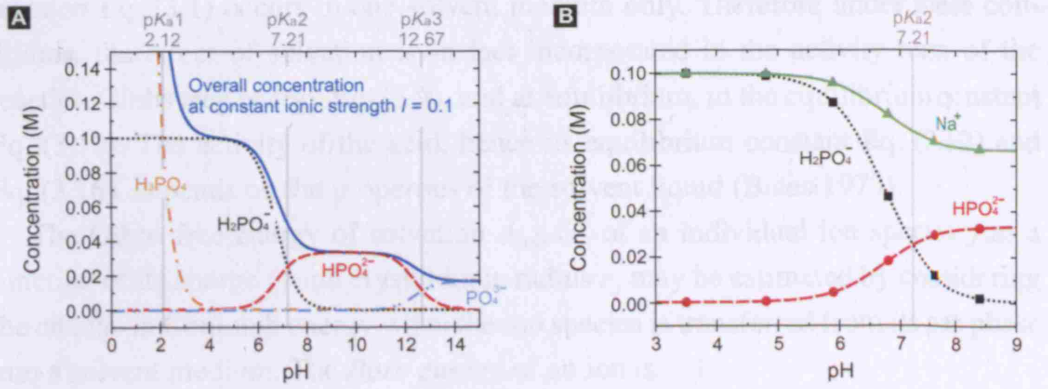

Fig. 3.1. Concentration of ion species present in a constant ionic strength $I = 0.1$ sodium phosphate solution is pH dependent. (A) Concentration of phosphate anion species between pH 0 and 15; (B) Concentration of monovalent phosphate $H_2PO_4^-$, divalent phosphate HPO_4^{2-}, and sodium cations Na^+ at typical pH values investigated herein, that is, at pH 3.5, 4.8, 5.9, 6.8, 7.6, and 8.4.

with an H– O– H bond angle of 104.523° (Burgess 1978). Electrostatic interactions between water's dipoles give rise to an associated, three-dimensional network of hydrogen bonds O–H $\cdots$ O produced in liquid water, whereby each water molecule is thought to be coordinated with about four nearest neighbour water molecules with a typical half-life of only 10^{-11} s (Burgess 1978). This intrinsic solvation, or *hydration* as water is the solvent, of water molecules comprising the bulk solvent liquid may be represented by $H_2O \cdots (H_2O)_n$ with $n \simeq 4$.

Turning back to the acid dissociation reaction Eq. (3.1), on the left hand side, $H_2O(l)$ is a water molecule of the bulk solvent liquid $H_2O \cdots (H_2O)_n$. The protonated acid molecule HA(aq) is solvated, too, thereby the solvation of the acid arises from the attractive electrostatic interaction between the dipole of the H–A bond of the acid and the dipoles of adjacent water molecules $HA \cdots (H_2O)_m$ with $m \neq n$ in general, depending on the magnitude of acid's dipole. The subsequent proton transfer from the acid molecule to the water molecule produced two ions on the right hand side of Eq. (3.1), namely, a solvated hydronium cation $H_3O^+ \cdots (H_2O)_{n'}$ and a solvated acid anion $A^- \cdots (H_2O)_{m'}$. The charge/dipole electrostatic interaction is stronger than the dipole/dipole interaction, which is reflected in the distance dependence of the electrostatic free energy of $\propto 1/r^2$ for charge/fixed dipole and $\propto 1/r^3$ for free dipole/fixed dipole (Israelachvili 1992). Therefore the acid dissociation reaction Eq. (3.1) involves an increased extent of solvation in the forward reaction, and vice visa in the reverse reaction, that is $n' > n$ and $m' > m$.

Although the process of solvation itself is associated with changes in the Gibbs free energy and termed the Gibbs free energy of solvation, the acid dissociation

reaction Eq. (3.1) occurs in one solvent medium only. Therefore under these conditions, the effect of solvation is in fact incorporated in the activity term of the reaction Gibbs free energy Eq. (3.9), and at equilibrium, in the equilibrium constant Eq. (3.10). The activity of the acid, hence its equilibrium constant Eq. (3.12) and Eq. (3.16), depends on the properties of the solvent liquid (Bates 1973).

The Gibbs free energy of solvation $\Delta_{\text{solv}}G^\circ$ of an individual ion species j as a function of its charge z_j and crystal ionic radius r_j may be estimated by considering the change in Coulomb energy when the ion species is transferred from its gas phase into a solvent medium. The *Born energy* of an ion is

$$\Delta_{\text{solv}}G^\circ = -\frac{z_j^2 e^2 N_A}{8\pi\,\varepsilon_0\, r_j}\left(1-\frac{1}{\varepsilon}\right), \tag{3.17}$$

where e is the elementary charge, N_A is the Avogadro number, ε_0 is the permittivity of vacuum, and ε is the dielectric constant of the solvent medium. For water with $\varepsilon \simeq 78$ and at 25 °C, Eq. (3.17) reduces to

$$\Delta_{\text{solv}}G^\circ = \frac{z_j^2}{\left(r_j / \text{Å}\right)} \times \left(-686\ \text{kJ mol}^{-1}\right), \tag{3.18}$$

where $\left(r_j / \text{Å}\right)$ is the crystal ionic radius in Å (Israelachvili 1992).

Eq. (3.18) shows that the extent of hydration increases with the charge of an ion and inversely with its crystal radius. In fact, the strong coordination of water molecules to ions with high charge-to-radius ratio causes the effective radii of these ions to become larger, which are termed the *hydrated radii* of ions. Water molecules directly coordinated to an ion form the *primary hydration shell*, whereas water molecules that change their coordination due to the presence of the primary hydration shell form the *secondary hydration shell* (Keeler and Wothers 2003).

3.5 Acid/Base Reactions at Surfaces

When acid/base reactions occur only in dilute aqueous solutions, resultant effects may be interpreted in terms of electrostatics between weakly interacting ions. At the surface of a solid surface, however, ions will be present at *excess* concentrations, which arise due to the entropy of mixing and mutual repulsion between like charged ions (Israelachvili 1992). Therefore, it is important to establish a basic relation between the acid/base equilibria in dilute aqueous solutions and at surfaces.

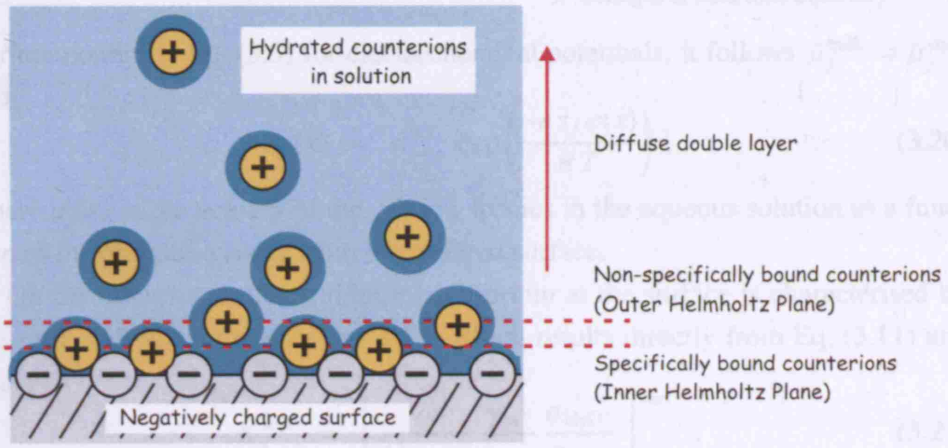

Fig. 3.2. Illustration of the electric double layer.

The chemical potential of an ion is defined as the partial molar quantity of Gibbs free energy with respect to the ion. Owing to the strength of electrostatic interactions, however, this rigorous thermodynamic definition may be approximated by the *electrochemical potential* after Guggenheim

$$\tilde{\mu}_j = \mu_j + e\, z_j\, \varphi(x)\,, \tag{3.19}$$

which separates the chemical contribution μ_j from the electrostatic contribution $e\, z_j\, \varphi(x)$, with $e\, z_j$ the charge of the ion and $\varphi(x)$ the electrostatic potential at position x in an aqueous solution (Rusanov 1996).

The deprotonation of a solid surface due to an acid/base reaction increases the density of negative surface charges. The charging of the surface gives rise to a potential difference between the negatively charged surface and the electrically neutral bulk solution, which in turn induces the accumulation of oppositely charged counterions, as well as the depletion of like-charged co-ions at the negatively charged surface. The distribution of counterions near a charged surface can be modelled by two distinct regions, which, together with the negatively charged surface, form an *electric double layer* and illustrated in Fig. 3.2. In the Stern or Helmholtz layer adjacent to the surface, specifically (also termed the inner Helmholtz plane) and non-specifically (also termed the outer Helmholtz plane) adsorbed counterions neutralise the surface charges. Whereas in the diffuse layer adjacent to the Stern layer, counterions are in rapid thermal motions and their distribution follows the Boltzmann distribution: let $x \equiv 0$ at the surface and $x \to \infty$ for the bulk solution so that the electrostatic potential in the bulk phase becomes $\varphi^{\text{bulk}} = 0$. From the equi-

librium condition Eq. (3.3) for electrochemical potentials, it follows $\tilde{\mu}_j^{\text{bulk}} = \tilde{\mu}_j^{\text{surf}}$ and

$$a_j(x) = a_j^{\text{bulk}} \exp\left(\frac{-e z_j \varphi(x)}{RT}\right), \tag{3.20}$$

where $a_j(x)$ is the activity of the jth ion species in the aqueous solution as a function of the distance x away from the charged surface.

On the other hand, the acid/base equilibrium at the surface is characterised by the surface dissociation constant K_a^{surf}, which results directly from Eq. (3.11) and reads

$$K_a^{\text{surf}} = \left[\frac{\alpha}{(1-\alpha)} \frac{\gamma_{A^-}}{\gamma_{HA}} \frac{a_{H_3O^+}}{a_{H_2O}}\right]^{\text{surf}}, \tag{3.21}$$

where the superscript 'surf' refers to surface reactions and α is the degree of deprotonation of the acidic surface $\alpha/(1-\alpha) = m_{H_3O^+}/m_{HA}$ expressed relative to the molality of hydrogen ions (Israelachvili 1992).

The surface activities of ions participating in the acid/base equilibrium Eq. (3.21), such as the surface activity of hydrogen ions $a_{H_3O^+}^{\text{surf}}$, may be now related to the activity of ions in the bulk solution by inserting Eq. (3.20) at $x = 0$:

$$K_{H_3O^+}^{\text{surf}} = \left[\frac{\alpha}{(1-\alpha)} \frac{\gamma_{A^-}}{\gamma_{HA}} \frac{1}{a_{H_2O}}\right]^{\text{surf}} a_{H_3O^+}^{\text{bulk}} \exp\left(\frac{-e\varphi(0)}{RT}\right) \tag{3.22}$$

where the subscript of $K_{H_3O^+}^{\text{surf}}$ indicates that the dissociation constant involves hydrogen ions. Therefore, provided that the dissociation constants of ion species present in an aqueous solution are known, it is possible to relate the acid/base equilibria given by Eq. (3.12) for the bulk solution to the acid/base equilibria given by Eq. (3.21) occurring at the surface.

The surface charge density is implied by the degree of deprotonation α in Eq. (3.22). However, if there is no exchange of matter between the surface and the aqueous solution, and the interest focuses primarily on the calculation of the charge density as a function of distance x away from the charged surface, the Poisson-Boltzmann equation may be used. This equation is obtained by combining the Boltzmann distribution Eq. (3.20) and the Poisson equation $\partial^2\varphi(x)/\partial x^2 = -z_j e\rho(x)/\varepsilon\varepsilon_0$, where $\rho(x)$ is the charge density.

To complete this chapter, let us consider a typical experimental situation associated with this work, namely, a buffer solution of sodium phosphates at a constant bulk ionic strength of $I = 0.1$ brought in contact with the surface of a carboxylic acid terminated SAM. The excess surface ionic strength implied by Eq. (3.22) has dramatic consequences for the acid/base equilibria at the carboxylic acid terminated

surface (Harding et al. 2006): firstly, the $\mathrm{p}\,a_{\mathrm{H_3O^+}}$ at the surface is lower than in the bulk. For example under these conditions, bulk pH 8 corresponds to surface pH 6. Therefore, the apparent surface $\mathrm{p}\,K_\mathrm{a}$, which is also termed surface $\mathrm{p}\,K_{1/2}$ for a surface acid, will be higher when related to the bulk pH. Furthermore, a complete surface deprotonation will not be achieved even at bulk pH 10. Secondly, there will be a competing binding between hydrogen ions and sodium ions onto the deprotonated sites of the surface acid. Whereas in the bulk solution, sodium cations do not take part in the acid/base equilibria due to the high equilibrium constant of sodium ions $K_\mathrm{Na} \gtrsim 1$. Thirdly, the excess surface ionic strength depends on the degree of surface deprotonation therefore non-constant, irrespective of the constancy of the bulk ionic strength. Under these conditions, the surface ionic strength is about 1 at bulk pH 7, which increases to 6 at bulk pH 10. Finally, the roles of solute and solvent become increasingly interchangeable with surface excess ionic strength, not only for ions and water molecules, but also for the densely packed SAMs themselves. Eq. (3.22) shows that the acid/base equilibria depend upon the activities of all solutes and solvents comprising the interface thus highly specific. Therefore, it is important to account for excess interfacial properties when interpreting cantilever experiments.

4. Concepts of Surface Stress

The unit of surface stress is force per unit length (N/m), which gives already an initial understanding of the notion of surface stress: when an in-plane force acts at one surface of a cantilever and along one of its axes, the force may be large enough to cause a change in the cantilever curvature. If the force is repulsive, the cantilever surface expands, generating a compressive surface stress. Conversely, if the force is attractive, the cantilever surface contracts, generating a tensile surface stress. Surface stress is the central principle of the cantilever technique, and this work is about measurements of surface stress. Therefore, it is helpful to develop a more formal understanding of the concepts of surface stress.

The first part of this chapter is concerned with the mechanics of solid bodies, based upon the theory of elasticity according to standard text books (Landau and Lifshitz 1986; Nye 1957). Although the theory of elasticity is a self-consistent theory, it assumes the amount of matter to be fixed. Therefore, a link between the mechanics and chemistry is developed independently by thermodynamics, which is a widely practiced approach (Müller and Saúl 2004; Ibach 1997; Haiss 2001). However, recent reviews provided by Rusanov showed that surface thermodynamics based on Gibbs's equilibrium principle described both mechanical and chemical interactions self-consistently, including adsorption and dissolution, as well as line tension or wetting (Rusanov 1996; 2005). It would be therefore favourable to adopt Gibbsean surface thermodynamics entirely. Owing to the chronological development of this work, though, the theory of mechanochemistry is given in the second part of this chapter as an extension of the theory of elasticity. However, details are discussed in Rusanov's reviews.

4.1 Theory of Elasticity

4.1.1 Bulk Elasticity

Strain tensor. In a cartesian coordinate system, we consider two arbitrary points of a solid with position vectors $\boldsymbol{r}^{(i)} = \left(x_1^{(i)}, x_2^{(i)}, x_3^{(i)}\right)$, where the superscripts $i = 1, 2$ denote the points. When they are displaced to $\boldsymbol{r}'^{(i)} = \left(x_1'^{(i)}, x_2'^{(i)}, x_3'^{(i)}\right)$, the resultant deformation is described by their displacement vectors $\boldsymbol{u}^{(i)} = \boldsymbol{r}'^{(i)} - \boldsymbol{r}^{(i)}$. This is illustrated in Fig. 4.1. Therefore, the distance vector between the points after the displacement is defined by their distance vector before the displacement and the difference in their displacement vectors: $\mathrm{d}\boldsymbol{r}' = \mathrm{d}\boldsymbol{r} + \mathrm{d}\boldsymbol{u}$. For a displacement which is small with respect to the distance, it follows $\mathrm{d}l'^2 = \mathrm{d}l^2 + 2\sum_{ij} e_{ij}\,\mathrm{d}x_i\,\mathrm{d}x_j$, where $\mathrm{d}l = |\mathrm{d}\boldsymbol{r}|$ and $\mathrm{d}l' = |\mathrm{d}\boldsymbol{r}'|$. The symmetric tensor e_{ij} is called the *strain tensor*, which is expressed as follows:

$$e_{ij} = \frac{1}{2}\left(\frac{\partial u_i}{\partial x_j} + \frac{\partial u_j}{\partial x_i}\right) + O\left(\partial^2 u\right), \tag{4.1}$$

Note that in the one-dimensional case, a principal value of the strain tensor equals the relative extension in the direction of the corresponding principal axis: $(\mathrm{d}x_i' - \mathrm{d}x_i)/\mathrm{d}x_i'$, where $i = 1, 2, 3$ for the ith principal axis.

Stress tensor. When a body is not deformed, it is in its equilibrium state, that is, the resultant forces acting in the body are zero. When an external force is applied on the body, a deformation occurs, and the resultant forces tend to return the body to the equilibrium state. In the theory of elasticity, any interaction is neglected, which is short-ranged with respect to the extent of the deformation. Therefore, internal stresses arising from intermolecular interactions are taken as zero, so the resultant forces effectively act only at the *surface* of the body. Mathematically, the relation

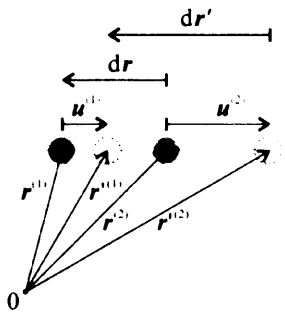

Fig. 4.1. Displacement of two points.

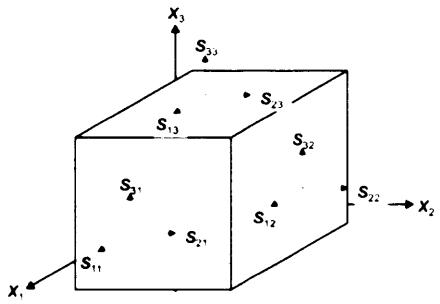

Fig. 4.2. Stress components of a homogeneously stressed unit cube. Reproduced from Müller and Saúl (2004).

between the external force acting on the body and the resultant force at its surface is expressed as follows:

$$\int F_i \, \mathrm{d}V = \int \sum_j \frac{\partial s_{ij}}{\partial x_j} \, \mathrm{d}V = \oint \sum_j s_{ij} \, \mathrm{d}f_j , \tag{4.2}$$

where $\mathrm{d}V$ is the volume element of the body, and $\mathrm{d}f_j \equiv n_j \, |\mathrm{d}\boldsymbol{f}|$ is the jth component of the surface element $\mathrm{d}\boldsymbol{f}$ with its outward unit normal vector $\boldsymbol{n}$. From this equation, it follows that the ith component of the force F_i is the divergence of a tensor of rank two, $\boldsymbol{s}$, which is called the *stress tensor*. The component s_{ij} of the stress tensor is the ith component of the force per unit area with the outward surface normal parallel to the x_i axis. Similarly, a consideration regarding the moment of the forces $\boldsymbol{M} = \boldsymbol{F} \times \boldsymbol{r}$ present at the surface of the body results in the symmetry of the stress tensor, $s_{ij} = s_{ji}$. Fig. 4.2 illustrates the stress tensor components for the three visible faces of a unit cube.

Therefore when the body is in equilibrium, the following conditions are fulfilled: firstly, in absence of an external force, the internal stresses in every volume element must balance. Secondly, if an external force is applied on the entire body, the sum of the applied force and the internal stresses in every volume element must vanish. Thirdly, external forces acting at every surface element must be balanced by the internal stresses at the surface element. The equilibrium conditions can be summarised as

$$\begin{aligned} \sum_j \frac{\partial s_{ij}}{\partial x_j} + F_i^{\mathrm{ext}} &= 0 \qquad && \text{(bulk)} \\ \sum_j s_{ij} \, n_j &= F_i^{\mathrm{surf}} && \text{(surface)} \end{aligned} \tag{4.3}$$

$\boldsymbol{F}^{\text{ext}}$ is the external force per unit volume acting in the bulk, $\boldsymbol{F}^{\text{surf}}$ is the external force per unit area acting at the surface of the body, and $\boldsymbol{n}$ is the outward surface normal.

Hooke's Law. The *Hooke's law* relates the bulk stress to the strain tensor and vice versa. Below the elastic limit of the body, any deformation of the body is recoverable, that is, elastic, and stress and strain are directly proportional to one another:

$$\begin{aligned} e_{ij} &= \sum_{kl} C_{ijkl}\, s_{kl} \\ s_{ij} &= \sum_{kl} S_{ijkl}\, e_{kl} \end{aligned} \tag{4.4}$$

where C_{ijkl} are the compliance coefficients and S_{ijkl} are the stiffness coefficients.[1] They are both fourth-rank tensors, and their components are called stiffness and compliance constants, respectively. The constants are characteristic to a specific material, and describe its mechanical properties in three dimensions. The 81 components of each of these tensors result from 9 components of both e_{ij} and s_{ij}. However the symmetry intrinsic to the tensors reduces the number of independent components to 21. The symmetry extrinsic to a crystalline material leads to a further reduction of the components (Landau and Lifshitz 1986).

Elastic energy. Any elastic deformation of a solid is associated with changes in its elastic energy. Consider a solid in Fig. 4.3 that is subject to some external force. A partial volume V of the solid much smaller than the solid itself is then exposed to the following two forces: firstly, the force $\boldsymbol{F}^{\text{surf}}$ exerted by the rest of the solid at the surface A of the partial volume. Secondly, the external force $\boldsymbol{F}^{\text{ext}}$ acting on the entire solid, e.g. gravity. When V is given a virtual, that is infinitesimal displacement $\delta\boldsymbol{u}$ as a result of some internal forces, the virtual work δW done by the acting forces against the displacement field is

$$\delta W = \oint_A \sum_i F_i^{\text{surf}}\, \delta u_i \, \mathrm{d}A + \int_V \sum_i F_i^{\text{ext}}\, \delta u_i \, \mathrm{d}V\,. \tag{4.5}$$

If the system is in equilibrium, the equilibrium conditions Eq. (4.3) should be satisfied, and the forces acting on V are related to the bulk stress tensor s_{ij}. By using the definition of the strain tensor Eq. (4.1), the infinitesimal changes in the elastic energy δW results in

[1] Note that conventionally, $\boldsymbol{C}$ is termed the stiffness tensor, and $\boldsymbol{S}$ is termed the compliance tensor (Müller and Saúl 2004).

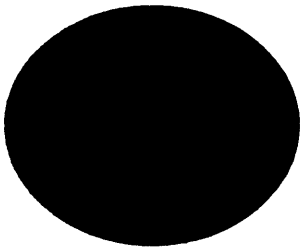

Fig. 4.3. If a solid (dark grey) is subject to an external force (light grey), a partial volume V of the solid (grey) is subject to both the external force and the force applied by the rest of the solid at surface A (red) with normal vector $\boldsymbol{n}$ of the partial volume. Reproduced from Müller and Saúl (2004).

$$\delta W = \int_V \sum_{ij} s_{ij}\, \delta e_{ij}\, \mathrm{d}V\,. \tag{4.6}$$

The integrand can be considered as the density of the elastic energy, $\delta w = \sum_{ij} s_{ij}\, \delta e_{ij}$. For a linear elastic solid described by Eq. (4.4), δe_{ij} equals to $\sum_{kl} C_{ijkl}\, \delta s_{kl}$ thus enabling an integration over the unit stress tensor element δs_{kl}. The total elastic energy results in $W = 1/2 \int_V \sum_{ij} s_{ij}\, e_{ij}\, \mathrm{d}V$. In absence of external forces, the elastic energy can be calculated as

$$W = \frac{1}{2} \oint_A \sum_i F_i^{\mathrm{surf}}\, u_i\, \mathrm{d}A\,, \tag{4.7}$$

that is, as half the work done by the forces acting at the surface against the surface displacement.

4.1.2 Interfacial Excess Quantities

The preceding section concerned homogeneous bulk solids with three uniform directions along the principal axes. The planar surface of a homogeneous solid is characterised by only two uniform directions along its principal axes, thus extensive quantities will exhibit excess across the interface along the surface normal. Elastic energy, as will be analysed in the next section, is an extensive quantity, which will give rise to the representation of surface stress and strain as the interfacial excess of bulk stress and strain, respectively. However, in this section, we will first consider Gibbs's method to calculate interfacial excess quantities (Rusanov 2005; Müller and Saúl 2004).

Let two phases α and β be characterised by some homogeneous and extensive quantities G^α and G^β. In Fig. 4.4, a cross section of α and β along the z-axis is shown. The two phases are brought into contact and separated by a planar interface at $z = z^0$ that is termed the Gibbs dividing surface. The density of the total extensive quantity G per unit interface area is denoted by $g(z)$, which corresponds to the constant areal density g^α and g^β in the bulk phases of α and β. As illustrated in the figure, the net extensive quantity G, indicated by the shadowed area under the profile of $g(z)$, equals to the sum of G^α and G^β, plus an excess quantity G^{interf} at the interface. Therefore it follows

$$G^{\text{interf}} = A^{\alpha,\beta} g^{\text{interf}} = A^{\alpha,\beta}\left[\int_{z^\alpha}^{z^\beta} g(z)\,\mathrm{d}z - g^\alpha(z^0 - z^\alpha) - g^\beta(z^\beta - z^0)\right], \qquad (4.8)$$

where $A^{\alpha,\beta}$ is the interface area, and g^{interf} the areal density at the interface. Note that G^{interf} is independent of the choice of the integration limit, if $z^\alpha \le \xi^\alpha$ and $z^\beta \ge \xi^\beta$.

4.1.3 Surface Stress and Strain

The elastic energy is an extensive quantity. As such, Eq. (4.8) results in a representation of the elastic energy as an excess quantity at the interface. By applying Eq. (4.6) on a system comprising two homogeneous materials α and β, we write

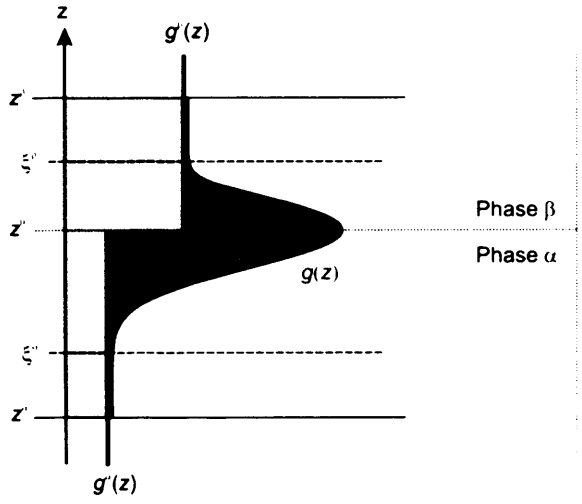

Fig. 4.4. The red curve indicates the profile $g(z)$ of the areal density of an extensive quantity G. The density profile of the homogeneous phase α is g^α and the density profile of the homogeneous phase β is g^β. The interfacial excess of G corresponds to the dark grey area. Reproduced from Müller and Saúl (2004).

$$\delta W^{\text{interf}} = \int_{z^\alpha}^{z^\beta} \sum_{ij} s_{ij}(z)\,\delta e_{ij}(z)\,\mathrm{d}V - \sum_{ij} s_{ij}^{\alpha}\,\delta e_{ij}^{\alpha} V^{\alpha} - \sum_{ij} s_{ij}^{\beta}\,\delta e_{ij}^{\beta} V^{\beta}, \quad (4.9)$$

where the integrand gives the bulk stress and the strain profiles across the interface, and V^α and V^β are the volumes of the bulk phases. Eq. (4.9) can be separated in perpendicular and parallel contributions with respect to the interfacial area, by decomposing the stress and strain tensors in normal and parallel components as follows:

$$\omega = \begin{pmatrix} \omega_{11}^{\parallel} & \omega_{12}^{\parallel} & 0 \\ \omega_{21}^{\parallel} & \omega_{22}^{\parallel} & 0 \\ 0 & 0 & 0 \end{pmatrix} + \begin{pmatrix} 0 & 0 & \omega_{13}^{\perp} \\ 0 & 0 & \omega_{23}^{\perp} \\ \omega_{31}^{\perp} & \omega_{32}^{\perp} & \omega_{33}^{\perp} \end{pmatrix}, \quad (4.10)$$

where ω is either $\boldsymbol{s}$ or $\boldsymbol{e}$. Let the following two equilibrium conditions be fulfilled: firstly, the non-gliding condition, that is, a virtual interfacial deformation occurs coherently: $\delta \boldsymbol{e}^{\parallel} = \delta \boldsymbol{e}^{\parallel\alpha} = \delta \boldsymbol{e}^{\parallel\beta}$. Secondly, the condition of mechanical equilibrium. In absence of external forces, Eq. (4.3) takes the form $\partial s_{iz}/\partial z = 0$, that is, the normal components of the stress tensor are homogeneous in the whole system: $s_{ij}^{\perp}(z) = s_{ij}^{\perp\alpha} = s_{ij}^{\perp\beta}$. Under these conditions, the excess interfacial elastic energy of the system given in Eq. (4.9) reads finally:

$$\delta W^{\text{interf}} = \sum_{ij} \left[\delta e_{ij}^{\parallel}\,\sigma_{ij} + s_{ij}^{\perp}\,\delta \epsilon_{ij} \right] A^{\alpha,\beta}, \quad (4.11)$$

where

$$\sigma_{ij} = \frac{1}{A^{\alpha,\beta}} \left[\int_{z^\alpha}^{z^\beta} s_{ij}^{\parallel}(z)\,\mathrm{d}V - s_{ij}^{\parallel\alpha} V^{\alpha} - s_{ij}^{\parallel\beta} V^{\beta} \right], \quad (4.12)$$

and

$$\epsilon_{ij} = \frac{1}{A^{\alpha,\beta}} \left[\int_{z^\alpha}^{z^\beta} e_{ij}^{\perp}(z)\,\mathrm{d}V - e_{ij}^{\perp\alpha} V^{\alpha} - e_{ij}^{\perp\beta} V^{\beta} \right]. \quad (4.13)$$

According to the definition of the interfacial excess quantity given in Eq. (4.8), Eq. (4.12) and Eq. (4.13) represent the interfacial excess quantity of the parallel component of the bulk stress tensor and the perpendicular component of the bulk strain tensor, respectively. Owing the equilibrium conditions as discussed above, the normal component of the bulk stress tensor and the parallel component of the bulk strain tensor are homogeneous across the interface, and do not contribute to the interfacial energy. To conclude, σ_{ij} and ϵ_{ij} define the *in-plane stress* and *out-of-plane strain*, which, provided that the equilibrium conditions are satisfied, are intrinsic interfacial quantities.

Let now be a solid surface exposed to vacuum. Then the stress and strain at the surface A^α of the solid are given by Eq. (4.12) and Eq. (4.13), that is,

$$\sigma_{ij}^{\text{surf}} = \frac{1}{A^\alpha}\left[\int_{z^\alpha}^{z^0} s_{ij}^{\parallel}(z)\,\mathrm{d}V - s_{ij}^{\parallel\alpha} V^\alpha\right], \tag{4.14}$$

and

$$\epsilon_{ij}^{\text{surf}} = \frac{1}{A^\alpha}\left[\int_{z^\alpha}^{z^0} e_{ij}^{\perp}(z)\,\mathrm{d}V - e_{ij}^{\perp\alpha} V^\alpha\right]. \tag{4.15}$$

In consideration of Eq. (4.14) and Eq. (4.15), the following three general statements hold: firstly, the surface excess quantities can be positive or negative. In particular by convention, a positive surface stress due to a contraction of the surface is called *tensile*, while a negative surface stress due to an expansion of the surface is called *compressive*. Secondly, if the solid has a crystalline structure, the value of the surface stress depends on the crystallographic face. Thirdly, the surface stress tensor of a two-dimensionally isotropic solid is $\sigma_{ij}^{\text{surf}} \equiv \sigma\,\delta_{ij}$, and in particular, the elastic energy change simplifies to

$$\delta W^{\text{surf}} = \sigma A^\alpha \sum_{ij} \delta e_{ij}^{\parallel}\,\delta_{ij}\,. \tag{4.16}$$

4.1.4 Bending Beam Technique

The measurement of surface stress is widely performed via the so-called bending beam technique, whereby measured changes in the curvature of a cantilever is attributed to the difference in surface stress between the upper and the lower surface of the cantilever.

The relation between the change in surface stress and the cantilever curvature can be derived from the equilibrium condition for the elastic energy of the cantilever as follows (Ibach 1997): consider a rectangular cantilever with length L, which is large with respect to its width w, which itself is large with respect to its thickness t. The x- and y-axis, respectively, is attached to the long and the short side of the cantilever at its midplane, and the origin of the z-axis intersects the midplane. It is assumed that stress and strain are small and symmetrically distributed with respect to the midplane, or the *neutral plane* of the cantilever. This is illustrated in Fig. 4.5. For simplicity, we further assume that the deformation of the cantilever occurs two-dimensionally isotropic, and only bulk stress and strain in the x- and y-axes are

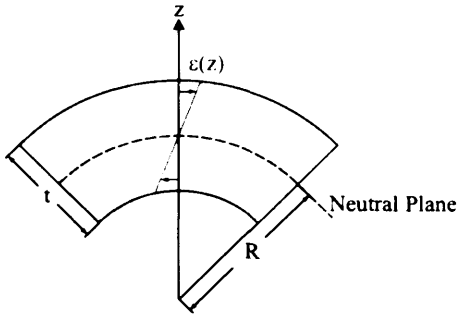

Fig. 4.5. Strain $e(z)$ due to uniaxial deformation of a cantilever, which is compressive above the neutral plane and tensile below the neutral plane. R is the radius of the curvature of the deformed cantilever, and t is the cantilever thickness. Reproduced from Ibach (1997).

predominant contributions to the resultant deformation: $e_{11} = e_{22} = \kappa z$, where κ denotes the cantilever curvature.

By decomposing the cantilever system into the bulk part and the two surfaces, the difference between the system elastic energy before and after the deformation may be written as

$$W^{\text{system}} = W^{\text{surf}(+)} + W^{\text{surf}(-)} + W^{\text{bulk}}, \tag{4.17}$$

where the superscripts (+) and (-) denote top and the underside of the plate, respectively. By using Eq. (4.16) and neglecting the change in the surface area along the z-axis $A(z) \equiv A$, the sum of the elastic energy at both the surfaces results in $W^{\text{surf}} = -\left(\sigma^{(-)} - \sigma^{(+)}\right) A\kappa t$. On the other hand, Eq. (4.6) leads to the elastic energy of the bulk, $\delta W^{\text{bulk}} = A \int \sum_i s_{ii}(z)\, \delta e_{ii}(z)\, \mathrm{d}z$. From the generalised Hooke's law Eq. (4.4) for the given conditions, $e_{ii} = \sum_k C_{iikk}\, s_{kk}$, it follows $s_{ii} = E_B/(1 - \nu_B)\, e_{ii}$, where $E_B = 1/C_{1111}$ is the Young's modulus, and $\nu_B = -C_{1122}/C_{1111}$ the Poisson's ratio of the bulk material. By performing the integration from $-\kappa t/2$ to $+\kappa t/2$, the bulk elastic energy change results in the following expression: $W^{\text{bulk}} = A\, E_B/(1 - \nu_B)\, \kappa^2 t^3 / 12$. For a given value of differential surface stress $\Delta\sigma \equiv \left(\sigma^{(-)} - \sigma^{(+)}\right)$, the system energy has its minimum at a particular curvature κ_m. The condition $(\partial W^{\text{system}} / \partial \kappa)_{\kappa=\kappa_m} = 0$ leads finally to the *Stoney's* equation,

$$\Delta\sigma = \frac{1}{6} \frac{E_B}{1 - \nu_B} t^2 \kappa_m, \tag{4.18}$$

which relates the curvature of the plate to its differential surface stress.

The original derivation of the Stoney's equation considered only a uniaxial cantilever bending (Stoney 1909), and differs from Eq. (4.18) in the factor $1/(1+\nu_B)$. The equation can be generalised for anisotropic cantilever deformations, by replacing the compliance coefficients C_{1111} and C_{1122} by their effective values. For a cubic

crystal, for example, the orientation dependent Young's modulus is (Nye 1957)

$$E_{\mathrm{B}}^{(\mathrm{cubic})} = \frac{1}{C_{1111} - 2(C_{1111} - C_{1122} - 2C_{2323})(l_1^2 l_2^2 + l_2^2 l_3^2 + l_3^2 l_1^2)} \tag{4.19}$$

and the Poisson's ratio is (Brantley 1973)

$$\nu_{\mathrm{B}}^{(\mathrm{cubic})} = -\frac{C_{1122} + (C_{1111} - C_{1122} - 2C_{2323})(l_1^2 m_1^2 + l_2^2 m_2^2 + l_3^2 m_3^2)}{C_{1111} - 2(C_{1111} - C_{1122} - 2C_{2323})(l_1^2 l_2^2 + l_2^2 l_3^2 + l_3^2 l_1^2)}, \tag{4.20}$$

where l_i and m_i are the components of the two orthonormal vectors $\boldsymbol{l}$ and $\boldsymbol{m}$ defining a plane with respect to the <100> cubic axes. The ratio $E_{\mathrm{B}}^{(\mathrm{cubic})} / \left(1-\nu_{\mathrm{B}}^{(\mathrm{cubic})}\right)$ is invariant within the {100} planes, therefore the Stoney's equation Eq. (4.18) for (100) oriented crystals may be considered isotropic.

4.2 Theory of Mechanochemistry

Chemical reactions give rise to changes in the composition and amount of matter in a particular system thus changes in its Gibbs free energy. Although the theory of elasticity (Landau and Lifshitz 1986) itself is self-consistent and facilitated the formulation of the Stoney's equation Eq. (4.18), the amount of matter was assumed to be fixed. It described the elasticity of lattices, rather than the matter attached to them. In order to link the elasticity of lattices to chemical reactions, surface thermodynamics must be considered separately (Müller and Saúl 2004). However, as recently reviewed by Rusanov (1996; 2005), surface thermodynamics based upon Gibbs's equilibrium principle describes both mechanical and chemical interactions self-consistently, including surface tension arising from adsorption and dissolution, as well as line tension or wetting. To maximise the simplicity of the theory of mechanochemistry, it would be therefore favourable to replace the first sections of this thesis in light of Gibbsean surface thermodynamics. Owing to the chronological development of this work, though, the theory of mechanochemistry is touched upon as an extension of the theory of elasticity. Differences between the formulation of the two theories (such between Piola and Cauchy stress tensor) are neglected in this work, however, details are discussed in Rusanov's reviews (1996; 2005).

4.2.1 Phase Equilibrium Condition

Gibbs distinguished between two species of particles (molecules, atoms, and ions) constituting a completely elastic solid: firstly, non-diffusive, immobile species that

are firmly fixed by some 'passive resistance' at their lattice sites and behave as an ideal solid. Secondly, 'fluids absorbed by the solid' that are mobile species and behave as a fluid (Rusanov 1996; 2005). When a transport process occurs and generates a chemical potential gradient in the solid, mobile species will redistribute to sustain the uniformity of their chemical potential, whereas the non-uniformity of the chemical potential of the immobile, non-diffusive species will persist.

When a solid comprising t immobile species is brought in contact with a solvent liquid, the solid will be subject to both the hydrostatic pressure and dissolution. Gibbs established the equilibrium condition for such a solid (Rusanov 1996; 2005): let the soluble solid be a parallelepiped whose faces are oriented normal to the principal axes x_i with $i = 1, 2, 3$ of a cartesian coordinate system, such as illustrated in Fig. 4.2 for a unit cube. The hydrostatic pressure acts always as a normal force at the faces of a solid. If, imaginary, three different liquids of different pressures p_i are assigned to each of the principal axes x_i with $i = 1, 2, 3$, then the bulk stress tensor Eq. (4.2) assumes a diagonal form with principal values $s_i = -p_i$. The chemical potential of the t th immobile species dissolved in the i th liquid may be denoted by $\mu_{t(i)}^{\text{liquid}}$. The Gibbs's phase equilibrium condition then reads

$$\frac{f - s_i - \sum_m \mu_m^{\text{solid}} c_m}{c_t} = \mu_{t(i)}^{\text{liquid}}, \tag{4.21}$$

where f is the Helmholtz free energy per unit volume; μ_m^{solid} is the chemical potential and c_m the concentration of the m th mobile species of the solid; c_t is the concentration of the t th immobile species of the solid (or their amount per unit volume).

Since the left-hand side of Eq. (4.21) refers entirely to the solid phase, its interpretation as the chemical potential of the t th immobile species of the solid in contact with the i th liquid

$$\mu_{t(i)}^{\text{solid}} = \frac{f - s_i - \sum_m \mu_m^{\text{solid}} c_m}{c_t} \tag{4.22}$$

results in the equality of the chemical potentials $\mu_{t(i)}^{\text{solid}} = \mu_{t(i)}^{\text{liquid}}$ at the solid/liquid interface, that is the equilibrium condition Eq. (3.3) for physico-chemical processes in conventional terms (Atkins and de Paula 2006).

4.2.2 Chemical Potential Tensor

The identity Eq. (4.22) relates the chemical potential $\mu_{t(i)}^{\text{solid}}$ of the t th immobile species of the solid and the principal values s_i of the diagonalised stress tensor $s_{ij}\,\delta_{ij}$

in a linear manner thus implies the *tensorial* nature of the chemical potential $\mu^{\text{solid}}_{t(i)}$. The chemical potential of the t th component of a system is conventionally defined as $\mu_t = (dF/dN_t)_{T,V,N_{t'\neq t}}$, that is, the change in the Helmholtz free energy F when the amount N_t of the t th component of the system changes at constant temperature T, volume V, and the amount $N_{t'\neq t}$ of the other components $t' \neq t$ constituting the system. Since all these thermodynamic properties are typical *scalars*, in particular the conjugate quantity N_t the amount or mass of the t th component of the system, Eq. (4.22) that stated the chemical potential to be a tensor imposed a fundamental problem.

Rusanov proposed to reformulate the definition of the chemical potential for anisotropic solids by introducing the notions of the volume displacement tensor V_{ij} and the mass displacement tensor $N_{t(ij)}$ of the t th immobile species of the solid:

$$\begin{aligned} V_{ij} &= A_i\, e_{ij}\,, \\ N_{t(ij)} &= c_t\, V_{ij}\,, \end{aligned} \tag{4.23}$$

where e_{ij} is the bulk strain (or displacement) tensor, A_i with $i = 1,2,3$ is the area of the face of the solid perpendicular to the principal axis i, and c_t is the initial concentration of the t th immobile species of the solid. The tensorial nature of the mass displacement tensor originates from the strain tensor, therefore not the mass itself but the displacement of mass is directional. Eq. (4.23) gives the fundamental relation between the theory of elasticity and the theory of mechanochemistry.

The so-defined chemical potential tensor $\mu_{t(ij)}$ of the t th immobile species of the solid reads

$$\mu_{t(ij)} = \left(\frac{\partial F}{\partial N_{t(ij)}}\right)_{T,V_{ij},N_{t'\neq t(ij)}}\,, \tag{4.24}$$

where F is the Helmholtz free energy, $N_{s(ij)}$ is the mass displacement tensor of the t th immobile species of the solid, T is the absolute temperature, V_{ij} is the volume displacement tensor, and $N_{t'\neq t\,(ij)}$ is the mass displacement tensor of the $t' \neq t$ th immobile species of the solid. The chemical potential tensor is interpreted as the change in the Helmholtz free energy of the solid when mass is transferred into the fixed volume of the solid from a particular direction against the 'passive resistance' (against diffusivity) that determines the elasticity of the solid. The anisotropy of the chemical potential thus reproduces the anisotropy of the bulk stress of the solid. Conversely, for mobile species of the solid and fluids in contact with the solid that do not experience the 'passive resistance', the transfer of mass cannot depend on

the direction thus the chemical potential tensor reduces to the conventional form $\mu_{m(ij)} \equiv \mu_m \delta_{ij}$ for the m th mobile species.

4.2.3 Fundamental Equation

By accounting for the tensorial representation of the chemical potential Eq. (4.24), the differential fundamental equation[2] for Helmholtz free energy F of a completely elastic, Gibbsean solid reads

$$\mathrm{d}F = -S\,\mathrm{d}T + \sum_{i,j=1}^{3} s_{ij}\,\mathrm{d}V_{ij} + \sum_{i,j=1}^{3} \mu_{t(ij)}\mathrm{d}N_{t(ij)} + \sum_{m} \mu_m \mathrm{d}N_m \,, \tag{4.25}$$

where $-S\,\mathrm{d}T$ is the standard entropic term that represents the thermochemical effect; $\sum_{ij} s_{ij}\mathrm{d}V_{ij}$ is the change in elastic energy due to volume expansion of the solid that represents the thermomechanical effect; $\sum_{ij} \mu_{t(ij)}\mathrm{d}N_{t(ij)}$ is the change in elastic energy due to increased concentration of the immobile species of the solid and $\sum_m \mu_m \mathrm{d}N_m$ is the change in Helmholtz free energy due to increased concentration of the mobile species of the solid that represent the mechanochemical effects (Rusanov 1996; 2005).

The integral form of Eq. (4.25) at constant temperature and along a particular principal axis $i = 1, 2, 3$ is

$$F = s_{ii}V_{ii} + \mu_{t(ii)}N_{t(ii)} + \sum_{m} \mu_m N_m \,, \tag{4.26}$$

Note that Eq. (4.26) is equivalent to Eq. (4.22).

The Gibbs free energy G associated with Eq. (4.26) is obtained by adding the volume expansion work $-s_{ii}V_{ii}$ to Helmholtz free energy F:

$$G = \mu_{t(ii)}N_{t(ii)} + \sum_{m} \mu_m N_m \,. \tag{4.27}$$

The differentiation of Eq. (4.27), $\mathrm{d}G = \mathrm{d}F - \mathrm{d}(s_{ii}V_{ii})$ by inserting Eq. (4.25) results in the definition of the chemical potential $\mu_{t(ii)}$ of the t th immobile species of the solid as the partial molar Gibbs free energy

[2] A fundamental equation is constructed by combining the First and the Second Law of thermodynamics. It is applicable for both reversible and irreversible processes in a given system (Atkin and de Paula 2006).

$$\mu_{t(ii)} = \left(\frac{\partial G}{\partial N_{t(ii)}}\right)_{T,s_{ii},N_{t'\neq t(ii)},N_m}, \tag{4.28}$$

at constant temperature T, bulk stress s_{ii}, amount $N_{t'\neq t(ii)}$ of other immobile species $t \neq t'$, and amount N_m of mobile species m. This is an analogue to the definition of chemical potential as the partial molar Gibbs free energy as is familiar in chemistry, whereby the volume expansion work $+pV$ for ideal liquids and gases is replaced by $-s_{ii}V_{ii}$ for ideal solids in Eq. (4.27). In chemistry, Gibbs free energy but not Helmholtz free energy is almost always considered. This is because the majority of laboratory chemical reactions occurs at constant system pressure. The associated decrease in the Gibbs free energy ΔG is the measure for the spontaneity of a chemical reaction, which is a consequence of the Second Law of thermodynamics (Atkins and de Paula 2006; Keeler and Wothers 2003).

4.2.4 Interfacial Fundamental Equation

The fundamental equations given in the previous section concerned the bulk solid phase with three uniform directions. An interface has only two uniform directions along the principal axes $i = 1, 2$ of the dividing surface, whereas extensive quantities will exhibit excess across the interface along the third principal axis $i = 3$ normal to the dividing surface. Since each of the free energy components in Eq. (4.25) is an extensive quantity, the corresponding interfacial excess free energy components can be calculated using Eq. (4.8) as

$$\mathrm{d}\bar{F} = -\bar{S}\,\mathrm{d}T + A\sum_{i,j=1}^{2}\sigma_{ij}\mathrm{d}e^{\parallel}_{ij} + A\sum_{i,j=1}^{2}g_{t(ij)}\frac{\mathrm{d}N_{t(ij)}}{N_t} + \sum_m \mu_m \mathrm{d}\bar{N}_m\,, \tag{4.29}$$

where $\bar{F}$ is interfacial excess Helmholtz free energy, $\bar{S}$ is interfacial excess entropy, A is dividing surface area, σ_{ij} is interfacial excess of bulk stress or mechanical surface tension[3], $e^{\parallel}{}_{ij}$ is tangential strain, $g_{t(ij)}$ is interfacial excess chemical potential of the t th immobile species, $\mathrm{d}N_{t(ij)}/N_t$ is relative tangential change in the amount of the t th immobile species, and $\bar{N}_m$ is interfacial excess amount of the m th mobile species.

Surface free energy $\bar{f}$ corresponds to the areal density of interfacial excess free energy Eq. (4.29), which is obtained by replacing $\mathrm{d}\bar{F} \equiv A\mathrm{d}\bar{f} + \bar{f}\mathrm{d}A$, $\mathrm{d}\bar{S} \equiv A\mathrm{d}\bar{s}$, $\mathrm{d}\bar{N}_m \equiv A\mathrm{d}\Gamma_m$, and $\mathrm{d}A/A \equiv \mathrm{d}e^{\parallel}_{ij}\delta_{ij}$ as

[3] Mechanical surface tension is termed elsewhere in this thesis 'surface stress'. The reasons for why Rusanov did not use the term 'surface stress' were discussed in his review (2005).

$$\mathrm{d}\bar{f} = -\bar{s}\mathrm{d}T + \sum_{i,j=1}^{2}\left(\sigma_{ij} - \bar{f}\delta_{ij}\right)\mathrm{d}e_{ij}^{\parallel} + \sum_{i,j=1}^{2} g_{t(ij)}\frac{\mathrm{d}N_{t(ij)}}{N_t} + \sum_{m}\mu_m \mathrm{d}\Gamma_m \,. \qquad (4.30)$$

This is the differential excess fundamental equation for Helmholtz free energy.

A further important interfacial excess quantity is the thermodynamic surface tension γ, which was defined by Gibbs as the work of formation of unit new surface area by cutting up a solid body (Rusanov 1996; 2005). Consider a soluble parallelepiped as in Section 4.2.1 that is brought in contact with its saturated solution. If at a given temperature, volume, chemical potentials of mobile species, and the amount of the immobile species, the parallelepiped is cut in two pieces and the equimolecular surface coincides with the dividing surface, the total volume of the parallelepiped remains constant and only surface work is produced. The thermodynamic surface tension for this process may be estimated as the interfacial excess of the free energy of the immobile species of the solid, $F^{\text{immobile}} = s_{ii}V_{ii} + \mu_{t(ii)}N_{t(ii)}$ with the principal axes $i = 1, 2$ of the dividing surface, as

$$\gamma\delta_{ij} = \sigma_{ij} + g_{t(ij)} \,. \qquad (4.31)$$

Therefore the sum of the principal values of mechanical tension tensor and excess chemical potential tensor equals surface tension $\gamma = \sigma_{ii} + g_{t(ii)}$ for $i = 1, 2$, which is a scalar thus non-directional. Note that Eq. (4.31) represents a central statement of the theory of mechanochemsitry: the difference between the thermodynamic surface tension and the mechanical surface tension is caused by the *non-uniformity* of the chemical potential across the solid/liquid interface. If the chemical potential was uniform, this difference would be caused by the adsorption free energy $\mu_t\Gamma_t$ of the mobile species t only. At the equimolecular surface that is defined as $\Gamma_t = 0$, the thermodynamic surface tension equals the mechanical surface tension $\gamma = \sigma$, which is the well-known result for liquids.

The overall surface free energy of the equimolecular dividing surface of a Gibbsean solid is related to Eq. (4.31) as

$$\bar{f} = \gamma + \sum_{m}\mu_m\Gamma_m \,. \qquad (4.32)$$

Therefore surface free energy equals thermodynamic surface tension *only* for solid in vacuum, that is, if there is no adsorption of mobile species.[4]

[4] Surface free energy and thermodynamic surface tension are widely used interchangeably in the literature.

The differential excess fundamental equation Eq. (4.30) can now be expressed in terms of thermodynamic surface tension by inserting Eq. (4.31) and differentiated Eq. (4.32) to give

$$\mathrm{d}\gamma = -\bar{s}\mathrm{d}T + \sum_{i,j=1}^{2}\left(\sigma_{ij} - \gamma\delta_{ij}\right)\left(\mathrm{d}e_{ij}^{\parallel} - \frac{\mathrm{d}N_{t(ij)}}{N_t}\right) - \sum_{m}\Gamma_m\mathrm{d}\mu_m \,. \tag{4.33}$$

As can be seen in this equation, a translational motion of the system $\mathrm{d}e_{ij}^{\parallel} = \mathrm{d}N_{t(ij)}/N_t$ does not contribute to a change in the surface free energy or thermodynamic surface tension. The second, mechanical term is specific for solids only. As for Eq. (4.31), the difference between solids and liquids is implied in $\left(\sigma_{ij} - \gamma\delta_{ij}\right)$ and caused by the non-uniformity of the chemical potential. Several further relations follow from this important equation:

Firstly, for liquids ($\sigma = \gamma$) as well as for non-deformable ($\mathrm{d}e_{ij}^{\parallel} = 0$) solids of a given mass ($\mathrm{d}N_{t(ij)} = 0$), Eq. (4.33) yields the *Gibbs adsorption* equation

$$\mathrm{d}\gamma = -\bar{s}\mathrm{d}T - \sum_{m}\Gamma_m\mathrm{d}\mu_m \,. \tag{4.34}$$

Secondly, at constant temperature, chemical potentials of mobile species, and the amount of an immobile species, Eq. (4.33) yields the *Shuttleworth-Herring* relation

$$\sigma_{ij} = \gamma\delta_{ij} + \frac{\partial\gamma}{\partial e_{ij}^{\parallel}} \,, \tag{4.35}$$

which states that the difference between the mechanical surface tension and the thermodynamic surface tension arises due to changes in the thermodynamic surface tension with surface strain. By relating again to Eq. (4.31), the changes in the thermodynamic surface tension with surface strain is attributed to the non-uniformity of the chemical potential.

Thirdly, for a two-dimensionally isotropic interface $\sigma_{ij} \equiv \sigma\delta_{ij}$ and at constant amount of immobile species, Eq. (4.33) yields the *Eriksson* relation

$$\mathrm{d}\gamma = -\bar{s}\mathrm{d}T + (\sigma - \gamma)\,\mathrm{d}\ln A - \sum_{m}\Gamma_m\mathrm{d}\mu_m \,, \tag{4.36}$$

which implies also the Shuttleworth's relation Eq. (4.35) for two-dimensionally isotropic interfaces. At a given temperature and a mobile species m', Eq. (4.36) states that

$$\left(\frac{\partial\sigma}{\partial\mu_{m'}}\right)_A = -\left(\frac{\partial(\Gamma_{m'}A)}{\partial A}\right)_{\mu_{m'}} . \tag{4.37}$$

This relation predicts that the increased chemical potential at a fixed surface area accompanying a *positive* adsorption of the mobile species m' gives rise to an increase in the *repulsive* (or negative) magnitude of mechanical surface tension $\partial\sigma/\partial\mu_{m'} < 0$, which is equivalent to the situation of an *enlarged* surface area at a fixed chemical potential due to the excess amount of adsorbates $\partial(\Gamma_{m'}A)/\partial A > 0$.

4.2.5 Excess Electrochemical Potential

When ions are present in the solution, the adsorption equation Eq. (4.33) may be expressed in terms of the electrochemical potential Eq. (3.19), that is $\tilde{\mu}_n = \mu_n + e z_n \varphi$ for the nth ion species that was introduced in relation to surface acid/base reactions in Section 3.5.

To establish a relation between ion adsorption and thermodynamic surface tension, all mobile species are subdivided into three groups (Rusanov 1996): firstly, completely neutral, non-charged species that do not produce ions that will be termed 'neutral' species. Secondly, charged species either entirely in the solid phase or entirely in the fluid phase when their distribution is restricted, or throughout the system when their distribution is not restricted, whose combinations yield neutral substances (for example via ion exchange) that will be termed 'combined neutral' species. Thirdly, excess ions in the solid phase and oppositely charged ions in the fluid phase that are together electrically neutral but do not yield a neutral substance that will be termed 'combined charged' species. These three groups replace the last term in Eq. (4.33) and represented as follows:

$$-\sum_r \Gamma_r \mathrm{d}\mu_r - \sum_q \Gamma_q \mathrm{d}\tilde{\mu}_q - \Gamma^\alpha \mathrm{d}\tilde{\mu}^\alpha - \Gamma^\beta \mathrm{d}\tilde{\mu}^\beta , \tag{4.38}$$

where the first term with subscript r refers to the neutral species, the second term with subscript q refers to the combined neutral species, and the third term with superscript α refers to a combined charged species in the solid phase, and the fourth term with superscript β refers to the combined charged species in the fluid phase. It is assumed that there is only one pair of combined charged species without loss of generality.

When accounted for Eq. (4.38) the equation for the thermodynamic surface tension reads (Rusanov 1996):

$$d\tilde{\gamma} = d\gamma - \sum_q \Gamma_q \, d\tilde{\mu}_q - \Theta \, d(E + K) , \tag{4.39}$$

where the first term corresponds to Eq. (4.33) and includes the neutral species, the second term corresponds to the combined neutral species, and the third term results from the combined charged species. In the third term, $\Theta = \Gamma^\alpha z^\alpha e = -\Gamma^\beta z^\beta e$ is the surface charge of the solid phase per unit interfacial area. The difference in the electrochemical potentials across the interface was defined as $\tilde{\mu}^\alpha/z^\alpha - \tilde{\mu}^\beta/z^\beta \equiv e(E+K)$, where the quantities E and K have specific terminologies in the theory of electrocapillarity: E is the electromotive force of a cell with such a reference electrode chosen so as to make K a function of temperature and pressure only (Rusanov 1996). At constant temperature and pressure, as well as for constant chemical and electrochemical potentials of the mobile species, Eq. (4.39) assumes a generalised form of the Lippmann equation for a deformable solid electrode, whereas if the solid electrode is non-deformable, the equation changes to the classical Lippmann equation $d\tilde{\gamma}/dE = \Theta$, which represents a central relationship in the theory of electrocapillarity.

5. Measurement of Surface Stress

A hundred years ago in 1909, Stoney reported the first measurement of surface stress using a cantilever. He used a centimetre-scaled steel ruler and measured its millimetre-ranged deformation upon the deposition of metallic thin films. The surface stress difference between the upper and the lower surface of the ruler, which he was able to measure was in the range of kN/m. This is a million times larger than the mN/m sensitivity readily achieved today. An examination of Eq. (4.18) shows that even though the factors related to the mechanical properties are similar to the cantilevers used in this work, in fact, it is the limit of optical detection that gives rise to the enormous improvement in the magnitude of measurable surface stress changes. This chapter details the materials and methods involved in the measurement of surface stress. We note that herein, surface stress measurements were performed on the Veeco Scentris (Veeco Instruments Inc., Santa Barbara, CA, U.S.A.) that was recently withdrawn from the market in 2004 due to a range of different technical and economical issues.

5.1 Overview

Multiple arrays of eight rectangular Si(100) cantilevers each measuring 500 μm in length, 100 μm in width and 0.9 μm in thickness with a nominal spring constant of 0.02 N/m, were coated on one side with a thin film of gold (20 nm gold with a 2 nm titanium adhesion layer). Individual cantilevers were functionalised with either 16-mercaptohexadecanoic acid ($HS(CH_2)_{15}COOH$, herein termed MHA) or 1-hexadecanethiol ($HS(CH_2)_{15}CH_3$, herein termed HDT) via incubation in an array of glass microcapillaries. Reference cantilevers were coated with the non-ionisable HDT, which has an identical chain length and reportedly similar packing density to MHA (Nuzzo, Dubois, and Allara 1990) but differs in the terminal methyl group (Fig. 5.1A). The modified cantilever array was then mounted in a sealed liquid cell. A home-built gravity flow system was developed in order to control the exchange of up to six different sodium phosphate solutions via an automated valve (Fig. 5.1B).

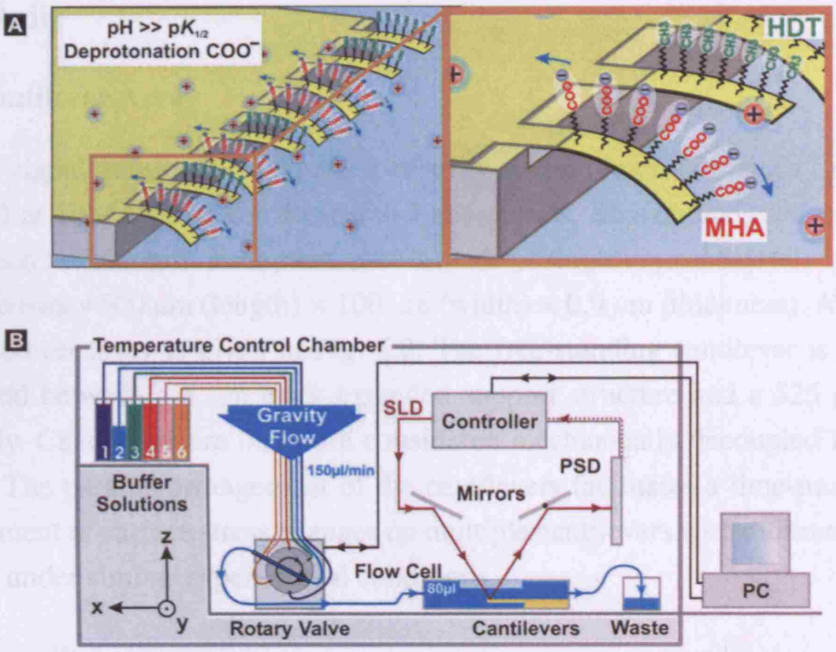

Fig. 5.1. (A) Schematic figure to illustrate the principle of differential surface stress titration of MHA, using reference HDT coated cantilevers. (B) Experimental apparatus to optically detect cantilever bending in different liquid environments.

All signals were acquired under an average liquid flow rate of 150±30 µL/min. Variations in flow rate within this range were not found to substantively affect the equilibrated bending signals. The absolute deflection at the free-end of each cantilever z_{abs} was measured using a time-multiplexed optical detection system in different liquid environments (Scentris Veeco Instruments Inc., Santa Barbara, CA, U.S.A.). Herein the raw data are presented without any baseline corrections. The bending signal was subsequently converted into a difference in surface stress between the upper and lower sides of the cantilever Δz_{abs} using the Stoney's equation Eq. (4.18), where L is the effective length of the cantilever going up to 500 µm, t = 0.9 µm is the thickness, and $E/(1-\nu)$ is the ratio between the Young's modulus E and Poisson ratio ν of Si(100) which is invariant within the 100 planes (Brantley 1973). The differential surface stress $\Delta\sigma_{\text{diff (MHA/HDT)}}$ specific to MHA ionisation was calculated by subtracting the reference HDT absolute surface stress $\Delta\sigma_{\text{abs (HDT)}}$ from the MHA absolute surface stress $\sigma_{\text{abs (MHA)}}$, that is, $\Delta\sigma_{\text{diff (MHA/HDT)}} = \sigma_{\text{abs (MHA)}} - \sigma_{\text{abs (HDT)}}$. In this thesis, a positive absolute deflection corresponds to the upwards bending of the cantilever due to a tensile surface stress and a negative absolute deflection to the downwards bending of the cantilever due to a compressive surface stress, in accord with the common sign convention (Chapter 4).

5.2 Details

5.2.1 Cantilever Array

The core signal transducing element is an array of eight microfabricated cantilevers produced at IBM Rüschlikon Research Laboratories, Switzerland, and purchased from Veeco Instruments. Each cantilever is made of single crystal Si(100) with nominal dimensions 500 μm (length) × 100 μm (width) × 0.9 μm (thickness). A drawing of a cantilever array is given in Fig. 5.2. The free-standing cantilever is clamped at one end between a 5 μm thick extended support structure and a 525 μm thick chip body. Cantilevers are therefore considered mechanically decoupled from one another. The parallel arrangement of the cantilevers facilitates a time-multiplexed measurement of surface stress changes on multiple cantilevers with different surface coatings under similar experimental conditions.

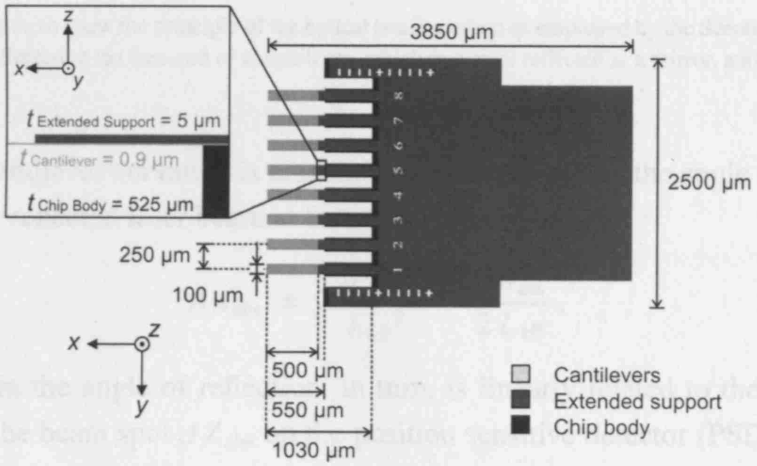

Fig. 5.2. A drawing to show the dimensions of an array of eight microfabricated Si(100) cantilevers fabricated at IBM Rüschlikon.

5.2.2 Optical Beam Method

The absolute bending of all eight cantilevers was monitored using the time multiplexed optical beam method with a single position sensitive detector (Scentris, Veeco Instruments Inc., Santa Barbara, CA, U.S.A.). For typical cantilever deflections $\lesssim 1$ μm that are much smaller than the length of the cantilever, the change in cantilever curvature $\Delta\kappa_{\mathrm{abs}}$ is linearly proportional to the change in cantilever deflection Δz_{abs} measured at the effective length L_{eff} of the 500 μm long cantilever. The

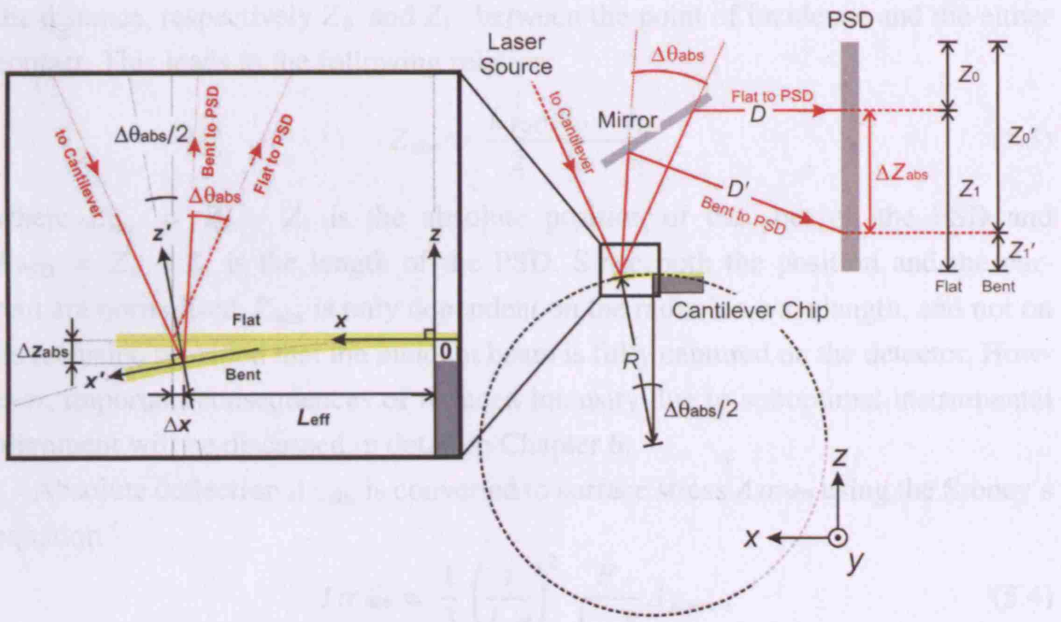

Fig. 5.3. Schematic to show the principle of the optical beam method as employed by the Scentris instrument. A laser beam is reflected at the free-end of a cantilever, which in turn is reflected at a mirror, and finally detected on a PSD.

change in cantilever curvature is also linearly proportional to the angle of reflection $\Delta\theta_{\mathrm{abs}}$ of the reflected laser beam at the effective length:

$$\Delta\kappa_{\mathrm{abs}} = 2\frac{\Delta z_{\mathrm{abs}}}{L_{\mathrm{eff}}^2} = \frac{\Delta\theta_{\mathrm{abs}}}{2L_{\mathrm{eff}}}, \tag{5.1}$$

the change in the angle of reflection, in turn, is linearly related to the change the position of the beam spot ΔZ_{abs} on the position sensitive detector (PSD) located in distance D from the position of reflection on the cantilever:

$$\Delta Z_{\mathrm{abs}} = D\Delta\theta_{\mathrm{abs}} = \frac{4D}{L_{\mathrm{eff}}}\Delta z_{\mathrm{abs}}, \tag{5.2}$$

therefore, a sub-μm cantilever deflection Δz_{abs} is amplified by the physical distance D between the cantilever and the PSD to a sub-mm ΔZ_{abs} change in the beam spot position on the PSD. The principle of the optical detection is depicted in Fig. 5.3.

The PSD installed in the cantilever instrument consists of a silicon photodiode. This is an one-dimensional PSD, with an active area of 2 mm (width) × 10 mm (height). An incident superluminescent diode (SLD) beam generates a photocurrent $I = I_0 + I_1$, which flows from the point of incidence through a uniform resistive layer to both the electrodes. Therefore, both I_0 and I_1 are inversely proportional to

the distance, respectively Z_0 and Z_1, between the point of incidence and the either contact. This leads to the following relation:

$$Z_{abs} = \frac{L_{PSD}}{2} \frac{I_0 - I_1}{I_0 + I_1}, \tag{5.3}$$

where $Z_{abs} = Z_0 - Z_1$ is the absolute position of the spot on the PSD and $L_{PSD} = Z_0 + Z_1$ is the length of the PSD. Since both the position and the current are normalised, Z_{abs} is only dependent on the radiation wavelength, and not on its intensity, provided that the incident beam is fully captured on the detector. However, important consequences of reduced intensity due to suboptimal instrumental alignment will be discussed in detail in Chapter 6.

Absolute deflection Δz_{abs} is converted to surface stress $\Delta \sigma_{abs}$ using the Stoney's equation

$$\Delta \sigma_{abs} = \frac{1}{3} \left(\frac{t}{L_{eff}} \right)^2 \frac{E}{1 - \nu} \Delta z_{abs}, \tag{5.4}$$

where t is the thickness of the cantilever, E the Young's modulus, and ν is the Poisson's ratio (Stoney, 1909). A derivation of this equation was given in Section 4.1.4. Both E and ν for Si(100) depend on the crystallographic orientation, however the ratio $E/(1-\nu)$ is invariant within the (100) planes. Therefore the Si(100) is mechanically isotropic. By using the compliance constants reported by Brantley (1973), the resultant ratio is $E/(1-\nu) = 180.5$ GPa.[1] Fig. 5.4 shows the orientation of Si(100) along the principal axes of an IBM cantilever.

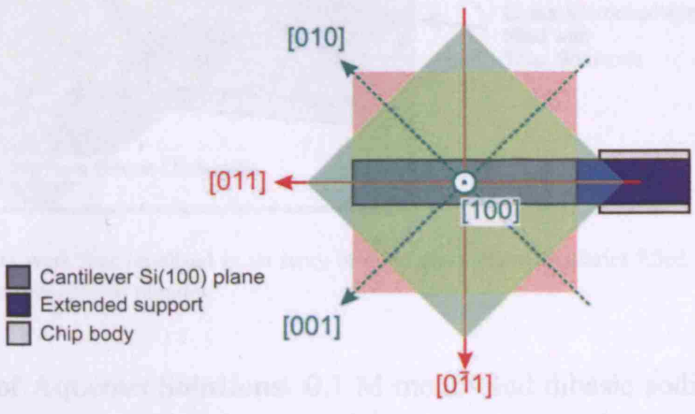

Fig. 5.4. Orientation of Si(100) along the principal axes of a cantilever.

[1] The reported compliance constants for Si(100) are as follows: $C_{1111} = 0.768$, $C_{1122} = -0.214$, and $C_{2323} = 0.315$ in (10^{-11} m^2/N). The subscripts 1, 2, and 3 denote the principal axes of a cartesian coordinate system. Note that Brantley uses the matrix representation of the stress and strain tensor, in which $s_{44} \equiv 4 S_{2323}$.

5.2.3 Protocol

Preparation of Cantilevers and Silicon Wafers. Cantilever arrays were first cleaned with freshly prepared piranha solution (at ratio 1:1 H_2SO_4 and H_2O_2 - CAUTION: piranha solution is hazardous and can cause explosions or severe skin burns if not handled with great care) for 20 minutes, and rinsed thoroughly in deionised water. Second, the arrays were immersed into a solution comprising H_2O:H_2O_2:NH_4OH (at ratio 1:1:1) for 10 minutes, and again rinsed thoroughly with deionised water. Finally, the arrays were rinsed with pure ethanol and dried on a hotplate at 75 °C. Thereafter, cantilever arrays were evaporated on one side with a thin film of gold (E-beam evaporation, 20 nm Au with 2 nm Ti or Cr adhesion layer, BOC Edwards Auto 306, U.K.), at a base pressure of about 2×10^{-7} mbar, and an evaporation rate of 0.04 nm/s for Ti and 0.07 nm/s for Au, measured directly above the source. Freshly evaporated cantilevers were sealed under argon and functionalised within a few hours after the evaporation. Thereby the cantilevers were incubated in an array of eight glass microcapillaries filled in random order with either 4 mM HDT or MHA for 20 minutes, and rinsed in pure ethanol and deionised water. This is illustrated in Fig. 5.5. Functionalised cantilevers were then stored in a Petri dish filled with ultrapure water (18.2 MOcm resistivity, Millipore Co., Billerica, MA, U.S.A.) at room temperature until use.

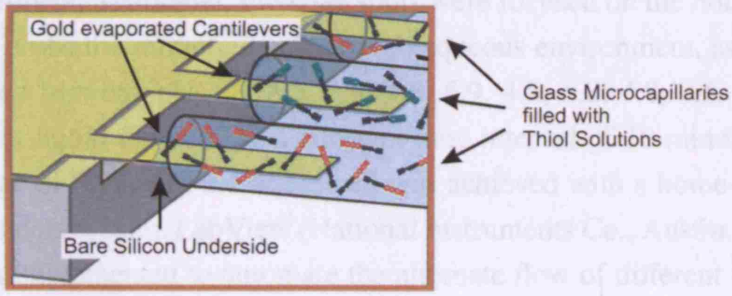

Fig. 5.5. Cantilevers were functionalised in an array of eight glass microcapillaries filled with different thiol solutions in random order for 20 minutes.

Preparation of Aqueous Solutions. 0.1 M mono- and dibasic sodium phosphate salts were dissolved in ultrapure water and diluted according to the pH values 4.8, 5.9, 6.8, 7.6, and 8.4 to maintain a constant ionic strength of $I = 0.1$. The ionic strengths were calculated by assuming the literature pK_a values for the phosphoric acid (*The CRC Handbook of Chemistry and Physics*, 86th ed., 2005). The pH value was measured using a commercial pH meter (Mettler-Toledo Ltd., Leicester, U.K.).

Similarly, the pH 5.4 and 6.8 sodium phosphate $Na_{(3-x)}H_xPO_4$ aqueous solutions at three different ionic strengths of I = 0.1, 0.01, and 0.001 were prepared by diluting the mono- and dibasic phosphate solution. After adjusting the pH values, the solutions were filtered using 0.2 μm filters (Millipore). The pH 4.5 and 9.0 ammonium phosphate $(NH_4)_{(3-x)}H_xPO_4$ aqueous solutions at I = 0.1 were prepared following the equivalent protocol used for the sodium phosphate solutions. Phosphoric acid H_3PO_4 and ammonium hydroxide NH_4OH, respectively, at I = 0.1 were used to decrease and increase the pH value where necessary. The ammonia/ammonium chloride and nitrate buffers were prepared by adjusting the pH of the 0.1 M NH_4Cl and 0.1 M NH_4NO_3 aqueous solutions using 4.0 M ammonium hydroxide solutions to pH 9.0, respectively. By assuming the literature pK_a value for the ammonia (*The CRC Handbook of Chemistry and Physics*, 86th ed., 2005), the resulting solutions had an ionic strength of I = 0.1. The solutions were then degassed via 30 minutes ultrasonication and saturated with argon thereafter. All chemicals were purchased from Sigma-Aldrich (Sigma-Aldrich Co., St. Louis, MO, U.S.A.).

Refractive Index Change Test. The absolute bending of all eight cantilevers was monitored using the Scentris instrument. The functionalised cantilever array was mounted in a sealed liquid chamber with a volume of approximately 80 μL. The liquid cell and each aliquot of aqueous solutions were placed into the temperature controlled cabinet to allow for temperature equilibration for at least 12 hours prior to each experiment. Thereafter, the laser spots were focused on the non-deformable chip body to probe the refractive index of the aqueous environment, as the solution pH was cycled between pH 4.8, 3.5, 4.8, 4.8, 5.9, 4.8, 6.8, 4.8, 7.6, 4.8, 8.4, 4.8 under constant liquid flow and at a constant time interval of 10 minutes. The efficient exchange of liquids in the liquid cell was achieved with a home-built gravity flow microfluidics system. LabView (National Instruments Co., Austin, TX, U.S.A.) software was implemented to automate the alternate flow of different pH solutions via a 6-way valve (Serial MVP, Hamilton, Reno, NV, U.S.A.).[2] Typical absolute deflection signals acquired in this so-called refractive index change test using sodium phosphate solutions is shown in Fig. 5.6. As can be seen in the figure, peaks were measured in the absolute deflection signals with the onset of liquid exchange. The magnitude and direction of the apparent deflection signals depended on the concentrations of the exchanged solutions: an increase in the solution concentration resulted in an apparent downward deflection signal, while a decrease in the solution

[2] The LabView software was written and implemented by Michael Neumann from the Department of Physics, Royal Holloway, University of London.

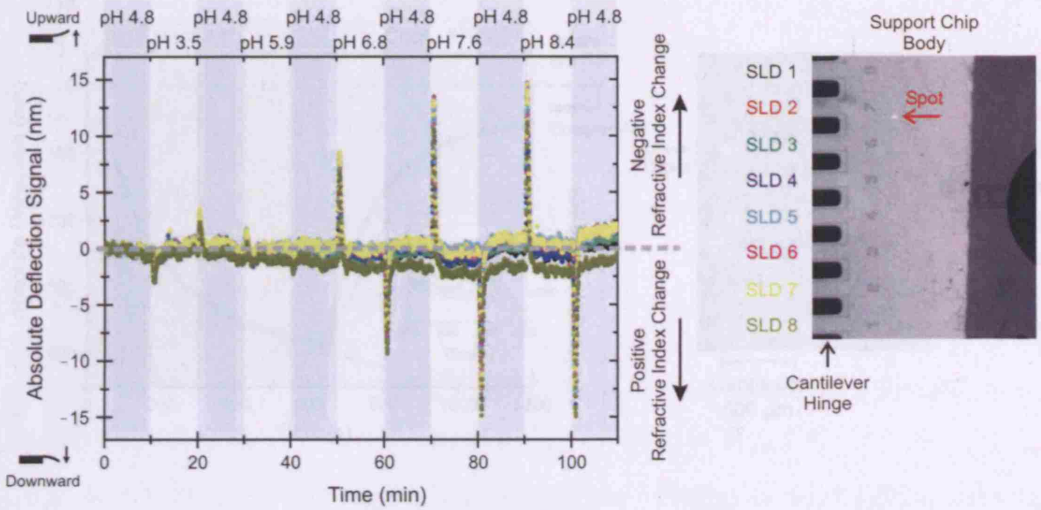

Fig. 5.6. Typical deflection signals acquired on the chip body to probe the changes in the refractive index of the aqueous environment, as the pH was switched between H 4.8, 3.5, 4.8, 4.8, 5.9, 4.8, 6.8, 4.8, 7.6, 4.8, 8.4, 4.8 under constant liquid flow and at a constant time interval of 10 minutes.

concentration resulted in an apparent upward deflection signal. This is in agreement with the expected cantilever signals according to the Snell's law. However, the deflection signals measured after the completion of a liquid exchange was found to be independent of the solution pH. Therefore, the apparent deflection signals were attributed to some inhomogeneities in the solution refractive index caused during the mixing process of the pH solutions. Since the chip body is non-deformable, this measurement served also to probe the stability of the SLD signals. Stable signals were found to drift by ~2 nm per hour, as can be seen in the figure.

Heating Test. Subsequent to the refractive index change test, the heating test was performed that relies on the bimetallic effect of the gold coated cantilevers to align the each SLD spot onto the free-end of each cantilever on the array. This is important to ensure that the effective length of all eight cantilevers is equivalent. Upon heating the entire liquid cell by 1 °C, all eight cantilevers were observed to bend downward due to the stronger expansion of the gold film relative to the bulk silicon material. The relative standard deviation among the absolute bending signals were maintained to less than 2 per cent. A typical measurement is shown in Fig. 5.7. Herein, a positive deflection signal is defined as a tensile surface stress whereas a negative signal correlates to compressive stress, in agreement with the common sign convention.

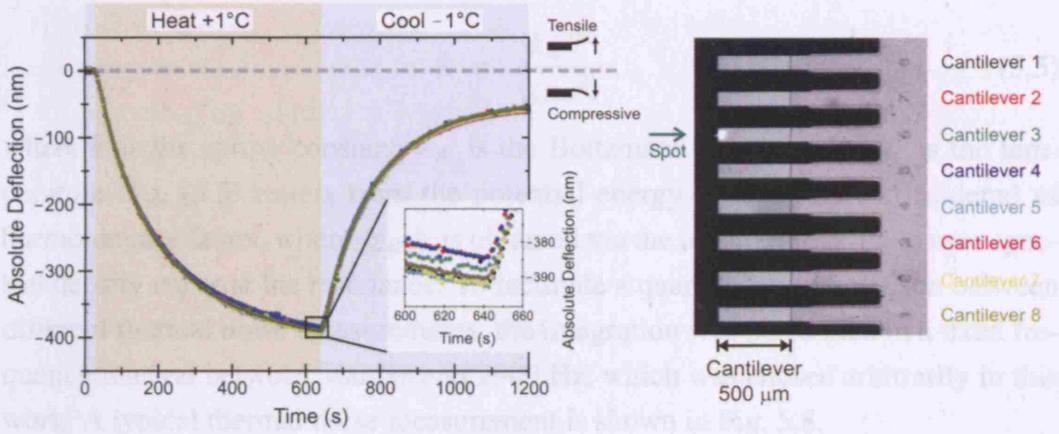

Fig. 5.7. Typical deflection signals acquired upon aligning the lasers on the free-end of cantilevers and heating the entire liquid cell by 1 °C to induce a bimetallic effect on gold coated cantilevers. An optimal SLD/cantilever alignment resulted in a relative standard deviation of less than 2 per cent among the eight heating signals.

Measurement of Spring Constant. To determine the spring constant of cantilevers, the thermal noise of cantilevers was measured, which arose due to the Brownian motion of the cantilevers at their resonant frequencies (Hutter and Bechhoefer 1993). The spring constant of the cantilevers is related to the time-averaged

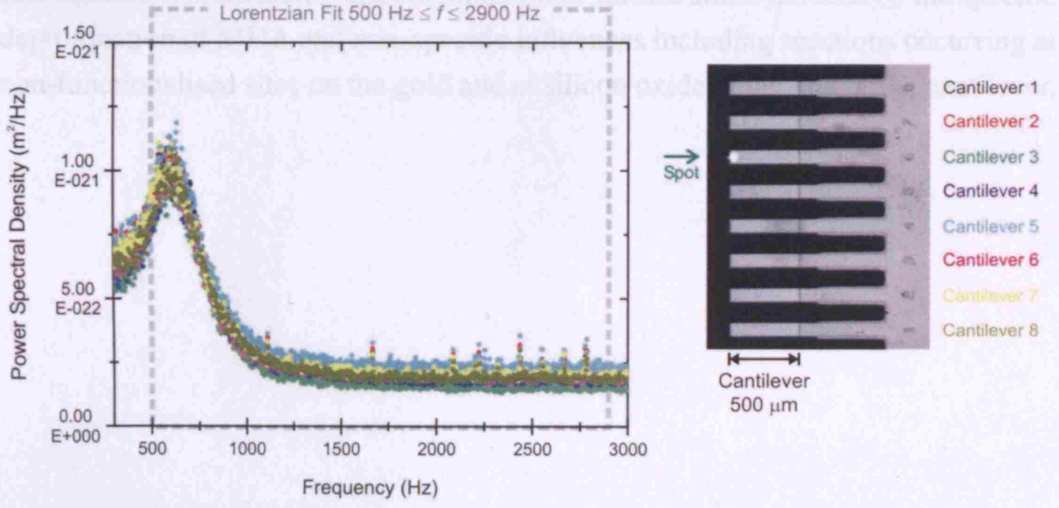

Fig. 5.8. Typical deflection signals due to thermal fluctuation of cantilevers. The measured signals were Fourier-transformed to obtain the power spectral densities in the frequency domain to calculate the spring constants of cantilevers.

absolute deflection signal $\langle z_{abs} \rangle$ as

$$k = \frac{k_B T}{\langle z_{abs}{}^2 \rangle}, \tag{5.5}$$

where k is the spring constant, k_B is the Boltzmann constant, and T is the temperature. Eq. (5.5) results from the potential energy of cantilevers considered as harmonic oscillators, where $\langle z_{abs} \rangle$ is obtained via the integration of the power spectral density curve at the resonance. To facilitate a quantitative comparison between different thermal noise measurements, the integration was performed in a fixed frequency interval between 500 Hz and 2900 Hz, which was chosen arbitrarily in this work. A typical thermal noise measurement is shown in Fig. 5.8.

Core Measurement. The preceding control measurements allowed the core surface stress measurement to be finally performed. Fig. 5.9A shows the raw deflection signals of a typical MHA-coated cantilever and a HDT-coated cantilever upon switching between pH 4.8/8.4/4.8 liquid environments. It can be seen that at pH 4.8, the deflection signal was stable under constant liquid flow. Upon switching to pH 8.4, where the carboxylic acid terminating self-assembled monolayers (SAMs) are expected to be deprotonated, the cantilever bent downwards corresponding to a compressive surface stress. When the aqueous environment was switched back to pH 4.8, the bending signal returned towards the zero deflection baseline. The absolute deflection is attributed to a combination of surface stress induced by the specific deprotonation of MHA and non-specific influences including reactions occurring at non-functionalised sites on the gold and at silicon oxide underside of the cantilever,

changes in refractive index or in the temperature of the aqueous environment. These non-specific effects will affect both MHA and HDT signals to the same extent, and are eliminated by taking a differential measurement (MHA minus HDT absolute signals). The corresponding differential signals are shown in Fig. 5.9B. Care was taken to investigate the influence of liquid flow rate during gravity flow on deflection signal. While the kinetics of deflection signal was indeed found to depend on differences in flow rate, the equilibrium differential signal was found not to be substantively affected by flow rate under the conditions investigated herein. All signals were acquired under a liquid flow rate of 150 ± 30 μL/min at the beginning of a measurement, which decreased at a constant rate of 0.25 ± 0.03 μL/min during the measurements.

5.3 Characterisation Measurements

Cantilever samples exhibit composite layers of different surface morphology and chemical composition, rather than a single crystal of silicon. The cross section of a SAM-functionalised cantilever is illustrated in Fig. 5.10. The following sections summarise measurements performed to characterise the composite layers and supplemented by literature data.

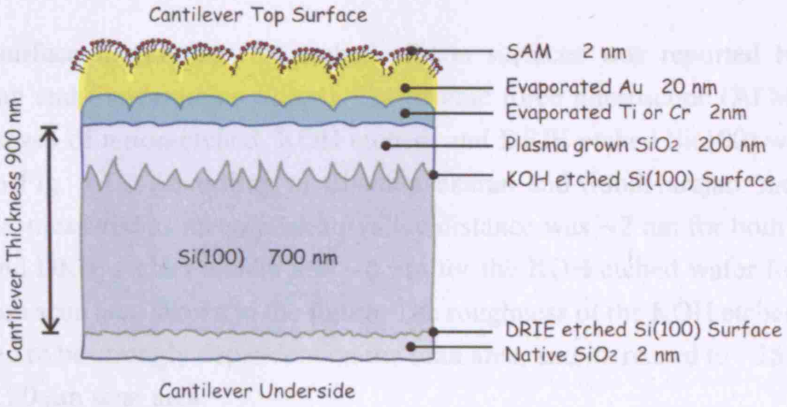

Fig. 5.10. Illustration to show the composite layers associated with a functionalised cantilever.

5.3.1 Surface Morphology

Si(100) cantilever arrays were fabricated by standard microfabrication procedures, which involved the chemical etching of silicon (100) on insulator wafers.[3] At the top surface of a silicon on insulator wafer, wet anisotropic KOH etch was applied, which produced well-defined, that is uniform and reproducible, sharp structures. A KOH etched silicon surface is very rough compared to the non-etched original surface. In order to reduce the surface roughness, a 200 nm SiO_2 layer was grown by oxygen plasma on top of the KOH etched surface. At the underside, dry deep reactive ion etch (DRIE) was applied, which was a rapid procedure and generated smooth surfaces comparable to the non-etched surface.

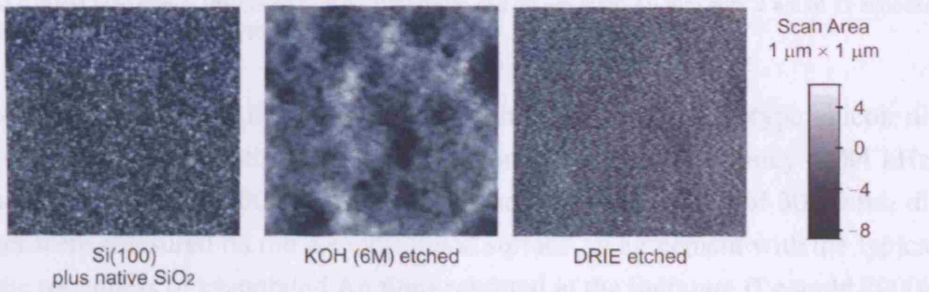

Fig. 5.11. AFM topography images of non-etched, KOH-etched, and DRIE-etched Si(100) surfaces. Adopted from Chandrasekaran and Sundararajan (2004).

The surface morphology of etched silicon surfaces was reported by Chandrasekaran and Sundararajan (2004). The atomic force microscope (AFM) topography images of a non-etched, KOH etched, and DRIE etched Si(100) wafers are shown in Fig. 5.11. According to Chandrasekaran and Sundararajan, the surface roughness measured as mean peak-to-valley distance was ~2 nm for both the non-etched and DRIE etched wafers and ~6 nm for the KOH etched wafer for a the 1 μm × 1 μm scan area shown in the figure. The roughness of the KOH etched surface was found to be strongly dependent on the scan area, and increased to ~25 nm for a 20 μm × 20 μm scan area.

Fig. 5.12 shows typical AFM topography images of bare silicon and Au/Ti evaporated silicon wafers prepared in parallel to cantilever arrays. The scan area was 500 nm × 500 nm. The images were acquired under ambient conditions, using

[3] Personal communication from U. Drechsler from IBM Rüschlikon.

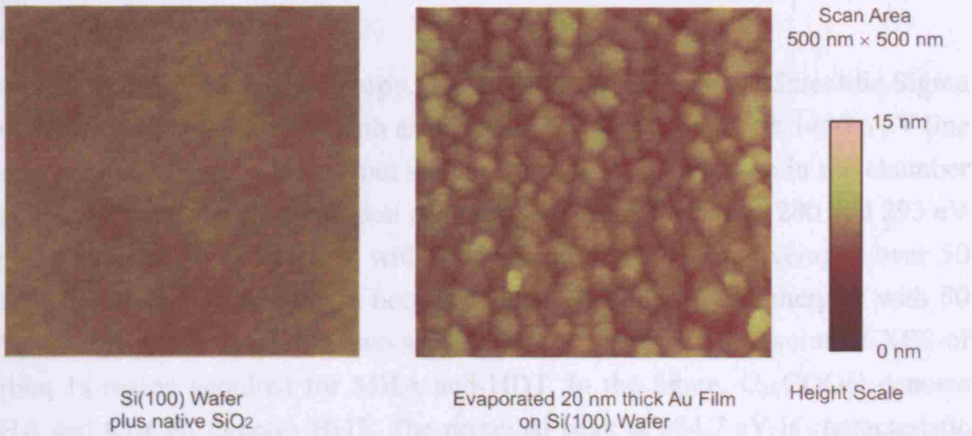

Fig. 5.12. AFM topography images of bare Si(100) wafer and 20 nm thick Au film with 2 nm of Ti adhesion layer evaporated on a piece of Si(100) wafer.

Veeco Dimension AFM in tapping mode with a Veeco OTR8 A-type silicon nitride tip with a nominal tip radius of 15 nm and a resonant frequency of 84 kHz. Compared with the Si(100) surface that is essentially flat, grains of 30-40 nm diameter were measured on the Au evaporated surface, in agreement with the typical surface roughness of evaporated Au films reported in the literature (Leopold 2000). Preliminary measurements performed on free-standing cantilevers showed surface morphologies comparable to the rigid wafers.

5.3.2 Surface Chemistry of SAMs

Perhaps the most widely followed protocol to prepare alkanethiol SAMs on gold is the overnight incubation of a gold-evaporated, thick substrate in 1 mM ethanolic thiol solution (Bain et al. 1989). The geometry of the eight cantilevers tethered to a single support chip body prevents the application of this standard protocol to cantilever arrays. In this work, cantilevers are incubated in 4 mM ethanolic thiol solution for 20 minutes via the microcapillary array technique developed previously at IBM (Bietsch et al. 2004). Therefore to compare the SAMs used in this work with literature SAMs, the SAMs were characterised by X-ray photoelectron spectroscopy (XPS), variable angle spectroscopic ellipsometry, and contact angle goniometry.[4] Given the miniaturised geometry of cantilevers, characterisation of the SAMs was

[4] The XPS and variable angle spectroscopic ellipsometry measurements were performed by Marilyne Sousa from IBM Rüschlikon.

performed instead on silicon wafers, which had been functionalised in parallel to silicon cantilevers.

X-ray Photoelectron Spectroscopy. Spectra were taken on a VG Scientific Sigma Probe Spectrometer equipped with an aluminum Al K_α source with 1486.6 eV line energy and approximate beam spot size of 400 μm^2. The pressure in the chamber was 3×10^{-9} mbar. High resolution carbon C(1s) spectra between 280 and 293 eV binding energies were acquired with a 40 eV pass energy and averaged over 50 scans, as well as survey spectra between 0 and 600 eV binding energies with 80 eV pass energy averaged over two scans. Fig. 5.13 shows high resolution XPS of carbon 1s region acquired for MHA and HDT. In the figure, $C_{16}COOH$ denotes MHA and $C_{16}CH_3$ denotes HDT. The principal peak at 284.7 eV is characteristic for aliphatic hydrocarbons. The spectra were normalised with respect to the absolute count measured at the principal peak. The high binding energy peak in the MHA spectrum at 289.3 eV arises from the bond between an α-carbon and a carbonyl group C=O. Our data are in excellent agreement with published work by Bain et al. (1989). Control spectra acquired on bare Si(100) wafers were obtained relative to the absolute counts of MHA and HDT measured at the principal peak. The small peak observed at 284.7 eV on Si(100) may be attributed to hydrocarbon contaminants adsorbed from ambient air during sample preparation, or adsorption from thiol solution. However, there was no evidence of specific thiol adsorption on Si(100). The corresponding survey spectra acquired for binding energies between 0

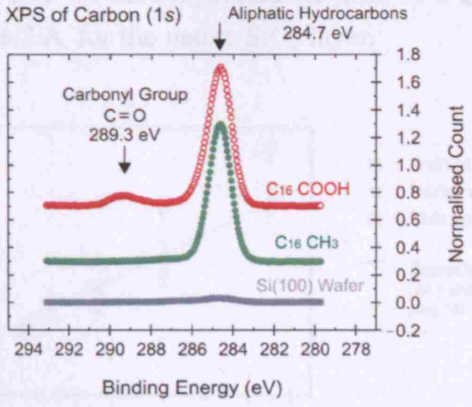

Fig. 5.13. High resolution XPS spectra of carbon 1s region acquired on MHA and HDT coated samples and bare Si(100) control sample that had been prepared in parallel to the cantilever arrays. The data were acquired by Marilyne Sousa from IBM Rüschlikon.

and 600 eV did not show Ti (2s) and (2p) signals, therefore there was no evidence of an out-diffusion of Ti at the gold surface.

Ellipsometric Thickness. Ellipsometric thicknesses of the SAMs as well as the lower layers, that is, from top Au, Ti, and SiO_2, were determined with a J.A. Woollam variable angle spectroscopic ellipsometer using wavelengths between 300 and 1000 nm, a step interval of 10 nm, and at angles 65°, 70°, and 75°. The following ellipsometric thickness was measured and shown in Fig. 5.14: 6 Å for mercaptopropionic acid $HS(CH_2)_2COOH$; 12 Å for mercaptooctanoic acid $HS(CH_2)_7COOH$; 14 Å for mercaptoundecanoic acid $HS(CH_2)_{10}COOH$; and 20 Å for mercaptohexadecanoic acid $HS(CH_2)_{15}COOH$ (herein termed MHA). For these measurements, an empirical measurement error of 2 Å was assumed. Ellipsometry reported in early studies by Bain et al. (1989) and Porter et al. (1987) on methyl terminated SAMs are also shown in the figure, as well as the expected thickness for each chain length based on fully extended alkane molecules tilted 30° from the surface normal giving rise to 1.5 Å thickness increase per methylene group (Bain et al. 1989). The ellipsometric thicknesses measured in this work were in an excellent agreement with the expected values. Conversely, the measurements reported by Bain et al. deviated at shorter chain lengths and the measurements reported by Porter et al. deviated at higher chain lengths from the expected values. However, it should be noted that carboxylic acid terminated SAMs are prone to non-specific adsorption of hydrocarbon contaminants from ambient air, thereby increasing the measured ellipsometric thickness (Ulman 1991). The following thicknesses for the layers below the SAMs were measured: 217 ± 5 Å for the evaporated Au film; 37 ± 2 Å for the evaporated Ti adhesion layer; 23 ± 2 Å for the native SiO_2 layer.

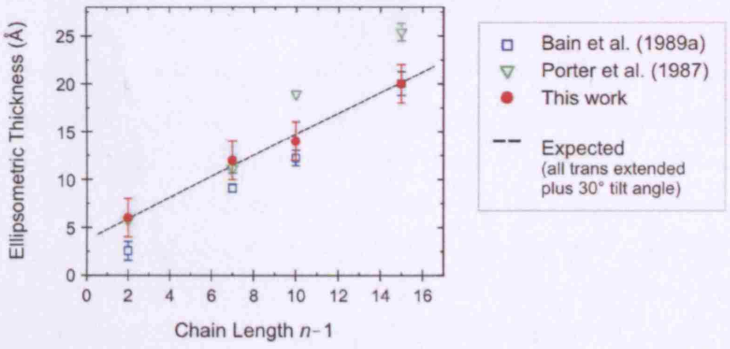

Fig. 5.14. Variable angle spectroscopic ellipsometry of carboxylic acid terminated SAMs of chain lengths 2, 7, 10, and 15. The data were acquired by Marilyne Sousa from IBM Rüschlikon.

Contact Angle Goniometry. Contact angles were probed in air with a Krüss DSA10 contact angle goniometer. Samples coated with the hydrophilic, carboxylic acid terminated MHA SAM was completely wetted by H_2O, that is showed contact angles smaller than about 10°. Conversely, samples coated with the hydrophobic, methyl terminated HDT SAM showed an advancing H_2O contact angle of $111 \pm 2°$ and an advancing hexadecane contact angle of $49 \pm 2°$. An initial volume of 15 μL and injection rate of 80 μL/min were used in these measurements. Fig. 5.15 shows a typical drop image acquired on a HDT coated sample.

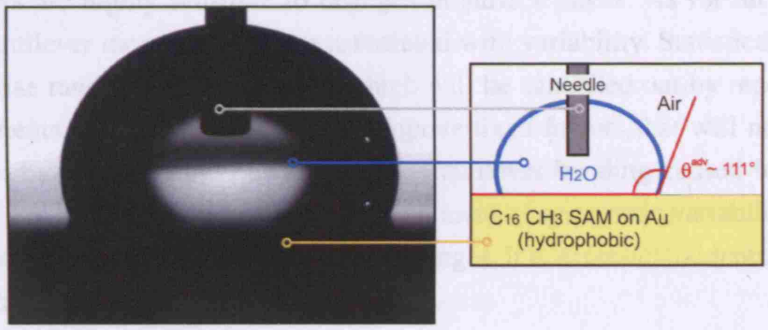

Fig. 5.15. Typical drop image of a water drop on hydrophobic HDT-coated sample under ambient air to measure the advancing contact angles.

6. Variability of Surface Stress Measurement

6.1 Introduction

Cantilevers are highly sensitive to changes in surface stress. As for all measurements, cantilever measurements are associated with variability. Statistical variability comprise random factors, each of which will be cancelled out by repeating the measurements. Systematic variability comprise fixed factors that will not be cancelled out by repeating the measurements. Cantilever bending caused by specific chemical and biological interaction is a component of systematic variability. Therefore, in order to probe small surface stress changes, it is *essential* to identify sources of random and systematic variability.

Perhaps the most effective and widely accepted approach is to ignore those components of measurement variability associated with an observation that are robust against everyday experimental factors. By design, cantilever arrays are robust against experimental factors that act on the time scale $\sim 10^0$ s of the rate of observation and affect all cantilevers on a single cantilever array to the same extent. However, problems arise when the same experimental factors act on a larger time scale. If these factors cause changes in measured cantilever bending signals that are larger than changes the bending signals caused by specific chemical and biological interactions, the bending signals will render non-specific, including the differential signals.

Repeated measurements have been constantly taken during the course of this work. In the initial measurements, it was found that strongly deformed cantilevers generated only 10% - 60% of bending signals compared with flat cantilevers. Bending signals acquired on the same flat cantilevers differed by 70% in two separate measurements performed in two consecutive days. Further, bending signals acquired in the same measurement on strongly deformed cantilevers decreased by 60% in a non-linear fashion over a time period of six hours.

This chapter investigates different sources of measurement variability associated with cantilever measurements. Criteria will be finally given according to which the cantilever array data presented in this work will be analysed.

6.2 Results

6.2.1 Software Development

The bending signals obtained from a cantilever array experiment are typically associated with multiple factors such as separate cantilever arrays, an individual cantilever within the array, number of repeated measurements, and, in case of the pH experiments as presented herein, deprotonation or protonation reactions. We have developed an evaluation algorithm and a software for a rapid analysis of large data sets with minimal user bias (Watari et al. 2007). The software was written in IDL.[1] The IDL code was excluded from this thesis owing to its length compared to its simple functionality.

Consider an experiment performed in a single cycle of pH 4.8/5.9/4.8 sodium phosphate solutions at constant ionic strength of $I = 0.1$. Further results related to the same experiment will be presented in Chapter 7. This experiment involved a total of 19 cantilevers distributed on four separate cantilever arrays and coated with either 1-hexadecanethiol ($HS(CH_2)_{15}CH_3$, herein termed HDT) or 16-mercaptohexadecanoic acid ($HS(CH_2)_{15}COOH$, herein termed MHA) self-assembled monolayer (SAM). Two measurements were made on each cantilever, first the deprotonation absolute stress on switching from pH 4.8 to pH 5.9 and then the protonation absolute stress on switching back to pH 4.8. It should be noted that the following criteria were applied to discard an individual cantilever from the evaluation: (a) broken or visibly damaged cantilevers and (b) cantilevers that failed the heating test performed to align the superluminescent diode (SLD) with the cantilever array. Both criteria were applied consistently throughout the data presented in this section, in Section 6.2.2, and in Chapter 7. The principle of the raw data evaluation algorithm is demonstrated in Fig. 6.1 using an absolute signal (hollow black squares) acquired by switching from pH 4.8/5.9/4.8 sodium phosphate solutions. A linear fit was applied to the raw time-deflection data points generated in each particular liquid environment. Subsequently, the fitted curves were extrapolated (green

[1] IDL 6.0, ITT Visual Information Solutions Co., Boulder, CO, U.S.A.

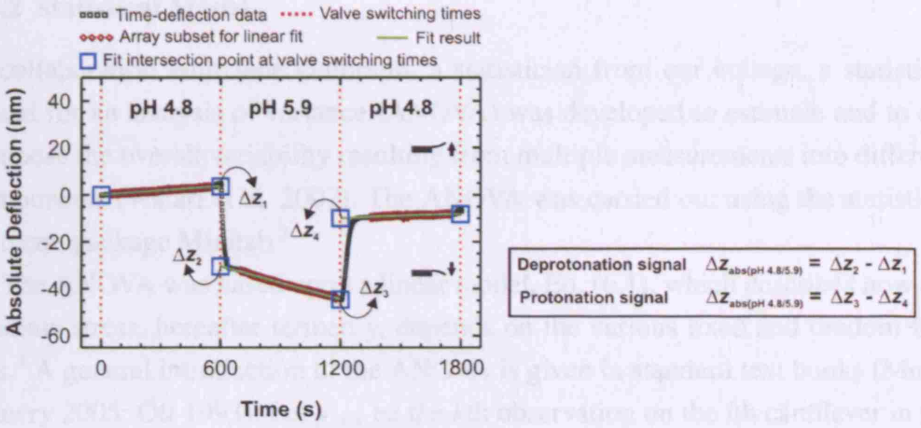

Fig. 6.1. Equilibrium stress signals are measured using the semi-automated software.

solid lines) to the onsets of liquid exchange (light blue hollow squares) to calculate the following two bending signals: (1) the deprotonation signal $z_{\text{abs (pH4.8/5.9)}}$ triggered by pH switch from 4.8 to 5.9 (2) and the protonation signal $z_{\text{abs (pH5.9/4.8)}}$ triggered by pH switch from 5.9 back to 4.8. In both cases the bending signal (the vertical difference between the blue squares in Fig. 6.1) was calculated by subtracting the intersection value of the fitted curve obtained at pH 5.9 from the intersection value of the fitted curve obtained at pH 4.8. The resulting bending signals obtained from the IDL software were converted to measures of absolute stress using Stoney's equation Eq. (4.18). With the effective length of cantilever L_{eff} = 450 μm used in these measurements, the resultant deflection-to-stress conversion factor was 0.24067 mN/m per 1 nm cantilever deflection. Finally, measured bending signals were structured according to the statistical model presented in the next section and tables generated for further analysis.

The linear fit was applied to all deflection signals presented in this thesis, which showed satisfactory agreement in the majority of measurements. Though a few deflection signals exhibited non-linear time-dependence and were not described well by the linear fit, such as the pH 4.8/3.5/4.8 sodium phosphate signals measured on the cantilever coated with C_8COOH SAM on chip G16, which will be presented in Chapter 10. Future experiments to investigate the kinetics of surface stress evolution will involve investigation of the use of non-linear functions to fit the raw data.

6.2.2 Statistical Model

In collaboration with Jane Galbraith, a statistician from our college, a statistical model for an analysis of variance (ANOVA) was developed to estimate and to decompose the overall variability resulting from multiple measurements into different components (Watari et al. 2007). The ANOVA was carried out using the statistical software package Minitab.[2]

The ANOVA was based upon a linear model, Eq. (6.1), which describes how the absolute stress, hereafter termed y, depends on the various fixed and random factors.[3] A general introduction to the ANOVA is given in standard text books (Montgomery 2005; Ott 1993). Let y_{stik} be the kth observation on the ith cantilever in the (st)th cell (Array s and SAM t), then:

$$y_{stik} = M + A_s + T_t + (AT)_{st} + u_{sti} + P_k + (AP)_{sk} + (TP)_{tk} + (ATP)_{stk} + e_{stik} \quad (6.1)$$

with $k = 1, 2$; $i = 1, .. n_{st}$; $t = 1, 2$; $s = 1, 2, 3, 4$; where appropriate constraints are put on the fixed parameters (to remove redundancy). The random errors, u_{sti} and e_{stik}, are assumed to be normally distributed with variances σ_u^2 and σ_e^2, respectively. The method of measuring the stresses using the IDL fit software presented in the previous section has two consequences: firstly, the contrast between deprotonation and protonation will be confounded with any order effect, since deprotonation is always measured first. Secondly, the within-cantilever measurement errors, e_{sti1} and e_{sti2}, could be correlated. The correlation between e_{sti1} and e_{sti2} is ρ, but otherwise all u's and e's are assumed to be independent. The within-cantilever random error, e_{stik}, models the unexplained or residual variation for a single cantilever, while the between-cantilever error, u_{sti}, accounts for the extra differences between cantilevers (in the same array and with the same SAM) over and above that which would arise from the within-cantilever variation. The parameters A_s, T_t, P_k represent the main effects of the three fixed factors, cantilever array, SAM, and deprotonation/protonation, respectively. The remaining parameters are the two and three term interactions of these three factors. The number, n_{st}, of cantilevers in each Array by SAM cell are given in Table 6.2.2. Ideally, and by our design, each cantilever array would contain the same number (four) of cantilevers coated with MHA as with HDT, however, as explained earlier some cantilevers could not be used.

Table 6.2 gives the absolute stresses for these 19 cantilevers, the means and the differences for the deprotonation and protonation pairs, and the Array by SAM

[2] Minitab 13.32, Minitab Inc., State College, PA, U.S.A.

[3] In this section stress was termed y to avoid confusion with variance σ.

	Array (s)				
SAM (t)	1	2	3	4	**Totals** ($\sum_s n_{st}$)
1 (HDT)	3	2	2	2	9
2 (MHA)	3	2	2	3	10
Totals ($\sum_t n_{st}$)	6	4	4	5	19

Table 6.1. Number n_{st} of cantilevers in each array by SAM cell.

cell means. On examination Array 3 appears atypical. For our purpose, which is to gain understanding of the processes, it is important to retain atypical results, although, before the technology is ready to be used diagnostically, some further inclusion/exclusion protocols may need to be developed.

The ANOVA partitions the Corrected Total Sum of Squares $\sum_{s,t,i,k} (y_{stik} - \bar{y}_{....})^2 = 335.26$ according to the individual Sources of Variability, where $\bar{y}_{....} = (1/38) \sum_{s,t,i,k} y_{stik} = -5.34$ mN/m. The resultant ANOVA table is shown in Table 6.3. Each of rows 2 to 10 in Table 6.3 corresponds to a factor, an interaction or a random term in the model Eq. (6.1). Please note that more significant figures have been used in the calculations than are shown in Tables 6.2 and 6.3.

The Sequential Sum of Squares given in column 3 of Table 6.3 corresponds to the decrease in the residual sum of squares when a new term is added to the model containing all those terms added prior to this new term (terms were added in the order shown in the table). Conversely, the Adjusted Sum of Squares given in column 4 corresponds to the decrease in the residual sum of squares when a new term enters a model which already contains all the other terms. Here we use the sequential sum of squares as we are primarily interested in the effects which arose from the difference in the SAM cantilever coating. However, the use of the adjusted sum of squares was found not to alter the qualitative results of the ANOVA. The Sequential Mean Squares given in column 5 of Table 6.3 were obtained by dividing a sequential sum of squares by its Degrees of Freedom, given in column 2 of Table 6.3. The F-value given in column 6 of Table 6.3 is the mean square ratio, that is, the mean square for a particular source of variability divided by the mean square for its associated random error term. The p-value in column 7 of Table 6.3 is the probability of obtaining such a large F-value if the true value of the relevant parameters were zero. A small p-value is interpreted as evidence that the relevant parameters are not zero.

Array (s)	SAM* (t)	Cantilever $i(st)$	Deprotonation (mN/m) y_{sti1}	Protonation (mN/m) y_{sti2}	Mean (mN/m) $1/2(y_{sti1}+y_{sti2})$	Difference (mN/m) $(y_{sti1}-y_{sti2})$
1	1	1	−8.50	−8.40	−8.45	−0.10
1	1	2	−9.51	−9.24	−9.37	−0.26
1	1	3	−8.52	−8.23	−8.38	−0.29
1	1	Mean	−8.84	−8.62	−8.73	−0.22
1	2	1	−7.70	−7.51	−7.61	−0.19
1	2	2	−7.89	−7.58	−7.74	−0.31
1	2	3	−7.63	−7.48	−7.56	−0.14
1	2	Mean	−7.74	−7.52	−7.64	−0.21
2	1	1	−7.73	−7.32	−7.52	−0.41
2	1	2	−6.93	−6.74	−6.84	−0.19
2	1	Mean	−7.33	−7.03	−7.18	−0.30
2	2	1	−6.76	−6.45	−6.61	−0.31
2	2	2	−6.93	−6.74	−6.84	−0.19
2	2	Mean	−6.52	−6.06	−6.29	−0.46
3	1	1	−1.42	−1.83	−1.62	0.41
3	1	2	−0.96	−1.44	−1.20	0.48
3	1	Mean	−1.19	−1.64	−1.41	0.45
3	2	1	1.54	1.37	1.46	0.17
3	2	2	0.00	−0.34	−0.17	0.34
3	2	Mean	0.77	0.52	0.64	0.35
4	1	1	−5.17	−5.22	−5.20	0.05
4	1	2	−5.44	−5.49	−5.46	0.05
4	1	Mean	−5.31	−5.35	−5.33	0.05
4	2	1	−5.13	−4.86	−4.99	−0.26
4	2	2	−4.21	−3.87	−4.04	−0.34
4	2	3	−4.19	−4.00	−4.09	−0.19
4	2	Mean	−4.51	−4.24	−4.38	−0.26

* SAM: t = 1 for HDT and t = 2 for MHA.

Grand Mean −5.34 mN/m

Table 6.2. Table of data, means, and differences.

The Within-Cantilever Error mean square in row 10 estimates the *effective* within-cantilever error variance, $\sigma_e^2(1-\rho)$, and Between-Cantilever Error mean square in row 5 estimates the total between-cantilever error variance, $\sigma_e^2(1+\rho)+2\sigma_u^2$. From the F- and p-values in row 5 there is clear evidence that the total between-cantilever error variance is greater than the effective within-cantilever error variance, however, we cannot determine how much this is due to σ_u^2 rather than to ρ. Fortunately, the interpretation of the rest of the ANOVA table is not affected. Deprotonation/Protonation and its interactions with Array and SAM in the lower half of

1	2	3	4	5	6	7
Sources of Variability	**DF** *	**Sequential Sum of Squares $(mN/m)^2$**	**Adjusted Sum of Squares $(mN/m)^2$**	**Sequential Mean Square $(mN/m)^2$**	***F*-value**	***p*-value**
Array	3	312.368	311.229	104.123	185.58	< 0.0005
SAM	1	14.003	14.623	14.003	24.96	< 0.0005
Array × SAM	3	1.841	1.841	0.614	1.09	0.392
Between-Cantilever Error	11	6.172	6.172	0.561	95.34	< 0.0005
Deprotonation/Protonation	1	0.118	0.072	0.118	20.06	0.001
Array × Deprotonation/Protonation	3	0.602	0.600	0.201	34.12	< 0.0005
SAM × Deprotonation/Protonation	1	0.056	0.063	0.056	9.49	0.010
Array × SAM × Deprotonation/Protonation	3	0.034	0.034	0.011	1.91	0.187
Within-Cantilever Error	11	0.065	0.065	0.006		
Corrected Total	37	335.259				

* DF: Degrees of freedom.

Table 6.3. ANOVA for the cantilever array data.

Table 6.3 involve only within-cantilever variation as the deprotonation and protonation reactions were observed on the same cantilever, so the appropriate random variation term is the mean square 0.006 in row 10. This allows quite small main effects and interactions to be detected (rows 6, 7, and 8). There is evidence that the magnitude of the absolute deprotonation stress tends to be slightly more negative (compressive) than the absolute protonation stress, and that the size of this difference varies between SAMs (greater for MHA than for HDT) and between cantilever arrays. Array, SAM, and Array by SAM in the upper half of Table 6.3, involve the total between-cantilever error variance, so the appropriate denominator mean square is 0.562 in row 5. From the F- and p-values in rows 2, 3, and 4, we conclude that there is clear evidence of differences between cantilever arrays and between SAMs but no evidence of an interaction. This is important as it suggests that the differential stress will not change from one cantilever array to another. To estimate the differential stress between MHA and HDT we used $(1/4)\ \sum_s\ (\bar{y}_{s2\cdot\cdot} - \bar{y}_{s1\cdot\cdot}) = 1.24$ mN/m. This has standard error $\sqrt{(7/64)\ (\sigma_e^2\,(1+\rho) + 2\sigma_u^2)}$, where $\bar{y}_{st\cdot\cdot} = (1/2\,n_{st})\ \sum_{i,k}\ y_{stik}$ is the (st)th cell mean. Using the mean square in row 5 to estimate $\left(\sigma_e^2\,(1+\rho) + 2\sigma_u^2\right)$ gives an estimated standard error of 0.24 mN/m. Finally, it is useful to estimate the change in differential stress between protonation and deprotonation. We averaged the estimates for each array, giving $(1/4)\ \sum_s\ ((\bar{y}_{s2\cdot2} - \bar{y}_{s1\cdot2}) - (\bar{y}_{s2\cdot1} - \bar{y}_{s1\cdot1})) = 0.18$ mN/m with standard error $\sqrt{(7/16)\,\sigma_e^2\,(1-\rho)}$. When the residual error mean square (row 10) is substituted for $\sigma_e^2\,(1-\rho)$, this gives an estimated standard error of 0.05 mN/m. Thus the study has shown that from the 38 observations for pH 5.9 and using sodium phosphate solutions we were able to estimate the differential stress with a relative standard error of about 20%. Under these conditions the differential stress was tensile. The measurement of differential stress made during protonation was slightly more positive (tensile) than during deprotonation, the difference being measured in our experiment with a relative standard error of about 30%.

Future work will further investigate the nature and chemical implications of different sources of variation, including the within- and between-cantilever effects of successive cycles and measurement order (Galbraith et al. 2007).

6.2.3 Instrument Alignment

One important assumption underlying an ANOVA is the homogeneity of errors. The errors resulting from *individual* measurements appeared to satisfy this assumption, however, the errors resulting from *multiple* measurements were highly inhomogeneous. The high inhomogeneity observed in particular in the initial mea-

surements prevented the use of the statistical model for the analysis of multiple measurements. Interestingly in these measurements, the homogeneity of errors appeared also to be reflected in the variability of 'heating signals'. Since 'heating signals' are generated by the bimetallic effect as described in Section 5.2.3, cantilevers prepared under equivalent conditions, that is, fabricated from the same silicon wafer, deposited in parallel with gold and its adhesion layer, plus SAM, were expected to generate highly reproducible 'heating signals'. In individual measurements, the SLD/cantilever alignment resulted in a relative standard deviation below 2.5%. However, the corresponding error of mean 'heating signals' resulting from multiple measurements was found to be up to an order of magnitude higher, even if the measurements were taken on the same cantilever array. The high variability in multiple measurements was observed on cantilevers with different initial curvatures. Cantilevers that exhibited large initial curvature generated small signals compared to cantilevers without large initial curvature. On the same cantilevers without large initial curvature, the magnitude of 'heating signals' acquired in multiple measurements depended on its relative position to the position sensitive detector (PSD). The magnitude of the chemically specific signals acquired in the subsequent core surface stress measurement appeared to scale with the magnitude of 'heating signals' to a remarkable extent, provided that the cantilevers had not suffered from obvious mechanical damages or contamination. These suggested an important role of the alignment between the cantilever and the PSD. This section describes the effect of cantilever/PSD alignment, which was identified as the largest source of measurement error associated with the data presented in this work.

A schematic of the Scentris instrument is given in Fig. 6.2A and includes the following components: (1) the tube comprising a kinematic stage to effect a change in the (x, y)-position of the SLD spots on the cantilever surface and a two-lens condensor; (2) the first, fixed concave mirror that reflects the SLD beams toward the cantilevers (3); the x-position of the SLD spot and the cantilever free end in the figure is located 650 μm to the left of the hinge of the ceramic stage (4), when the right side of the flow cell is aligned with the left side of the stainless steel pillar (5). This x-position was defined as the default x-position of cantilevers. The SLD beams are thereafter reflected at the second, rotatable flat mirror (6) toward the PSD. There is a window (7) placed in front of the rotatable mirror and the PSD is not directly visible. The dimensions and relative positions of these components were estimated

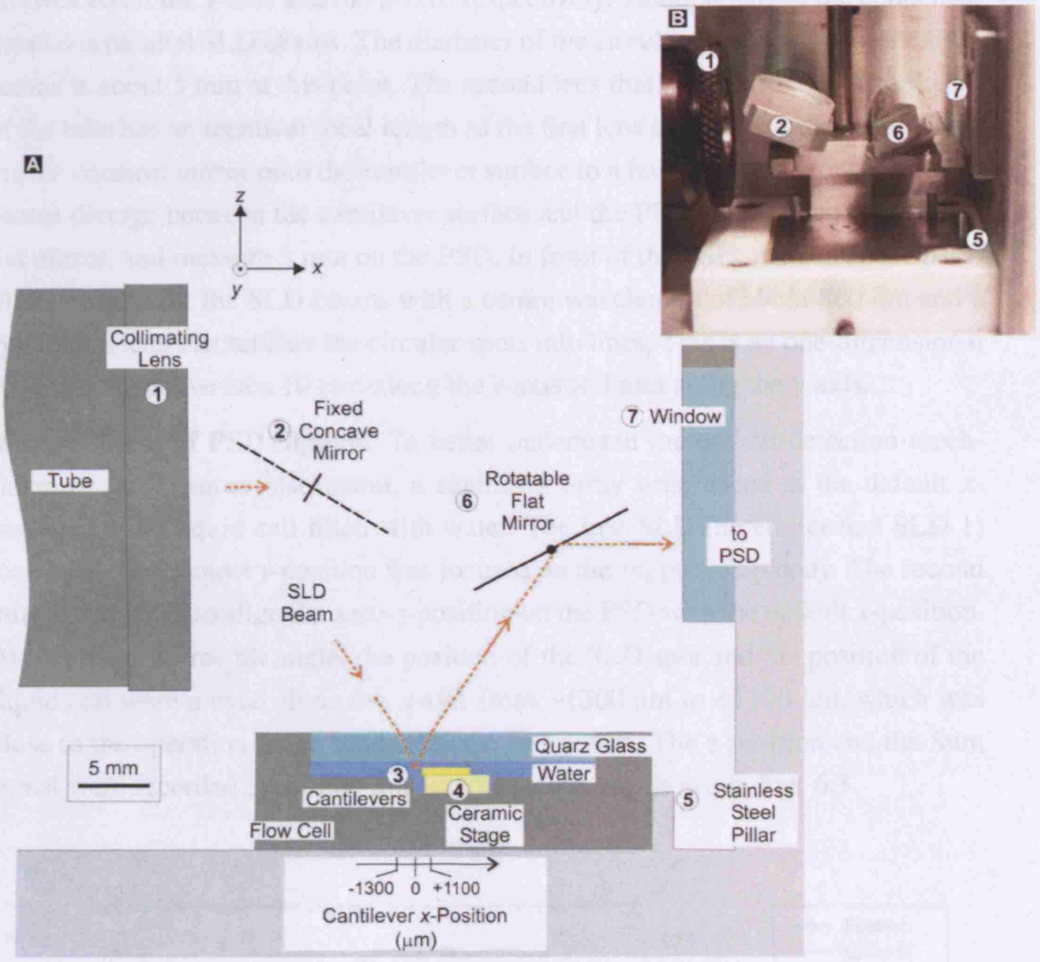

Fig. 6.2. A drawing of the Scentris instrument **(A)** to reconstruct the optical path reproduced from the picture shown in **(B)**.

from Fig. 6.2B, a picture taken by a digital camera.[4] The (x, z)-position of the cantilever array in the liquid cell was reproduced from technical drawings.[5]

Although details of the optical path from the tube to the first fixed mirror to the cantilevers, as well as the optical path between the rotatable mirror and the PSD are unavailable, some important information have been provided by the Veeco company. Eight optical fibres are assembled using v-grooves. There is an aperture in front of the v-grooves to reduce the spot size. Changes in the x-y-position of an SLD spot at the cantilever surface appeared to be effected by a rotation of the v-

[4] The picture was provided by Dr. Christian K. Riener, formerly postdoctoral fellow at LCN and UCL.
[5] Scentris Veeco Instruments Inc., Santa Barbara, CA, U.S.A.

grooves about the y-axis and the z-axis, respectively. The first lens of the condensor generates parallel SLD beams. The diameter of the circular cross section of the SLD beams is about 5 mm at this point. The second lens that is visible at the right hinge of the tube has an identical focal length as the first lens and focuses the SLD beams via the concave mirror onto the cantilever surface to a few tens of microns. The SLD beams diverge between the cantilever surface and the PSD via the second rotatable flat mirror, and measure 5 mm on the PSD. In front of the PSD, there is an IR-pass-filter adjusted for the SLD beams with a centre wavelength of about 860 nm and a cylindrical lens that renders the circular spots into lines. This is an one-dimensional PSD with an active area 10 mm along the z-axis × 2 mm along the y-axis.

Measurement of PSD Signals. To better understand the optical detection mechanism of the Scentris instrument, a cantilever array was placed at the default x-position in the liquid cell filled with water. The first SLD (herein termed SLD 1) located at the topmost y-position was focused on the support chip body. The second mirror was tilted to align the zero-z-position on the PSD with the default x-position. At this fixed mirror tilt angle, the position of the SLD spot and the position of the liquid cell were moved along the x-axis from −1300 μm to +1100 μm, which was close to the operation range limited by the instrument. The z-position and the Sum signal were recorded every 200 μm and the results are shown in Fig. 6.3.

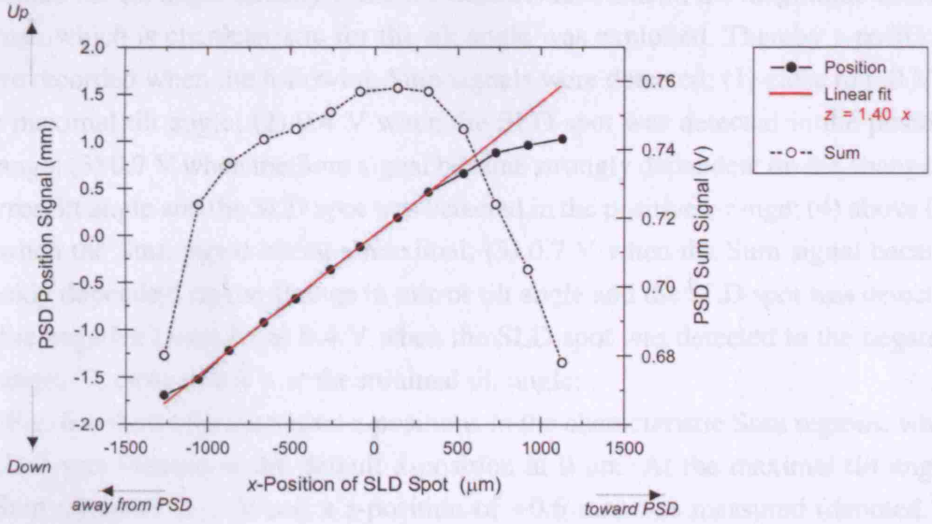

Fig. 6.3. PSD position and Sum signals measured at a fixed mirror tilt angle and as a function of the x-position of cantilever free end. The linear fit resulted from the measured PSD positions in the x-range between −900 μm and +300 μm.

It was found that the sign of the PSD z-position signals was positive for the positions located higher than the zero-z-position and negative for the positions located lower than the zero-z-position. The sign of the raw cantilever bending signals calculated by the Scentris instrument was inverted according to the protocol used by the same research group[6] and specific to the Scentris instrument.

A linear relation between the x-position and the z-position was observed in the central x-range between -900 μm and $+300$ μm at this fixed mirror tilt angle. The fit resulted in a slope of 1.40 and the corresponding z-range on the PSD extended from -1.26 mm to $+0.42$ mm. The apparent cantilever deflection signal calculated by the Scentris software was ~3120 nm per 1 mm change in the z-position.

The Sum signal increased weakly from 0.74 mV at -900 μm to 0.76 mV at -100 μm and remained constant up to $+300$ μm. In the upper x-range $> +300$ μm and the lower x-range < -900 μm, the measured z-positions were found to deviate from expected values based on the extrapolation of the linear fit. The discrepancy increased with the distance from the central linear region. The measured z-position reached 64% of the expected signal at $+1100$ μm and 95% at -1300 μm. The associated Sum signals were also found to strongly decrease with distance, which measured 0.68 V at the outmost x-positions.

To probe the full z-range of the PSD, the tilt angle of the second mirror was varied from the maximal angle to the minimal angle. Since it is not possible to measure the tilt angle directly using the Scentris instrument, the magnitude of Sum signal, which is characteristic for the tilt angle was exploited. Thereby z-positions were recorded when the following Sum signals were detected: (1) close to 0.0 V at the maximal tilt angle; (2) 0.4 V when the SLD spot was detected in the positive z-range; (3) 0.7 V when the Sum signal became strongly dependent on the change in mirror tilt angle and the SLD spot was detected in the positive z-range; (4) above 0.7 V when the Sum signal became maximal; (5) 0.7 V when the Sum signal became weakly dependent on the change in mirror tilt angle and the SLD spot was detected in the negative z-range; (6) 0.4 V when the SLD spot was detected in the negative z-range; (7) close to 0.0 V at the minimal tilt angle;

Fig. 6.4 shows the measured z-positions in the characteristic Sum regions, when SLD 1 was focused at the default x-position at 0 μm. At the maximal tilt angle, a Sum signal of 0.11 V and a z-position of $+0.6$ mm was measured (denoted by Maximal tilt). With decreasing tilt angle, the Sum signal reached 0.40 V at $+4.0$ mm (denoted by '+'0.4 V). When the tilt angle was further decreased, the Sum signal

[6] Personal communication from my supervisor Dr. McKendry

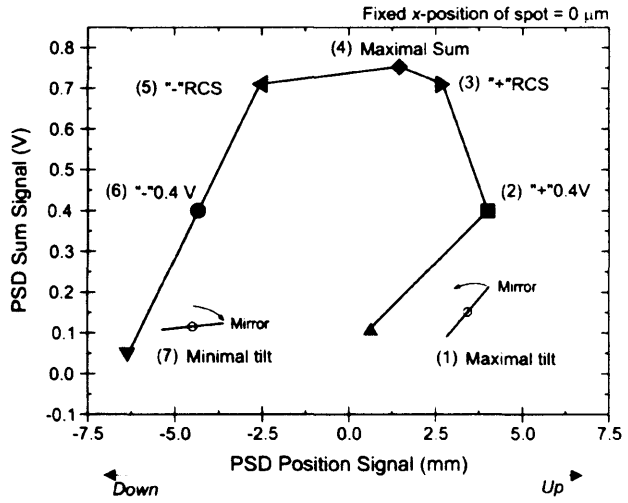

Fig. 6.4. Characteristic Sum regions were observed along the linear PSD as the mirror was tilted from the maximal tilt to the minimal tilt.

reached 0.71 V at +2.7 mm and became only weakly dependent on the change in the tilt angle when the spot entered the region of constant Sum (denoted by '+'RCS). The maximal Sum signal of 0.75 V was measured at +1.5 mm (denoted by Maximal sum). Then at −2.5 mm, the Sum signal decreased to 0.71 V when the SLD spot came off the region of constant Sum (denoted by '−'RCS). Thereafter the Sum signal decreased strongly with decreasing tilt angle and reached 0.40 V at −4.3 mm (denoted by '−'0.4 V). Finally at the minimal tilt angle, the Sum signal was reduced to 0.05 V and a z-position of −6.4 mm was measured (denoted by Minimal tilt).

Fig. 6.5 shows the effect of the x-position of the SLD spot on the location of the characteristic Sum regions along the z-axis of the PSD and the magnitude of the associated Sum signals, which was measured by focusing SLD 1 at multiple x-positions between −1300 μm and +1100 μm. In the central x-regime between −500 μm and +100 μm, the characteristic Sum regions did not change strongly with the x-position. In particular, the region of constant Sum extended from −2.5 mm to +2.5 mm, in which the maximal Sum signal measured 0.76 V. However, the z-length of the region of constant Sum as well as the associated Sum signals were found to become smaller, almost but not strictly symmetrically with increasing distance away from this central x-regime. At −1300 μm, the z-length of the region of constant Sum was 1.2 mm and the maximal Sum was 0.68 V. At +1100 μm, the z-length was 2.4 mm and the maximal Sum was 0.73 V. While the location of '−'0.4 V and '−'RCS in the negative z-range remained constant along the x-axis, the shrinkage of the

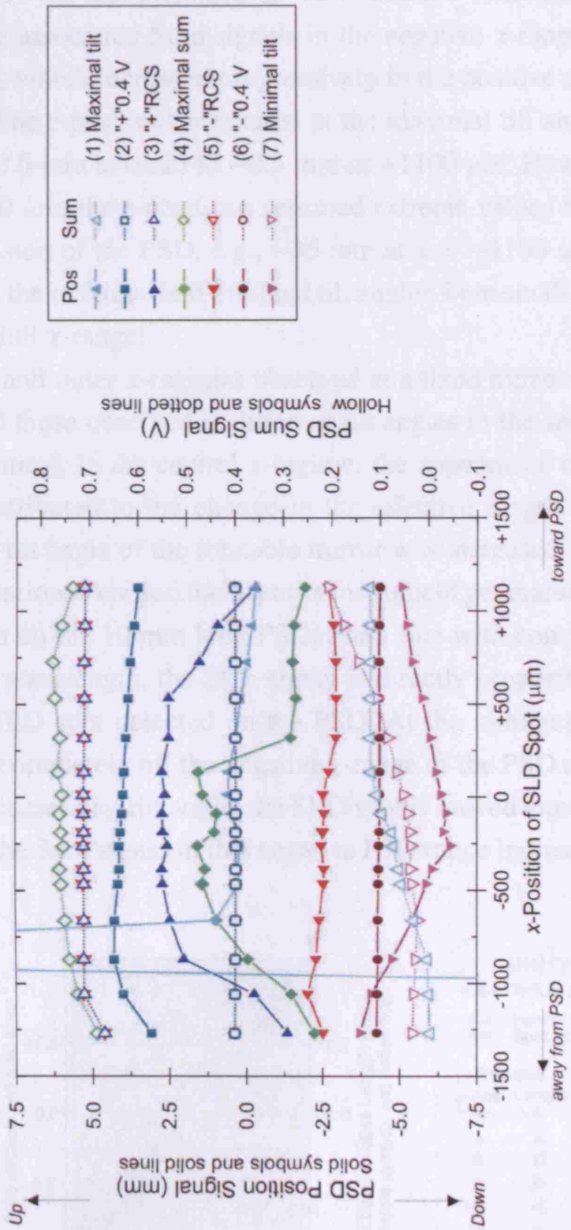

Fig. 6.5. Measurement of characteristic Sum regions over the full *x*-range. Symbols are identical to those used in the previous figure.

region of constant Sum was primarily caused by the downward shift of the Sum regions located in the positive z-range, that is, Maximal sum, '+' RCS, and '+' 0.4 V. The z-position measured at the minimal tilt angle reached a minimum of −6.6 mm at $x = -300$ μm and increased to −3.7 mm at −1300 μm and to −5.1 mm at +1100 μm. The associated Sum signals in the negative x-range remained constant at about 0.03 V, which increased progressively in the positive x-range up to 0.21 V at +1100 μm. The z-positions measured at the maximal tilt angle at $x > -500$ μm ranged from +0.6 mm at 0 μm to −0.3 mm at +1100 μm. However in the negative x-range < -500 μm, the z-positions resumed extreme values much larger than the physical dimension of the PSD, e.g., −35 mm at $x = -1100$ μm. The Sum signals associated with the maximal and minimal tilt angles were small and remained below 0.2 V over the full x-range.

The central and outer x-regimes observed at a fixed mirror tilt angle in the first experiment and those observed at different tilt angles in the second experiment are essentially identical. In the central x-regime, the appearance of the region of constant Sum is attributed to the change in the effective length of the SLD spot on the PSD as the tilt angle of the rotatable mirror was increased. This is illustrated in Fig. 6.6. As mentioned earlier, the Scentris instrument generates line-like SLD spots of 5 mm length on the 10 mm long PSD. For a line with constant intensity profile and a constant wavelength, the Sum signal is directly proportional to the effective length of the SLD spot detected on the PSD. At the minimal tilt angle, the SLD spot is located completely off the negative z-range of the PSD and no Sum signal is detected. With increasing tilt angle, the SLD spot is moved along the z-axis onto the PSD surface. The Sum signal in this negative PSD range increases strongly with tilt

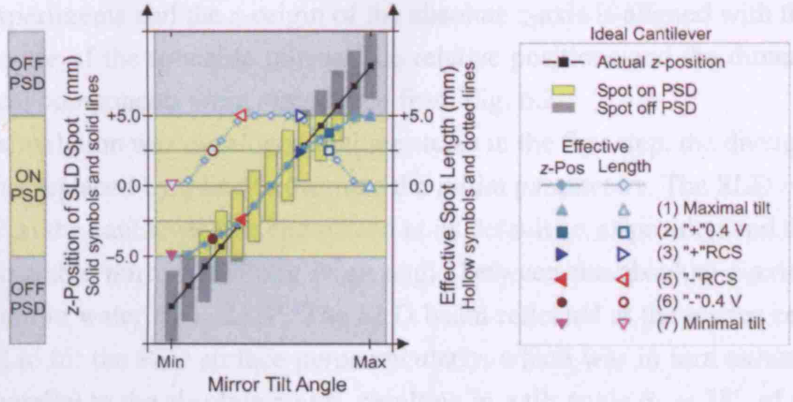

Fig. 6.6. Scheme to rationalise the characteristic Sum regions measured on a flat substrate.

angle until the 5 mm long SLD spot is fully detected by the PSD at the z-position of about −2.5 mm. This is the onset of the region of constant Sum that extends to about +2.5 mm, above which the SLD spot comes off the PSD surface and the Sum signal starts again to decrease. At the maximal tilt angle, the SLD spot is located completely off the positive z-range and the Sum signal is reduced back to zero. This effect limits the maximal z-range of the region of constant Sum to 5 mm and will be termed 'off-PSD' effect hereafter.

The cause of the reduced region of constant Sum observed in the outer x-regime is less obvious. Since the reduction occurred only at higher tilt angles of the rotatable mirror, this effect may be attributed to the clipping of an SLD spot on the mirror and will be termed 'off-mirror' effect hereafter.

It is clear from Fig. 6.6 that the actual z-position of the SLD spot and its effective position are not identical if it is detected outside of the region of constant Sum. The intended working range of the Scentris instrument is the PSD region free of the off-PSD and off-mirror effect. Note that the scheme does not fully agree with the measured tilt angle dependence of the PSD signals in the central x-regime shown in Fig. 6.5, including the presence of maximal Sum as well as the PSD signals generated below '−'0.4 V and above '+'0.4 V.

Simulation of PSD Signals. To investigate the optical detection mechanism of the Scentris instrument further, a simulation of PSD signals was developed and written in Maple 6 (Waterloo Maple Inc., Waterloo, Canada). The Maple code was omitted from this thesis due to its length.

The simulation parameters are summarised in Fig. 6.7. Note that all values given in this section were rounded to an empirical significance. In the figure, the x-origin of the absolute x-axis is aligned with the zero-x-position of cantilever free end used in the experiments and the z-origin of the absolute z-axis is aligned with the height of the centre of the rotatable mirror. The relative positions and the dimensions of the optical components were reproduced from Fig. 6.2.

The simulation was developed in three steps: in the first step, the diverging SLD beam was replaced by a line to estimate the initial parameters. The SLD beam was reflected at the cantilever free end placed at its default (x, z)-position and the centre of the rotatable mirror, resulting in an angle between the absolute z-axis and the SLD beam in water $\theta_w = 25.3°$. The SLD beam reflected at the mirror centre was assumed to hit the PSD surface perpendicularly, which was in turn assumed to be placed parallel to the absolute z-axis, resulting in a tilt angle $\beta_0 = 28°$ of the rotatable mirror. The distance between the centre of the mirror and the x-position of the

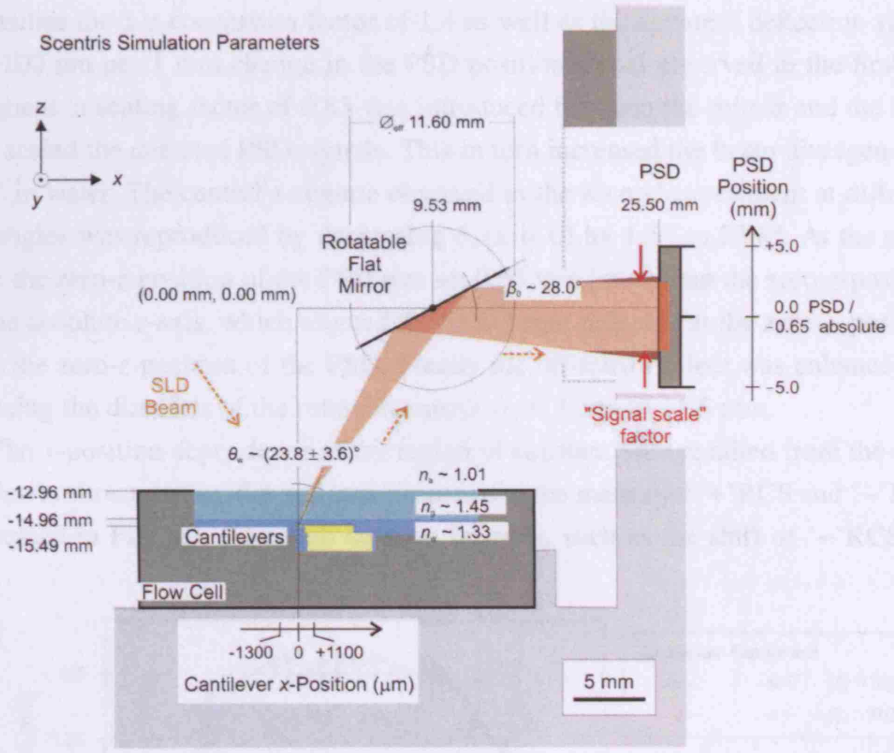

Fig. 6.7. Scheme to summarise the final simulation parameters. The simulation included the optical path from the cantilever free end via the rotatable mirror to the PSD.

PSD was estimated to be 16.0 mm, which resulted from the nm-to-mm conversion formula Eq. (5.2) specific to the Scentris instrument by assuming a distance 18.7 mm between the cantilever free end and the centre of of the mirror.

In the second step, the SLD beam was rendered 2-dimensional by including the beam divergence. The SLD spot has a length of 5 mm on the PSD, which limits the divergence angle to 6° in water. This gives a typical spot length of 6 mm along the mirror, about 50% of the diameter of the rotatable mirror. Since the translation of the SLD spot along the x-axis appears to be effected by a rotation of the v-grooves about the y-axis in the tube, θ_w can be expected to be dependent on the x-position of the SLD spot. A linear dependence was assumed based upon the linear x-z-relation observed at a fixed tilt angle in the first experiment. The linear function $\theta_w(x) = 25.3 - 1050x$ was obtained by taking into account the spot length along the mirror.

In the final step, parameters were readjusted to reproduce the experimental data. To realise the x-z-conversion factor of 1.4 as well as the apparent deflection signal of 3100 nm per 1 mm change in the PSD position signal observed in the first experiment, a scaling factor of 0.83 was introduced between the mirror and the PSD that scaled the detected PSD signals. This in turn increased the beam divergence to 7.2° in water. The central x-regime observed in the second experiment at different tilt angles was reproduced by decreasing $\theta_w(x = 0)$ by 1.5° to 23.8°. At the same time the zero-z-position of the PSD was set 0.65 mm lower than the zero-z-position of the absolute z-axis, which aligned the SLD beam reflected at the zero-x-position with the zero-z-position of the PSD. Finally the off-mirror effect was enhanced by reducing the diameter of the rotatable mirror by 0.7 mm to 11.6 mm.

The x-position dependence of the region of constant Sum resulted from the simulation is shown in Fig. 6.8 and superimposed to the measured '+'RCS and '−'RCS presented in Fig. 6.5. Although detailed features, such as the shift of '−'RCS to-

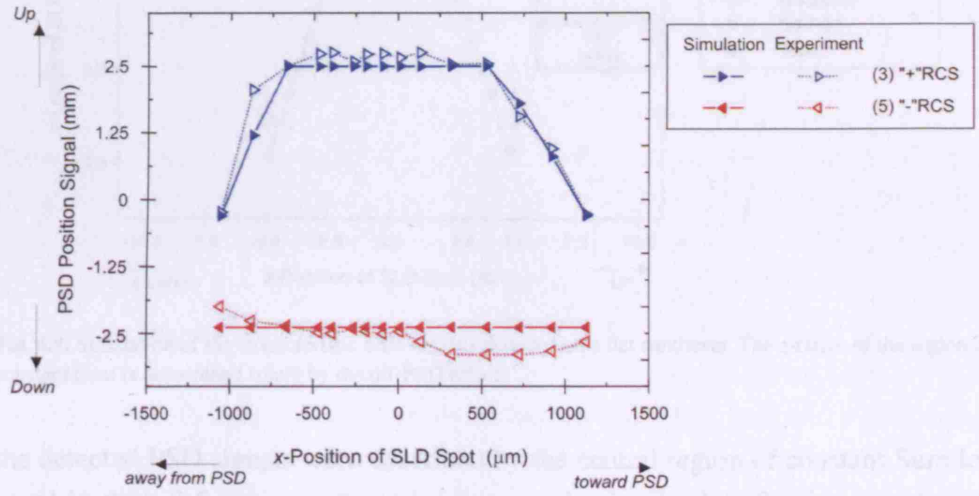

Fig. 6.8. Simulated and measured z-positions of the region of constant Sum as a function of the x-position of the cantilever free end. The off-PSD and off-mirror effect were successfully reproduced by the simulation.

ward lower PSD positions at positive x-positions or increased z-length of RCS at $x = -900$ μm in the experimental data remained unexplained, the off-mirror effect as well as the off-PSD effect were reproduced by the simulation well.

The findings so far were concerned with flat substrates. When an SLD beam is reflected at the surface of a cantilever with non-zero initial curvature, it will point away from the centre of the rotatable mirror thus from the centre of the PSD. There-

fore detected PSD signals may be influenced by the off-mirror and the off-PSD effect even if the cantilever was placed at the default x-position, depending on the magnitude of the initial curvature.

Effect of Initial Cantilever Curvature. To investigate the effect of initial cantilever curvature on detected PSD signals, control PSD signals generated by an 'ideal' cantilever without initial curvature was first simulated. The cantilever was placed at the default x-position and the tilt angle of the rotatable mirror was increased from 15° lower than the default tilt angle of 28° to 15° higher tilt angle at a step of 1.5°. The results are shown in Fig. 6.9. As shown qualitatively in Fig. 6.6,

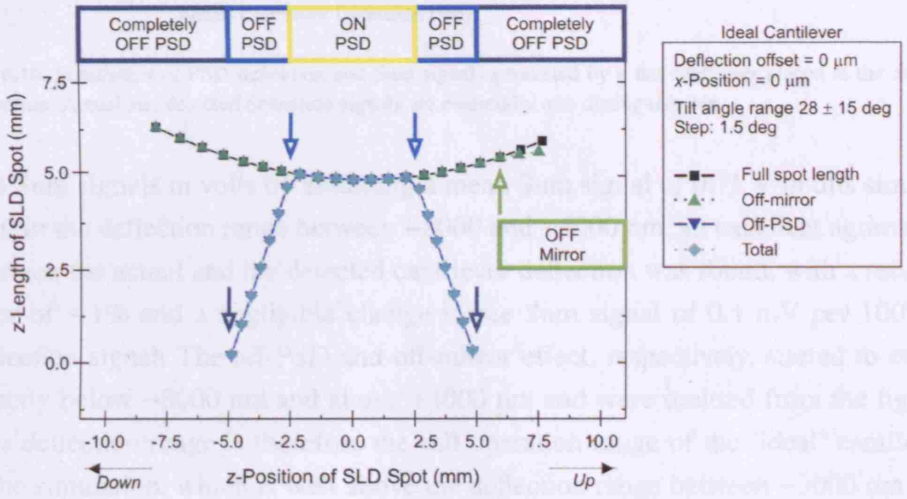

Fig. 6.9. Simulation of the characteristic Sum regions detected on a flat cantilever. The z-range of the region of constant Sum is determined solely by the off-PSD effect.

the detected PSD signals were described by the central region of constant Sum located in the ±2.5 mm z-range and a linear reduction in the effective spot length above and below the region of constant Sum, as the SLD spot was moved across the PSD surface. The parabolic change in the full spot length with the mirror tilt angle was associated with the linear cross-section of the SLD beam with constant intensity profile assumed in the simulation. The onset of the off-mirror effect started only above the detection range of the PSD at ~40°, therefore the off-mirror effect did not influence the detected PSD signals under these conditions.

Deflection and Sum PSD signals generated by the 'ideal' cantilever placed at the default x-position and at the fixed default tilt angle are shown in Fig. 6.10. Actual cantilever deflection was the input parameter. Detected spot lengths were converted

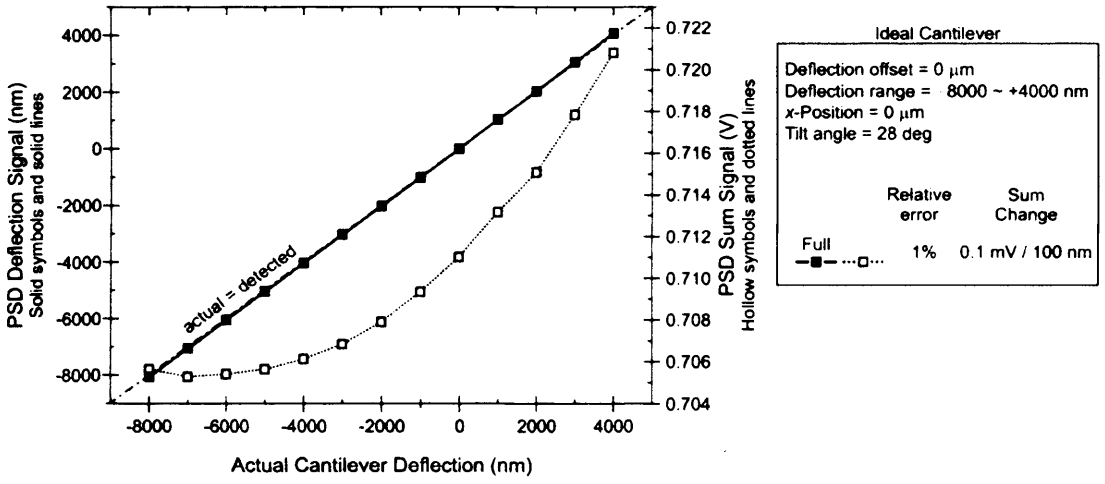

Fig. 6.10. Simulation of PSD deflection and Sum signals generated by a flat cantilever placed at the default x-position. Actual and detected deflection signals are essentially non-distinguishable.

into Sum signals in volts by assuming a mean Sum signal of 0.71 V in this simulation. In the deflection range between −8000 and +4000 nm, an excellent agreement between the actual and the detected cantilever deflection was found, with a relative error of ~ 1% and a negligible change in the Sum signal of 0.1 mV per 100 nm deflection signal. The off-PSD and off-mirror effect, respectively, started to effect directly below −8000 nm and above +4000 nm and were omitted from the figure. This deflection range is therefore the full operation range of the 'ideal' cantilever in the simulation, which is well above the deflection range between −3000 nm and +1000 nm required in a typical cantilever measurement presented herein.

Simulations were repeated using identical parameters but the deflection offset of −15 μm to simulate an excessively deformed cantilever due to a compressive surface stress acting upon the gold-coated top surface of the cantilever. In the first simulation shown in Fig. 6.11 to probe the PSD signals as a function of the mirror tilt angle, the SLD spot reflected at the curved cantilever was located more than 10 mm below the detection range of the PSD at the minimal tilt angle of 13°. With increasing tilt angle, the SLD spot was moved upward along the z-axis, however, the SLD spot on the mirror started to clip at the left hinge of the mirror already below the detection range of the PSD. When the spot was moved onto the PSD surface, between −5.0 and ~−2.5 mm PSD position, the detected signals were dominated by the off-PSD effect since its dependence on the mirror tilt angle is much stronger than the off-mirror effect. Then between ~−2.5 and ~+2.5 mm PSD position free

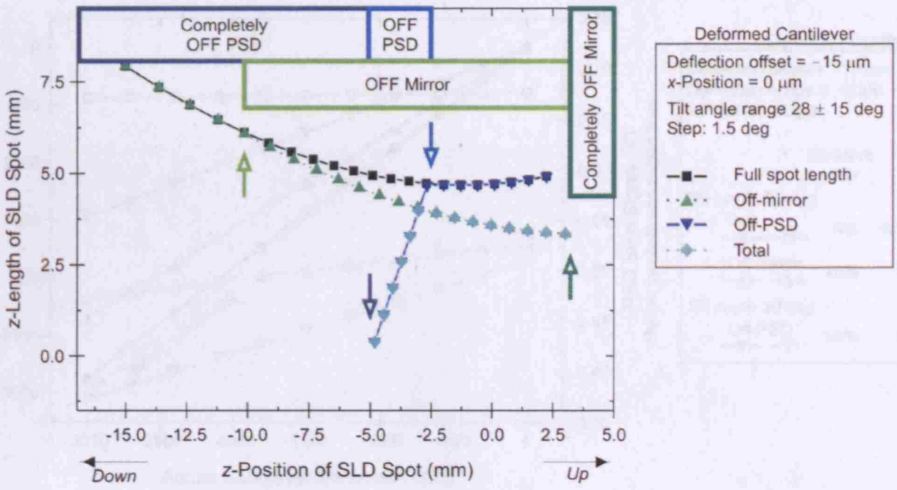

Fig. 6.11. Simulation of the characteristic Sum regions detected on an excessively curved cantilever. The region of constant Sum was completely displaced by the off-mirror effect.

of the off-PSD effect, the detected PSD signals were characterised by the off-mirror effect. The detected spot length decreased weakly with increasing tilt angle until the SLD spot was moved completely off the surface of the mirror at ~+2.5 mm PSD position. The full spot length could not be detected on the PSD over the entire tilt angle range. Consequently, the signals generated by the deformed cantilever were inherently associated with errors.

The deflection signals generated by the deformed cantilever were simulated in the negative deflection range between 0 and −3000 nm and at two different mirror tilt angles: firstly at 36° to simulate the full deflection signals free of both the off-mirror and off-PSD effect as well as the deflection signals affected by the off-mirror effect only. Secondly at 30° to simulate the deflection signals affected mainly by the off-PSD effect. The results are shown in Fig. 6.12. The full deflection signals generated by the deformed cantilever deviated slightly more from the actual cantilever deflection than those generated by the 'ideal' cantilever, with a relative error of 4% and a change in the Sum signal of about 0.2 mV per 100 nm cantilever deflection. The deflection signals modulated by the off-mirror effect were smaller than the actual cantilever deflection, associated with a relative error of 20% and a Sum signal change of 2 mV per 100 nm cantilever deflection. The deflection signals modulated by the off-PSD effect were the smallest and associated with the largest relative error of 50% and a Sum signal change of 5 mV per 100 nm cantilever deflection.

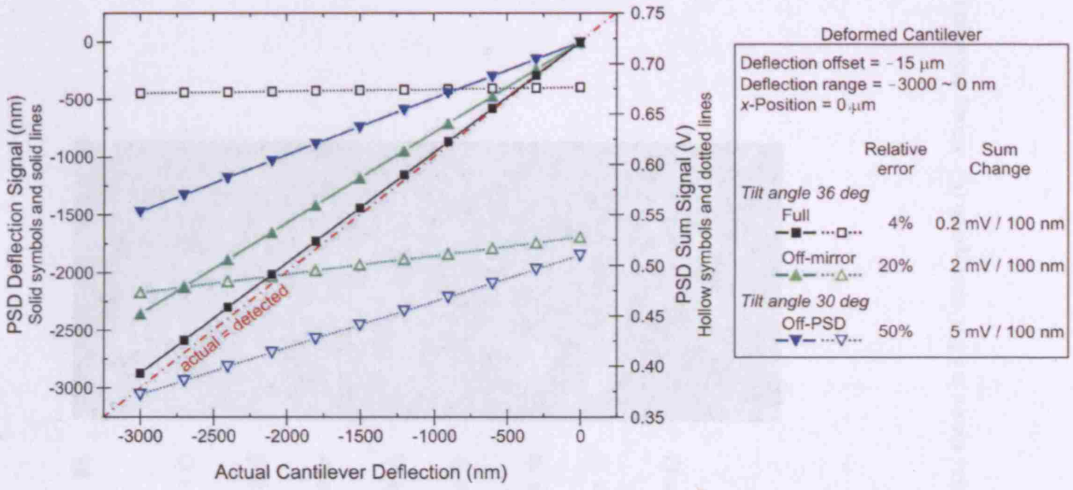

Fig. 6.12. Simulation of PSD deflection and Sum signals generated by an excessively curved cantilever placed at the default x-position. The presence of initial curvature alone can cause up to 50% discrepancy between the actual and detected deflection signals.

The results obtained from the simulation were indeed observed in experiments and appeared to give the correct order of magnitude of the off-mirror and the off-PSD effect. Discrepancies are expected to arise from the linear cross-section and the constant intensity profile of the SLD spot assumed throughout the simulation.

As described in Section 5.2.3, 'heating tests' were performed to align the eight cantilevers with the eight SLDs. Example 'heating signals' are shown in Fig. 6.13, which were generated due to the bimetallic effect upon increasing and subsequently decreasing the temperature of the flow cell by 1 °C. The absolute cantilever deflection signals and the PSD position signals are shown in (A); the associated changes in the Sum signals and their absolute values are shown in (B); a differential interference contrast (DIC) micrograph of the cantilever array is shown in (C). In the micrograph, the magnitude of the initial cantilever deformation is indicated by the colour gradient along the long axis of a cantilever relative to the colour of the flat hinge region. It can be seen that Cantilever 6 and Cantilever 7 were strongly deformed. The six other cantilevers were considered flat.

The deflection signals generated by the six flat cantilevers after ten minutes resulted in a mean and standard deviation of -401 ± 4 nm. This is an example of well aligned cantilevers that passed the criterium of 2.5% relative standard deviation. The corresponding PSD position signals were within the z-range of -1 and $+0.5$ mm, which is a typical variability in the PSD positions measured on cantilevers presented

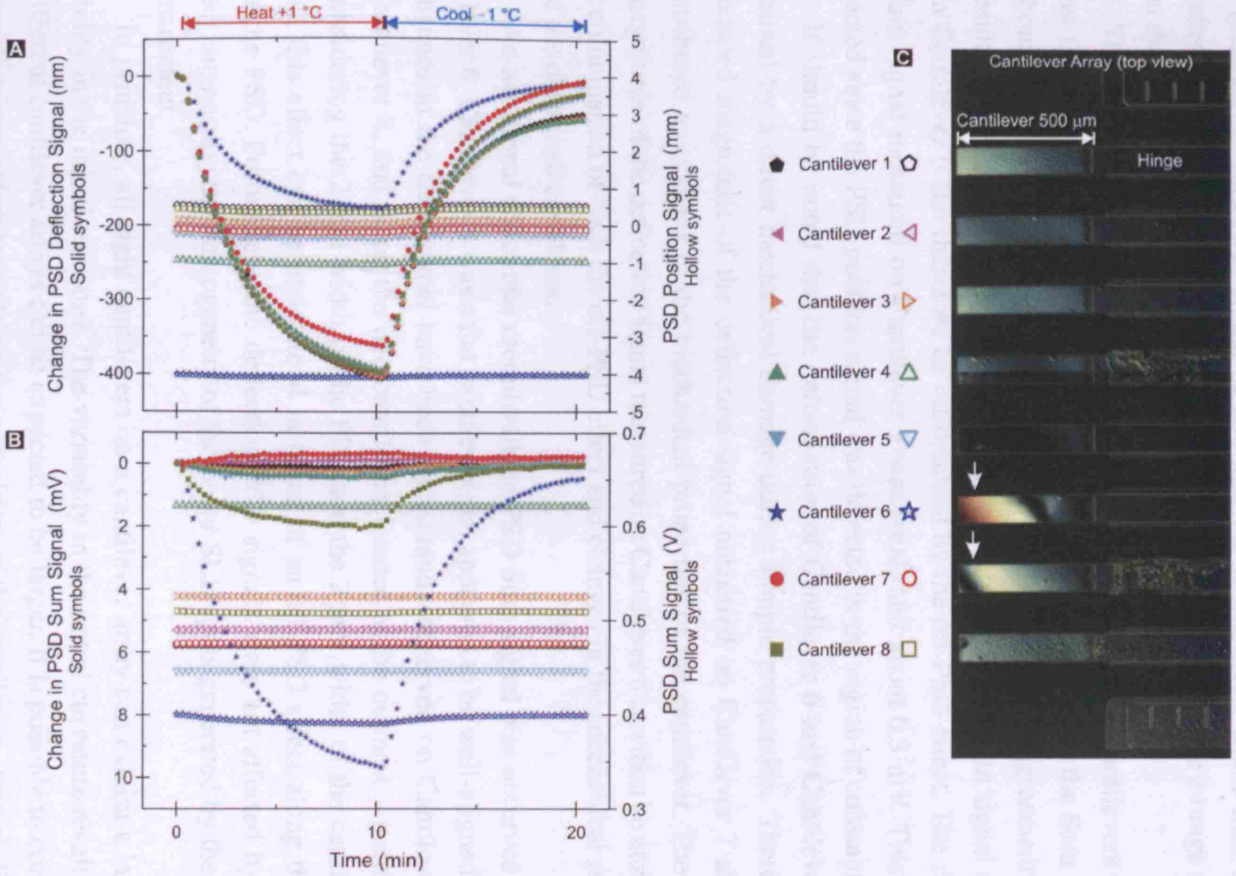

Fig. 6.13. PSD deflection/position signals **(A)** and PSD Sum signals **(B)** acquired in a heating test on the cantilever array shown in a DIC micrograph **(C)**. Strong deformation of Cantilever 6 and 7 was caused by direct mechanical damage during sample preparation.

herein. The corresponding deflection signal generated by Cantilever 6 measured only 150 nm. The low PSD position signal of −4 mm suggested the presence of a strong initial deformation, in agreement with the optical micrograph. Cantilever 7 generated a deflection signal of 350 nm, yet substantively lower than the mean deflection signal. However the PSD position signal was within the z-range observed on the flat cantilevers.

The associated changes in Sum signals acquired on the flat cantilevers were below 0.5 mV. In contrast, Cantilever 6 exhibited a large change in the Sum signal of about 10 mV. The magnitude of these signals were in excellent agreement with the results obtained from the simulation. The large change in the Sum signal observed on Cantilever 6 can therefore be rationalised by the off-PSD effect. The change in Sum signal measured on Cantilever 7 was small and about 0.3 mV. This was expected since the PSD position signal was detected in the region of constant Sum.

It should be noted that the deformation of Cantilever 6 and Cantilever 7 was caused by a direct mechanical damage during sample preparation. Therefore the reduced magnitude of the deflection signal measured on Cantilever 7 should be attributed to changes in the mechanical properties of the cantilever. The reduced magnitude of the deflection signal measured on Cantilever 6 can then be attributed to a combination of both the off-PSD effect and changes in the mechanical properties of the deformed cantilever.

An additional effect that modulated the PSD Sum signal was observed on Cantilever 8. Cantilever 8 was a flat cantilever that appeared to be well-aligned. Similar changes in the Sum signal have been occasionally observed on Cantilever 1 and Cantilever 8, that is, on the two cantilevers located at the outmost y-positions. By considering the 2 mm width of the PSD and the 2 mm width of the cantilever array, this effect can be understood in terms of an off-PSD effect along the y-axis of the PSD. Fortunately, the deflection PSD signals were not affected by this effect, suggesting the homogeneity of the linear SLD spots generated by the Scentris instrument.

In principle, all eight cantilevers on a cantilever array can exhibit a large variability in the initial curvature. The variability in the initial curvature resulting from different cantilever arrays can be expected to be larger. It is possible to compensate the off-mirror effect by shifting the x-position of the cantilevers, though limited to the x-range between −1300 and +1100 μm. In typical pH measurements presented herein, cantilevers tended to show downward initial deflection and a downward drift of 2000 nm over six hours. The range of the initial cantilever deflection that can be

fully compensated by positioning the cantilevers at $x = -1300$ μm under these conditions was estimated to be between -10 and -2 μm based on the simulation.

In this section, it was proposed that the relative positions between the cantilever, the rotatable mirror, and the PSD alone can cause a relative measurement error of up to 50%. Importantly, this will affect both the absolute and differential cantilever deflection signals. Therefore the evaluation of cantilever array data must be performed with great care. The simulation was found to be useful to estimate the magnitude of the off-mirror and the off-PSD effect, plus the tolerance for the range of initial cantilever deflection that can be fully compensated by adjusting the x-position of the cantilever free end. Though it should be noted that the parameters used in the simulation may not be accurate. For example, when considering the relative position of the first fixed mirror and the default cantilever position estimated from Fig. 6.2, θ_w would be only about 20°, that is, 4° lower than the assumed angle. Moreover, the linear cross-section of the SLD spot and the constant intensity profile assumed in this simulation can be expected to underestimate the off-mirror effect. Further technical details of the Scentris instrument are necessary to improve the simulation. The most effective solution to minimise the off-mirror effect would be to minimise the initial cantilever deflection, which is primarily generated during the evaporation procedure. Alternatively, the deflection signals may be calibrated using cantilevers with different initial curvatures. This would require an external rotary actuator with 10^{-1} rad accuracy to mimic the ~ 10 μm initial cantilever deflection and a second rotary actuator with 10^{-5} rad accuracy to mimic the ~ 1 nm deflection signals. Future experiments will further investigate the mechanisms of the Scentris instrument.

6.2.4 Other Factors

While the cantilever/SLD alignment described in the previous section helped to identify and to analyse the largest source of measurement error associated with this work, it is important to consider other experimental factors that can affect the measured cantilever signals. This section gives a brief overview of these other experimental factors.

Thermo-Mechanical Stability of Scentris. In addition to the cantilever/PSD alignment, a second factor specific to the Scentris instrument appeared to be the thermo-mechanical stability of the entire device. The SLD sources generated a measurable amount of heat during its operation. The temperature measured at the rear side of the instrument close to the SLD sources was about 2 °C higher than the

temperature measured about 20 cm away at the same height in the temperature control cabinet. When the instrument was used constantly over a time period of several weeks, PSD signals generated by some but not all SLDs were superimposed to fluctuations that appeared on a variable time scale from a few minutes to several days. These fluctuations appeared to randomly affect different SLDs however were found to disappear completely upon resting the instrument for two weeks. Owing to the reproducibility, this effect was attributed to differential thermal expansion of some unknown optical components. Statistical analysis of a stable and an unstable measurement acquired on flat cantilevers on the same cantilever array showed that the mean differential pH signals acquired over six hours in the unstable measurement was slightly reduced to about 90%, however the standard errors of estimated means increased by a factor of two. The heating signals acquired in these measurements were in excellent agreement, -80.45 ± 1.31 mN/m in the stable and -80.49 ± 1.25 mN/m in the unstable measurement using all eight cantilevers, each with a Sum change of below 0.5 mV. This suggested that the fluctuations did not affect signals acquired on the time scale of 10 minutes, and that the cantilever/PSD alignment was equivalent in both measurements.

Mechanically Damaged Cantilevers. Another important factor that can affect the measurement of surface stress is the mechanical properties of cantilevers. As described in Section 5.2.3, the spring constant of cantilevers was measured prior to each core surface stress measurement. A statistical analysis of spring constants acquired on 44 cantilevers distributed on six cantilever arrays resulted in a weighted average and standard error of 7.9 ± 0.2 mN/m. Further results will be presented separately in Section 10.3. These experiments were performed under optimised conditions and on relatively flat cantilevers. However, spring constants measured on deformed cantilevers will be affected by the cantilever/PSD alignment and mechanical damages cannot be probed independently of the alignment effect. At present, mechanical properties are assumed to be constant for all cantilevers, by assuming the Young's modulus and Poisson's ratio for Si(100) reported by Brantley (1973). Thus a variability in the mechanical properties of damaged cantilevers will directly scale the measured deflection signals. Future work will use an external device such as profilometer to probe the mechanical properties of cantilevers as a function of the initial curvature.

Sample Contamination. Two major sources of sample contamination may be given. Firstly, the cross-contamination of cantilevers caused during the functionalisation procedure. Secondly, ageing of cantilevers during storage or due to re-

peated use. A certain amount of sample contamination should always be assumed. Under optimised conditions, the contamination of cantilevers appeared not to affect the measurement reproducibility. In contrast to mechanical damages, however, these effects are not visible and difficult to quantify. When an otherwise stable surface stress measurement performed on a particular cantilever array resulted in low differential pH signals relative to repeated measurements performed on other cantilever arrays, a sample contamination was suspected. An example of aged sample was chip E15 presented in Chapter 8. This sample was used only after 2 months of storage in the original bottle transported from IBM Rüschlikon, that is, without replacing the container and water. Although cantilevers appeared to be free of damage and measurements were acquired under optimised instrumental alignment, the pH 4.8/8.4/4.8 sodium phosphate differential signal used as control in this work measured only ~50% of the magnitude measured on the majority of 'good' cantilevers, that is, freshly prepared, flat cantilevers free of visible mechanical damages stored in clean water.

Thermo-Mechanical Properties of Cantilevers. Heating signals are generated due to differential thermal expansion coefficients of cantilever surface layers. A thick gold film expands more strongly than a thin gold film, therefore the variability in the thickness of evaporated gold film was of concern. Cantilever bending due to thermal effects has been investigated by Barnes et al. (1994). Upon the basis of their calculations, an 1 nm increase in the thickness of gold film would give rise to ~4% increase in the bending signal.

To probe the nominal thickness of 20 nm of gold film, silicon wafers were evaporated in parallel to cantilever arrays and the thickness was measured using a spectroscopic ellipsometer (Section 5.3.2). The measured thickness ranged from 20 to 23 nm for gold and from 3 to 4 nm for titanium over a distance of about 20 cm, each with an empirical measurement error of ± 2 Å. Since the cantilevers were loaded on dedicated holders separated by a maximal distance of about 10 cm, the within-batch variability of the bending signals due to differences in the gold film thickness was estimated to be in the order of 5%. The between-batch variability in the gold film thickness may not be substantively higher, considering the remarkable reproducibility of heating signals of about 80-85 mN/m acquired on C_{16} SAM coated cantilevers in pH 4.8 sodium phosphate solution, which were prepared in four different batches over a time period of 16 months. This also limits potential effects arising from the variability in the morphology of gold film. The important role of gold morphology on surface stress generation has been investigated by Godin et al. (2004). The

variability can be expected to increase when different evaporators were employed, however. Future work will investigate the effects of evaporation parameters on the thickness and morphology of gold films.

Purity of Chemicals. An important role of thiol purity on the generation of surface stress was anticipated. Thiols used in the course of this work originated from four different sources: firstly, purified C_{16} thiols provided by Dr. Emmanuel Delamarche from the IBM Rüschlikon; Secondly, 85-98% purity thiols purchased from Sigma-Aldrich; Thirdly, 99% purity C_{11} thiols purchased from Asemblon; Fourthly, purified fluorinated thiols provided by Prof. T. Randall Lee from the University of Houston. All other chemicals were of reagent grade. In the majority of experiments presented herein, the control C_{16} SAMs were formed from thiols provided by Dr. Delamarche. Thiols purchased from Sigma-Aldrich were used in an initial measurement and in a final measurement. In the initial measurement, the control differential signal acquired in pH 4.8/8.4/4.8 sodium phosphate solutions measured only ~ -3 mN/m, while in the final measurement, the control signals ranged from -6 to -14 mN/m. In both measurements, the cantilevers exhibited strong initial deformation, and the variability was attributed alignment/mechanical effect. To conclude, the purity of chemicals was not the major source of measurement variability in this work.

6.3 Discussion

The systematic measurement of cantilever bending signals using the semi-automated software, the rigorous statistical analysis, and the simulation of the Scentris instrument identified the least controlled experimental factor associated with this work: the surface stress itself. The high sensitivity of cantilevers to surface stress changes allows us to detect small bending signals. However, the high sensitivity is the downside of this mechanical sensor at the same time. The evaporation of gold and adhesion layer can generate large interfacial stress, giving rise to a large initial curvature of an evaporated cantilever. Bending signals generated by deformed cantilevers cannot be fully detected by the Scentris instrument, resulting in a reduction of PSD signals. Cantilevers are also prone to mechanical damages. If a cantilever exhibits initial curvature due to changes in its mechanical properties, the instrumental alignment effect and the mechanical effect cannot be separated. Both these factors will directly scale the detected PSD signals, including the absolute and the differential deflection signals, plus the associated errors. Typical differential signals measured 20% - 30% of the corresponding absolute signals. Effects between

different differential signals are often smaller. However, a 60% reduction of detected bending signals has been observed on a single cantilever array within a single measurement and the reduction occurred in a non-linear fashion in time. Therefore the cantilever array data must be analysed with great care. ANOVAs based on our statistical model will become critical for clinical applications of cantilever sensors. Yet this will require a better control of the mechanical properties of cantilevers.

It is now possible to formulate the criteria for the analysis of cantilever array data. The priority was given to the most accurate thus representative method adequate for individual measurements.

Firstly, cantilevers with visible mechanical damages or contamination were discarded. Individual cantilevers that generated obviously low or high heating signals were discarded. The mean and standard deviation of heating signals generated by the remaining cantilevers were calculated. Cantilever signals with a relative standard deviation larger than 2.5% were discarded from further analysis.

Secondly, the heating deflection signals obtained from multiple measurements were compared. If the cantilevers were prepared in parallel using the same cantilever coatings and if the heating tests were performed in the same aqueous environment, the mean heating deflection signals should agree within the relative standard deviation. This is particularly true if repeated measurements were acquired on the same cantilever array.

Thirdly, the heating Sum signals were inspected. Empirically, Sum changes below 0.5 mV per heating signal appears to be harmless. If larger Sum signal changes were observed, Sum signal changes measured in different pH cycles were inspected. A time dependence of the changes in the Sum signal indicated a time dependence of the alignment effect. A better approach was to perform a second heating test immediately after the core surface stress measurement. The magnitude of the mean heating signal was compared to the mean heating signal acquired prior to the core surface stress measurement and the variability in the Sum signal changes were inspected.

If there was no evidence of alignment and/or mechanical effect, single measurements were evaluated using appropriate single-array ANOVAs according to Section 6.2.2. Further, if the standard errors obtained from single-array ANOVAs were homogeneous, multiple measurements would be analysed using an appropriate multiple-array ANOVA. However, since the cause of the observed inhomogeneity of errors is currently under investigation, most of the multiple measurements presented herein were analysed by weighting the means and standard errors obtained

from single-array ANOVAs, for which no assumption of homogeneous errors was required: let t_i with $i = 0, 1, .., n$ be n independent estimators of θ and let the variance of t_i be $Var(t_i) = 1/w_i$. Then

$$t^* = \frac{\sum_i w_i t_i}{\sum_i w_i} \tag{6.2}$$

is the minimum variance estimator of θ with variance

$$Var(t^*) = \frac{1}{\sum_i w_i} . \tag{6.3}$$

If, however, only a single cantilever was involved in an individual independent estimator, Eq. (6.2) and Eq. (6.3) will favour automatically the single-cantilever estimator. This is because the variance associated with the single-cantilever estimator is given by the within-cantilever variance only, which is an order of magnitude smaller than the between-cantilever variance, as we have seen previously. Therefore in this case, the means obtained from single-array ANOVAs were averaged

$$\bar{t} = \frac{\sum_i t_i}{n} \tag{6.4}$$

and the variance of the average was estimated as

$$Var(\bar{t}) = \frac{1}{n^2} \sum_i Var(t_i) \tag{6.5}$$

without weights. An example case is the C_8COOH signal obtained from chip J06 and G16 presented in Chapter 10.

Conversely, if there was evidence of alignment/mechanical effect, signals generated by different cantilevers within a single cantilever array should not be treated as independent observations. Instead, measurements acquired on different cantilevers with the same cantilever coating within a single cantilever array were averaged to give one independent observation. Then the averages obtained from multiple cantilever arrays were averaged and its variance calculated to estimate the overall mean and the associated variance, respectively.

Note that the estimated mean differential signal was obtained by subtracting the estimated mean absolute signal of a first cantilever coating from the estimated mean absolute signal of a second cantilever coating. The estimated variance of the estimated mean differential signal is then the sum of the estimated variance of the absolute signal of the first cantilever coating and the estimated variance of the absolute signal of the second cantilever coating. The corresponding estimated standard error of the estimate mean is the square-root of the estimated variance.

6.4 Conclusion

This chapter addressed different sources of variability associated with the measurement of surface stress using cantilevers. The development of semi-automated fit software, statistical model, and simulation of cantilever bending signals identified the least controlled experimental factor associated with this work: the surface stress itself. Initial cantilever deformation arising from excessive surface stress alone was found to cause a relative error of several tens of percent, which affected both the absolute and differential signals. Thus cantilever array data must be analysed with great care. Basic criteria for the evaluation of cantilever array data were formulated. Our statistical model will become essential for clinical applications of cantilever sensors. Yet this will require a better control of different sources of variability, in particular the mechanical properties of cantilevers.

7. Surface Stress Titration

7.1 Introduction

When a chemical or biological reaction occurs on one surface of a cantilever, a surface stress is generated, which causes the deflection of the free-end of the beam. The range of biological systems which have been probed via this novel sensing mechanism extends from DNA hybridisation (Fritz et al. 2000a; McKendry et al. 2002; Fritz et al. 2002; Mukhopadhyay et al. 2005; Shu et al. 2005) to protein recognition (Fritz et al. 2000a; Backmann et al. 2005; Wu et al. 2001; Savran et al. 2004), and cell adhesion (Ilic et al. 2001; Park et al. 2005) but there is much debate in the literature about the underlying molecular transduction mechanisms. To realise potential sensor and microrobotic applications, it is essential to learn to control both the direction and amplitude of cantilever motion. It has been proposed that electrostatic interactions play an important role in surface stress (Fritz et al. 2000a; McKendry et al. 2002; Shu et al. 2005) yet interpretation of measurements is hindered by the inherent complexity of biomolecules with multiple functional and zwitterionic groups. In contrast, alkanethiols form well-defined self-assembled monolayers (SAMs) on gold surfaces, where the surface properties are controlled by the chain length and terminal group (Nuzzo and Allara 1983; Bain et al. 1989; Nuzzo, Dubois, and Allara 1990). In particular, the acid-base properties of carboxylic acid terminating SAMs such as mercaptohexadecanoic acid, which can be controlled via the pH of the liquid environment, offer an ideal system for fundamental studies with broad applicability to colloidal science, catalysis, protein folding and membrane biophysics. While acid-base reactions of SAMs have previously been studied on cantilevers, results have varied widely (Raiteri, Butt, and Grattarola 2000; Fritz et al. 2000b) and have been typically limited due to either lack of mechanical sensitivity or the use of only single cantilever measurements. Single cantilever measurements are notoriously problematic since non-specific reactions, including changes in temperature, refractive index and reactions occurring on the underside of a cantilever can dominate the value of an absolute signal. Differential

measurements using in situ reference cantilevers tailored with control, non-reactive coatings have been shown to be essential to detect chemically specific surface forces and enable multiple reactions to be probed in parallel, under similar experimental conditions (Fritz et al. 2000a; Fritz et al. 2000b; McKendry et al. 2002; Shu et al. 2005). Fritz et al. reported differential investigations of surface stress on SAMs but only repulsive forces were detected in one aqueous environment and no statistical analysis was performed (Fritz et al. 2000b). Many fundamental questions remain concerning the mechanisms of pH-triggered in-plane bonding and surface stress action along the cantilever. How strong are the in-plane forces associated with the surface $pK_{1/2}$, at which half the population of terminal carboxylic acid groups will be protonated and half are deprotonated? Further, how are these forces influenced by the presence of anions and cations in the aqueous solution?

7.2 Results

7.2.1 Cantilever Effective Length

The bending signals of an array of eight microcantilevers were monitored using a time-multiplexed optical detection scheme as the pH of sodium phosphate solution at a constant ionic strength of I = 0.1 was cycled between pH 4.8 and 8.4. To investigate the homogeneity of pH-triggered surface stress action along the long axis of the micromechanical cantilever, initial experiments measured the bending signal at different positions on the beam structure, that is, starting from the 5.9 μm thick extended support to the 0.9 μm thick cantilever at the effective lengths 65, 130, 265, 385, and 470 μm by moving the laser position, as shown in Fig. 7.1A. To ensure that the laser spots were aligned at equivalent positions for all cantilevers, heating tests that rely on the bimetallic effect were first performed at each effective length prior to the pH measurements. Fig. 7.1B shows the raw bending signals for a typical cantilever coated with 16-mercaptohexadecanoic acid ($HS(CH_2)_{15}COOH$, herein termed MHA) upon switching between pH 4.8/8.4/4.8 liquid environments. It can be seen that at pH 4.8 the bending signal was stable under constant liquid flow. Upon switching to pH 8.4, where the carboxylic acid terminating SAMs are expected to be ionised, the cantilever bent downwards corresponding to a compressive surface stress. When the aqueous environment was switched back to pH 4.8, the bending signal returned towards the zero stress baseline. The pH-triggered change in cantilever bending profile shown in Fig. 7.1C was determined by plotting the equilibrium pH 8.4 bending signal at each effective length (full circles and

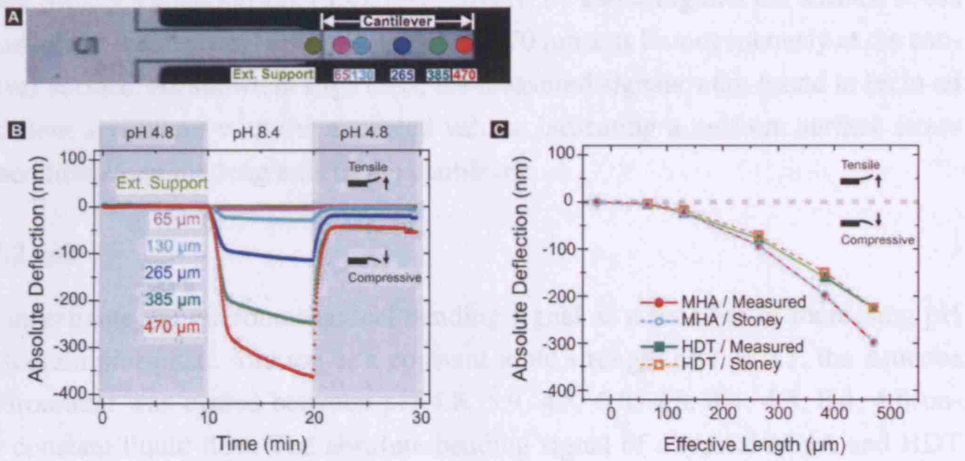

Fig. 7.1. (A) Micrograph of a single cantilever to show the effective lengths investigated: extended support structure (dark yellow), 65 µm (magenta), 130 µm (cyan), 265 µm (blue), 385 µm (green), and 470 µm (red). (B) Raw absolute signals associated with pH 4.8/8.4/4.8 sodium phosphate cycle taken at the given effective lengths on a MHA-coated cantilever. (C) Equilibrium pH 4.8/8.4/4.8 MHA (circles) and HDT (rectangles) absolute signals as a function of the effective length (solid symbols and solid line), superimposed on expected values according to the Stoneys equation (symbols and dashed lines). Note that owing to the small standard errors for these measurements, the error bars associated with each data point are not visible in (C).

solid lines). Thereby each data point represents the mean and standard error of the deprotonation $\Delta z_{\text{abs(pH 4.8/8.4)}}$ absolute bending signals associated with the switch from pH 4.8 to 8.4, and protonation $\Delta z_{\text{abs(pH 4.8/8.4)}}$ absolute bending signals associated with the switch from pH 8.4 back to 4.8, taken on two cantilevers coated with MHA (red circles in Fig. 7.1C) and two cantilevers coated with hexadecanethiol ($HS(CH_2)_{15}CH_3$, herein termed HDT; green circles in Fig. 7.1C), respectively. Both deprotonation and protonation reactions refer to the reference pH 4.8, that is, both the deprotonation and protonation absolute bending signals are determined by subtracting the signal observed at pH 4.8 from the signal observed at pH 8.4. The absolute deflection is attributed to a combination of surface stress induced by the specific ionisation of MHA and non-specific influences including reactions occurring at non-functionalised sites on the gold and at silicon oxide underside of the cantilever, changes in refractive index or in the temperature of the aqueous environment. These non-specific effects will affect both MHA and HDT signals to the same extent, and are eliminated by taking a differential measurement (MHA minus HDT absolute signal). The measured bending profile was then superimposed on the expected profile of MHA (light blue hollow circles and dotted lines in Fig. 7.1C) and HDT (orange hollow circles and dotted lines in Fig. 7.1C) signals according

to the Stoney's equation Eq. (5.4), respectively, by assuming that the surface stress measured at the maximal effective length of 470 μm acts homogeneously at the cantilever surface. As shown in Fig. 7.1C, the measured signals were found to be in an excellent agreement with the expected values, indicating a uniform surface stress generation along the long axis of the cantilever.

7.2.2 pH

To investigate the micromechanical bending signal as a function of increasing pH of sodium phosphate solution at a constant ionic strength of $I = 0.1$, the aqueous environment was cycled between pH 4.8, 5.9, 4.8, 6.8, 4.8, 8.4, 4.8, 8.4, 4.8 under constant liquid flow. The absolute bending signal of a typical MHA and HDT coated cantilever is shown in Fig. 7.2A. Alternate injections of pH 4.8 phosphate solution served as an important control to investigate the reversibility of deprotonation/protonation reactions, since at this pH the largest fraction of surface carboxylic acids have been assumed to be protonated. Upon injecting increasingly

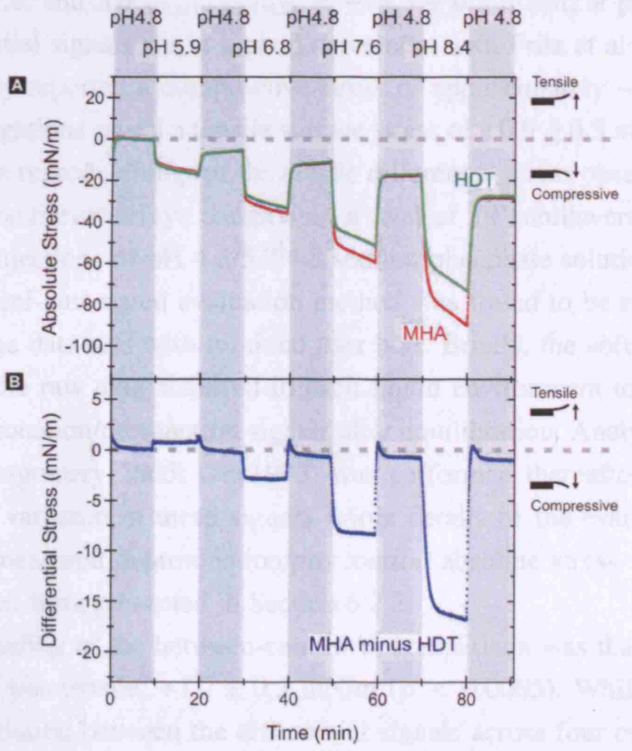

Fig. 7.2. (A) Absolute surface stress signals for MHA and HDT cantilevers as a function of sodium phosphate solution pH at constant ionic strength $I = 0.1$. (B) Differential signal (MHA minus HDT).

higher pH solutions (5.9, 6.8, 7.6, 8.4) it can be seen that both MHA and reference HDT cantilevers bent downwards corresponding to a compressive absolute surface stress (cantilever bending away from the gold coating, as illustrated in Fig. 5.1). The corresponding differential signals specific to the MHA surface ionisation are shown in Fig. 7.2A. It can be seen that upon switching from pH 4.8 to pH 5.9 the difference in absolute bending between the MHA cantilever and HDT cantilever was positive reaching an equilibrium signal $\Delta z_{\text{diff(pH 4.8/5.9)}} = 2.7$ nm under constant liquid flow, which corresponds to a tensile differential stress $\Delta \sigma_{\text{diff(pH 4.8/5.9)}} = 0.6$ mN/m. When the pH was cycled back to pH 4.8, the differential signal was observed to return to the baseline, $\Delta \sigma_{\text{diff(pH 5.9/4.8)}} = 0.7$ mN/m. Upon switching to more alkaline pH environments, the resulting differential signals rendered increasingly more compressive. The estimated mean differential stress and standard error resulted from a single cantilever array comprising three MHA and three HDT coated cantilevers, three pH cycles, and deprotonation/protonation reactions was estimated to be $\Delta \sigma_{\text{diff(pH 4.8/5.9/4.8)}} = +0.9 \pm 0.3$ mN/m at pH 5.9, $\Delta \sigma_{\text{diff(pH 4.8/6.8/4.8)}} = -2.4 \pm 0.6$ mN/m at pH 6.8, $\Delta \sigma_{\text{diff(pH 4.8/7.6/4.8)}} = -7.7 \pm 0.6$ mN/m at pH 7.6, and $\Delta \sigma_{\text{diff(pH 4.8/8.4/4.8)}} = -14.5 \pm 0.5$ mN/m at pH 8.4. The observed differential signals are in a good agreement with Fritz et al. (2000b), however, while they reported a compressive stress of approximately −2 mN/m at pH 5.9, our investigations reveal a tensile surface stress of $+0.9 \pm 0.3$ mN/m.

To probe the reproducibility of the tensile differential stress observed at pH 5.9, four separate cantilever arrays comprising a total of 19 cantilevers were exposed to successive injections of pH 4.8/5.9/4.8 sodium phosphate solutions. The development of a semi-automated evaluation method was found to be essential for the analysis of large data sets with minimal user bias. Briefly, the software generated a linear fit to the raw data acquired in each liquid environment to determine the absolute deprotonation/protonation signals after equilibration. Analysis of variance (ANOVA; Montgomery 2005; Ott 1993) was performed thereafter to investigate the sources of variation in these signals. More details of the evaluation method, including the measured deprotonation/protonation absolute stress signals and the statistical model, were presented in Section 6.2.2.

The main finding of the between-cantilever comparison was that the mean differential stress was tensile, $+1.2 \pm 0.3$ mN/m ($p < 0.0005$). While there was no evidence of variation between the differential signals across four cantilever arrays ($p = 0.4$), clear evidence of variation was found in the corresponding absolute stress

($p < 0.0005$), thus emphasising the importance of differential stress measurements. The total between-cantilever variance was estimated to be 0.56 $(mN/m)^2$.

The effective variance of the within-cantilever measurement error was estimated to be only 0.006 $(mN/m)^2$. This allowed us to probe very small changes in surface stress, which would otherwise be masked by the approach commonly used to evaluate differential measurement (Fritz et al. 2000a; Fritz et al. 2000b; McKendry et al. 2002; Backmann et al. 2005; Shu et al. 2005). The small effective within-cantilever variance revealed an estimated mean difference, in the protonation minus deprotonation differential stress signal, of +0.18 ± 0.05 mN/m ($p = 0.01$). This hysteresis showed no evidence of variation between the four cantilever arrays ($p = 0.2$), but again clear evidence of variation was found in the corresponding absolute stress ($p < 0.0005$).

Our work confirms the importance of differential measurements. Multiple observations on the same cantilever, on different cantilevers and different cantilever arrays allow more precise estimation of the generated surface stress. Ongoing experimental and statistical work will further investigate the various sources of variation of both between- and within-cantilever effects, including successive cycles and measurement order (Galbraith et al. 2007).

7.2.3 Ionic Strength

Building upon the titration studies described above, our next experiments probed the differential bending response to different ionic strengths of sodium phosphate aqueous solutions. Fig. 7.3A and B shows typical absolute and differential measurements, respectively, taken on a cantilever array comprising three MHA and four HDT coated cantilevers. The cantilever array was exposed to an alternate injection of pH 5.4 and 6.8 sodium phosphate solutions prepared at the ionic strengths I = 0.1, 0.01 and 0.001. Statistical analysis of the differential stress found that in-plane MHA forces were dependent upon ionic strength when the pH was varied between 5.4 and 6.8. The 5.4/6.8 pH switch at the highest and default ionic strength of I = 0.1, gave a compressive differential surface stress of −2.6 ± 0.8 mN/m. However when the ionic strength was reduced by an order of magnitude to I = 0.01, the pH 5.4/6.8 differential bending response was observed to invert to give a tensile differential surface stress signal of +2.8 ± 0.6 mN/m. Upon further reducing the ionic strength to I = 0.001, the tensile signal increased to +5.7 ± 0.3 mN/m.

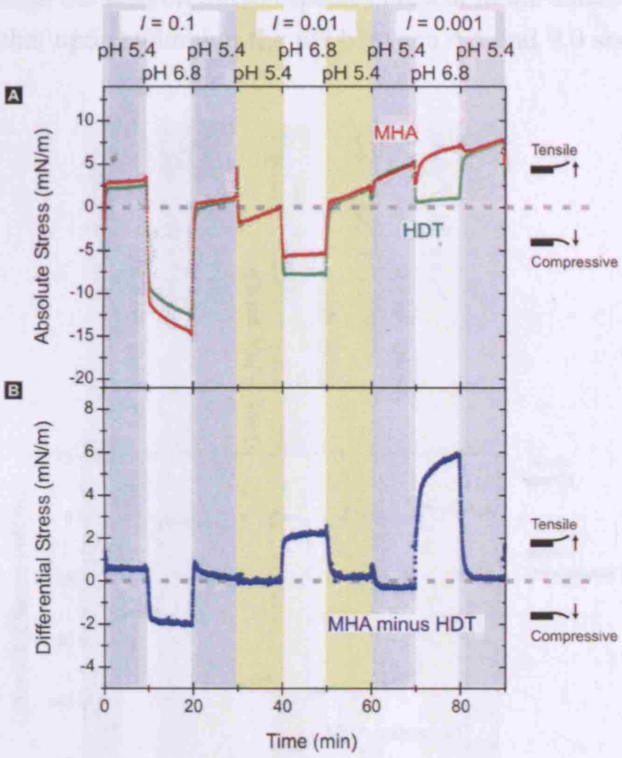

Fig. 7.3. (A) Absolute and (B) differential surface stress change associated with alternate injection of pH 5.4 and 6.8 sodium phosphate solutions with decreasing ionic strengths I = 0.1, 0.01, and 0.001.

7.2.4 Anion / Cation Species

To further investigate the role of the aqueous environment on MHA surface stress, our studies extended to probe the effect of different counter- and co-ions. The surface stress triggered by the pH 4.5/9.0/4.5 switch (at constant ionic strength I = 0.1) was compared for two different cations; sodium and ammonium phosphate (Na^+, NH_4^+). Then the influence of different anions was probed by comparing pH 9.0 ammonium chloride and ammonium nitrate (Cl^-, NO_3^-) in addition to the ammonium phosphate ($H_xPO_4^{-(3-x)}$). Fig. 7.4 shows the differential signal when the MHA/HDT cantilever array was exposed to the following series of aqueous environments; pH 4.5/9.0/4.5 sodium phosphate ($Na_{3-x}H_xPO_4$); pH 4.5/9.0/4.5 ammonium phosphate ($(NH_4)_{3-x}H_xPO_4$); pH 9.0 ammonia/ammonium chloride (NH_3^+/NH_4Cl); pH 4.5 ammonium phosphate, pH 9.0 ammonia/ammonium nitrate (NH_3^+/NH_4NO_3); pH 4.5 ammonium phosphate, and pH 4.5 sodium phosphate. The statistical analysis of differential signals revealed that the bending response is not only dependent on the pH

or the ionic strength but also on the ion species present in the aqueous environment. Fig. 7.4 shows that upon switching the pH between 4.5 and 9.0 sodium phosphate

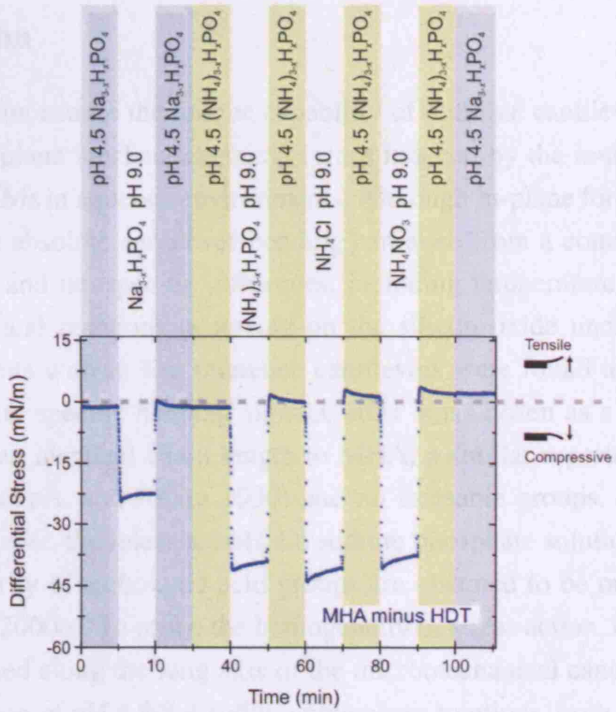

Fig. 7.4. Typical differential measurement to probe the effect of counter and co-ions. The signal was obtained upon alternate injection of I = 0.1 pH 4.5/9.0/4.5 $Na_{(3-x)}H_xPO_4$, pH 4.5/9.0/4.5 $(NH_4)_{(3-x)}H_xPO_4$, pH 9.0 NH_3^+/NH_4Cl, pH 4.5 $(NH_4)_{(3-x)}H_xPO_4$,pH 9.0 NH_3^+/NH_4NO_3, pH 4.5 $(NH_4)_{(3-x)}H_xPO_4$, and pH 4.5 $Na_{(3-x)}H_xPO_4$.

solution, a compressive differential stress of -13.6 ± 3.9 mN/m was observed. This is in agreement with the data shown in Fig. 7.2 and served as another important control measurement. When the solution was switched from pH 4.5 sodium phosphate to pH 4.5 ammonium phosphate, a small compressive signal of -0.3 ± 0.1 mN/m was detected, though ANOVA showed that there was no strong evidence for this effect (p = 0.08). Whereas when the aqueous solution was switched between pH 4.5 and 9.0 ammonium phosphate, the in-plane surface forces increased to -47.2 ± 4.8 mN/m. The magnitude of the compressive differential stress observed in the ammonium phosphate solution was found to be comparable to the signal of ammonium nitrate -50.4 ± 5.2 mN/m and ammonium chloride -47.5 ± 5.1 mN/m.

It should be noted that a common reference pH 4.5 ammonium phosphate solution was employed for these anions.

7.3 Discussion

Our findings demonstrate the unique capability of multiple cantilever arrays to detect specific in-plane mechanochemical forces induced by the ionisation reactions of the MHA SAMs in aqueous environments. Although in-plane force titration studies showed that absolute cantilever bending can arise from a combination of both specific effects and nonspecific influences, including temperature, changes in refractive index, and reactions occurring on the silicon oxide underside, differential measurements with in situ reference cantilevers were found to be essential to probe chemically specific bending signals. HDT was chosen as a reference SAM because it has an identical chain length to MHA, a similar reported packing density (Nuzzo, Dubois, and Allara 1990) and no ionisable groups. In addition to a reference cantilever, the reference pH 4.8 sodium phosphate solution was used, because the majority of carboxylic acid groups are assumed to be protonated at this pH (Fritz et al. 2000b). To probe the homogeneity of stress action, the bending profile was measured along the long axis of the micromechanical cantilever. Upon the alternate injection of pH 4.8/8.4 sodium phosphate solutions, both MHA and HDT were found to exhibit a constant cantilever curvature, in agreement with the Stoneys equation Eq. (5.4). The validity of this equation has recently been subject to much debate in the literature (Jeon and Thundat 2004; Mertens, Álvarez, and Tamayo 2005; Rasmussen, Hansen, and Boisen 2005; Klein 2000; Sader 2001). However, in this literature, critical parameters varied including the specific experimental or modelled system under investigation (bimetallic heat transduction or SAM formation), the environment (vacuum, air, or liquid), cantilever geometry and material. These factors may, at least in part, explain the discrepancies in the direction and homogeneity of the reported bending signals. In contrast, here we have optimised the surface chemistry and fluid flow to ensure the rapid and homogeneous exchange of different liquid environments to induce specific chemical reactions at the cantilever solid-liquid interface. Under these optimised conditions, our findings show that the surface stress profile along the long axis of the cantilever beam induced by SAM ionisation can be accurately described by the Stoneys equation, indicating a homogeneous surface stress transduction.

The development of an automated raw data evaluation algorithm was found to be essential to evaluate large data sets with minimal user bias. Moreover, the analysis of variance model for the multiple cantilever array data allowed us to estimate the differential stress and its variance, and, importantly, to deconvolute the different sources of variability which result from multiple measurements on separate cantilever arrays. It is important to note that although a number of groups have reported surface stress measurements on a range of different chemical and biological systems, to date there has been no detailed study of the statistical variability of measurements and yet this is essential for all potential sensing applications. Here we show that the development of a statistical model for the cantilever array data is particularly important to probe the small tensile surface stress observed at pH 5.9, that is $+1.2 \pm 0.3$ mN/m. Previous pH titration surface stress studies on acid terminating SAMs have varied widely, and are largely limited due to the use of single cantilever measurements (Raiteri, Butt, and Grattarola 2000). Our findings are in good agreement with the differential measurements of Fritz et al. (2000b) for pH > 6.8 but differences became more prominent at low pH, where herein the sign of small surface stress inverted to give a tensile mean differential stress. Fritz reported a small compressive surface stress of approximately -2 mN/m at pH 5.9, however no detailed statistical analysis was performed to assess the statistical significance of this observation. In contrast, here thirty-eight measurements were made on a total of nineteen cantilevers distributed on four separate cantilever arrays, and analysed via an ANOVA based on a statistical model. It should also be noted that differences in surface stress to published data may arise due to sample preparation, for example molecular packing and gold morphology. In this study, SAMs were characterised using XPS, ellipsometry, and contact angle goniometry (Section 5.3.2) and were shown to be in excellent agreement with high quality SAMs reported in published data (Bain et al. 1989; Nuzzo, Dubois, and Allara 1990).

To rationalise the cantilever bending response as a function of the increasing pH of sodium phosphate aqueous solution, we propose a simple model comprising three distinct pH regimes determined by the ionisation state of the carboxylic acid terminating SAM, as illustrated in Fig. 7.5. We will initially consider the three different pH regimes (I-III) in turn, and then extend our discussion to consider the influence of solution phase ions on in-plane MHA forces (IV).

In the first regime at low pH, the MHA SAM is assumed to be fully protonated and the in-plane interaction is governed by the formation of attractive neutral hydrogen bonds COOH $\cdots$ COOH (Fig. 7.5, I). With increasing pH, the second regime

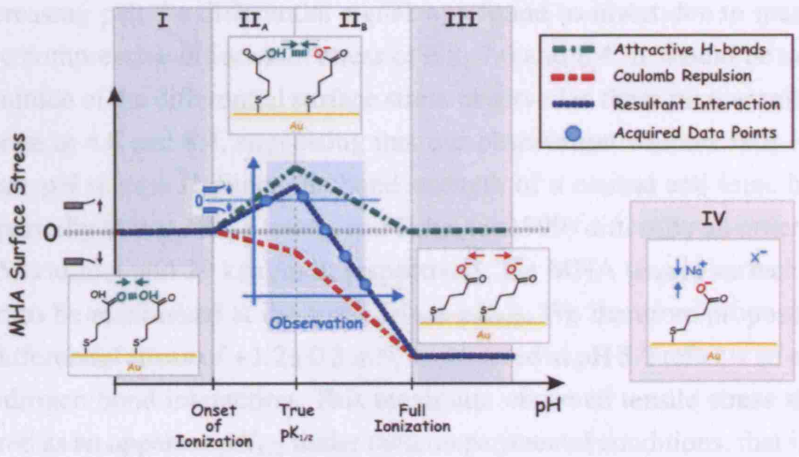

Fig. 7.5. MHA surface ionisation state in different pH regimes.

starts with the onset of ionisation to yield a negatively charged carboxylate ion and then extends to the pH at which full ionisation of every surface acid group is achieved (Fig. 7.5, II). This regime is further subdivided into two parts; from the onset of ionisation to the p$K_{1/2}$ is termed IIA, while from the p$K_{1/2}$ to full ionisation is IIB. In IIA, as the pH is increased, adjacent deprotonated and protonated carboxylic acid groups can form in-plane attractive ionic hydrogen bonds $COO^- \cdots COOH$. By definition the number of ionic H-bonds formed will become maximal at the surface p$K_{1/2}$. Whereas in IIB as the pH is increased above the surface p$K_{1/2}$, there will be electrostatic repulsion between adjacent deprotonated carboxylic acid groups $COO^- \cdots COO^-$. However in IIA and IIB, the resultant in-plane force (blue dotted line) will be a superposition of both the attractive ionic hydrogen bonding (green dotted line) and coulomb repulsion (red dotted line) as shown in Fig. 7.5. In the third distinct pH regime of this model, the SAM is fully ionised and the resultant force is governed by electrostatic repulsion (Fig. 7.5, III).

The model in Fig. 7.5 can be applied to the experimental surface stress profile of MHA measured herein, although our data constitute an observation window onto the true surface stress titration behaviour. This is illustrated by the relative coordinate system of the window in Fig. 7.5 (blue axes) with respect to the coordinate system of the model (black axes). At the lower pH limit of 4.8 used herein, the largest fraction of surface carboxylic acids is assumed to be protonated and thus served as the reference zero stress state for all cantilever measurements. We show that the magnitude of in-plane attractive forces reached a maximum at pH 5.9 and

with increasing pH, the differential signal was found to invert due to increasingly repulsive compressive differential stress at 6.8, 7.6 and 8.4. It should be noted that the magnitude of the differential surface stress observed in these measurements does not saturate at 4.8 and 8.4, suggesting that our observation window falls in the intermediate pH regime II. Since the bond strength of a neutral and ionic hydrogen bond reportedly (Meot-Ner, Elmore, and Scheiner 1999) differs by an order of magnitude, 5 kcal/mol and 29 kcal/mol, respectively, the MHA tensile surface stress is expected to be maximised at the true surface $pK_{1/2}$. We therefore propose that the tensile differential stress of +1.2±0.3 mN/m observed at pH 5.9 reflects an enhanced ionic hydrogen bond interaction. This maximum observed tensile stress should be considered as an apparent $pK_{1/2}$ under these experimental conditions, that is $I = 0.1$ sodium phosphate solution. The compressive surface stress observed at pH 6.8 relative to pH 4.8 indicates that the true surface $pK_{1/2}$ lies within the range pH 4.8 to 5.9. The measured apparent surface $pK_{1/2}$ implies an alkaline shift compared to the pK_a of carboxylic acid groups in bulk solution phase, for example acetic acid 4.76 (*The CRC Handbook of Chemistry and Physics*, 86th ed., 2005). This alkaline shift has been reported in the literature (Holmes-Farley et al. 1988; Lee et al. 1994; Vezenov et al. 1997; Van der Vegte and Hadziioannou 1997; Smith et al. 2000; Wang, Frostman, and Ward 1992; Schweiss et al. 2001; Gershevitz and Sukenik 2004; Konek et al. 2004) and may be attributed to coulombic interactions between the neighbouring deprotonated carboxylic acid groups, dipole/dipole interactions between the carboxylic acid groups and the aqueous phase, or the dielectric contrast between the hydrocarbon monolayer ($\varepsilon_{\text{Alkanes}} \sim 2$) and the aqueous phase ($\varepsilon_{H_2O} \sim 80$; *The CRC Handbook of Chemistry and Physics*, 86th ed., 2005) promoting ion migration towards the lower dielectric (Holmes-Farley et al. 1988). Yet while previous titration studies such as chemical force microscopy probed the out-of-plane forces acting between two approaching surfaces coated with carboxylic acid terminating SAMs (Vezenov et al. 1997; Van der Vegte and Hadziioannou 1997; Smith et al. 2000), this technique cannot probe in-plane forces, and moreover is limited by the liquid confinement effects. Contact angle goniometry has detected an increase in the hydrophobicity of the carboxylic acid terminating SAMs associated with the formation of in-plane hydrogen bonds (Lee et al. 1994). However the applicability of this technique in determining the surface free energy has been subject to debate (Fowkes 1964; Bain et al. 1989; Holmes-Farley et al. 1988; Lee et al. 1994), as the nature of the three-phase boundary is yet not well understood. Therefore even though different techniques have been used to investigate the titration behaviour of

surface tethered carboxylic acid groups, the cantilever array experiments herein represent a unique approach to probe directly the chemically specific in-plane forces generated at the liquid/solid interface. It is important to appreciate that the differential surface stress measurements using free-standing cantilevers reported herein offer the first direct measure of the in-plane attractive forces exerted by the formation of ionic hydrogen bonds associated with the surface $pK_{1/2}$. By assuming the reported packing density of 21.4 Å^2 per alkanethiol (Strong and Whitesides 1988), the observed tensile differential MHA surface stress of 1.2 ± 0.3 mN/m at the apparent $pK_{1/2}$ translates into an average in-plane attractive force of 1 pN exerted by each pair of adjacent MHA molecules, although this estimate does not consider inherent roughness of the surface but only the geometry of the cantilever.

However the simple model of in-plane differential stress generation in the intermediate pH regime based upon the attractive hydrogen bond interaction and repulsive coulomb interaction should be applied with caution. While it appears intuitive that the observed compressive differential surface stress at pH = 6.8 primarily arises from the electrostatic repulsion between the adjacent deprotonated carboxylic acid groups, our investigations reveal the important role of the counterions and co-ions present in the aqueous environment (Fig. 7.5, IV). It was expected that at pH 6.8, a decrease in ionic strength from I = 0.1, 0.01 to 0.001, would increase the Debye screening length and so in turn, increase the in-plane electrostatic repulsion giving rise to an increased compressive differential surface stress. However herein we report the opposite effect: as the ionic strength was decreased, the compressive differential stress signal at I = 0.1 was observed to invert and became increasingly tensile at lower ionic strengths of I = 0.01 and I = 0.001. At present the relation between the ionic strength and MHA surface stress is not well understood. Indeed, one must not only consider the in-plane attractive and repulsive interaction between carboxylic acid groups but also the pH dependent ion concentration of the bulk sodium phosphate solution ions (Fig. 3.1), and the interaction of solution phase ions at the MHA/liquid interface. The important role of solution ions on MHA in-plane forces was highlighted by the results shown in Fig. 7.4 (Fig. 7.5, IV). A comparison of the pH 4.5/9.0 switch for two different monovalent cations, Na^+ and NH_4^+, both probed in phosphate solution at a constant ionic strength of I = 0.1, found that the in-plane surface forces were more than two-fold larger for ammonium than for sodium cations. Whereas, interestingly, statistical analysis of three different anion species at pH 9.0 (HPO_4^{2-}, Cl^- and NO_3^-) found the mean compressive differential stress signals were not distinguishable within the associated standard errors, estimated by

an ANOVA. These findings show the significant effect of different cations on the magnitude of MHA in-plane forces at pH 9.0. One might suggest that the smaller sodium cations are able to screen the repulsive forces between negatively charged COO^- groups more efficiently than larger ammonium cations, based upon literature crystal ionic radius of 0.95 Å and 1.48 Å, respectively (Nightingale 1959). However, the corresponding hydrated radii are similar, 3.58 Å and 3.31 Å for sodium and ammonium cation (Nightingale 1959). Future work will involve a systematic study of different mono-, di- and trivalent cations to investigate the effects of ion size and hydration on the generation of deprotonation induced MHA in-plane forces.

7.4 Conclusion

To conclude, systematic differential surface stress titration measurements have shown the sensitivity to detect attractive in-plane forces associated with ionic hydrogen bond formation at the apparent surface $pK_{1/2}$, and the electrostatic repulsion between deprotonated carboxylic acid groups at elevated pH. Our studies reveal the dominant role of counterions in the aqueous environment in the generation of in-plane mechanochemical forces which controls both the magnitude and direction of cantilever motion. These surface in-plane forces will become increasingly important as the dimensions of the solid shrink down to the nanometre scale. Understanding the complex dynamic three-phase equilibrium between hydrophilic and hydrophobic SAMs, interfacial ions and water molecules and the bulk solution presents a challenging goal for both experiment and theory. Ongoing experiments will probe the ionic strength dependence over the full pH range, different monovalent and divalent ions plus the influence of SAM chain length and terminal groups, including OH and NH_2 functionalities. These findings will provide new insights into the fundamental mechanisms of surface stress generation, which have broad implications in the study of biochemical interfaces from molecular thin films to cellular membranes.

8. Effect of Monovalent and Divalent Cations

8.1 Introduction

The important role of pH, ionic strength, and solution phase ions in the generation of pH-induced surface stress at the carboxylic acid terminated surface of mercapto-hexadecanoic acid self-assembled monolayers (SAMs) was described in Chapter 7. These findings form the basis of an initial model of pH-induced surface stress that involved the generation of attractive in-plane forces associated with ionic hydrogen bond formation at the apparent surface $pK_{1/2}$, and the electrostatic repulsion between deprotonated carboxylic acid groups at elevated pH. Furthermore, the strong effect of monovalent sodium/ammonium cations motivated a systematic investigation of cation specific effects. The purpose of this chapter was therefore to address the following three questions: firstly, how does the MHA surface stress depend on the crystal ionic radii of monovalent cations? Secondly, how does the cation specific effect depend on the solution pH? Finally, what is the effect of divalent cations?

In the first part of this chapter, the effects of lithium Li^+, sodium Na^+, and potassium K^+ are investigated, which are three Group I monovalent cations. The sodium cation is the standard cation probed throughout this work, and has a crystal ionic radius of 0.95 Å. The crystal ionic radius of the lithium cation is smaller (0.6 Å), and that of the potassium cation is larger (1.33 Å) than the sodium cation (Nightingale 1959). The initial experiment investigated the onset of the MHA deprotonation at pH 3.5, which is lower than the reference pH 4.8 used in this work. Thereafter, surface stress titration experiments were performed to probe the in-plane ionic hydrogen bonds in the intermediate pH regime between 4.8 and 6.8, as well as the charge/charge repulsion between deprotonated surface carboxylic acids in the higher pH regime between pH 7.6 and 8.4. Owing to the low solubility of the dibasic lithium phosphate Li_2HPO_4, mixed solutions of monobasic phosphate MH_2PO_4 and hydroxide MOH for each cation M = Li^+, Na^+, and K^+ were prepared instead of mixed solutions of monobasic and dibasic phosphate. In the second part of this chapter, further pH measurements were performed to probe the effect of divalent

Cation	Crystal Ionic Radius (Å)	Hydrated Radius (Å)
Li^+	0.60	3.82
Na^+	0.95	3.58
K^+	1.33	3.31
Cs^+	1.69	3.29
Mg^{2+}	0.65	4.28

Table 8.1. Crystal ionic radii and hydrated radii of the cations probed in this chapter (Nightingale 1959).

magnesium using magnesium chloride $MgCl_2$. To ensure a sufficient buffering capacity of the aqueous phase, magnesium chloride at an ionic strength of 0.01 was mixed with monobasic and dibasic sodium phosphate solutions $Na_{3-x}H_xPO_4$ at an ionic strength of 0.1, giving an overall ionic strength of $I = 0.11$. In further measurements, the relative effect between the divalent magnesium Mg^{2+} and monovalent cations were investigated using aqueous solutions of LiCl, NaCl, and KCl, and CsCl, each mixed with monobasic and dibasic sodium phosphate at the constant overall ionic strength of $I = 0.11$. The crystal ionic radii as well as the hydrated radii of the cations investigated in this chapter are summarised in Table 8.1.

Cantilever arrays were coated with either mercaptohexadecanoic acid ($HS(CH_2)_{15}COOH$, herein termed MHA), or hexadecanethiol ($HS(CH_2)_{15}CH_3$, herein termed HDT). The differential signal, calculated as (MHA minus HDT signal), was attributed to specific surface stress changes due to the pH-induced deprotonation of the MHA SAM. Repeated measurements were acquired on four cantilever array samples, which are given in Table 8.1. However, these initial measurements were associated with substantive measurement variability. On the other hand, these observations established the basis for the important findings described

	Chip ID				
SAM	E15	E12	E13	105	**Totals**
$C_{16}COOH$	4 (3)	3	3 (1)	3 (2)	13 (9)
$C_{16}CH_3$	4 (2)	4	4 (3)	3 (2)	15 (11)
Totals	8 (5)	7	6 (5)	6 (4)	-

Table 8.2. Overview of the maximal number of cantilevers on the four cantilever arrays used to probe the effect of cations. The numbers in brackets correspond to the minimal numbers of cantilevers that were available in repeated measurements.

in Chapter 6, which facilitated the experiments presented in the following chapters to be performed and interpreted more adequately. Therefore in this chapter, measurements acquired on chip E15 are presented, which were performed under the most optimised conditions among the repeated measurements. However, the results obtained from the repeated measurements performed on the other cantilever arrays were found to be qualitatively consistent.

8.2 Results

8.2.1 Monovalent Cations

The effect of monovalent cations on the deprotonation specific differential stress was investigated in aqueous solutions comprising monobasic phosphate MH_2PO_4 and hydroxide MOH, where M equaled lithium, sodium, and potassium, at a constant ionic strength of $I = 0.1$.

To probe the onset of acid deprotonation, the cantilever array was exposed to pH 4.8/3.5/4.8 switch of, in turn, lithium phosphate/hydroxide, sodium phosphate/hydroxide, and potassium phosphate/hydroxide aqueous solutions. Fig. 8.1 shows typical raw differential signals obtained from the three measurements. When the pH of sodium phosphate/hydroxide solution was reduced from the reference

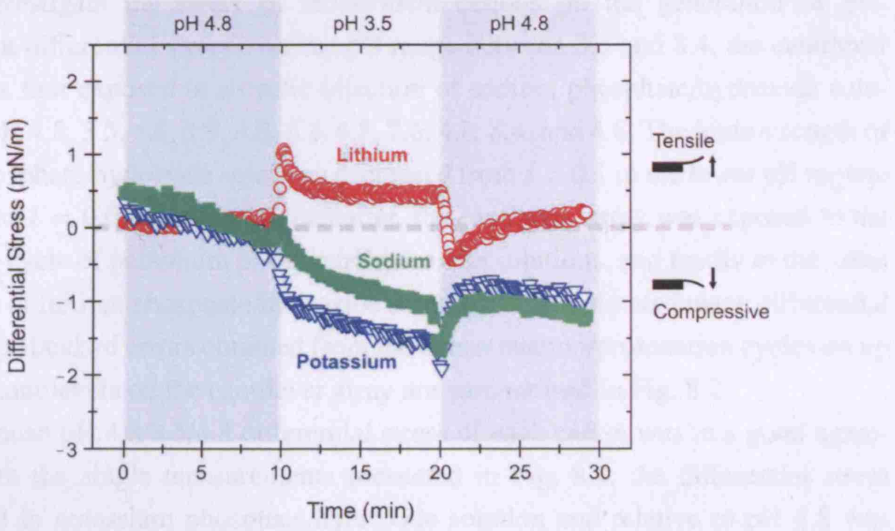

Fig. 8.1. Typical raw differential stress signals acquired upon pH 4.8/3.5/4.8 switch of lithium, sodium, and potassium phosphate/hydroxide solutions, respectively.

pH 4.8 to 3.5, a small compressive differential stress of −0.4 mN/m was measured. In the potassium solution, the magnitude of small compressive differential stress increased to −0.9 mN/m, whereas in the lithium solution, a tensile differential stress of +0.6 mN/m was measured. The differential signals returned toward the zero-stress baseline upon increasing the solution pH from 3.5 back to 4.8. These measurements suggested that a small, yet deprotonation-specific differential stress was generated at this low pH. This is an important result that suggested that the onset of the deprotonation of surface carboxylic acids occurred *below* the reference pH 4.8 employed throughout this work. Since the measurement of a deprotonation-induced differential stress should refer to the highest protonation state of surface carboxylic acids, the compressive differential stress of −0.4 mN/m measured upon the pH 4.8/3.5 switch of sodium solutions was in fact a *tensile* differential stress of +0.4 mN/m relative to pH 3.5. Likewise, the compressive differential stress of −0.9 mN/m measured in potassium solutions was a tensile differential stress of +0.9 mN/m measured relative to pH 3.5. Finally, the tensile differential stress of +0.6 mN/m measured in lithium solutions was a compressive differential stress of −0.6 mN/m measured relative to pH 3.5. Thus the deprotonation-induced compressive differential stress from pH 3.5 to 4.8 increased as $Li^+ > Na^+ > K^+$, that is, with crystal ionic radii of the three cations. Hereupon, the discussion of deprotonation-specific surface stress changes will be referred to the lowest pH and to the highest protonation state of surface carboxylic acids, that is, to the measurements performed at pH 3.5.

To investigate the effect of monovalent cations on the generation of pH-dependent differential stress over the pH range between 3.5 and 8.4, the cantilever array was first exposed to a cyclic injection of sodium phosphate/hydroxide solutions at pH 4.8, 3.5, 4.8, 5.9, 4.8, 6.8, 4.8, 7.6, 4.8, 8.4, and 4.8. The ionic strength of these phosphate/hydroxide solutions decreased from $I = 0.1$ in the lower pH regime by 0.01 to $I = 0.09$ at pH 8.4. Thereafter, the cantilever array was exposed to the same pH cycle of potassium phosphate/hydroxide solutions, and finally to the same pH cycle of lithium phosphate/hydroxide solutions. The estimated mean differential stress and standard errors obtained from the deprotonation/protonation cycles on up to eight cantilevers on the cantilever array are summarised in Fig. 8.2.

The mean pH 4.8/3.5/4.8 differential stress of each cation was in a good agreement with the single measurements presented in Fig. 8.1: the differential stress measured in potassium phosphate/hydroxide solution and relative to pH 4.8 was compressive and -1.4 ± 0.4 mN/m; the differential stress measured in sodium phosphate/hydroxide solution and relative to pH 4.8 was compressive and -0.5 ± 0.2

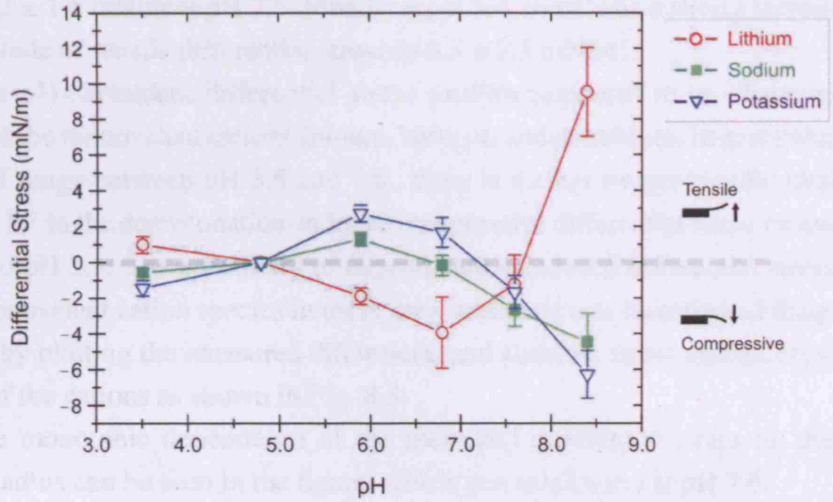

Fig. 8.2. Differential stress measured between pH 3.5 and 8.4. Each data point corresponds to the estimated mean and standard error obtained from deprotonation/protonation signals and up to eight cantilevers on chip E15.

mN/m; the differential stress measured in lithium phosphate/hydroxide solution and relative to pH 4.8 was tensile and 1.0 ± 0.5 mN/m.

Within the pH range from 5.9 to 8.4, the pH-dependence of measured sodium differential signals was qualitatively consistent with the data presented in the previous chapter in Fig. 7.2B. At pH 5.9, a tensile differential stress of 1.3 ± 0.4 mN/m was measured. Thereupon, the magnitude of measured compressive differential stress increased progressively with pH, that is, from −0.2±0.6 mN/m at pH 6.8, to −2.7±0.9 mN/m at pH 7.6, and finally to −4.4 ± 1.6 mN/m at pH 8.4. Thus the profile of pH-dependent differential stress observed in sodium phosphate/hydroxide solutions in this pH range can be characterised by the increase in the tensile differential stress from pH 4.8 to 5.9, and the progressive increase in the compressive differential stress from pH 5.9 to 8.4. A similar pH-dependent differential stress profile was observed in potassium phosphate/hydroxide solutions. At pH 5.9, the tensile differential stress increased further to 2.7 ± 0.5 mN/m. Thereupon, the magnitude of compressive differential stress increased with pH, that is, from 1.7 ± 0.8 mN/m at pH 6.8, to −1.7 ± 0.9 mN/m at pH 7.6, and finally to −6.3 ± 1.3 mN/m at pH 8.4. However, the pH-dependent profile of lithium differential stress was found to be strikingly different. There was an increase in the compressive differential stress from −1.9 ± 0.5 mN/m measured at pH 5.9 to −4.0 ± 2.0 mN/m at pH 6.8. Thereafter, there was a weak decrease in the magnitude of compressive differential stress

to -1.2 ± 1.6 mN/m at pH 7.6. Finally at pH 8.4, there was a strong increase in the magnitude of tensile differential stress to 9.5 ± 2.5 mN/m.

The pH-dependent differential stress profiles appeared to be characteristic to each of the monovalent cations lithium, sodium, and potassium. In particular, within the pH range between pH 3.5 and 7.6., there is a clear cation-specific trend $Li^+ > Na^+ > K^+$ in the deprotonation-induced compressive differential stress measured relative to pH 3.5. The specificity of deprotonation-induced differential stress toward the monovalent cation species in these measurements was investigated diagrammatically by plotting the measured differential and absolute stress against crystal ionic radii of the cations as shown in Fig. 8.3.

The monotonic dependence of the measured differential stress on the crystal ionic radius can be seen in the figure, which was minimised at pH 7.6.

The magnitude of the absolute COOH and CH_3 stress signals was found to be substantively larger than the corresponding differential signals. On going from pH 3.5 to 8.4, the magnitude of compressive absolute stress increased progressively. Interestingly, the absolute CH_3 stress revealed cation-specific effect, that is, $K^+ > Na^+ > Li^+$ in the order of increasing compressive absolute stress. This cation-specific effect was present in the full pH range between 3.5 and 8.4 relative to the lowest pH 3.5, and increased progressively with pH. This effect is most prominent at pH 7.6 as the cation-specific effect in the differential stress was minimised at this pH.

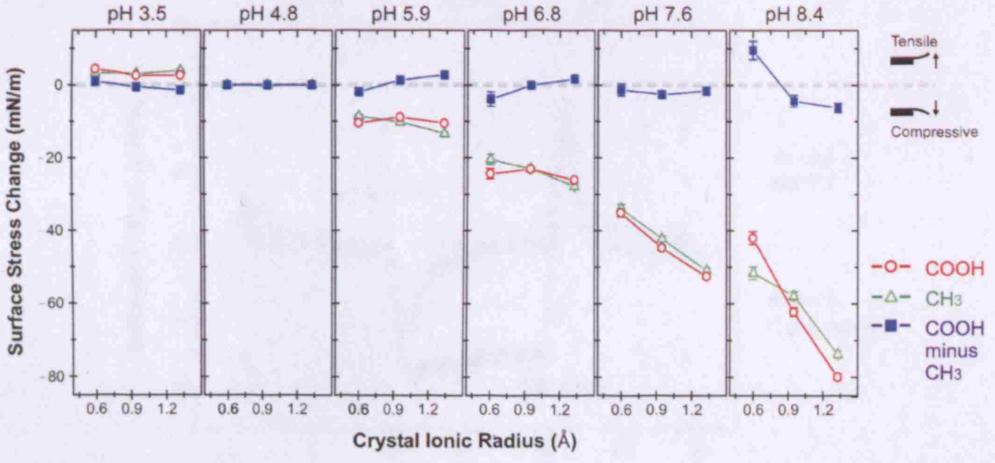

Fig. 8.3. Absolute and differential stress measured between pH 3.5 and 8.4 as a function of crystal ionic radii of lithium, sodium, and potassium. Each data point corresponds to the estimated mean and standard error obtained from deprotonation/protonation signals and up to eight cantilevers on chip E15

It is clear from these data that both the differential surface stress and the absolute surface stress exhibited cation-specific effects. The generation of absolute CH_3 stress was most likely to be independent of the deprotonation of surface carboxylic acids. However, a distinction between the different cation-specific effects is difficult. Consider, for example, the tensile differential lithium signal observed upon pH 4.8/8.4/4.8 switch. Was the tensile differential stress caused by an increased absolute COOH signal, or was it caused by a reduced absolute CH_3 signal?

8.2.2 Divalent Cations

To investigate the cation-specific effects in the generation of differential and absolute surface stress further, the cantilever array was exposed to pH 4.8/6.8/4.8 aqueous solutions comprising monobasic NaH_2PO_4 and dibasic Na_2HPO_4 sodium phosphate at a constant ionic strength of 0.1 that contained added caesium chloride CsCl at an ionic strength of 0.01. Subsequently, the cantilever array was exposed to pH 4.8/6.8/4.8 monobasic and dibasic sodium phosphate solutions that contained added magnesium chloride $MgCl_2$ at an ionic strength of 0.01. In both measurements, the overall ionic strength of the aqueous phosphate/chloride solutions was constant and $I = 0.11$. Typical raw differential signals acquired in the two measurements are shown in Fig. 8.4. As can be seen in the figure, there was a clear difference between

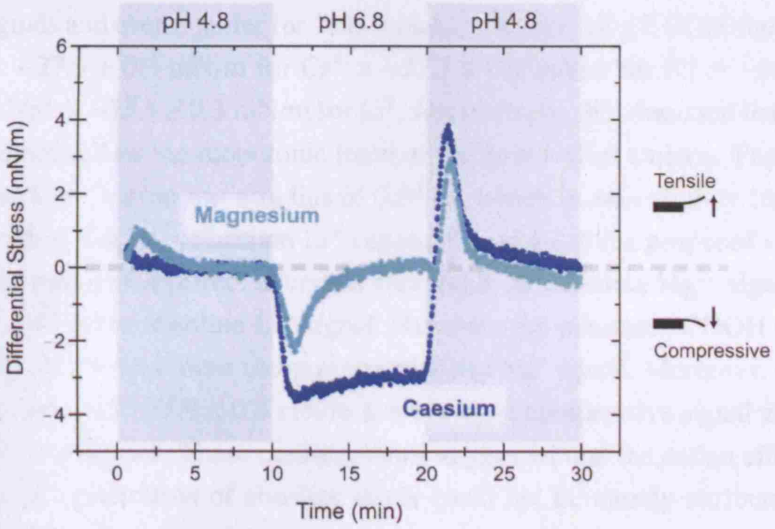

Fig. 8.4. Typical raw differential stress signals acquired upon pH 4.8/6.8/4.8 switch of phosphate buffers with added caesium and magnesium chloride salt, respectively.

the two measurements. The equilibrium differential stress measured upon increasing the solution pH from 4.8 to 6.8 was −2.7 mN/m in the sodium phosphate/caesium chloride solution, and −0.4 mN/m in the sodium phosphate/magnesium chloride solution. Upon decreasing the pH from 6.8 back to 4.8, the differential signals returned toward the zero-stress baseline.

To investigate if the difference in the cationic radius gave rise to the observed effect, the cantilever array was first exposed to successive pH 4.8/6.8/4.8 cycles of aqueous solutions comprising monobasic and dibasic sodium phosphate at an ionic strength of 0.1 that contained added chloride salt of, in turn, sodium Na^+, caesium Cs^+, and magnesium Mg^2+ cation at an ionic strength of 0.01. In a subsequent measurement, the cantilever array was exposed to successive pH 4.8/6.8/4.8 cycles of aqueous solutions comprising monobasic and dibasic sodium phosphate at an ionic strength of 0.1 that contained added chloride salt of, in turn, lithium Li^+, sodium Na^+, and potassium K^+ cation at an ionic strength of 0.01. Fig. 8.5 shows the estimated means and standard errors obtained from the deprotonation/protonation cycles of up to eight cantilevers probed in these measurements. The absolute COOH and CH_3 signals are shown in (A) and the corresponding differential signals are shown in (B), as a function of the crystal ionic radii of the cations.

The absolute equilibrium stress measured upon the pH 4.8/6.8/4.8 cycles was compressive. The diagram suggested a monotonic increase in the magnitude of compressive absolute stress signals with ionic radius, although this effect was small for COOH signals and even smaller for CH_3 signals. The following COOH signals were measured: -27.9 ± 0.3 mN/m for Cs^+ > -27.1 ± 0.3 mN/m for K^+ > -26.2 ± 0.2 mN/m for Na^+ > -25.1 ± 0.3 mN/m for Li^+. Interestingly, the measured magnesium signals did not follow the monotonic trend of the monovalent cations. The divalent magnesium Mg^{2+} cation has a radius of 0.65 Å, which is only slightly larger than the ionic radius 0.60 Å of lithium Li^+ cation. Therefore, if the proposed cation effect was attributed to the effect of crystal ionic radii, the absolute Mg^{2+} signal would be comparable to the absolute Li^+ signal. However, the measured COOH signal of -26.9 ± 0.3 mN/m was more compressive than the Na^+ signal. Moreover, the measured CH_3 signal of -25.9 ± 0.4 mN/m was the most compressive signal among all the cations investigated. These measurements suggested that the cation effect associated with the generation of absolute stress could not be merely attributed to the effect of crystal ionic radii of the cations.

The corresponding differential stress signals were -2.2 ± 0.5 mN/m for Li^+, -2.7 ± 0.4 mN/m for Na^+, -2.0 ± 0.5 mN/m for K^+, and -2.8 ± 0.5 mN/m for Cs^+.

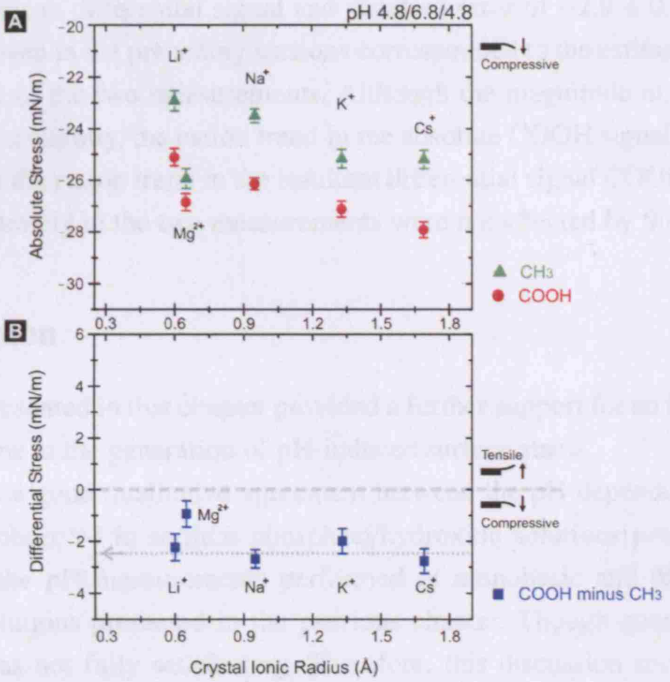

Fig. 8.5. (A) Absolute and (B) differential stress measured in pH 4.8/6.8/4.8 switch of phosphate buffers with added lithium, sodium, potassium, caesium, and magnesium chloride salt, respectively. Each data point corresponds to the estimated mean and standard error obtained from deprotonation/protonation signals and up to eight cantilevers on chip E15.

Thus the measured differential stress was not distinguishable within the associated standard errors, suggesting that the differential stress was generated independently of the monovalent cations present in the aqueous phase under these conditions, that is, at the low concentration of chloride relative to the concentration of sodium phosphate that acted as a 'background' buffer medium. However, the Mg^{2+} differential stress of -0.9 ± 0.5 mN/m differed substantively from the differential stress associated with the monovalent cations, as was already suggested in the single measurement presented in Fig. 8.4.

It should be noted that the repeated measurement of Na^+ signals in the two measurements served as an important control. In the first $Li^+/Na^+/K^+$ measurement, the estimated mean Na^+ signal and standard error was -26.6 ± 0.4 mN/m for COOH and -24.3 ± 0.4 mN/m for CH_3 terminated SAM, resulting in an estimated mean differential signal and standard error of -2.3 ± 0.6 mN/m. In the second $Na^+/Cs^+/Mg^{2+}$ measurement, the estimated mean Na^+ signal and standard error was -25.9 ± 0.3 mN/m for COOH and -23.0 ± 0.3 mN/m for CH_3 terminated SAM, resulting in

an estimated mean differential signal and standard error of -2.9 ± 0.4 mN/m. The Na^+ signals given in the preceding sections corresponded to the estimated mean and standard error of the two measurements. Although the magnitude of the measured signals differed slightly, the cation trend in the absolute COOH signal and CH_3 signal, as well as the cation trend in the resultant differential signal COOH minus CH_3, observed separately in the two measurements were not affected by this difference.

8.3 Discussion

The results presented in this chapter provided a further support for an important role of solution ions in the generation of pH-induced surface stress.

There was a good qualitative agreement between the pH dependence of differential stress observed in sodium phosphate/hydroxide solutions presented in this chapter and the pH measurements performed in monobasic and dibasic sodium phosphate solutions presented in the previous chapter. Though quantitatively, the agreement was not fully satisfactory. Therefore, this discussion section is subdivided into three parts. In the first part, we will apply the hydrogen bond attraction versus charge repulsion model directly to the differential data presented in this chapter and extend this model to include the observed cation-specific effects in the pH-triggered MHA surface stress. In the second part, we will investigate the causes of quantitative discrepancies observed in the different chapters. In the third part, we will discuss the cation-specific effects observed in the absolute signals.

The small differential stress observed at pH 3.5 suggested that the onset of the deprotonation of surface carboxylic acids occurred at a pH value below the reference pH 4.8. The magnitude of tensile sodium differential stress was found to increase on going from pH 3.5 to 5.9, which may reflect the increased number of ionic hydrogen bonds $COO^- \cdots COOH$ that replaced neutral hydrogen bonds $COOH \cdots COOH$ as the pH approached the surface $pK_{1/2}$.

In the pH range between 3.5 and 7.6, the deprotonation-induced tensile differential stress was found to increase as $K^+ > Na^+ > Li^+$. The crystal ionic radii of these monovalent cations increased, therefore the density of positive charge decreased in this order. The strength of the in-plane ionic hydrogen bond depended on the charge/dipole attraction between the negative charge of a deprotonated carboxylic acid and the dipole of an adjacent, protonated carboxylic acid. A strong binding of a cation to the negatively charged carboxylate ion thus reduced the strength of the in-plane ionic hydrogen bond. This is illustrated in Fig. 8.6.

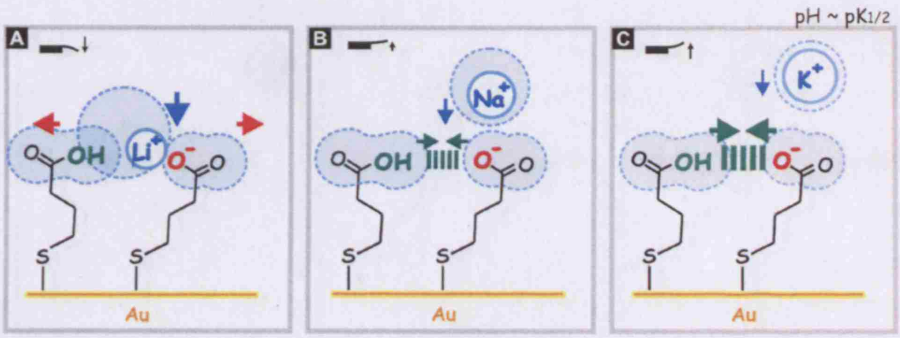

Fig. 8.6. Scheme to illustrate the proposed interactions in the intermediate pH regime close to the surface p$K_{1/2}$ between partially ionised and hydrated MHA SAM and hydrated (A) lithium, (B) sodium, and (C) potassium cations, respectively. The shaded areas illustrate hydrated radii of the cations and surface carboxylic acids.

The lithium cation was the smallest cation with the highest charge-to-radius ratio among the three cations investigated, which reduced the strength of in-plane attractive hydrogen bond most efficiently. In fact, the sign of stress inverted to give compressive differential stress. The high charge-to-radius ratio of lithium cation implied also its strong hydration, that is, a strong charge/dipole attraction between the lithium cation and the dipoles of adjacent water molecules. The steric (hard core) repulsion between the hydration shells of specifically bound lithium cations may be attributed to the observed compressive stress at the MHA/lithium solution interface. This was termed the 'repulsive hydration force' in Israelachvili's standard textbook (Israelachvili 1992). Conversely, the potassium cation with the lower charge density experienced a weaker charge/charge attraction to the negatively charged carboxylate ion than the sodium cation, which enhanced effectively the strength of the in-plane hydrogen bond hence the tensile differential stress.

The formation of neutral and ionic hydrogen bond between carboxylic acids and the role of hydration have been investigated by Meot-Ner, Elmore, and Scheiner (1999). For a range of different carboxylic acids at biological concentrations, they found that the formation of ionic hydrogen bonds between a deprotonated and a protonated carboxylic acid was favoured against their hydration, and reported associated energy gain in the order of 10^0 - 10^1 kcal/mol per bond. On the other hand, the hydration free energy of the three cations decreased as 117 kcal/mol for Li^+, 96 kcal/mol for Na^+, and 78 kcal/mol for K^+, according to Bates (1973) and the references therein. The hydration free energy reflects the ability of each cation to align the dipoles of adjacent water molecules with itself via the ion/dipole interaction

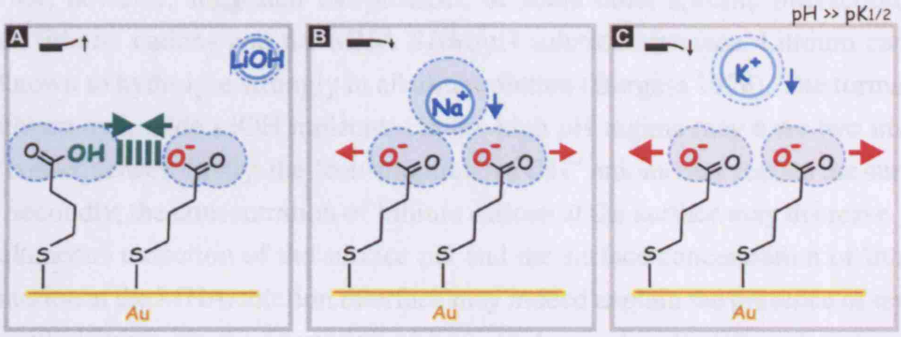

Fig. 8.7. Scheme to illustrate the proposed interactions in the high pH regime between hydrated MHA SAM and hydrated (A) lithium, (B) sodium, and (C) potassium cations, respectively.

and against the hydrogen bond network formed among the water molecules. Therefore, the difference in the hydration free energy of 21 kcal/mol between lithium and sodium may be sufficient to break the network of ionic hydrogen bond formed at the partially deprotonated MHA surface. Though the reported hydration free energies (Bates 1973) did not account for the ion/ion interactions or repulsive hydration forces expected at surface excess concentrations of electrolytes.

At the most basic pH 8.4 investigated herein, the largest fraction of surface carboxylic acids was deprotonated, yielding the highest density of negative charges at the MHA surface. The compressive differential stress observed in sodium solutions was attributed to the repulsive Coulomb force between the deprotonated negatively charged sites of the MHA surface. Therefore, the magnitude of compressive differential stress was expected to increase with decreasing charge/charge attraction between a cation and the deprotonated MHA surface, that is, with the crystal ionic radii of the three cations as $K^+ > Na^+ > Li^+$. This is illustrated in Fig. 8.7.

The proposed model for the high pH regime was in a good qualitative agreement with the observed surface stress. Although the effect of $K^+ > Na^+$ was small in the presented data, repeated measurements showed a qualitatively consistent trend. Moreover, this is consistent with the $NH_4^+ > Na^+$ data presented in the previous chapter. The cause of the tensile differential stress observed in lithium solutions was less obvious. Again, repeated measurements produced qualitatively consistent results. If the observed compressive differential stress in the intermediate pH regime was due to the steric repulsion between hydrated and specifically bound lithium cations, then we would expect a monotonically increasing compressive differential stress with pH. The inversion of the sign of differential stress between pH 6.8

and 8.4, however, suggested the presence of some other specific interaction between lithium cations and the MHA SAM/pH solution interface. Lithium cations are known to hydrolyse strongly in alkaline solution (Burgess 1978). The formation of lithium hydroxide LiOH molecules in the high pH regime may have two important consequences: firstly, the 'consumption' of OH^- anions may reduce the surface pH. Secondly, the concentration of lithium cations at the surface may decrease. The simultaneous reduction of the surface pH and the surface concentration of lithium counterion at the MHA/solution interface may indeed explain the presence of tensile differential stress via the formation of ionic hydrogen bonds, although at present, this is rather speculative. Future work will investigate the origins of lithium signals using mixed electrolytes at different ionic strengths and in different pH regimes.

The strong specific binding of divalent magnesium counterions was demonstrated in the second experiment. The compressive differential stress observed in monobasic/dibasic sodium solutions and added sodium chloride at pH 4.8/6.8 was attributed to the charge/charge repulsion between deprotonated negatively charged sites of the MHA surface, in agreement with the pH measurements presented in the previous chapter. Since at pH 6.8, the contribution of sodium cations was about eight-fold higher than the contribution of magnesium cations to the overall solution ionic strength of $I = 0.11$, the specific binding of magnesium cations can be expected to be hindered by the presence of excess sodium cations to some extent. Yet the observed reduction of the magnitude of compressive differential stress to about 50% of the corresponding differential stress generated by the monovalent cations suggested that the specific binding of divalent cations was strongly favoured. This is illustrated in Fig. 8.8. Based upon the simple argument of cationic valency divided by crystal ionic radius, the density of positive charge is almost two-fold higher in magnesium cations than in lithium cations. Therefore, the observed effect of the divalent magnesium cation may be attributed to the strong charge/charge attraction between the negatively charged sites of the MHA surface and the magnesium cations, resulting in the reduction of compressive differential stress. The strong charge screening effect by divalent cations compared with monovalent cations is consistent with the widely accepted literature findings (Israelachvili 1992).

The discussion so far allowed us to extend the hydrogen bond versus charge repulsion model to include the cation-specific effects. Although the measurement variability was discussed in detail in Chapter 6, quantitative consistency between the different pH measurements presented in the different chapters was non-satisfactory. This concerned primarily the small effect between potassium and sodium compared

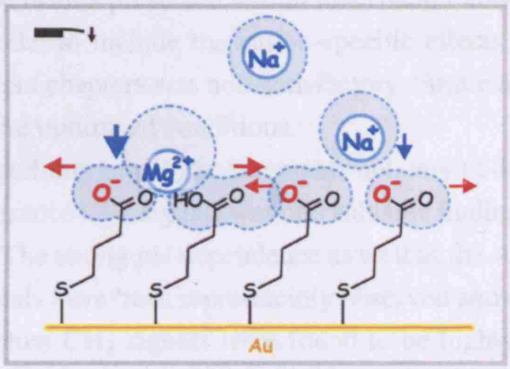

Fig. 8.8. Scheme to illustrate the proposed interactions at pH 6.8 between hydrated MHA SAM and hydrated magnesium and sodium cations.

with the effect between ammonium and sodium observed in the previous chapter, which will be discussed in some detail in the following section.

The discrepancy may be attributed to multiple causes: firstly, the sample probed in this chapter appeared to be aged or contaminated, due to extended storage and repeated use. The control pH 4.8/8.4 measurement in monobasic and dibasic sodium phosphate performed on this sample resulted in low differential signals ~−9 mN/m, compared with ~−15 mN/m obtained usually in measurements performed under optimised conditions. Repeated measurements on the three further cantilever arrays showed qualitatively consistent cation-specific effects, though the variability of these initial measurements was substantive. Secondly, the sample probed in the ammonium/sodium experiment was strongly deformed, with large sum changes and possibly altered mechanical properties of the cantilevers. The magnitude of systematic error associated with this sample is unknown at present. Thirdly, the ammonium/sodium experiment probed pH 4.5/9.0 change, thus the change in pH was 0.9 pH units larger than the cation experiment presented in this chapter. Fourthly, the effect of non-constant ionic strength on the pH-dependent solution ion concentration. In the mono/dibasic phosphate used in the ammonium/sodium experiment, the concentration of monovalent cation decreased from 0.10 M at pH 4.8 to 0.07 M at pH 8.4 at a constant ionic strength of $I = 0.1$. The concentration of monovalent cation in the phosphate/hydroxide solution used in this chapter decreased from 0.10 M at pH 4.8 to 0.06 M at pH 8.4, thereby the ionic strength of the solution decreased progressively from 0.1 at pH 4.8 to 0.09 at pH 8.4. All these effects will reduce the magnitude of compressive differential stress measured in the high pH

regime. Although the results presented within this chapter allowed us to extend our charge repulsion model to include the cation-specific effects, quantitative consistency between different chapters was non-satisfactory. Future measurements will be performed under more optimised conditions.

The good reproducibility of pH measurements not only of differential signals but also the absolute reference CH_3 signals was one valuable finding acquired during the course of this work. The strong pH dependence as well as the substantive magnitude of absolute CH_3 signals have been reproducibly observed and of particular interest. In this chapter, absolute CH_3 signals were found to be highly sensitive to cations in the aqueous phase. In fact, the absolute CH_3 signals were *more* sensitive than the corresponding differential signals. Both experiments found that the compressive absolute CH_3 signals increased with the ionic radii of monovalent cations, that is, as $K^+ > Na^+ > Li^+$ in the first experiment, and as $Cs^+ > K^+ > Na^+ > Li^+$ in the second experiment. Moreover, the pH measurements showed that this cation specific effect was also strongly dependent on the pH. This suggested that the cation effect and the pH effect were correlated.

A change in absolute stress can be caused at the upper cantilever surface or at the lower surface, and it is not possible to distinguish directly between the two surfaces. While the important role of the upper SAM-functionalised and gold-evaporated surface in the generation of absolute surface stress will be investigated in the following two chapters, the following sections discuss possible contributions arising from the lower cantilever surface, which comprised the native silicon oxide layer SiO_2.

When the surface of a silicon oxide SiO_2 is exposed to water, the chemisorption of water molecules yields the formation of surface silanol groups –SiOH. According to a comprehensive review provided by Parks (1965), the isoelectric point of a hydrous silicon oxide surface, which is the pH value at which the surface charge becomes zero, is 2.0 ± 0.2. Parks gives two primary surface ionisation/dissociation reactions that give rise to the formation of electric charges at the surface of a hydrous silicon: firstly, the amphoteric dissociation of surface –SiOH groups. Secondly, the amphoteric dissociation of $Si(OH)_4(aq)$ from the oxide surface.

The solubility of SiO_2 has been investigated extensively over the past decades,[1] and the monosilicic acid $Si(OH)_4$ is widely accepted today as the hydrated form of silica (Dove, Nizhou, and de Yereo 2005; House and Orr 1992). Early studies have reported $pK_{1/2}$ values of 9 - 10 for the acid/base reaction of the monosilicic acid (Alexander, Heston, and Iler 1954; Greenberg and Price 1957; van Lier, de Brun,

[1] The earliest publication cited by Alexander, Heston, and Iler (1954) dated back to 1855.

and Overbeek 1960). Therefore the corrosion of silica-based glasses increases progressively over the pH range from 2 to 12, and very strongly in the high pH regime (Bates 1973). It should be noted that the functionality of commercial pH meters rely on the change in the activity of hydrogen ions due to acid/base reactions of silicic acids present at the hydrated surfaces of silica glass membranes.[2] Although the amorphous structure of silica glass implies the substantive permeability toward solution ions and solvent molecules, surface ionisation and dissociation reactions that can take place at the aqueous phase/SiO_2 interface can be expected to be identical in both materials. Therefore, it would be rather surprising if the native dioxide SiO_2 layer of the bulk cantilever material did not respond to a change in pH. We propose that the storage in pH 4.8 phosphate solutions at a time constant of several days to months resulted in the formation of hydrous silicon oxide SiO_2 layer (Parks 1965) at the cantilever underside. The strong pH dependence of the absolute CH_3 signals may be correlated with the dissolution of $Si(OH)_4(aq)$ from the cantilever underside, which may be regarded as a *negative* adsorption, giving rise to a large *tensile* surface stress change. Moreover, a non-reversible dissolution of the cantilever underside material would be consistent with the pH-dependent downward drift of the cantilevers, giving rise to the hysteresis in the generation of absolute signals. For example, the hysteresis measured upon pH 4.8/8.4/4.8 switch was about −20 mN/m both in Fig. 9.1A and in Fig. 10.2A. In fact, the strongest drift, highest hysteresis, and highest uniformity among different cantilevers was observed on fresh samples, whereas the magnitude of these properties decreased with their repeated use. This may reflect the reactivity of a hydrous SiO_2 layer.

Subject to these considerations, the observed cation-specific effect $K^+ > Na^+ > Li^+$ in the order of increasing absolute CH_3 signals would imply an enhanced solubility of the hydrous oxide layer with increasing radii of monovalent cations. Glembocki et al. (1991) have investigated the effect of the molarity of KOH on the etch rate, or equivalently on the solubility, of silicon single crystals including Si(100), and reported a constant etch rate in the order of 10 nm/min between 0.1 M and 2 M at 23 °C. They investigated further the effect of NaOH and LiOH on the etch rate, and observed an increased molarity dependence in the order of LiOH > NaOH > KOH. Glembocki et al. argued that the etch rate increased with the concentration of OH^- ions and free, non-hydrating H_2O molecules. Based upon the literature activity coefficients, they proposed a model that correlate the hydration numbers of the alkali hydroxides, which decreased as LiOH > NaOH > KOH, with the observed

[2] Mettler-Toledo, Essex, England. A guide to pH measurement (1992).

increase in the etch rate of the silicon single crystals. Note that the identical order gives the tendency of the corresponding alkali cations to hydrolyse in the high pH regime, an argument we used above to rationalise the lithium differential signals.

At the first sight, Glembocki et al.'s studies appeared to show an opposite cation effect to our silicon dissolution model. However, the salt effect that was described first successfully by Brønsted (1923) is highly specific to both the cations and anions involved. In fact, the activity coefficient according to Robinson and Stokes (1949) decreases as LiOH > NaOH > KOH for alkali hydroxides, however, most of the salts reported, including monobasic phosphates and chlorides, exhibit the *opposite* trend. For example, the activity coefficient increases as LiCl > NaCl > KCl. The cation dependent trend of the activity coefficients appears to hold even in the high molarity range between 3 M and 6 M, which corresponds to the range of surface ionic strengths corresponding to the typical ionic strength of $I = 0.1$ used in this work (Harding et al. 2006). We may therefore apply Glembocki et al.'s hydration model to the observed cation effect in absolute CH_3 signals and indeed attribute the increased solubility of the cantilever underside material with increasing radii of monovalent cations $K^+ > Na^+ > Li^+$ in aqueous solutions of phosphates and chlorides. The effect of enhanced lithium hydrolysis in the high pH regime would then be to increase the compressive magnitude of absolute signals. In fact, the absolute CH_3 signal measured at pH 8.4 in lithium solutions appeared to be more compressive than expected, based upon the linear extrapolation of the strong dependence between sodium and potassium observed at pH 8.4, and the linear trend observed at pH 7.6.

Recently, Dove, Nizhou, and de Yereo (2005) proposed that the salt effect on the dissolution of quartz and silicate may be predicted by the theory of crystal growth. Cantilever arrays may be employed to probe this model. Future work will further investigate the origins of absolute signals in pH measurements, including the role of divalent cations and the effect of the activity of solution ions, as well as contributions from the SAM functionalised and gold evaporated upper cantilever surface.

8.4 Conclusion

The systematic pH measurements presented in this chapter enable specific effects of monovalent and divalent cations to be included in the model of pH-induced surface stress. Cationic counterions with high charge-to-radius diameter bind strongly at the partially deprotonated, carboxylic acid terminated surface and reduce the strength

of attractive charge/dipole hydrogen bond forces, charge/charge repulsion between negatively charged deprotonated sites, and generate repulsive hydration forces. The strong pH and cation specific effects observed in the absolute signals are rather unexpected. These specific effects may be attributed to the negative adsorption at the cantilever underside, that is, the dissolution of the hydrous silicon oxide surface. The crystal growth theory may be applied to investigate these observations in future.

9. Effect of SAM Terminal Functionality

9.1 Introduction

The model of pH-induced surface stress at the carboxylic acid terminated surface of mercaptohexadecanoic acid (MHA) self-assembled monolayers (SAMs) described in the previous chapters includes attractive in-plane forces associated with ionic hydrogen bond formation at the apparent surface $pK_{1/2}$, the electrostatic repulsion between deprotonated carboxylic acid groups at elevated pH, as well as specific binding of counterions to screen the in-plane electrostatic interactions and to generate repulsive hydration forces. While our studies so far have focused on the role of the aqueous environment, that is, pH, ionic strength, and monovalent and divalent counterions, the terminal functional group of SAMs determines the specific interfacial chemical reactions and therefore was expected to play an important role in the generation of pH-induced surface stress. For example in a basic aqueous environment, an acidic, carboxylic acid terminal group can provide a proton to lower the pH of the adjacent aqueous phase. Conversely in an acidic aqueous environment, a basic, amine terminal group can withdraw a proton to raise the pH of of the adjacent aqueous phase. The pH-induced surface stress may also depend on the hydrophilicity of the terminal group, such as the hydrophilic, hydroxyl terminal group and the hydrophobic methyl terminal group. Therefore the aim of this chapter was to investigate the effects of the SAM terminal functionality in the generation of pH-induced surface stress.

Each pair of cantilevers on a cantilever array was functionalised with one of the following four *n*-alkanethiol SAMs: (1) 11-mercaptoundecanoic acid $HS(CH_2)_{10}COOH$, (2) 11-amino-1-undecanethiol $HS(CH_2)_{11}NH_2$, (3) 11-hydroxy-1-undecanethiol $HS(CH_2)_{11}OH$, and (4) 1-undecanethiol $HS(CH_2)_{10}CH_3$. These thiols comprise eleven carbon atoms C_{11} with almost identical chain lengths $n-1 = 10$ or 11, and differ in the terminal functional group, that is, carboxylic acid COOH, amine NH_2, hydroxyl OH, and methyl CH_3 terminal group, respectively. Throughout this chapter, these SAMs will be termed according to their terminal functional

SAM	Chip ID				Totals
	I07	M18	L21	G23	
$C_{11}COOH$	2	0	2	2	6
$C_{11}NH_2$	2	2	2	2	8
$C_{11}OH$	2	2	2	2	8
$C_{11}CH_3$	2	2	1	1	6
Totals	8	6	7	7	28

Table 9.1. Overview of cantilevers on the four cantilever arrays used to probe the effect of SAM terminal functionality.

group. Long chain, high purity C_{16} SAMs with these terminal groups were not commercial available therefore C_{11} thiols were used instead. This design allowed all four terminal functionalities to be probed in parallel under similar experimental conditions, and moreover, the measurement of between-cantilever variability. The between-array variability was probed by preparing three further cantilever array samples with the same C_{11} SAM coatings. An overview of the cantilevers on the four cantilever arrays is given in Table 9.1.

9.2 Results

To investigate the effects of the terminal group of SAMs in the generation of pH-induced surface stress, cantilevers were exposed alternately to sodium phosphate $Na_{3-x}H_xPO_4$ solutions at pH 4.8, 3.5, 4.8, 5.9, 4.8, 6.8, 4.8, 7.6, 4.8, 8.4, and 4.8, and at a constant ionic strength of $I = 0.1$.

Fig. 9.1A shows typical raw absolute stress signals measured upon a pH 4.8/8.4/4.8 switch on four cantilevers, each functionalised with carboxylic acid COOH, amine NH_2, hydroxyl OH, and methyl CH_3 terminated C_{11} SAMs. The increase in the pH from 4.8 to 8.4 induced a compressive surface stress change on the four cantilevers. The absolute deprotonation signal acquired on the cantilever coated with methyl terminated, reference SAM was −43.5 mN/m upon equilibration. Relative to the reference deprotonation signal, the deprotonation signal of carboxylic acid terminated SAM was more compressive −52.3 mN/m, the deprotonation signal of amine terminated SAM was more tensile −34.5 mN/m, and the deprotonation signal of hydroxyl terminated SAM was close to the reference methyl signal −42.0 mN/m. When the pH was switched back to 4.8, all cantilevers bent upward

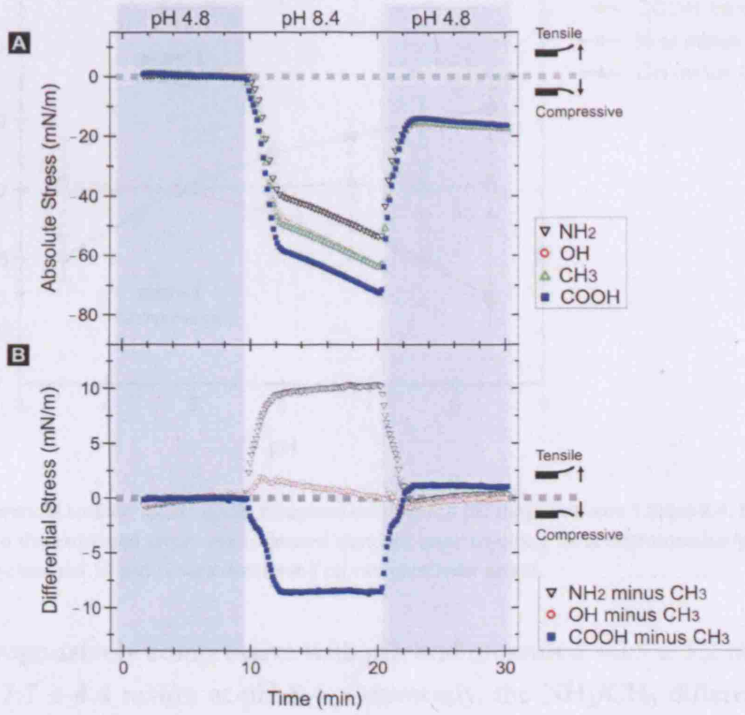

Fig. 9.1. Typical raw stress signals measured upon a pH 4.8/8.4/4.8 switch to probe the effect of SAM terminal group. (A) Absolute COOH, NH_2, OH, and CH_3 stress signals and (B) resultant differential stress signals, calculated as COOH minus CH_3, NH_2 minus CH_3, and OH minus CH_3, respectively.

toward the zero-stress baseline. The corresponding differential signals are shown in Fig. 9.1B. The following equilibrium, differential deprotonation signals were measured: a compressive $COOH/CH_3$ differential stress of −8.7 mN/m, calculated as COOH minus CH_3; A tensile NH_2/CH_3 differential stress of +9.0 mN/m, calculated as NH_2 minus CH_3; A small tensile OH/CH_3 differential stress of +1.5 mN/m, calculated as OH minus CH_3.

Fig. 9.2 shows the $COOH/CH_3$, NH_2/CH_3, and OH/CH_3 differential stress signals acquired over the full pH range between 3.5 and 8.4. Each data point represents the estimated mean and standard error obtained from the deprotonation and protonation signals measured over up to three consecutive pH cycles and on a total of 14 cantilevers distributed on chip I07 and M18. Chip L21 and G23 were excluded from the statistical analysis due to evidences of substantive systematic error as discussed in Chapter 6, although the measured differential data were qualitatively consistent. The progressive increase in the solution pH from 3.5 to 8.4 resulted in a monotonic trend in the estimated mean differential stress. The $COOH/CH_3$ differential stress

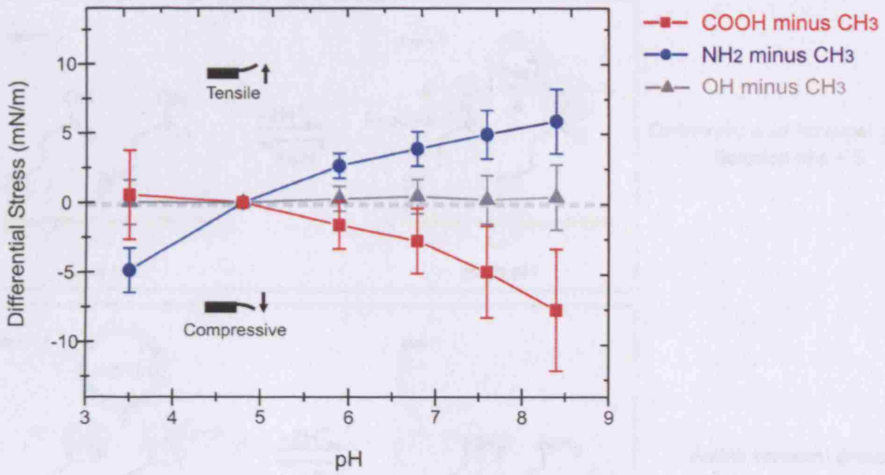

Fig. 9.2. Differential surface stress signals measured over the full pH range between 3.5 and 8.4. Each data point corresponds to the estimated mean and estimated standard error resulting from deprotonation/protonation, up to three pH cycles, and 14 cantilevers distributed on two cantilever arrays.

became progressively compressive with pH, and measured +0.5 ± 3.2 mN/m at pH 3.5 and −7.7 ± 4.4 mN/m at pH 8.4. Conversely, the NH_2/CH_3 differential stress was compressive −5.2 ± 0.1 mN/m at pH 3.5, rendered tensile +3.1 ± 0.4 mN/m at pH 5.9, and finally +7.8 ± 1.5 mN/m at pH 8.4. The OH/CH_3 differential stress was tensile and depended only weakly on pH, that is, +0.2 ± 0.1 mN/m at pH 3.5 and +1.5 ± 1.5 mN/m at pH 8.4. The large relative standard errors associated with the $COOH/CH_3$ differential signals were generated by I07. Unfortunately, no cantilever coated with COOH terminated SAM was available on chip M18 that generated particularly small relative standard errors.

9.3 Discussion

The results presented in this chapter suggested an important role of the terminal functionality of SAMs in the generation of pH-dependent surface stress. The pH-dependence of the measured differential stress was consistent with the expected pH-dependent deprotonation state of the SAM terminal groups, which provided a further support for the chemical specificity of these measurements. Fig. 9.3 shows a scheme of the model for the four different terminal groups, that is, (A) carboxylic acid COOH, (B) amine NH_2, (C) hydroxyl OH, and (D) methyl CH_3 terminal group. The observed $COOH/CH_3$ differential stress was qualitatively consistent with the re-

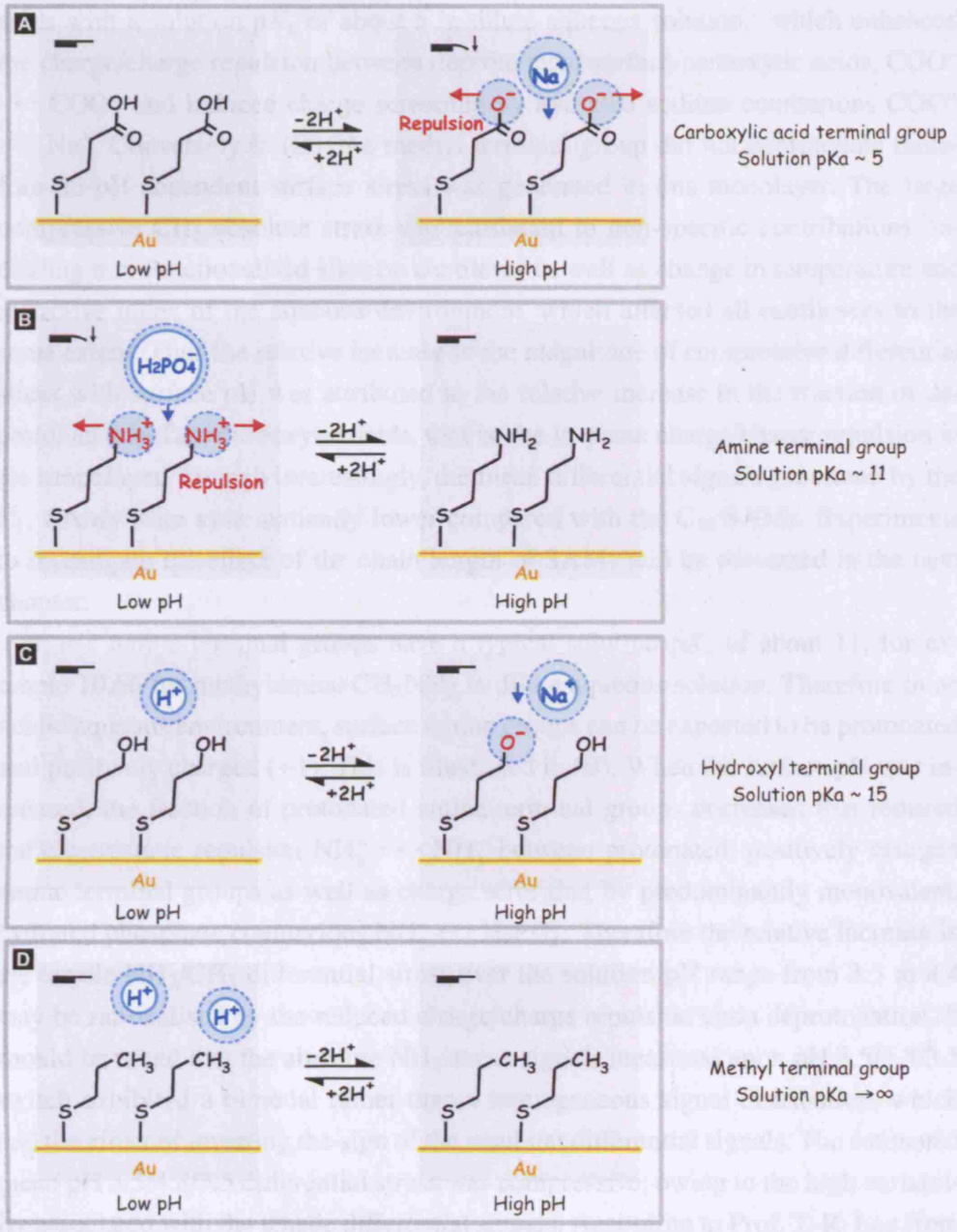

Fig. 9.3. Scheme to show the pH-dependent charge-repulsion model for (A) COOH, (B) NH_2, (C) OH, and (D) CH_3 terminal groups, respectively. The pK_a values given on the right were taken from the *CRC Handbook of Chemistry and Physics*, 86th ed., 2005.

sults presented in Chapter 7. As illustrated in (A), the progressive increase in the solution pH from 3.5 to 8.4 increased the fraction of deprotonated surface carboxylic

acids with a solution pK_a of about 5 in dilute aqueous solution,[1] which enhanced the charge/charge repulsion between deprotonated surface carboxylic acids, COO^- $\cdots$ COO^- and induced charge screening by hydrated sodium counterions COO^- $\cdots$ Na^+. Conversely in (D), the methyl terminal group did not deprotonate therefore no pH-dependent surface stress was generated in this monolayer. The large compressive CH_3 absolute stress was attributed to non-specific contributions, including non-functionalised sites on cantilever as well as change in temperature and refractive index of the aqueous environment, which affected all cantilevers to the same extent. Thus the relative increase in the magnitude of compressive differential stress with surface pH was attributed to the relative increase in the fraction of deprotonated surface carboxylic acids, that is, the in-plane charge/charge repulsion in the monolayer. Though interestingly, the mean differential signals generated by the C_{11} SAMs were systematically lower compared with the C_{16} SAMs. Experiments to investigate the effect of the chain length of SAMs will be presented in the next chapter.

Basic amine terminal groups have a typical solution pK_a of about 11, for example 10.66 for methylamine CH_3NH_2 in dilute aqueous solution. Therefore in an acidic aqueous environment, surface amine groups can be expected to be protonated and positively charged (+1). This is illustrated in (B). When the surface pH was increased, the fraction of protonated amine terminal groups decreased that reduced the electrostatic repulsion NH_3^+ $\cdots$ NH_3^+ between protonated, positively charged amine terminal groups as well as charge screening by predominantly monovalent, hydrated phosphate counterions NH_3^+ $\cdots$ $H_2PO_4^-$. Therefore the relative increase in the tensile NH_2/CH_3 differential stress over the solution pH range from 3.5 to 8.4 may be rationalised by the reduced charge/charge repulsion upon deprotonation. It should be noted that the absolute NH_2 stress signals measured upon pH 3.5/4.8/3.5 switch exhibited a bimodal rather than a homogeneous signal distribution, which had the effect of inverting the sign of the resultant differential signals. The estimated mean pH 3.5/4.8/3.5 differential stress was compressive, owing to the high variability associated with the tensile differential signals. According to Prof. T. R. Lee from the University of Houston, a synthetic chemist and former member of Whitesides's research group, amine terminated SAMs were particularly prone to contamination thus the quality of these SAMs was inherently poor. This may explain the relatively

[1] All pK_a values quoted in this work were taken from the *CRC Handbook of Chemistry and Physics*, 86th ed., 2005.

low popularity of these SAMs in the literature, despite the simple molecular structure. At present, there is no plausible explanation of this observation.

The hydroxyl terminal groups deprotonate only at very high pH values of about $pK_a \sim 15$ in dilute aqueous solution. Within the solution pH range between 3.5 and 8.4 investigated herein, the hydroxy terminal group can be expected to be, if at all, only weakly charged. This is illustrated in (C). According to our model, the differential OH/CH_3 stress is expected to be close to zero, which is indeed consistent with the data. Thus the difference in the hydrophilicity of the SAMs alone appeared not to trigger substantive differential surface stress. Although, the mean differential stress appeared to become weakly tensile with pH. One may therefore speculate that the tensile differential stress was generated by the formation of in-plane hydrogen bonds in the partially deprotonated hydroxy terminated SAM as the surface pH approached its surface $pK_{1/2}$. However, the associated standard errors were in the same order of magnitude as the estimated mean values. Moreover, the difference in the chain length, that is, $n - 1 = 11$ for hydroxy terminated SAM and $n - 1 = 10$ for the reference methyl terminated SAM, may give rise to subtle effects. Future experiments will extend the pH range to probe the surface $pK_{1/2}$ of hydroxy terminated SAMs.

The findings presented in this chapter are in a good qualitative agreement with literature surface titration studies that probed acidic and basic SAMs in aqueous environments. For example, in the chemical force microscopy work reported by Vezenov et al. (1997), the out-of-plane adhesion forces between tip and sample were found to be specific to the expected, pH-dependent deprotonation state of the carboxylic acid and amine terminated SAMs, whereas the adhesion forces measured using hydroxyl or methyl terminated SAMs did not depend on the surface pH. In the contact angle goniometry reported by Lee et al. (1994), the pH-dependent wettability of a range of different acidic and basic SAMs was investigated, which found the wettability again to be specific to the expected deprotonation state of the SAM terminal groups. Though the measurement of specific in-plane attractive and repulsive forces generated by SAMs themselves is a unique capability of cantilever arrays, without liquid confinement effect associated with the Chemical Force Microscopy or the presence of a three-phase boundaries associated with the contact angle goniometry. The complexity of the three-phase boundaries was also pointed out by Prof. C. D. Bain from the University of Durham, who has performed pioneering contact angle experiments on SAMs with Whitesides.

9.4 Conclusion

To conclude, the terminal functional group of SAMs plays an important role in the generation of pH-induced differential surface stress. The profile of pH-induced differential stress depends on the acid/base properties of the SAM terminal functionality, which provides a further support of the chemical specificity of these measurements. The sign and magnitude of differential surface stress is consistent with the model proposed in the preceding chapters. Our findings confirm the importance of the judicious choice of the reference terminal group and the use of multiple cantilevers to probe the chemically specific surface stress signals.

10. Effect of SAM Chain Length

10.1 Introduction

Our cantilever array studies have so far shown the important role of the pH, the cations and anions in the aqueous solution, and the terminal functionality of self-assembled monolayers (SAMs) in the generation of pH-induced differential stress at the SAM/aqueous solution interface. The reduced magnitude of the differential stress generated by C_{11} SAMs observed in the previous chapter compared with the initial measurements that employed C_{16} SAMs appeared to be related to the chain length of the SAMs. Therefore, the aim of this chapter was to systematically investigate the effect of the SAM chain length.

Equilibrium surface stress, as measured by cantilevers, is the in-plane component of balanced forces acting at the interface between the aqueous phase, the SAM, and the gold film, which are transduced onto the bulk cantilever material. The alkyl chains of SAMs comprise an intermittent phase between the aqueous phase and the solid phase, which have the role of transducing the in-plane forces from one interface to another. Therefore, the alkyl chains of SAMs can be expected to play a key role in the generation of surface stress. The role of alkyl chain length in the generation of surface stress has been previously investigated by Berger et al. (1997) and Godin et al. (2004b). Though these experiments focused on the surface stress generated during the SAM formation, and moreover the results have been subject to controversy: while Berger et al. reported a linear relation between the surface stress and chain length, Godin et al. found that the surface stress was independent of chain length. The aim of this chapter was therefore to investigate the effect of alkyl chain lengths on the generation of surface stress specific to the deprotonation of carboxylic acid terminated SAMs.

To investigate the effect of chain length of *n*-alkanethiols on the generation of surface stress, cantilevers were coated with carboxylic acid COOH and methyl CH_3 terminated SAMs of different alkyl chain lengths, that is, $n - 1 = 2, 7, 10$, and 15. A total of six cantilever arrays were prepared, each of which had two cantilevers

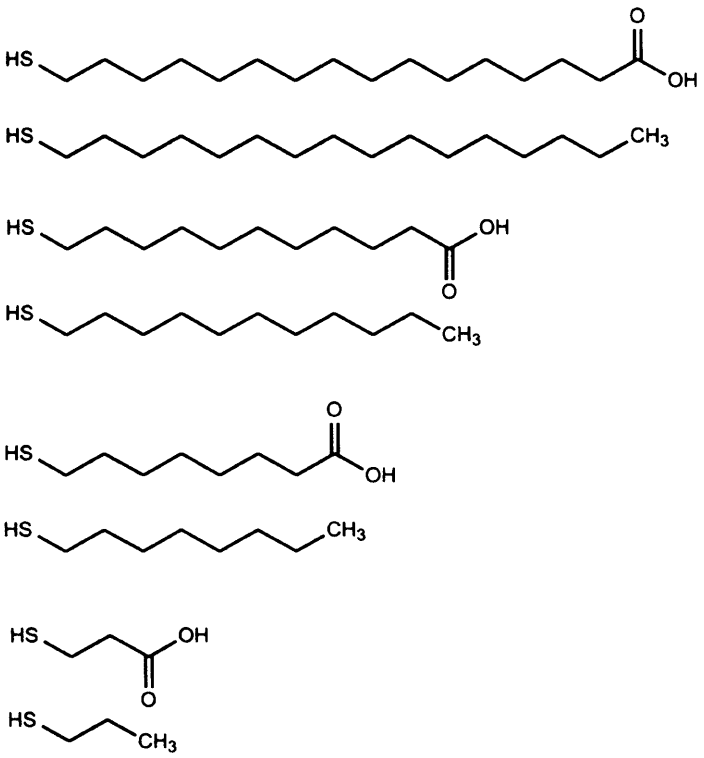

Fig. 10.1. Scheme to show the chemical structure of alkanethiol molecules used in this chapter to probe the chain length effect. Note that for each molecule, the topmost label on the right is a simplified, abbreviated term used herein.

	Chip ID						
SAM	J08	J18	J06	G16	J05	H14	**Totals**
C_3COOH	2	2	0	0	0	0	4
C_3CH_3	2	2	0	0	0	0	4
C_8COOH	0	0	2	1	0	0	3
C_8CH_3	0	0	2	2	0	0	4
$C_{11}COOH$	0	0	0	0	2	2	4
$C_{11}CH_3$	0	0	0	0	2	2	4
$C_{16}COOH$	1	2	2	1	2	2	10
$C_{16}CH_3$	2	2	1	2	2	2	11
Totals	7	8	7	6	8	8	44

Table 10.1. Overview of cantilevers on the six cantilever arrays used to probe the chain length effect.

coated with 16-mercaptohexadecanoic acid $HS(CH_2)_{15}COOH$, and two cantilevers coated with 1-hexadecanethiol $HS(CH_2)_{15}CH_3$. Throughout this chapter, SAMs will be termed C_nX, that is, according to the total number of carbon atoms n and the terminal functional group X of the SAMs. For example, mercaptohexadecanoic acid was termed MHA in other chapters and $C_{16}COOH$ in this chapter, and hexadecanethiol was termed HDT in other chapters and $C_{16}CH_3$ in this chapter. These C_{16} SAMs were characterised in detail in the preceding chapters and served also as a major control. The remaining four cantilevers on each cantilever array were coated with SAMs of shorter chain lengths as follows: two cantilevers were coated with 3-mercaptopropionic acid $HS(CH_2)_2COOH$ (termed C_3COOH in this chapter), and two with 1-propanethiol $HS(CH_2)_2CH_3$ (termed C_3CH_3 in this chapter) on two cantilever arrays J08 and J18, respectively. Two cantilevers were coated with 8-mercaptooctanoic acid $HS(CH_2)_7COOH$ (termed C_8COOH in this chapter), and two with 1-octanethiol $HS(CH_2)_7CH_3$ (termed C_8CH_3 in this chapter) on two cantilever arrays J06 and G16, respectively. Two cantilevers were coated with 11-mercaptoundecanoic acid $HS(CH_2)_{10}COOH$ (termed $C_{11}COOH$ in this chapter), and two with 1-undecanethiol $HS(CH_2)_{10}CH_3$ (termed $C_{11}CH_3$ in this chapter) on two cantilever arrays J05 and H14, respectively. A scheme to show the chemical structure of these molecules is shown in Fig. 10.1, and an overview of the cantilevers on the six cantilever arrays is given in Table 10.1.

The main source of the non-specific variability associated with this work was found to be the instrumental alignment specific to the Scentris instrument. As given in detail in Chapter 6, the magnitude of detected cantilever signals scaled with the initial curvature of cantilevers. The presence of an initial curvature alone was found to cause a relative variability as large as 50%, both in absolute and differential signals. The data presented in this chapter were generated by cantilevers that exhibited different initial curvatures. In fact, the initial curvatures themselves were subject to discussion. Therefore in this chapter, it is important to discuss the possible contributions arising from the instrumental alignment effect. Several pieces of evidence indicated that the measured cantilever signals were not affected substantively by the instrumental alignment effect: firstly, the magnitude of the initial deflection was small and about ± 2 μm. Secondly, the change in Sum signal associated with the heating signals was small. On four of the six cantilever arrays, the Sum signal change was close to zero. On two cantilever arrays, the Sum signal change was $\lesssim 0.5$ mV. However on all cantilever arrays, the Sum signal was independent of the initial curvature. Thirdly, differences in the magnitude of heating signals acquired

before and after the pH titration measurement were chain length dependent, but not dependent on the initial curvature. Fourthly, these differences could not be related to the expected magnitude of heating signals based on the magnitude of the downward drift of cantilevers during the pH titration measurement. Therefore, although it is not possible to completely exclude the instrumental alignment effect, evidence suggested that this effect was minimal.

10.2 Results

10.2.1 pH Measurement

The effect of alkyl chain length on the generation of deprotonation and protonation specific surface stress was probed by exposing the six cantilever arrays to an alternate injection of pH 4.8, 3.5, 4.8, 5.9, 4.8, 6.8, 4.8, 8.4, 4.8, 8.4, and 4.8 sodium phosphate $Na_{3-x}H_xPO_4$ solutions at a constant ionic strength of $I = 0.1$.

Fig. 10.2 shows typical raw absolute stress signals generated upon a pH 4.8/8.4/4.8 switch. COOH signals are shown in (A), and CH_3 signals are shown in (B). Note that these results were obtained from three cantilever arrays and one COOH/CH_3 cantilever pair for each chain length. The increase in the solution pH from 4.8 to 8.4 triggered the generation of a compressive surface stress on the eight cantilevers. The magnitude of the COOH deprotonation signals decreased with decreasing chain length, that is, from −63.5 mN/m for C_{16}, to −54.6 mN/m for C_{11}, to −42.6 mN/m for C_8. The difference between the C_8 and C_3 COOH signal was

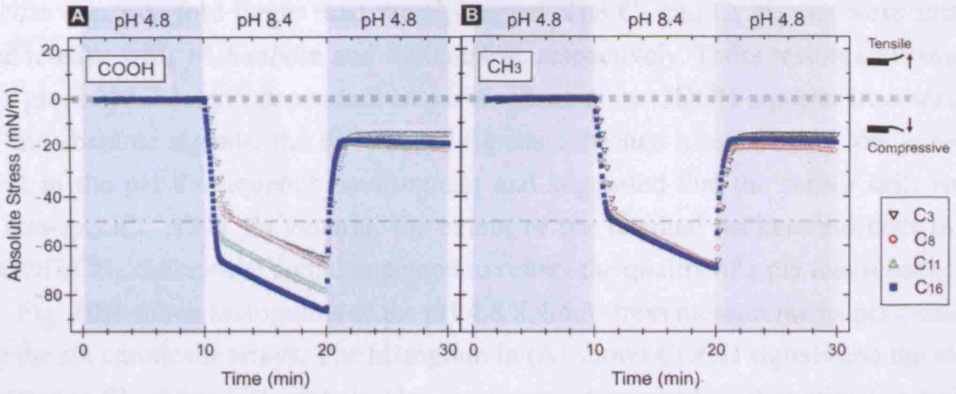

Fig. 10.2. Typical raw stress signals measured upon a pH 4.8/8.4/4.8 switch to probe the chain length effect of pH-triggered surface stress. (A) COOH and (B) CH_3 signals generated by cantilevers coated with C_3, C_8, C_{11}, and C_{16} SAMs.

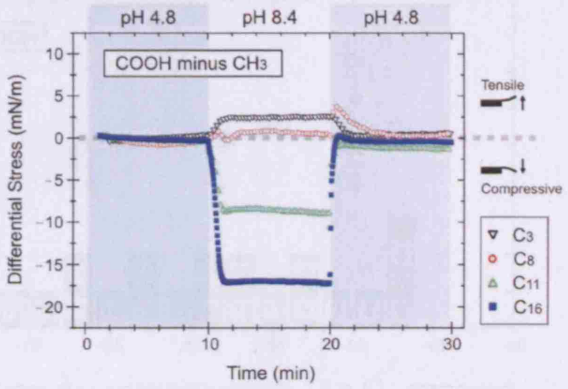

Fig. 10.3. Differential COOH minus CH_3 stress signals obtained from the raw absolute bending signals generated by cantilevers coated with C_3, C_8, C_{11}, and C_{16} SAMs shown in the previous figure.

small, though the magnitude −45.2 mN/m of the C_3 COOH signal was larger. In contrast, the magnitude of the CH_3 signals was found to be largely non-sensitive to the alkyl chain length, which measured −47.0 mN/m for C_{16}, −46.8 mN/m for C_{11}, −44.2 mN/m for C_8, and −47.2 mN/m for C_3. When the aqueous environment was switched back to the reference pH 4.8 solution, all cantilevers bent upward toward the zero-stress baseline.

Since the absolute signals contain non-specific components that are subject to high variability, it is important to evaluate the COOH/CH_3 differential signals specific to the acid deprotonation. The raw COOH/CH_3 differential signals are shown in Fig. 10.3. The mean differential deprotonation C_{11} signal of −7.8 mN/m is in an excellent agreement with the results presented in Chapter 9. The C_{16} signal of 16.5 mN/m was two-fold larger than the C_{11} signal. The C_8 and C_3 signals were small and tensile, with +1.6 mN/m and +2.0 mN/m, respectively. These results confirmed the gross chain length dependent trend of the absolute COOH signals. In contrast to the absolute signals, the differential signals exhibited a remarkably low sensor drift in the pH 8.4 aqueous environment and suggested that the sensor drift was a non-specific effect. In general, the extent of the residual background drift in a COOH/CH_3 differential signal appeared to reflect the quality of a pH measurement.

Fig. 10.4 shows histograms of the pH 4.8/8.4/4.8 stress measurements performed on the six cantilever arrays. The histogram in (A) shows COOH signals and the histogram in (B) shows CH_3 signals. One frequency corresponds to the estimated mean absolute stress of a single cantilever out of a total of a 44 cantilevers distributed on six cantilever arrays, obtained from deprotonation/protonation measurements re-

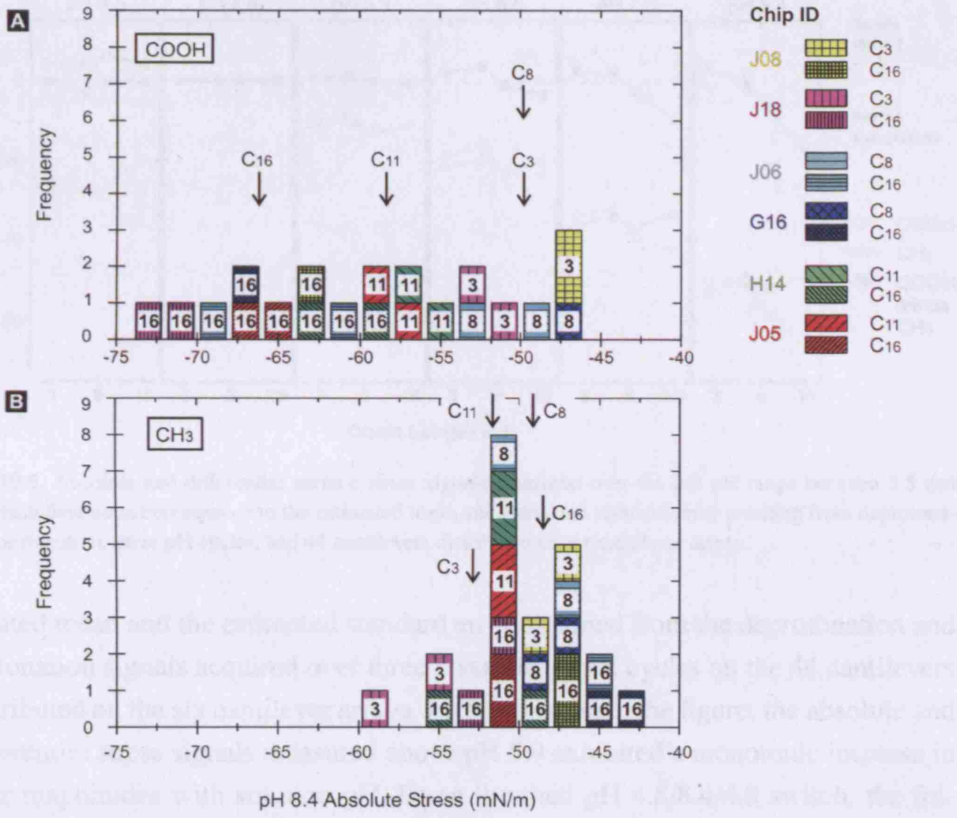

Fig. 10.4. Histogram of equilibrium absolute (A) COOH and (B) CH_3 signals acquired on cantilevers coated with C_3, C_8, C_{11}, and C_{16} SAMs. One frequency corresponds to the estimated mean absolute stress of a single cantilever out of a total of a 44 cantilevers distributed on six cantilever arrays, obtained from deprotonation/protonation measurements repeated over three consecutive pH cycles. The arrows in the histograms point to the overall estimated means of the eight different SAMs. The bin size was 2 mN/m.

peated over three consecutive pH cycles. The arrows in the histograms point to the overall estimated means of the eight different SAMs. There is a clear difference between the overall broad distribution of the COOH stress signals and the overall narrow distribution of the CH_3 stress signals. The histograms were found to reproduce the chain length dependence observed in the single measurements: the broadness of the distribution of the COOH signals resulted from the chain length dependence $C_{16} > C_{11} > C_8 \simeq C_3$. The narrowness of the distribution of the CH_3 signals resulted from a more homogeneous signal distribution without an obvious chain length effect.

The absolute and differential data acquired over the full pH range between 3.5 and 8.4 are summarised in Fig. 10.5. Each data point in the figure represents the es-

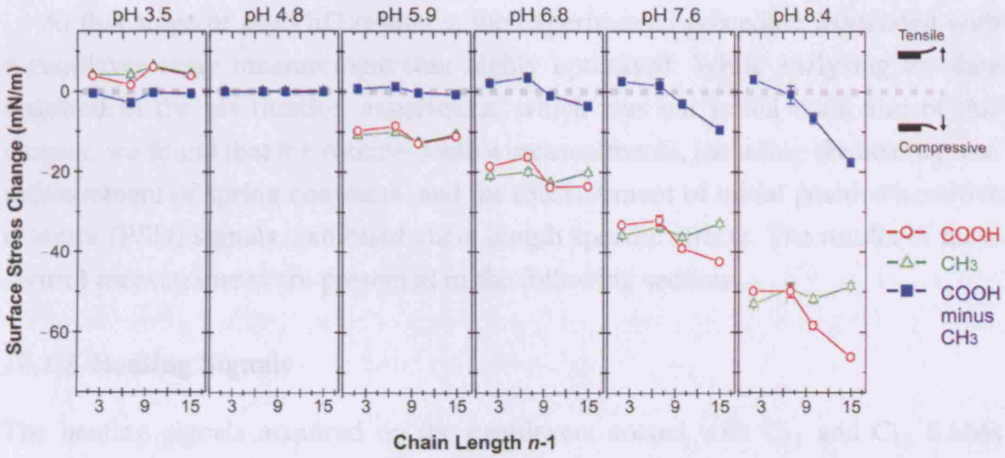

Fig. 10.5. Absolute and differential surface stress signals measured over the full pH range between 3.5 and 8.4. Each data point corresponds to the estimated mean and estimated standard error resulting from deprotonation/protonation, three pH cycles, and 44 cantilevers distributed on six cantilever arrays.

timated mean and the estimated standard error obtained from the deprotonation and protonation signals acquired over three consecutive pH cycles on the 44 cantilevers distributed on the six cantilever arrays. As can be seen in the figure, the absolute and differential stress signals measured above pH 5.9 exhibited a monotonic increase in their magnitudes with solution pH. Upon the final pH 4.8/8.4/4.8 switch, the following estimated mean differential signals and the estimated standard errors were obtained: $+3.0 \pm 0.8$ mN/m for C_3, -1.2 ± 4.0 mN/m for C_8, -7.6 ± 0.9 mN/m for C_{11}, and -17.1 ± 0.6 mN/m for C_{16}.

Conversely, the differential stress signals measured upon the pH 4.8/3.5/4.8 was -0.42 ± 0.36 mN/m for C_3, -2.75 ± 0.39 mN/m for C_8, -0.30 ± 0.15 mN/m for C_{11}, and -0.50 ± 0.22 mN/m for C_{16}. In other words, there appeared to be a relative increase in the tensile differential stress when the pH was increased from pH 3.5 to pH 4.8. This is in agreement with the observations presented in Chapter 8. The generation of the tensile differential stress from pH 3.5 to pH 4.8 may be attributed once again to the onset of the deprotonation of the carboxylic acid terminal groups, which increased the number of in-plane hydrogen bonds formed in the partially ionised carboxylic acid terminated SAMs. However, owing to the estimated standard errors that were in the same order of magnitude as the estimated means, an appropriate multiple array analysis of variance (ANOVA) may be employed in future to probe this effect in a more rigourous manner.

At this stage of my PhD research, the experimental procedure associated with a cantilever array measurement was highly optimised. While analysing the data acquired in the pH titration experiment, which was our initial main aim of this chapter, we found that the routine control measurements, including the heating test, measurement of spring constants, and the measurement of initial position sensitive detector (PSD) signals, exhibited chain length specific effects. The results of these control measurements are presented in the following sections.

10.2.2 Heating Signals

The heating signals acquired on the cantilevers coated with C_{11} and C_{16} SAMs on J05 and H14 reached ~ 80 mN/m, which suggested that the superluminescent diode (SLD)/cantilever alignment was well performed in both measurements. Interestingly, the equilibrium heating signals acquired on all other cantilever arrays appeared to be unusually high. Yet in all measurements, the associated Sum change was small and $\lesssim 0.5$ mV, that is, no obvious evidence of cantilever/PSD misalignment effect was observed. This motivated us to investigate the chain length specific effects in the measured heating signals in a systematic manner.

Typical raw heating signals of cantilevers coated with C_3, C_8, and C_{11} SAMs are shown in Fig. 10.6. Note that these signals were acquired on three cantilever arrays and in three measurements. The control C_{16} signals are omitted from the figure for clarity. As the liquid cell was heated by 1 °C, all three cantilevers bent downward due to the bimetallic effect. The equilibrium signal measured ten minutes after the

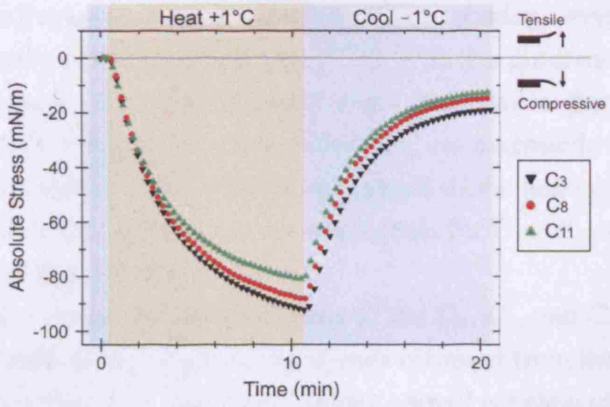

Fig. 10.6. Typical raw heating signals acquired on cantilevers coated with C_3, C_8, and C_{11} SAMs on three different cantilevers arrays and in three different measurements.

onset of heating was −92.1 mN/m for C_3, −87.9 mN/m for C_8, and −81.0 mN/m for C_{11}. When the liquid cell temperature was decreased to the initial value, the cantilevers bent upward toward the zero-stress baseline. In general, the heating signals were found to be larger than the corresponding cooling signals. For example in the figure, the magnitude of the cooling signals after the onset of liquid cell cooling and relative to the heating signal was 79.5% for C_3, 83.3% for C_8, and 84.4% for C_{11}. Although this effect appeared to be qualitatively reproduced in the majority of measurements, cooling signals exhibited somewhat less quantitative reproducibility and were therefore excluded from further analysis.

Histograms of heating signals acquired on the six cantilever arrays are summarised in Fig. 10.7. In (A), the upper histogram shows the heating signals generated by the cantilevers coated with C_3 SAMs, and the lower histogram shows the heating signals generated by the control cantilevers coated with C_{16} SAMs on the same cantilever arrays. Similarly in (B), the upper histogram shows the heating signals generated by the cantilevers coated with C_8 SAMs and the lower histogram shows the heating signals generated by the control cantilevers coated with C_{16} SAMs on the same cantilever arrays. Finally in (C), the upper histogram shows the heating signals generated by the cantilevers coated with C_{11} SAMs and the lower histogram shows the heating signals generated by the control cantilevers coated with C_{16} SAMs on the same cantilever arrays.

The heating signals generated by the total of 44 cantilevers ranged from ~−94 mN/m to ~−79 mN/m. Each heating signal acquired on a single cantilever array was associated with a relative standard deviation below 2.5%, which was the criteria for a successful SLD/cantilever alignment. The heating signals acquired on two separate cantilever arrays with the same cantilever coatings were in a good agreement. A comparison of histograms associated with the different chain lengths C_3, C_8, and C_{11} suggested a monotonic chain length dependence, that is, $C_3 > C_8 > C_{11}$, on the generation of heating signals. Moreover, the magnitude of the control C_{16} signals appeared also to scale with the magnitude of the heating signals generated by shorter chain length SAMs: C_{16} control signals for $C_3 > C_{16}$ control signals for $C_8 > C_{16}$ control signals for C_{11}.

The estimated mean and standard error of the C_3, C_8, and C_{11} heating signals, plus the associated control C_{16} heating signals obtained from the six cantilever arrays are shown in Fig. 10.8. The figure shows a small yet clear chain length dependence of the heating signals: −91.8 ± 0.5 mN/m for C_3 and −90.8 ± 0.3 mN/m for control C_{16} SAMs; −89.0 ± 0.8 mN/m for C_8 and −86.5 ± 0.9 mN/m for control C_{16}

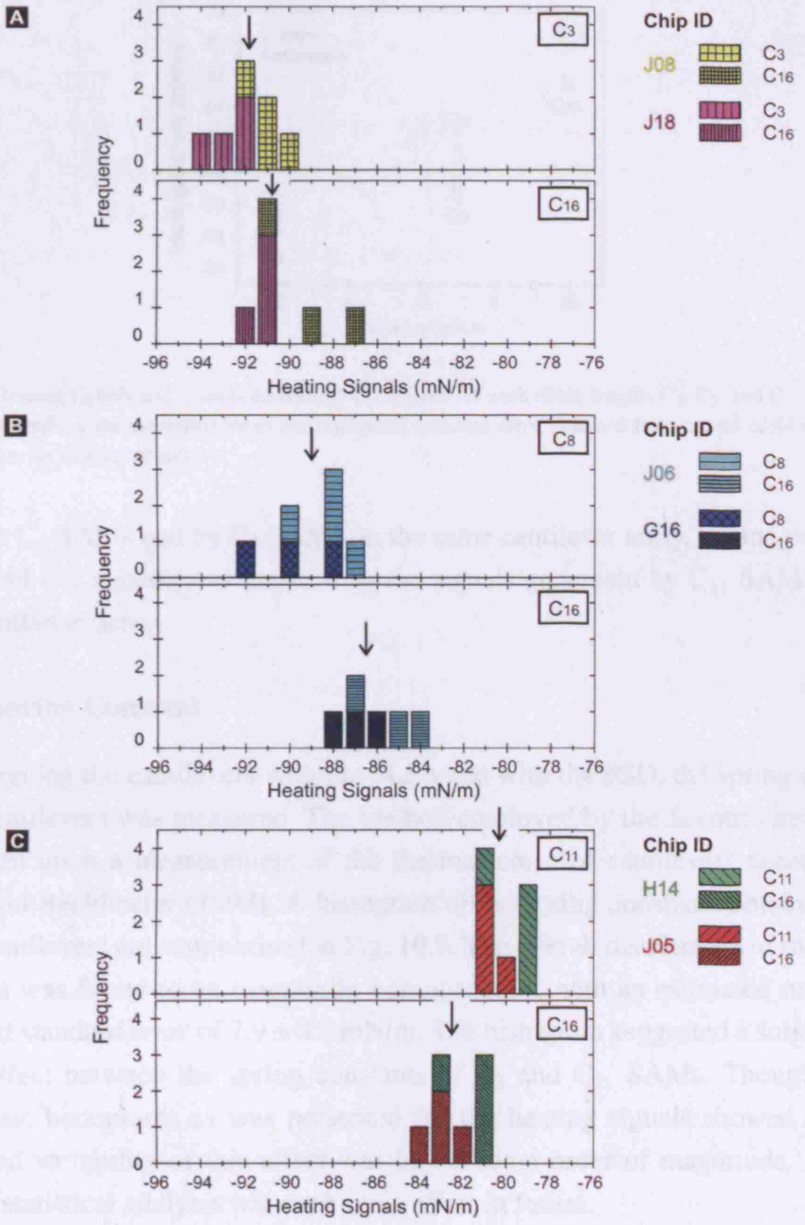

Fig. 10.7. Histogram of equilibrium heating signals measured on cantilevers coated with (A) C_3 and control C_{16} SAMs, (B) C_8 and control C_{16} SAMs, and (C) C_{11} and control C_{16} SAMs. The arrows point to the estimated mean associated with each histogram. One frequency corresponds to one cantilever out of a total of 44 cantilevers distributed on six cantilever arrays. The bin size was 1 mN/m.

SAMs; -80.3 ± 0.2 mN/m for C_{11} and -82.5 ± 0.4 mN/m for control C_{16} SAMs. Whereas the magnitude of the control C_{16} signals was *smaller* than the signals gen-

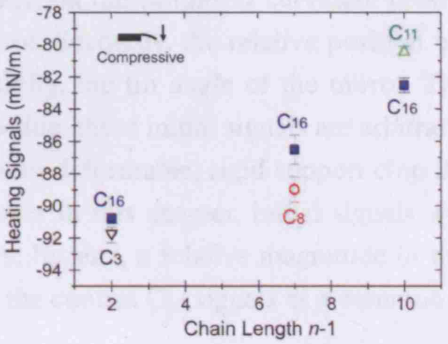

Fig. 10.8. Heating signals and associated control C_{16} signals for each chain lengths C_3, C_8, and C_{11}. Each data point corresponds to the estimated mean and estimated standard error obtained from a total of 44 cantilevers distributed on six cantilever arrays.

erated by C_3 SAMs and by C_8 SAMs on the same cantilever array, the magnitude of the control C_{16} signals was *larger* than the signals generated by C_{11} SAMs on the same cantilever array.

10.2.3 Spring Constant

Upon aligning the cantilevers with the SLDs and with the PSD, the spring constant of the cantilevers was measured. The method employed by the Scentris instrument was based upon a measurement of the thermal noise of cantilevers according to Hutter and Bechhoefer (1993). A histogram of the spring constants obtained from the 44 cantilevers are summarised in Fig. 10.9. The overall distribution of the spring constants was found to be essentially homogeneous, with an estimated mean and estimated standard error of 7.9 ± 0.2 mN/m. The histogram suggested a subtle chain length effect between the spring constants of C_3 and C_{11} SAMs. Though a plot of separate histograms as was presented for the heating signals showed that the associated variability of this effect was in the same order of magnitude. A more detailed statistical analysis will probe this effect in future.

10.2.4 Initial Stress

Initial PSD Stress Signals. Prior to the core surface stress measurement, the initial surface stress signals were measured on the individual cantilevers. The initial surface stress signals are those signals that result from the direct conversion of absolute PSD position signals into surface stress values (Fig. 5.3) and depend on the

following factors: firstly, on the cantilever curvature present prior to the core surface stress measurement. Secondly, the relative position between a cantilever free end and the PSD. Thirdly, the tilt angle of the mirror. Therefore without a common reference stress value, these initial signals are arbitrary. The optimal approach would be to take the non-deformable, rigid support chip body as a common reference (Fig. 7.1). However in this chapter, initial signals were acquired only at the free end of cantilevers. Instead, a relative magnitude of the initial signals may be estimated by defining the control C_{16} signals as a common reference for the shorter chain length SAMs.

The measurement results are shown in Fig. 10.10. In (A), the estimated mean and estimated standard error of the individual absolute initial stress signals generated by the cantilevers coated with C_3, C_8, and C_{11} are shown. In (B), the corresponding values for the associated control C_{16} SAMs are shown. In (C), the corresponding differential signals are shown, calculated as (C_n minus C_{16} signal) with $n = 3, 8, 11$. It should be noted that prior to each measurement, the average initial signal was aligned with the zero-PSD position. Therefore the sum of the individual initial stress signals measured on a single cantilever array was about zero, which served as an additional reference state.

The estimated mean absolute initial stress and the estimated standard error was 174 ± 34 mN/m for the C_3 and -149 ± 49 mN/m for the associated control C_{16} SAMs, giving rise to a tensile differential initial stress of 323 ± 59 mN/m. Further, the estimated mean absolute initial stress and the estimated standard error was 63 ± 165

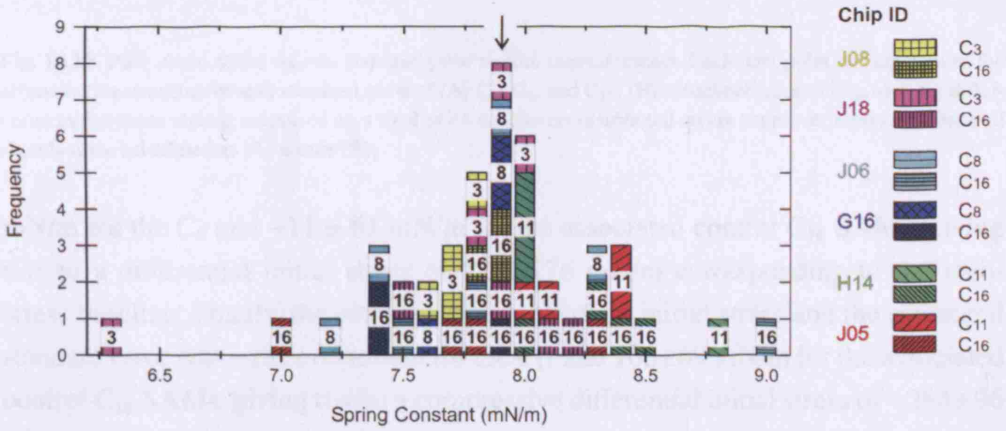

Fig. 10.9. Histogram of spring constants measured on cantilevers coated with C_3, C_8, C_{11}, and C_{16} SAMs. One frequency corresponds to one cantilever out of a total of 44 cantilevers distributed on six cantilever arrays. The bin size was 0.1 mN/m.

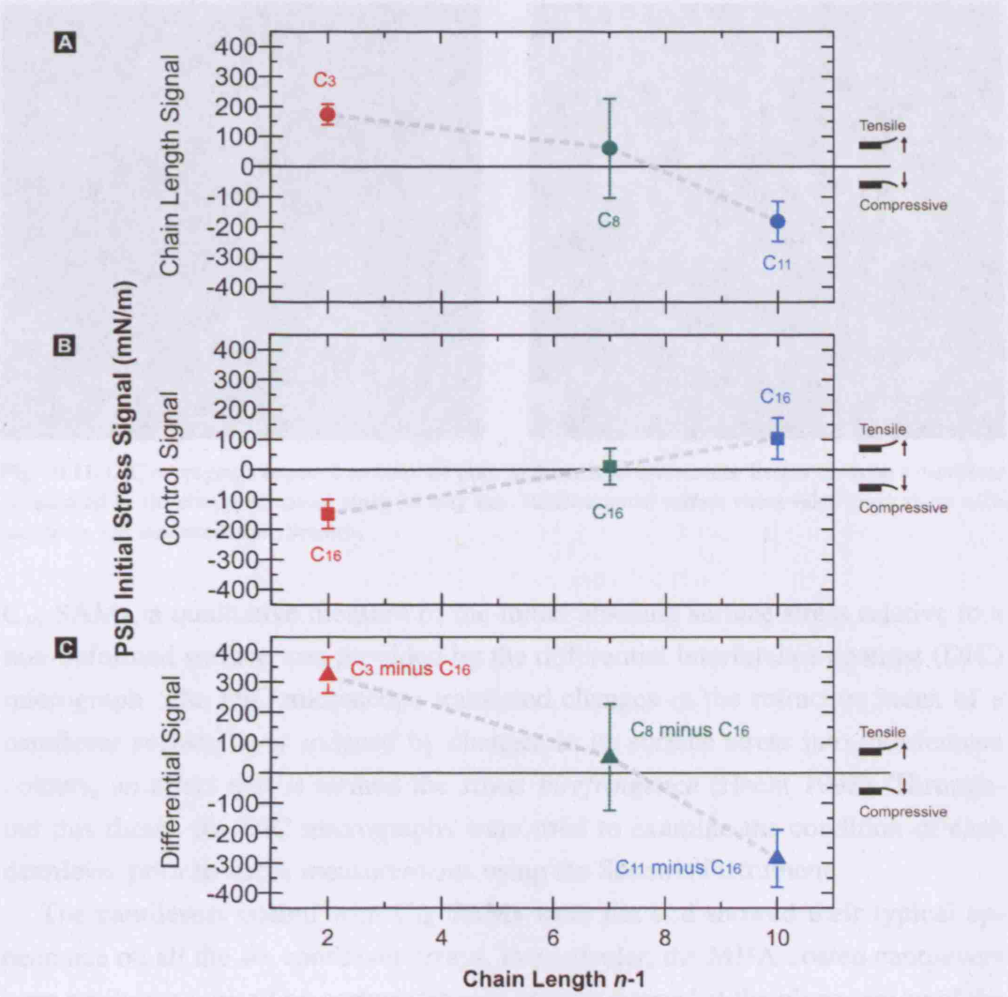

Fig. 10.10. PSD initial stress signals acquired prior to core measurements. Each data point corresponds to the estimated mean and estimated standard error of (A) C_3, C_8, and C_{11}, (B) associated control C_{16}, and (C) differential initial stress signals measured on a total of 44 cantilevers distributed on six cantilever arrays. Differential signals were calculated as (A) minus (B).

mN/m for the C_8 and -11 ± 61 mN/m for the associated control C_{16} SAMs, giving rise to a differential initial stress of 52 ± 176 mN/m corresponding to the zero-stress baseline. Finally, the estimated mean absolute initial stress and the estimated standard error was -181 ± 66 mN/m for the C_{11} and 103 ± 69 mN/m for the associated control C_{16} SAMs, giving rise to a compressive differential initial stress of -284 ± 96 mN/m.

Differential Interference Contrast Micrograph. While the initial PSD stress signals provided a quantitative measure of the initial absolute surface stress relative to

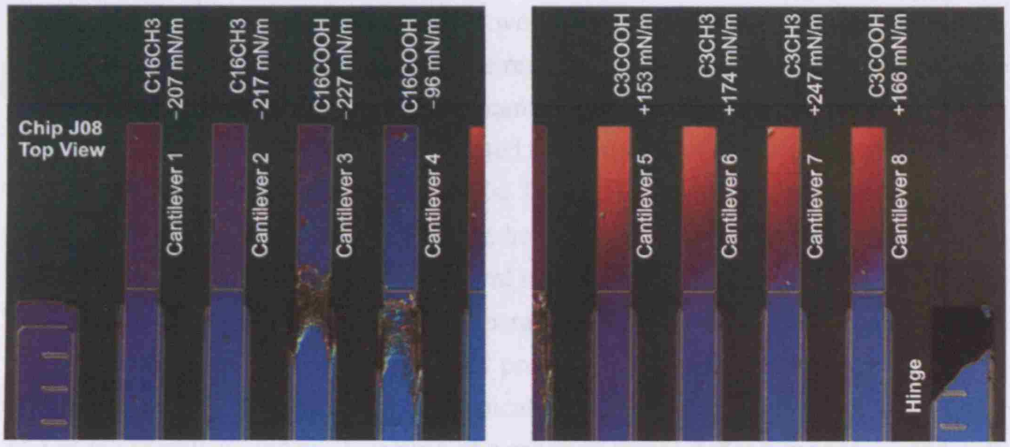

Fig. 10.11. DIC micrograph acquired on chip J08 prior to Scentris measurements. Excess stress on a cantilever is indicated by the change in colour along its long axis. Relative initial surface stress value given above each cantilever was measured using Scentris.

C_{16} SAMs, a qualitative measure of the initial absolute surface stress relative to a non-deformed surface was provided by the differential interference contrast (DIC) micrograph. The DIC microscope translated changes in the refractive index of a cantilever surface layer induced by changes in its surface stress into interference colours, an effect that is termed the *stress birefringence* (Hecht 1998). Throughout this thesis, the DIC micrographs were used to examine the condition of each cantilever prior to stress measurements using the Scentris instrument.

The cantilevers coated with C_{16} SAMs were flat and showed their typical appearance on all the six cantilever arrays. In particular, the MHA-coated cantilevers were easily recognised by carboxylic acid crystals formed at the hinge region of the cantilevers during functionalisation. The cantilevers coated with C_8 and C_{11} SAMs could not be optically distinguished from the cantilevers coated with C_{16} SAMs, except for the carboxylic acid terminated SAM coatings that did not form crystals at the hinge region. However, substantive initial stress was observed on the cantilevers coated with the shortest C_3 SAMs. Fig. 10.11 shows two DIC micrographs acquired consecutively on chip J08. The micrograph on the left shows Cantilever 1 to Cantilever 4 coated with C_{16} SAMs, plus the left half of Cantilever 5 coated with C_3 SAM; The micrograph on the right shows the right half of Cantilever 4, plus Cantilever 5 to Cantilever 8 coated with C_3 SAMs. This order of cantilever coating resulted from a random assignment. The presence of an excessive stress at the cantilever surface can be identified by comparing the colour of the cantilevers relative to the colour of the flat hinge region that served as an important reference. Note the

slightly different background tilt in the two micrograph halves giving rise to different in-plane colour gradients at the hinge region. The change in the colour from blue at the hinge region to orange toward the cantilever free end along the long axis of the cantilevers coated with C_3 SAMs indicated the presence of an initial excessive stress on the cantilevers coated with C_3 SAMs. The initial stress of these cantilevers appeared to be uniform and homogeneous, however no further attempts were made to quantify the initial stress from the optical micrographs. Conversely, the cantilevers coated with C_{16} SAMs showed a comparable initial stress to the reference hinge region, in agreement with micrographs previously acquired on cantilevers coated with these SAMs. By assuming the typical resolution of an optical microscope of $\simeq \lambda$ in the visible wavelength regime, the range of initial deflections associated with 'non-strained' cantilevers were estimated to be in the order of a micron. The surface stress values given at the top of the figure corresponds to the estimated mean initial PSD stress signals acquired on the individual cantilevers.

The combination of the DIC micrograph sand the initial PSD stress signals revealed the presence of an absolute tensile surface stress on the cantilevers coated with C_3 SAMs. These results suggested an important role of the chain length of SAMs in the generation of initial stress at the upper surface of cantilevers.

10.3 Discussion

The results presented in this chapter suggested an important role of the chain length of SAMs in the generation of surface stress. This Discussion section is subdivided into two parts: in the first part, the in-plane stress generated at the SAM/gold interface is discussed that had been already formed *prior* to the measurements. This includes the pH titration measurement, the heating tests, and the measurement of spring constants. In the second part, the in-plane stress generated *during* the formation of the SAM/gold interface is discussed. This includes the measurement of initial PSD stress signals and the DIC micrograph.

The chain length dependence of the observed deprotonation specific differential stress may be attributed to the effect of increased thickness according to the Stoney's equation Eq. (5.4): the surface stress $\Delta\sigma_s$ is directly proportional to the thickness of the thin film t_f multiplied by the constant in-plane force per unit area $\Delta\sigma_f$ acting upon the cross-sectional area of the thin film: $\Delta\sigma_s = \Delta\sigma_f t_f$. Therefore by assuming the measured ellipsometric thickness of the carboxylic acid terminated SAMs shown in Fig. 5.14, it is possible to calculate the deprotonation differen-

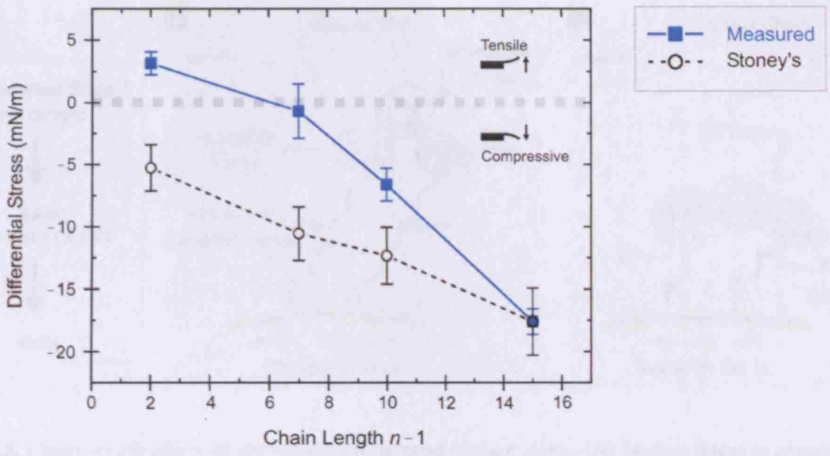

Fig. 10.12. Comparison between the measured differential stress and the differential stress predicted by the Stoney's equation. The latter was calculated relative to the measured differential stress on C_{16} SAMs.

tial stress predicted by the Stoney's equation relative to the C_{16} SAM. Fig. 10.12 shows the differential pH 4.8/8.4/4.8 stress according to Stoney superimposed to the measured mean differential pH 4.8/8.4/4.8 stress and associated standard errors. As can be seen in the figure, the monotonic chain length dependence of the deprotonation-specific surface stress is correctly given by this simple consideration. However, the measured chain length effect was stronger. For example, the calculated pH 4.8/8.4/4.8 differential stress ranged from -17 ± 4 mN/m for C_{16} to -5 ± 2 mN/m for C_3, whereas the corresponding differential stress ranged from -17.1 ± 0.6 mN/m for C_{16} to $+3.1 \pm 0.8$ mN/m for C_3.

The consideration based upon Stoney's relation made several basic assumptions. Firstly, the mechanical properties of SAMs were assumed to be independent of the chain length. Secondly, SAMs were assumed to be homogeneous thus their molecular structure was neglected. Thirdly, the in-plane electrostatic repulsion between negatively charged carboxylic acids was assumed to be independent of the chain length. The chain length dependent mechanical properties of SAMs have been investigated by several experimental and theoretical AFM friction studies (Lio, Charych, and Salmeron 1997; Zhang, Leng, and Jiang 2003). They have consistently found that short chain SAMs were more compliant whereas long chain SAMs were more rigid, and attributed to the chain length dependence of the lateral packing of these SAMs due to the attractive chain/chain van-der-Waals forces. In agreement with these studies, studies into the chain length dependent equilibrium

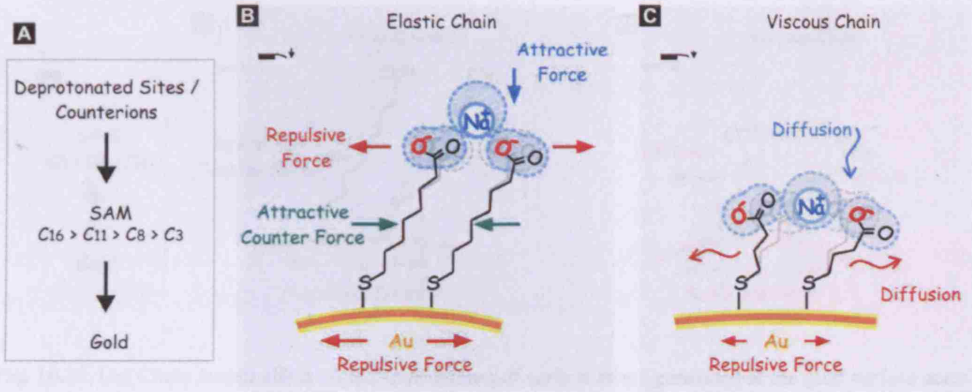

Fig. 10.13. Chain length effect on deprotonation-induced surface stress. (A) Surface stress is generated at the deprotonated sites of a carboxylic acid terminated SAM and transduced across the SAM to the underlying gold surface. (B) Elastic alkyl chain model. (C) Viscous alkyl chain model.

structure of SAMs have reported a disordered, liquid-like structure of short chain SAMs, and a more ordered, solid-like structure of long chain SAMs (Bain et al. 1989; Porter et al. 1987). The deprotonation of surface-tethered carboxylic acids can be expected to be dependent on the two-dimensional order of the acid terminal groups. Given the reported chain length dependence of structural order, the pH-dependence of acid deprotonation can be expected to be chain length dependent, though strong evidence for this effect has not yet been reported (Kakiuchi et al. 2000; Dai and Ju 2001).

Upon the basis of these literature SAM properties, the observed chain length dependence may be rationalised by applying Gibbs's model of a completely elastic solid to SAMs. In this model, as discussed by Rusanov (1996;2005) and reviewed in Section 4.2, any solid body is considered to consist of mobile, fluid-like components and immobile, solid-like components. When a carboxylic acid terminated SAM deprotonates and induces the adsorption of counterions, fluid-like, short chain SAMs will diffuse laterally to level out the excess chemical potential due to adsorption. Whereas solid-like, long chain SAMs will resist against the lateral diffusion by generating a counter-balancing in-plane force. This is illustrated in Fig. 10.13. According to Eq. (4.31) as well as to Eriksson relation Eq. (4.36), the contribution to surface stress change induced in short chain SAMs will thus be dominated by the thermodynamic surface tension, whereas the surface stress change induced in long chain SAMs will be a superposition of the thermodynamic surface tension and the excess chemical potential. Since changes in the thermodynamic surface tension and

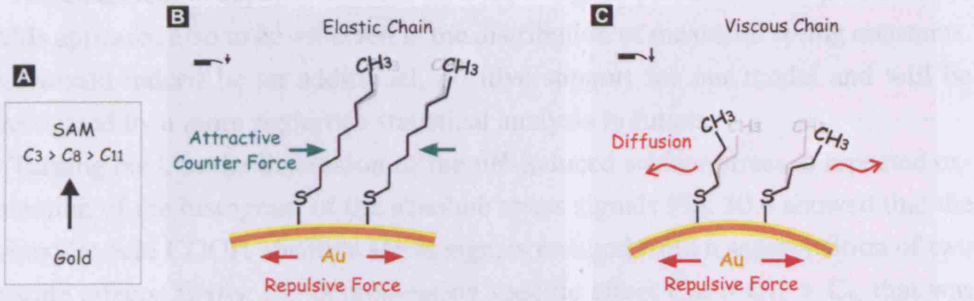

Fig. 10.14. (A) Chain length effect on the transduction of surface stress generated at the gold surface across a SAM. (B) Elastic alkyl chain model. (C) Viscous alkyl chain model.

the excess chemical potential due to adsorption of partially hydrated sodium counterions are expected to enlarge the SAM surface (Rusanov 1996;2005), one would expect a monotonic increase in the compressive surface stress with chain length. However, a tensile differential stress was measured for the shortest chain length C_3 SAM, which remained unexplained. At this point, before proceeding with the discussion of the tensile differential stress, let us first consider the origins of heating signals.

The primary component of surface stress in a heating signal was generated by the bimetallic effect, that is, the differential thermal expansion of the gold surface relative to the bulk cantilever material. As a secondary effect, a chain length dependent effect was observed, whereby the shortest chain length C_3 SAMs generated the largest heating signals: $C_3 > C_8 > C_{11}$. Again, this effect may be attributed to the difference in the mechanical properties of SAMs, that is, in-plane mechanical resistivity of SAMs against lateral diffusion due to the thermal expansion of the gold surface. This is illustrated in Fig. 10.14.

The magnitude of the heating signals generated by C_{16} SAMs on a single cantilever array was found to scale with the magnitude of the heating signals generated by the shorter chain length SAMs on the same cantilever array. This suggested a coupling of heating signals generated by different cantilevers on a single cantilever array, most likely to be caused by a cross-contamination of cantilever coatings. While the increased magnitude of the control signals generated by cantilever arrays with C_3 or C_8 SAM coated cantilevers was plausible, the decreased magnitude of the control signals in presence of C_{11} coated cantilevers was less plausible. Future experiments will further investigate the origin of reversed signal amplification, for example by probing different solution phase ions.

The chain length dependent effect $C_3 > C_8 > C_{11}$ of the mechanical properties of SAMs appeared also to be reflected in the distribution of measured spring constants. This would indeed be an additional, positive support for our model and will be investigated by a more rigourous statistical analysis in future.

Turning back to the discussion of the pH-induced surface stress, a repeated examination of the histogram of the absolute stress signals Fig. 10.4 showed that the carboxylic acid COOH absolute stress signals resulted from a superposition of two separate effects: firstly, the deprotonation specific effect $C_{16} > C_{11} > C_8$ that was consistent with the differential data. Secondly, the quasi-equality of $C_8 \simeq C_3$, effected by the reversed magnitude of C_3 absolute stress. A further piece of evidence of the presence of the latter effect was provided by the magnitude of the associated control C_{16} signals, although this effect was reduced by the large between-array variability: control signals for C_3 > control signals for C_8 > control signals for C_{11}. Yet more evidence of the latter effect was provided by the methyl CH_3 absolute stress signals. Again the between-array variability was large, however on each cantilever array with cantilevers coated with C_3 and C_8 SAMs, respectively, we observed C_3 > control C_{16} and C_8 > control C_{16}. Moreover on average, C_3 absolute signals were larger than C_8 absolute signals.

The additional chain length effect superimposed to the deprotonation specific chain length effect that was observed in the pH titration experiment would be plausible, if a compressive surface stress was generated in the gold surface layer. In contrast to the heating signals generated by the bimetallic effect, the absolute pH signals were generated upon pH switches. Therefore, the increase in the compressive surface stress in the gold surface layer upon a pH 4.8/8.4/4.8 switch may be attributed to changes in the amount or species of solution phase ions adsorbed on the gold surface, such as phosphate anions. However, future work will investigate the role of solution phase ions in the generation of surface stress in the gold surface layer.

By accounting for the compressive surface stress specific to the carboxylic acid deprotonation, and the compressive surface stress induced in the gold layer due to the non-specific adsorption of some unknown solution phase ions and molecules on *both* cantilevers coated with COOH or CH_3 terminated SAMs, an overall model of the chain length dependent, pH-induced surface stress may be proposed. The model is illustrated in Fig. 10.15 and consists of three regimes I, II, and III.

In the first regime of the model (Fig. 10.15, I), alkanethiols are considered as liquid molecules adsorbed on the gold surface, which show no resistance against

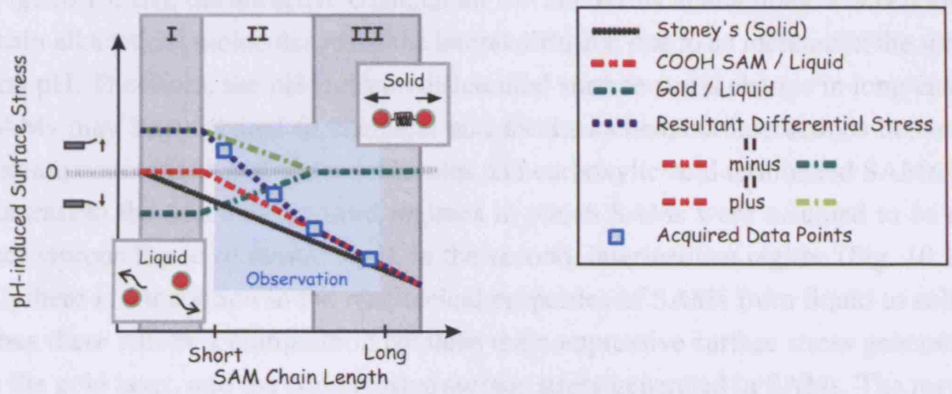

Fig. 10.15. Proposed mechanochemical model for the chain length dependent, pH-induced generation of surface stress.

lateral diffusion. Therefore, the pH-induced surface stress change in short chain SAMs may be attributed to chemical and mechanochemical interactions between the solution phase ions and liquid molecules including the alkanethiol molecules themselves, and the surface gold atoms, whose metallic bonds resist against lateral diffusion (green dash-dot-dashed line). An increase in the pH of sodium phosphate solution increased the following surface excess: firstly, negatively charged deprotonated surface carboxylic acids; secondly, sodium counterions and water molecules adsorbed onto the deprotonated sites; thirdly, divalent phosphate anions, sodium cations, and/or water molecules adsorbed directly onto the gold surface. Referring again to Eq. (4.31) and to Eriksson relation Eq. (4.36), these excess ions and molecules will contribute to the change in surface stress at the gold surface, that is, the change in thermodynamic surface tension as well as in excess chemical potential. Provided that the surface density of the shortest chain alkanethiol molecules is independent of the chain length, the excess amount of negative charges and adsorbates can be expected to be independent of the chain length. The consideration so far involved the absolute stress change in carboxylic acid terminated short chain SAMs, however, by further assuming that the surface density of the shortest chain alkanethiol molecules is independent of the terminal group, the resultant differential stress (dotted blue line) is calculated as COOH minus CH_3 signal, that is, zero (red dash-dot-dot-dashed line) minus the change in interfacial stress at the gold/liquid interface (green dash-dot-dashed line). Therefore, the sign of the change in interfacial stress at the gold/liquid interface becomes inverted, which is indicated by the *light* green dash-dot-dashed line in Fig. 10.15. In the third regime of the model

(Fig. 10.15, III), the attractive chain/chain van der Waals interactions between long chain alkanethiol molecules resist the lateral diffusion due to an increase in the solution pH. Therefore, the pH-induced differential surface stress change in long chain SAMs may be attributed to chemical and mechanochemical interactions between sodium counterions and water molecules and carboxylic acid terminated SAMs. In contrast to the first and the third regimes in which SAMs were assumed to be either viscous liquid or elastic solid, in the second, intermediate regime (Fig. 10.15, II), there is a transition in the mechanical properties of SAMs from liquid to solid. Thus there will be a competition between the compressive surface stress generated in the gold layer, and the compressive surface stress generated in SAMs. The resultant differential surface stress will be *tensile*, if the absolute stress at the gold/liquid interface is larger, and *compressive*, if the absolute stress at the SAM/liquid interface is larger. Finally, it should be noted that the mechanochemical component of surface stress in the third regime can be expected to be correctly described by the Stoney's equation. Therefore, the discrepancy between the Stoney's prediction and the model proposed herein may be attributed to the gold/liquid interactions in the first and the second regimes.

The model in Fig. 10.15 may applied to the observed chain length dependent differential stress profile in Fig. 10.12. The tensile differential stress observed for C_3 SAMs as well as the zero-differential stress observed for C_8 SAMs in the pH experiment suggest that these SAMs fall in the second regime of the model. The compressive stress generated in the gold film was larger than the deprotonation induced compressive stress transduced across the carboxylic acid terminated C_3 SAMs, giving rise to a tensile differential stress. Whereas in the carboxylic acid terminated C_8 SAMs, the compressive stress generated in the gold film was of comparable magnitude as the deprotonation induced compressive stress transduced across the SAMs, giving rise to a differential stress close to the zero-stress baseline. Importantly, the absolute CH_3 signals generated by C_{11} and C_{16} SAMs did not show the chain length effect due to the gold film and suggested that these CH_3 terminated long chain SAMs were resistent against ion penetration. This is in agreement with previous corrosion studies on these SAMs (Porter et al. 1987; Zamborini and Crooks 1998). No chain length effect was observed upon pH switch that appeared to be specific to the CH_3 terminal group, indicating that no measurable surface stress was generated upon pH switch in these SAMs. The interaction between the solution phase ions and the hydrophobic SAMs can thus be assumed to be negligible under these conditions. Furthermore, the resistance against ion penetration can be

expected to be also dependent on the terminal group due to differences in the molecular order and differences in strains. Considering the polarity of the COOH terminal group, one would expect COOH terminated SAMs to be more disordered than CH_3 terminated SAMs of identical chain length. However, no obvious effect of terminal group in the heating signals was measured in the pH 4.8 sodium phosphate solution, which supported that the molecular order of these SAMs were independent of the terminal group under these conditions. On the other hand, the distribution of control C_{16} signals generated by COOH terminated SAMs upon pH 4.8/8.4/4.8 switch was suggestive of the chain length effect due to gold, that is, $C_3 > C_8 > C_{11}$. This may reflect an enhanced ion penetration due to the additional strain induced in deprotonated COOH terminated SAMs. Therefore, it is not possible to separate completely the stress generation in the SAMs and the stress generation in the gold film in these measurements. In Fig. 10.15, C_{11} SAMs as well as C_{16} SAMs were assumed to fall in the third regime of the model, and the deprotonation-specific differential stress was attributed to chemical and mechanochemical in-plane forces between sodium counterions and water molecules and carboxylic acid terminated SAMs. This is in agreement with the results presented in the preceding chapters.

The discussion so far was concerned with surface stress changes generated in SAMs and in the gold film that had been already formed *prior* to the measurements. The initial surface stress that will be discussed hereupon was generated *during* the formation of the same SAMs on gold evaporated cantilevers, plus their subsequent equilibration in pH 4.8 sodium phosphate solution at a constant ionic strength of $I = 0.1$ at room temperature and over a time period of one month. Because these measurements were performed in pH 4.8 sodium phosphate solution, the component of surface stress specific to the acid deprotonation can be expected to be negligible. The primary component of initial surface stress can be therefore attributed to the equilibrium in-plane stress at the SAM/gold interface.

The close agreement between the chain length dependence of the initial stress and the chain length dependence of the heating signals suggested that the initial stress was indeed generated at the SAM/gold interface. Interestingly, the sign of the chain length effect was found to be reversed, that is, $C_3 > C_8 > C_{11}$ in the order of increasing *tensile* stress. If the measured surface stress was attributed to the surface stress acting upon the gold film counterbalanced by the SAMs of different rigidity and thickness, the reversed chain length effect would indicate a contraction of the gold surface layer due to a tensile surface stress. In fact, the presence of an absolute tensile surface stress on the cantilevers coated with C_3 SAMs was

revealed by the excess surface strain seen in the DIC micrograph. As a first approximation, the magnitude of this tensile absolute surface stress of +607 ± 56 mN/m was obtained by assuming that the cantilevers coated with C_{11} SAMs were free of excess surface strain, and that the control cantilevers coated with C_{16} SAMs exhibited identical initial stress. It should be noted that the presence of an excess surface strain on cantilevers coated with C_{11} SAMs cannot be excluded. Moreover in general, the cross-contamination of control C_{16} SAMs is expected to underestimate the magnitude of the chain length effect.

The generation of surface stress during the formation of SAMs and its chain length dependence have been investigated previously by Berger et al. (1997) and Godin et al. (2004a; 2004b). These studies agreed in that the formation of SAM induced a compressive surface stress change. However, the chain length dependence was subject to controversy: while Berger et al. reported a monotonic chain length dependence of the surface stress generated upon SAM formation, Godin et al. found that the surface stress was generated independent of the chain length. Furthermore, the reported surface stress values varied over two orders of magnitude, that is, from -10^{-1} to -10^{1} N/m. Godin et al. demonstrated that differences in the gold morphology alone can account for the discrepancies. Importantly, both studies used the cantilever itself as its own reference state, thus the sign and magnitude of the absolute stress remained uncertain.

According to Ibach (1997) and the references therein, an unreconstructed, clean Au(111) surface is unstable due to its high tensile stress of ~3 N/m. The surface is stabilised upon reconstruction that reduces the tensile surface stress to ~2 N/m by forming the characteristic, so-called herringbone pattern. Interestingly, Poirier (1997) and co-workers have observed a lifting of the herringbone reconstruction pattern during the formation of a SAM on Au(111). Furthermore, Biener, Biener, and Friend (2005) showed recently that the adsorption of bare sulphur atoms on Au(111) lifted the herringbone pattern. Note that the lifting of a herringbone pattern can only occur if the surface stress of the gold is lower than 2 N/m. The studies reported by Poirier and Friend have therefore demonstrated indirectly that the magnitude of the compressive surface stress in the gold increased during the SAM formation. This is, of course, consistent with the cantilever studies reported by Berger et al. and Godin et al.

While the literature is suggestive of a fundamental relation between the surface stress and the growth and structure of SAMs, experiments to relate the evolution of the absolute surface stress during SAM formation have not yet been performed,

rather than a change in the absolute surface stress. Depending on the magnitude of compressive surface stress change induced during SAM formation, the absolute stress in the gold may remain tensile or render compressive. The reported cantilever studies did not address this important question. Herein, the presence of tensile absolute stress in the gold film relative to a non-deformed surface and the associated chain length effect showed the importance of the overall force balance across the liquid/SAM/Au interfaces. However, the contribution of solvent molecules as well as solution phase ions to the observed tensile absolute stress is uncertain. Future experiments will investigate the relation between the absolute interfacial stress and the growth and structure of SAMs on Au(111) under ultrahigh vacuum conditions to control the surface cleanliness.

10.4 Conclusion

Our findings suggest an important role of the alkyl chain of SAMs in the generation of surface stress. A mechanochemical model was proposed to rationalise the chain length effect, which was based on Gibbs's phase equilibrium principle (Section 4.2). The positive adsorption of counterions and water molecules reduced the repulsive electrostatic forces between the deprotonated surface sites, by increasing the repulsive hydration forces in the surface layer at the same time. The overall repulsive electrostatic and hydration forces induced an attractive counter force in elastic, solid-like long chain SAMs, whereas viscous, liquid-like short chain SAMs diffused laterally to level out the excess chemical potential, therefore in-plane counter forces were generated primarily at the gold surface. Consequently, chemically specific surface stress (determined by the SAM terminal group) was more efficiently transduced across long chain SAMs to the bulk cantilever material. It is important to allow for a sufficient rigidity of the chemically specific cantilever surface coating. The balance between force and counter force is the fundamental mechanism of interfacial stress transduction. Therefore, the resultant change in the cantilever curvature is the sum of all in-plane forces across the aqueous solution/cantilever/aqueous solution interface. Future experiments to relate the evolution of absolute surface stress during SAM formation on different substrates may unveil a fundamental role of surface stress in the self-assembly of these molecular monolayers.

11. Conclusions and Future Work

This work has investigated basic origins of pH-induced surface stress at the interface between self-assembled monolayers (SAMs) and aqueous electrolyte solutions as a model biological system. Interfacial excess pH, ionic strength, counterions/co-ions, as well as SAM chain lengths and terminal functional groups, were found to induce highly specific chemical and mechanochemical in-plane forces that controlled both the magnitude and direction of cantilever motion. An overall model is presented in Fig. 11.1 to summarise the experimental findings discussed in the preceding chapters. This is based on Gibbs's phase equilibrium model of a completely elastic solid (Section 4.2), which states that the transduction of an in-plane force applied by liquid molecules onto the solid surface is determined by the strength of the 'passive resistance' (Gibbs 1878) of the solid surface against the lateral displacement.

At the upper, gold evaporated cantilever surface functionalised with carboxylic acid terminated long chain SAMs, an increase in the pH of sodium phosphate solution from an acidic regime to a basic regime increased the surface excess amount of deprotonated, charged surface carboxylic acids and positively adsorbed sodium counterions and water molecules. The positive adsorption of counterions and water molecules reduced the repulsive electrostatic force between the deprotonated surface sites, by increasing the repulsive hydration force in the surface layer at the same time. The repulsive electrostatic and hydration forces induced an attractive counter force in alkyl chains that are rendered laterally elastic due to the sufficiently strong, chain/chain attractive van der Waals forces. This is the 'passive resistance' of these SAMs that counteracts the lateral displacement. These attractive counter forces generated in SAMs were thereupon transduced onto the gold surface, which in turn induced repulsive forces in the gold surface layer, whose 'passive resistance' is given by the strength of the metallic bond between surface gold atoms. The balance between force and counter force is the fundamental mechanism of interfacial stress transduction. Therefore, the resultant change in the cantilever curvature is the sum of all in-plane forces across the aqueous solution/cantilever/aqueous solution interface.

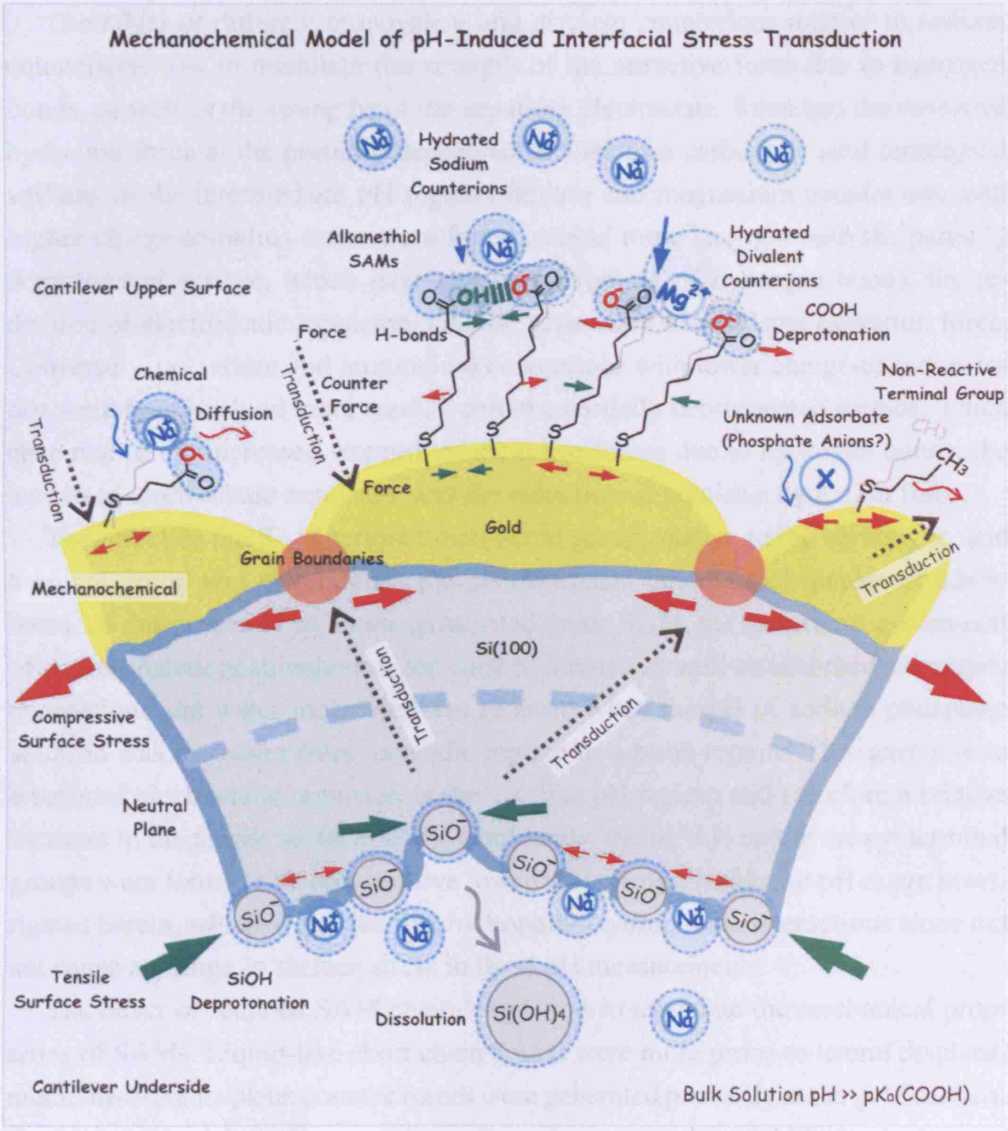

Fig. 11.1. Proposed mechanochemical model of pH-induced surface stress on a silicon cantilever functionalised on one side with carboxylic acid terminated SAMs on gold.

The effect of an intermediate pH regime close to the surface $pK_{1/2}$ was to produce a surface excess amount of in-plane attractive hydrogen bonds between protonated and deprotonated surface carboxylic acids, which gave rise to the contraction of the surface area. The attractive force acting between the SAM terminal groups generated a repulsive counter force between the alkyl chains, in turn inducing an attractive force at the underlying gold surface.

The effect of different monovalent and divalent counterions relative to sodium counterions was to modulate the strength of the attractive force due to hydrogen bonds, as well as the strengths of the repulsive electrostatic force and the repulsive hydration force at the partially deprotonated sites of a carboxylic acid terminated surface. In the intermediate pH regime, lithium and magnesium counterions with higher charge-to-radius ratios were found to bind more strongly onto the partially deprotonated surface, which gave rise to the rupture of hydrogen bonds, the reduction of electrostatic repulsion, and the generation of repulsive hydration force. Conversely, potassium and ammonium counterions with lower charge-to-radius ratios were found to bind more weakly onto the partially deprotonated surface, which gave rise to the increased strength of attractive forces due to hydrogen bonds, the increased electrostatic repulsion, and the reduction of repulsive hydration force.

The effect of the SAM terminal functional group relative to the carboxylic acid terminal group was to modulate the pH dependent amount and species of adsorbates. At the surface of an amine terminated, basic SAM, the surface excess amount of deprotonated, positively charged surface amines as well as adsorbed phosphate counterions and water molecules was reduced when the pH of sodium phosphate solution was increased from an acidic regime to a basic regime. This gave rise to a reduced electrostatic repulsion in the alkaline pH regime and therefore a relative increase in the tensile surface stress. Conversely, the methyl and hydroxyl terminal groups were found to be non-reactive toward pH change within the pH range investigated herein, which suggested that hydrophilic/hydrophobic interactions alone did not cause a change in surface stress in these pH measurements.

The effect of reduced SAM chain length was to modulate the mechanical properties of SAMs. Liquid-like short chain SAMs were more prone to lateral displacement, therefore in-plane counter forces were generated primarily at the gold surface. Consequently, chemically specific surface stress due to the SAM terminal group could not be efficiently transduced onto the bulk cantilever compared with more solid-like, long chain SAMs. It is important to allow for a sufficient rigidity of the chemically specific cantilever surface coating.

Further important findings resulted from this work concerned the origins of absolute bending signals in these pH measurements. The pH 4.8/8.4 switch of sodium phosphate solution was found to induce a compressive surface stress change in the gold surface layer. Since the compressive stress was measured on cantilevers coated with short chain SAMs and only weakly on cantilevers coated with long chain SAMs, this effect was attributed to the permeation of solution phase ions or

molecules across the liquid-like short chain SAMs and the subsequent adsorption onto the gold surface. The resultant pH-induced absolute stress at the gold evaporated upper surface was thus interpreted as a superposition of in-plane forces transduced from the liquid phase across SAMs to the gold surface and in-plane forces transduced from the gold surface across SAMs, thereby attributing the observed chain length dependence to the mechanical properties of alkyl chains, in agreement with the mechanochemical model proposed in Fig. 11.1. This model was supported also by the measurements of bimetallic stress and the spring constant of cantilevers.

Moreover, the high sensitivity and specificity of absolute stress signals on pH and cations suggested an important role of the lower cantilever surface that comprises a few nanometre thick layer of hydrous silicon oxide. Commercial pH meters rely on the change in the activity of hydrogen ions due to acid/base reactions of silicic acids $Si(OH)_4(aq)$ present at the hydrated surfaces of silica glass membranes, therefore, it would be rather surprising if the native dioxide SiO_2 layer of the bulk cantilever material did not respond to a change in pH or ions in solution. The pH and ion specificity of the absolute stress signals may be correlated with the dissolution of $Si(OH)_4(aq)$ from the cantilever underside, which may be regarded as a *negative* adsorption, giving rise to a large *tensile* surface stress change. Cantilevers may be used to probe the theory of crystal growth to probe the specific ion effects in the dissolution behaviour of silicate materials (Dove, Nizhou, and de Yereo 2005).

The magnitude of pH-induced absolute stress signals was typically three to four times larger than the corresponding differential signals. It seems surprising that the pH-induced absolute CH_3 signals did not show a strong monotonic chain length dependence as was observed in the bimetallic absolute stress signals. In fact, if the pH-induced absolute CH_3 stress was transduced across the SAM/gold interface, one would expect to observe a strong, monotonic chain length dependence according to the mechanochemical model. However, it is more simple to assume that the stress was *not* transduced across the SAM/gold interface. By further assuming that a tensile absolute stress was generated at the cantilever underside due to the dissolution of hydrous silicon oxide layer upon increasing the solution pH, the surface stress transduced across the bulk silicon cantilever material to the upper surface, yet not across the SAM/gold interface, suggested that the compressive surface stress at the upper surface was relieved along the grain boundaries of the evaporated gold surface. This is in agreement with cantilever studies reported by Godin et al. (2004a; 2004b), which showed an important role of the gold morphology in the generation of surface stress.

The conclusions so far concerned changes in surface stress in SAMs and in the gold film that had been already formed *prior* to the measurements. The initial surface stress generated *during* the SAM formation and subsequent storage in aqueous solution was found to be specific to the chain length of SAMs. In fact, the mechanochemical model proposed herein predicts an important role of the force balance between SAMs and the substrate. Future experiments to relate the evolution of absolute surface stress during SAM formation on different substrates may unveil a fundamental role of surface stress in the self-assembly of these molecular monolayers.

The results and the subsequent discussion of the results presented herein were only obtained upon a thorough optimisation of the technical aspects associated with this work. The development of a semi-automated fit software facilitated a systematic and rapid measurement of equilibrium bending signals with minimal user bias. The software has been continuously extended to handle different experiments flexibly, therefore, its further development is expected to follow with future experiments. For example, a precise control of the flow rate of electrolyte solutions will enable an investigation of the kinetics of surface stress generation, which will involve a fit of non-linear functions to the raw bending signals.

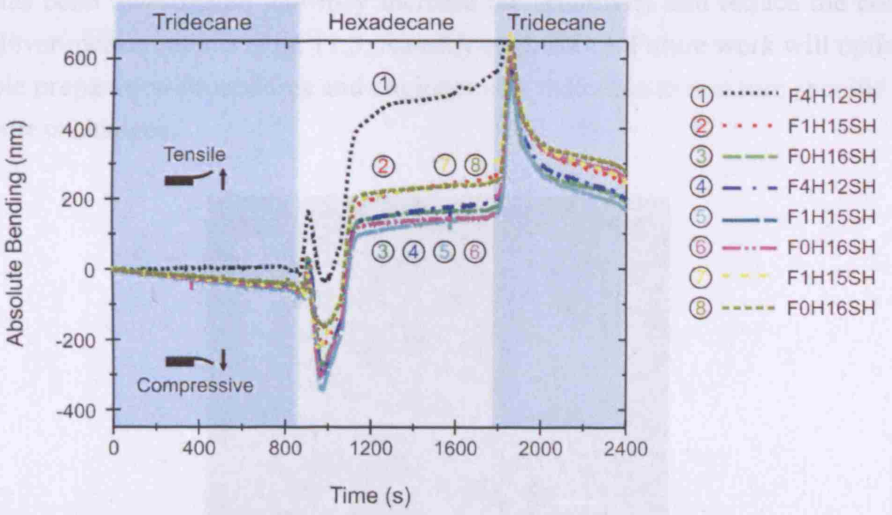

Fig. 11.2. Cantilever experiment to probe the effect of pure organic solvents tridecane and hexadecane, using C_{16} SAMs with zero $F_0H_{16}SH$, one $F_1H_{15}SH$, and four $F_4H_{12}SH$ terminally fluorinated carbon atoms. Owing to the substantive differences in the refractive index as well as the viscosity of the solvents, cantilever signals were determined by the cantilever position and not by the SAMs. Unpublished results by Watari et al. (2006), in collaboration with Prof. T. R. Lee's laboratory at the University of Houston.

The statistical model integrated basic statistical concepts such as random sampling and homogeneity of errors into cantilever measurements, rather than a mere analysis of the statistical significance.[1] The statistical analysis of the cantilever array data will develop with our understanding of cantilever array measurements.

The simulation of the Veeco Scentris instrument identified the initial deformation of cantilevers as an important source of measurement variability associated with this work. Understanding the functionality of a measurement device is critical both for the experimental design as well as for the interpretation of acquired data. For example, an experiment to probe different pure organic solvents cannot be performed using the Scentris instrument due to large differences in the refractive indices (Fig. 11.2). Future work will build new instruments to conduct more flexible research.

The gold evaporation procedure was found to be critical in controlling the magnitude of initial cantilever deformation, which required a high optimisation of evaporation parameters. The majority of cantilever array samples used in this work were prepared under already highly optimised conditions, using the facilities provided by the IBM Rüschlikon, including Prof. Gerber's and Dr. Delamarche's laboratories. Alternative cantilever materials that enable direct functionalisation without the need of evaporated thin films would be desirable. The use of SU8-photo resist has been investigated and may increase the sensitivity and reduce the cost of cantilever measurements (Fig. 11.3; Ransley et al. 2006). Future work will optimise sample preparation procedures and engineer new materials to measure specific surface stress changes.

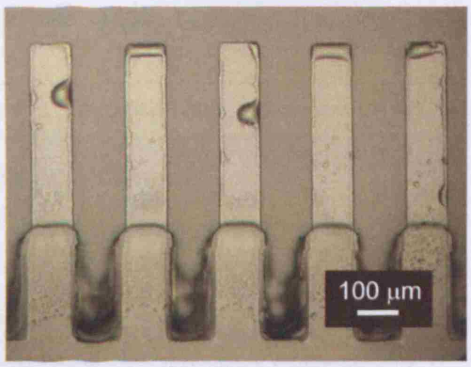

Fig. 11.3. Array of microfabricated SU-8 cantilevers. Unpublished results by J. H. T. Ransley et al. (2005).

[1] Something statistically significant may be of no practical importance, as pointed out by Jane Galbraith.

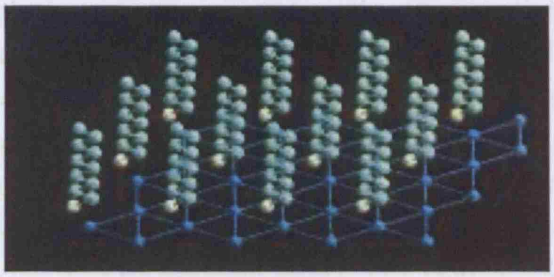

Fig. 11.4. Simulation of alkanethiol SAMs on Au(111). Unpublished results by Watari et al. (2004), in collaboration with Prof. A. Shluger's research group.

Experimental findings concerning model systems are particularly amenable to theoretical investigations. Preliminary attempts to model SAMs at these biochemical interfaces have been made in this work in collaboration with Dr. M. Sushko and Prof. A. Shluger from the LCN, as well as with Prof. J. H. Harding from the University of Sheffield. However, ongoing collaborative research include the development of physical models both at classical and quantum mechanical level, which will provide novel insights into the physical origins of surface stress generation (Fig. 11.4).

Clinical and biomedical applications of cantilevers represent a future mile stone (Fig. 11.5). The sensitivity and reproducibility are two important requirements for biosensing applications of cantilevers among others, including the selectivity, biocompatibility, portability, and cost. The results of pH and bimetallic stress measurements presented in this work can give an estimate for the current performance of cantilever arrays compared with commercial pH and temperature sensors under similar experimental conditions. Table 11 shows the *ideal* performance of cantilevers,

		Detection Limit	Standard Error	Commercial
pH	MHA/HDT	±0.05	±0.5	±0.01 [a]
	SiO_2 /HDT	±0.01		
Temperature		±0.003	±0.01	±0.01 [b]

[a] Delta 340, Mettler-Toledo Ltd., Leicester, U.K.
[b] TC-08 Thermocouple, Pico-Technology, Cambridgeshire, U.K.

Table 11.1. Detection limit and typical standard error of cantilever arrays compared with typical standard errors associated with commercial sensors in $I = 0.1$ buffered aqueous environments.

calculated from typical mean stress signals and the detection limit of 1 nm bending signal of the Scentris instrument, the *empirical* performance of cantilevers corresponding to typical standard errors associated with the measurements, as well as empirical performance of *commercial* sensors, estimated from typical measurement errors. The table suggests that the ideal performance of cantilever arrays may be comparable to commercial sensors, however, their empirical performance is substantively reduced due to measurement errors. The high sensitivity of bimetallic cantilevers to temperature changes has been reported in early studies (for example, Barnes et al. 1994). However, the complex and expensive optical read-out system of cantilevers is not yet competitive with the simple, robust, low-cost, and portable design of commercial thermocouple devices. Furthermore, bimetallic cantilevers must be chemically isolated to minimise surface stress changes due to chemical reactions.

Despite the basic issues associated with the practicality of cantilever sensors, the literature has demonstrated the capability of cantilevers to detect specific biochemical interactions, including DNA hybridisation or antibody-antigen recognition with nanomolar to picomolar detection sensitivities (for example, McKendry et al. 2002; Fritz et al. 2000). Understanding the origins of surface stress will become increasingly important as the dimensions of the solid shrink down to the nanometre molecular length scale. Based upon the knowledge of surface stress provided by this work concerning the pH, ionic strength, interfacial cations/anions, as well as

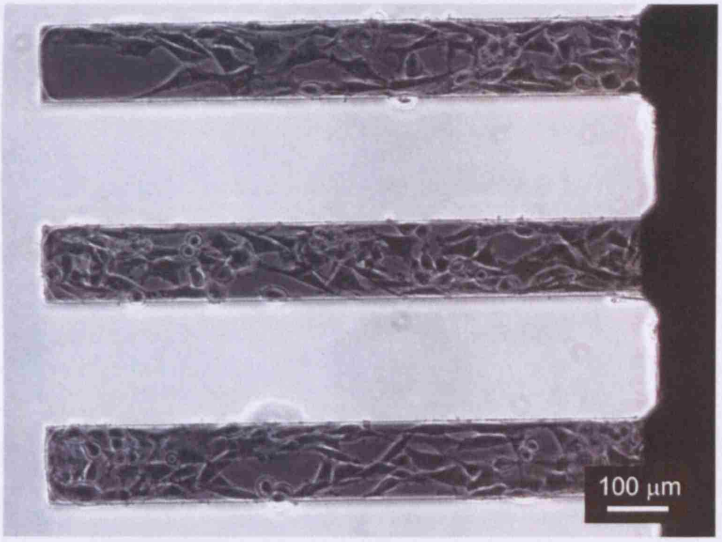

Fig. 11.5. Monitoring the proliferation of L6 myoblasts on cantilever arrays. Unpublished results by Watari et al. (2004).

mechanical properties and chemical functionality of SAMs, future experiments will extend to the study of biochemical interfaces from molecular thin films to cellular membranes.

Alexander, G. B., W. M. Heston, and R. K. Iler (1954): "The solubility of amorphous silica in water," *J. Phys. Chem.*, **58**, 453.

Arnold, R., W. Azzam, A. Terfort, and C. Wöll (2002): "Preparation, modification, and crystallinity of aliphatic and aromatic carboxylic acid terminated self-assembled monolayers," *Langmuir*, **18**, 3980.

Atkins, P., and J. de Paula (2006): *Atkins' Physical Chemistry*. Oxford Press, **8** edn.

Backmann, N., C. Zahnd, F. Huber, A. Bietsch, A. Plückthun, H. Lang, H.-J. Güntherodt, M. Hegner, and C. Gerber (2005): "A label-free immunosensor array using single-chain antibody fragments," *Proc. Natl. Acad. Sci. U.S.A.*, **102**, 14587.

Bain, C. D., E. B. Troughton, Y.-T. Tao, J. Evall, G. M. Whitesides, and R. G. Nuzzo (1989): "Formation of monolayer films by the spontaneous assembly of organic thiols from solution onto gold," *J. Am. Chem. Soc.*, **111**, 321.

Balzer, F., R. Gerlach, G. Polanski, and H.-G. Rubahn (1997): "Chain length dependence of the structure of alkane thiol films on Au(111)," *Chem. Phys. Lett.*, **274**, 145.

Barnes, J. R., R. J. Stephenson, C. N. Woodburn, S. O'Shea, M. E. Welland, T. Rayment, J. K. Gimzewski, and C. Gerber (1994): "A femtojoule calorimeter using micromechanical sensors," *Rev. Sci. Instrum.*, **65**, 3793.

Bates, R. G. (1973): *Determination of pH. Theory and Practice*. Wiley Press, **2** edn.

Berger, R., E. Delamarche, H. P. Lang, C. Gerber, J. K. Gimzewski, E. Meyer, and H.-J. Güntherodt (1997): "Surface stress in the self-assembly of alkanethiols on gold," *Science*, **276**, 2021.

Biener, M. M., J. Biener, and C. M. Friend (2005): "Revisiting the S-Au(111) interaction: static or dynamic?," *Langmuir*, **21**, 1668.

Bietsch, A., J. Zhang, M. Hegner, H. P. Lang, and C. Gerber (2004): "Rapid functionalization of cantilever array sensors by inkjet printing," *Nanotechnology*, **15**, 873.

Brantley, W. A. (1973): "Calculated elastic constants for stress problems associated with semiconductor devices," *J. Appl. Phys.*, **44**, 534.

Brønsted, J. N. (1923): "The individual thermodynamic properties of ions," *J. Am. Chem. Soc.*, **45**, 2898.

Brunt, T. A. (1997): "Surface stress measurements at the solid-liquid interface using a micromechanical sensor," Ph.D. thesis, University of Cambridge.

Burgess, J. (1978): *Metal Ions in Solution*. Wiley Press.

Chandrasekaran, S., and S. Sundararajan (2004): "Effect of microfabrication processes on surface roughness parameters of silicon surfaces," *Surface & Coatings Technology*, **188**, 581.

Clark Jr, L. C., G. Mishray, and R. P. Fox (1958): "Chronically implanted polarographic electrodes," *J. Appl. Physiol.*, **13**, 85. *Cited in* Cunningham (1998).

Cunningham, A. J. (1998): *Introduction to Bioanalytical Sensors*. Wiley Press.

Dai, Z., and H. Ju (2001): "Effect of chain length on the surface properties of ω-carboxy alkanethiol self-assembled monolayers," *Phys. Chem. Chem. Phys.*, **3**, 3769.

Dove, P. M., H. Nizhou, and J. J. de Yereo (2005): "Mechanisms of classical crystal growth theory explain quartz and silicate dissolution behavior," *Proc. Natl. Acad. Sci. U.S.A.*, **102**, 15357.

Dubois, L. H., and R. G. Nuzzo (1992): "Synthesis, structure, and properties of model organic surfaces," *Ann. Rev. Phys. Chem.*, **43**, 437.

Fenter, P., A. Eberhardt, K. S. Liang, and P. Eisenberger (1997): "Epitaxy and chainlength dependent strain in self-assembled monolayers," *J. Chem. Phys.*, **106**, 1600.

Fenter, P., P. Eisenberger, and K. S. Liang (1997): "Chain-length dependence of the structures and phases of $CH_3(CH_2)_{n-1}SH$ self-assembled on Au(111)," *Phys. Rev. Lett.*, **70**, 2447.

Fitts, W. P., J. M. White, and G. E. Poirier (2002): "Low-coverage decanethiolate structure on Au(111): substrate effects," *Langmuir*, **18**, 1561.

Fodor, S. P. A., R. J. L., P. M. C., S. L., L. A. T., and D. Solas (1991): "Light-directed spatially addressable parallel chemical synthesis," *Science*, **251**, 767. *Cited in* Cunningham (1998).

Fowkes, F. M. (1964): "Attractive forces at interfaces," *Ind. Eng. Chem.*, **56**, 40.

Fritz, J., M. K. Baller, H. P. Lang, H. Rothuizen, P. Vettiger, E. Meyer, H.-J. Güntherodt, C. Gerber, and J. K. Gimzewski (2000a): "Translating biomolecular recognition into nanomechanics," *Science*, **288**, 316.

Fritz, J., M. K. Baller, H. P. Lang, T. Struntz, E. Meyer, H.-J. Güntherodt, E. Delamarche, C. Gerber, and J. K. Gimzewski (2000b): "Stress at the solid-liquid interface of self-assembled monolayers on gold investigated with a nanomechanical sensor," *Langmuir* , **16**, 9694.

Fritz, J., E. B. Cooper, S. Gaudet, P. K. Sorger, and S. Manalis (2002): "Electronic detection of DNA by its intrinsic molecular charge," *Proc. Natl. Acad. Sci. U.S.A.* , 99, 14142.

Galbraith, J., M. Watari, M. A. Horton, and R. A. McKendry (2007): Unpublished results.

Gershevitz, O., and C. N. Sukenik (2004): "In situ FTIR-ATR analysis and titration of carboxylic acid-terminated SAMs," *J. Am. Chem. Soc.* , **126**, 482.

Gibbs, J. W. (1878): "On the equilibrium of heterogeneous substances," *Trans. Conn. Acad.* , **3**, 343. *Cited in* Rusanov (1996).

Glembocki, O. J., E. D. Palik, G. R. de Guel, and D. L. Kendall (1991): "Hydration model for the molarity dependence of the etch rate of Si in aqueous alkali hydroxides," *J. Electrochem. Soc.* , **138**, 1055.

Godin, M. (2004): "Surface stress, kinetics, and structure of alkanethiol self-assembled monolayers," Ph.D. thesis, McGill University.

Godin, M., P. J. Williams, V. Tabard-Cossa, O. Laroche, L. Y. Beaulieu, R. B. Lennox, and P. Grütter (2004): "Surface stress, kinetics, and structure of alkanethiol self-assembled monolayers," *Langmuir* , **20**, 7090.

Greenberg, S. A., and E. W. Price (1957): "The solubility of silica in solutions of electrolytes," *J. Phys. Chem.* , **61**, 1539.

Haiss, W. (2001): "Surface stress of clean and adsorbate-covered solids," *Rep. Progr. Phys.* , **64**, 591.

Harding, J. H., M. Watari, M. A. Horton, and R. A. McKendry (2006): Unpublished results.

Hecht, E. (1998): *Optics*. Addison-Wesley Press, **3** edn.

Holmes-Farley, S. R., C. D. Bain, and G. M. Whitesides (1988): "Acid-base behavior of carboxylic acid groups covalently attached at the surface of polyethylene: the usefulness of contact angle in following the ionization of surface functionality," *Langmuir* , **4**, 921.

House, W. A., and D. R. Orr (1992): "Investigation of the pH dependence of the kinetics of quartz dissolution at 25°C," *J. Chem. Soc. Faraday Trans.* , **88**, 233.

Hutter, J. L., and J. Bechhoefer (1993): "Calibration of atomic-force microscope tips," *Rev. Sci. Instrum.* , **64**, 1868. *Cited in* Veeco DI Scentris, Support Note 367, Revision B.

Ibach, H. (1997): "The role of surface stress in reconstruction, epitaxial growth and stabilization of mesoscopic structures," *Surf. Sci. Rep.* , **29**, 193.

Ilic, B., D. Czaplewski, M. Zalalutdinov, C. H. G., P. Neuzil, C. Campagnolo, and C. Batt (2001): "Single cell detection with micromechanical oscillators," *J. Vac. Sci. Technol. B* , **19**, 2825.

Israelachvili, J. (1992): *Intermolecular & Surface Forces*. Academic Press, **2** edn.

Jeon, S., and T. Thundat (2004): "Instant curvature measurement for microcantilever sensors," *Appl. Phys. Lett.* , **85**, 1083.

Kakiuchi, T., M. Iida, S. Imabayashi, and K. Niki (2000): "Double-layer-capacitance titration of self-assembled monolayers of ω-functionalized alkanethiols on Au(111) surface," *Langmuir* , **16**, 5397.

Keeler, J., and P. Wothers (2003): *Why Chemical Reactions Happen*. Oxford Press.

Klein, C. A. (2000): "How accurate are Stoneys equation and recent modifications," *J. Appl. Phys.* , **886**, 5487.

Konek, C. T., M. J. Musorrafiti, H. A. Al-Abadleh, P. A. Bertin, S. T. Nguyen, and F. M. Geiger (2004): "Interfacial acidities, charge densities, potentials, and energies of carboxylic acid-functionalized silica/water interfaces determined by second harmonic generation," *J. Am. Chem. Soc.* , **126**, 11754.

Landau, L. D., and E. M. Lifshitz (1986): *Theory of Elasticity*. Butterworth-Heinemann, **3** edn.

Lee, T. R., R. I. Carey, H. A. Biebuyck, and G. M. Whitesides (1994): "The wetting of monolayer films exposing ionizable acids and bases," *Langmuir* , **10**, 741.

Leopold, M. C. (2000): "Interfacial investigations of a biological electron transfer model: cytochrome c adsorbed on gold electrodes modified with self-assembled monolayers.," Ph.D. thesis, North Carolina State University.

Li, J., K. S. Liang, G. Scoles, and A. Ulman (1995): "Counterion overlayers at the interface between an electrolyte and an ω-functionalized monolayer self-assembled on gold. An X-ray reflectivity study," *Langmuir* , **11**, 4418.

Lide, D. R. (2005): *CRC Handbook of Chemistry and Physics*. CRC Press, **86** edn.

McKendry, R., J. Zhang, Y. Arntz, T. Strunz, M. Hegner, H. P. Lang, M. K. Baller, U. Certa, E. Meyer, H.-J. Güntherodt, and C. Gerber (2002): "Multiple label-free biodetection and quantitative DNA-binding assays on a nanomechanical cantilever array," *Proc. Natl. Acad. Sci. U.S.A.*, **99**, 9783.

Meot-Ner, M., D. E. Elmore, and S. Scheiner (1999): "Ionic hydrogen bond effects on the acidities, basicities, solvation, solvent bridging, and self-assembly of carboxylic groups," *J. Am. Chem. Soc.*, **121**, 7625.

Mertens, J., M. Álvarez, and J. Tamayo (2005): "Real-time profile of microcantilevers for sensing applications," *J. Appl. Phys. Lett.*, **87**, 234102.

Montgomery, D. C. (2005): *Design and Analysis of Experiments*. Wiley Press, **6** edn.

Mukhopadhyay, R., M. Lorentzen, J. Kjems, and F. Besenbacher (2005): "Nanomechanical sensing of DNA sequences using piezoresistive cantilevers," *Langmuir*, **21**, 8400.

Müller, P., and A. Saúl (2004): "Elastic effects on surface physics," *Surf. Sci. Rep.*, **54**, 157.

Nightingale, E. R. (1959): "Phenomenological theory of ion solvation. effective radii of hydrated ions," *J. Phys. Chem.*, **63**, 1381.

Nuzzo, R. G., and D. L. Allara (1983): "Adsorption of bifunctional organic disulfides on gold surfaces," *J. Am. Chem. Soc.*, **105**, 4481.

Nuzzo, R. G., L. H. Dubois, and D. L. Allara (1990): "Fundamental studies of microscopic wetting on organic surfaces. 1. Formation and structural characterization of a self-consistent series of polyfunctional organic monolayers," *J. Am. Chem. Soc.*, **112**, 558.

Nye, J. F. (1957): *Physical Properties of Crystals*. Oxford University Press.

O'Dwyer, C., G. Gay, B. Viaris de Lesegno, and J. Weiner (2004): "The nature of alkanethiol self-assembled monolayer adsorption on sputtered gold substrates," *Langmuir*, **20**, 8172.

Ott, R. L. (1993): *An Introduction to Statistical Methods and Data Analysis*. Duxbury Press, **4** edn.

Park, J., J. Ryu, S. K. Choi, E. Seo, J. M. Cha, S. Ryu, J. Kim, B. Kim, and S. H. Lee (2005): "Real-time measurement of the contractile forces of self-organized cardiomyocytes on hybrid biopolymer microcantilevers," *Anal. Chem.*, **77**, 6571.

Parks, G. A. (1965): "The isoelectric points of solid oxides, solid hydroxides, and aqueous hydroxo complex systems," *Chem. Rev.*, **65**, 177.

Poirier, G. E. (1997): "Characterization of organosulfur molecular monolayers on Au(111) using scanning tunneling microscopy," *Chem. Rev.*, **97**, 1117.

——— (1999): "Coverage-dependent phases and phase stability of decanethiol on Au(111)," *Langmuir*, **15**, 1167.

Poirier, G. E., and P. E. D. (1996): "The self-assembly mechanism of alkanethiols on Au(111)," *Science*, **272**, 1145.

Porter, M. D., T. B. Bright, D. L. Allara, and C. E. D. Chidsey (1987): "Spontaneously organized molecular assemblies. 4. Structural characterization of n-alkyl thiol monolayers on gold by optical ellipsometry, infrared spectroscopy, and electrochemistry," *J. Am. Chem. Soc.*, **109**, 3559.

Raiteri, R., H.-J. Butt, and M. Grattarola (2000): "Changes in surface stress at the liquid/solid interface measured with a microcantilever," *Electrochim. Acta*, **46**, 157.

Ramsay, G. (1998): *Commercial Biosensors*. Wiley Press.

Ransley, J. H. T., M. Watari, D. Sukumaran, R. A. McKendry, and A. A. Seshia (2006): "SU8 bio-chemical sensor microarrays," *Microelectronic Engineering*, **83**, 1621.

Rasmussen, P. A., O. Hansen, and A. Boisen (2005): "Cantilever surface stress sensors with single-crystalline silicon piezoresistors," *Appl. Phys. Lett.*, **86**, 203502.

Robinson, R. A., and R. H. Stokes (1949): "Tables of osmotic and activity coefficients of electrolytes in aqueous solution at 25 °C," *Trans. Faraday Soc.*, **45**, 612.

Rusanov, A. I. (1996): "Thermodynamics of solid surfaces," *Surf. Sci. Rep.*, **23**, 173.

——— (2005): "Surface thermodynamics revisited," *Surf. Sci. Rep.*, **58**, 111.

Sader, J. E. (2001): "Surface stress induced deflections of cantilever plates with applications to the atomic force microscope: rectangular plates," *J. Appl. Phys.*, **89**, 2911.

Savran, C. A., S. M. Knudsen, A. D. Ellington, and M. S. R. (2004): "Micromechanical detection of proteins using aptamer-based receptor molecules," *Anal. Chem.*, **316**, 3194.

Schreiber, F. (2000): "Structure and growth of self-assembling monolayers," *Prog. Surf. Sci.*, **65**, 151.

Schwartz, D. K. (2001): "Mechanisms and kinetics of self-assembled monolayer formation," *Annu. Rev. Phys. Chem.* , **52**, 107.

Shu, W., D. Liu, M. Watari, C. K. Riener, T. Strunz, M. E. Welland, S. Balasubramanian, and R. A. McKendry (2005): "DNA molecular motor driven micromechanical cantilever arrays," *J. Am. Chem. Soc.* , **127**, 17054.

Sjölander, S., and S. Urbanicky (1991): "Integrated fluid handling system for biomolecular interaction analysis," *Anal. Chem.* , **63**, 2338. *Cited in* Ramsay (1998).

Smith, D. A., M. L. Wallwork, J. Zhang, J. Kirkham, C. Robinson, A. Marsh, and M. J. Wong (2000): "The effect of electrolyte concentration on the chemical force titration behavior of ω-functionalized SAMs: evidence for the formation of strong ionic hydrogen bonds," *J. Phys. Chem. B* , **104**, 8862.

Stoney, G. G. (1909): "The tension of metallic films deposited by electrolysis," *Proc. Roy. Soc. London, Ser. A.* , **82**, 172.

Strong, L., and G. M. Whitesides (1988): "Structures of self-assembled monolayer films of organosulfur compounds adsorbed on gold single crystals: electron diffraction studies," *Langmuir* , **4**, 546.

Ulman, A. (1991): *An Introduction to Ultrathin Organic Films: From Langmuir-Blodgett to Self-Assembly*. Academic Press.

——— (1996): "Formation and structure of self-assembled monolayers," *Chem. Rev.* , **96**, 1533.

van der Vegte, E. W., and G. Hadziioannou (1997): "Acid-base properties and the chemical imaging of surface-bound functional groups studied with scanning force microscopy," *J. Phys. Chem. B* , **101**, 9563.

van Lier, J. A., P. L. de Brun, and J. T. G. Overbeek (1960): "The solubility of quartz," *J. Phys. Chem.* , **64**, 1675.

Vericat, C., M. E. Vela, and R. C. Salvarezza (2005): "Self-assembled monolayers of alkanethiols on Au(111): surface structures, defects and dynamics," *Phys. Chem. Chem. Phys.* , **7**, 3258.

Vettiger, P., M. Despont, U. Drechsler, U. Durig, W. Haberle, M. Lutwyche, H. Rothuizen, R. Stutz, R. Widmer, and G. K. Binnig (2000): "The "millipede" - Nanotechnology entering data storage," *IBM J. Res. Dev.* , **44**, 323.

Vezenov, D. V., A. Noy, L. F. Rozsnyai, and C. M. Lieber (1997): "Force titrations and ionization state sensitive imaging of functional groups in aqueous solutions by chemical force microscopy," *J. Am. Chem. Soc.* , **119**, 2006.

Wang, J., L. M. Frostman, and M. D. Ward (1992): "Self-assembled thiol monolayers with carboxylic acid functionality: measuring pH-dependent phase transitions with the quartz crystal microbalance," *J. Phys. Chem.* , **96**, 5224.

Watari, M. (2003): "Application of an array of point-like shear forces on living cells," Diploma thesis, University of Heidelberg.

Watari, M., J. Galbraith, H. P. Lang, M. Sousa, M. Hegner, C. Gerber, M. A. Horton, and R. A. McKendry (2007): "Investigating the molecular mechanisms of in-plane mechanochemistry on cantilever arrays," *J. Am. Chem. Soc.* , **129**, 601.

Wu, G. H., H. F. Ji, K. Hansen, T. Thundat, R. Datar, R. Cote, M. F. Hagan, A. K. Chakraborty, and A. Majumdar (2001): "Origin of nanomechanical cantilever motion generated from biomolecular interactions," *Proc. Natl. Acad. Sci. U.S.A.* , **98**, 1560.

Zamborini, F. P., and R. M. Crooks (1998): "Corrosion passivation of gold by n-alkanethiol self-assembled monolayers: effect of chain length and end group," *Langmuir* , **14**, 3279.